SAFETY AND SERVICEABILITY OF EMBANKMENT UNDER SEASONAL VARIATIONS AND EXTREME CLIMATE

ARWAN APRIYONO

A THESIS SUBMITTED IN PARTIAL FULFILLMENT
OF THE REQUIREMENT FOR THE DEGREE OF
DOCTOR OF ENGINEERING IN CIVIL ENGINEERING
SCHOOL OF ENGINEERING
KING MONGKUT'S INSTITUTE OF TECHNOLOGY LADKRABANG
2023

Copyright Page

Thesis	Safety and Serviceability of Embankment Under Seasonal Variations and Extreme Climate
Student	Arwan Apriyono
Student ID.	63601249
Degree	Doctor of Engineering
Program	Civil Engineering
Year	2023
Thesis Advisor	Assoc. Prof. Dr. Viroon Kamchoom

ABSTRACT

Serviceability is one of the primary issues in the design of earthwork. In terms of fine-grain material, the problem will be more sophisticated due to the presence of desiccation cracks. The cracks may provide a preferential path-flows for water infiltration, leading to stability problems, caused by the increase in water content. On the other hand, the amount of evaporation may double with the increase in soil surface area. The fluctuation of pore water pressure during seasonal variations owing to the wetting and drying cycles will promote serviceability problems in the embankment. Moreover, the impact of extreme climate as a result of climate change is inevitable and will deteriorate embankment problems. Accordingly, it is important to study fine grained embankment behaviour under seasonal variation and extreme climate conditions. The aims of this study are (i) to observe crack intensity and propagation along the season; (ii) to observe the PWP response of the embankment with desiccation cracks under evaporation and rainfall; (iii) to observe slope deformation under seasonal variation; and (iv) to predict PWP and deformation under extreme climate conditions.

To facilitate this research, a full-scaled embankment model has been built. Arrays of sensors, such as PWP and volumetric water content sensors were also deployed to investigate hydraulic parameters over the research duration. Following this, a set of weather station was also installed in the research location to obtain associated weather data (i.e., rainfall, humidity, air temperature, solar radiation, and wind speed). To forecast extreme weather data, a bias-correction and spatial disaggregation (BCSD) method was employed, considering 30 years of historical weather data.

The result indicates that the value of CIF at near surface area during severe drought climate (second year) was 1.6 times higher than that in the first year (moderate drought) attributed to higher air temperature and less rainfall intensity during severe drought, promoting more significant soil shrinkage. Furthermore, drying and wetting cycle triggered the existence of non-connected cracks at the middle depth of the embankment which was less affected by seasonal condition, promoting the increase in CIF. 5) Since experienced with more extreme climate condition in the second year, the embankment tended to have lower minimum VWC in the second summer, rather than the first summer, attributed to the higher evaporation and less rainfall intensity during severe dry increasing soil moisture deficit, and thus decreasing VWC. In the context of CIF and VWC correlation, higher CIF tend to have lower and more fluctuated value of VWC in association with higher evaporation value. Moreover, compared to near surface area, the same range of AWB and CIF at the deeper depth produced more fluctuated value of VWC.

In the context of extreme climate, extreme dry conditions produced higher y-axis displacements, compared to current and wet climate conditions. It can be attributed to the modest rainfall intensity during extreme dry climate. Therefore, embankment experienced notable shrinkage, resulting in significant y-axis displacement. In addition, the PWP value contributed to a greater degree of fluctuation in the FOS value during extreme dry conditions than during extreme wet conditions. As the PWP decreased to its minimum value at the end of the dry season, the value of FOS increased significantly (2.3). On the contrary, the FOS plummeted by approximately 1.0 at the beginning of the rainy season due to the increase in PWP.

Acknowledgment

Firstly, I would like to express my profound gratitude to my honourable advisor, Assoc. Prof. Viroon Kamchoom, Ph. D for his advisory and hospitality during my study. I am very blessed and fortune to have him as my advisor. Since I literally started from scratch, I truly believe that this research would have not completed without his help and encouragement. I would also like to extend my sincere appreciation to all of the committee members for their advice during my study and my defence.

Secondly, I would like to thank my research's partner, Mas Sony, Mbak Yuliana and Tapakorn Sakolpanya for their friendship and partnership. I cannot complete my research on time without your help and support. I am so happy to have such responsible and kind friends as you. I hope we can continue our collaboration in the future. I also must acknowledge the funding and support for this research, provided by King Mongkut's Institute of Technology Ladkrabang (The Grants No KDS 2020/017).

A Special thanks to my lovely wife who has accompanied me patiently throughout our time in Thailand. I can feel that it was not easy to live far away from our family, especially during the pandemic. However, with your love and compassion, we can overcome all of those situations together. Last but not least, I would like to thank Bapak, Ibu, Babe, Mama, Puthut, Putri and Idut for their continuous support during my studies.

List of Content

List of Figure

List of Table

Chapter 1 Introduction

1.1 Background and Significant of The Problem

Stability and serviceability issues of the embankment is inevitably as the effect of seasonal behaviour. In the last decade, many earthworks failure have been reported in associated with serviceability issue (Fredlund and Rahardjo, 1993; Ranjan and Rao, 2000; Briggs et al., 2019). Inappropriate consideration during design or implementation deteriorated the problem, triggering more sophisticate condition in the structure. As a result, emergency repair was estimated to be 10 times higher than regular maintenance (Glendinning et al., 2014). Yet, in the worst case, slope failure will cause fatal consequences in the future, such as loss of human life (Postill, 2018). Therefore, a basic and advanced knowledge of their behaviour is essential for design purposes. Since it has complicated mechanism, the study of serviceability issue is challenging for researchers, particularly in fine-grained materials that PWP plays an important role (Nyambayo et al., 2004; Hughes et al., 2009; Rouainia et al., 2009; Glendinning et al., 2014; Smethurst et al., 2015).

The present of cracks is one of sophisticated issue occurred in natural or engineered clay construction. It is well-known that cracks can significantly influence both stability and serviceability problem in earth work (Baker, 1981; Lee et al., 1988; Chowdhury and Zhang, 1991; Shrestha et al., 2019). Crack will lead preferential pathway of water infiltration in soil, inducing the increase in hydraulic conductivity and PWP. Thus, soil shear strength will be vigorously decrease, triggering slope instability (Peron, Delenne, et al., 2009; Li and Zhang, 2010; Li et al., 2011). On the other hand, cracks existence raises actual evaporation with respect to an increase in evaporative surface from one-dimensional to three-dimensional pattern (Song and Cui, 2019; Cui et al., 2021). Based on Kuhn and Zornberg (2006), evaporation rate can be double with cracking, compared to initial compacted soil. Consequently, it causes considerably decrease in both soil water content and PWP, altering hydro-mechanical behaviour of soil.

As external factor, extreme climate as a result of climate change is the most advanced issue that must be considered in the earthwork structure design. It has already proven that extreme climate has the potential to have a greatly effect on the infrastructure, especially in soil structure such as embankment (Hughes et al., 2009; Dijkstra and Dixon, 2010; Assadollahi and Nowamooz, 2020a). Climate change will lead the increasing of extreme rainfall and drought, ratcheting stability and serviceability problem in the embankment (Davies et al., 2008; Hudacsek et al., 2009; Hughes et al., 2009; An et al., 2018). This will induce the alteration of annual PWP cyclic in the slope, resulting higher PWP in the rainy season and lower PWP during dry season. Moreover, this condition will change cyclic water balance variation, causing loads fluctuation to the fill material within the embankments. These higher range of both water content and PWP cyclic have a significant impact on infrastructure slope serviceability such as triggering progressive failure (Vaughan et al., 1979; Leroueil, 2001; Ridley et al., 2004; Hudacsek et al., 2009; Glendinning et al., 2014; Smethurst et al., 2015).

Since climate is multi-scalar phenomenon and related to multi-discipline of knowledge, selecting the appropriate parameter to represent their condition is essential. The Standardized Precipitation Evapotranspiration Index (SPEI), developed by Vicente-Serrano et al (2010) and (Begueria et al. (2014) is widely-used in many field of knowledge to evaluate climate in any particular area (Yang et al., 2016; Muangthong et al., 2020). This index combines the advantages of two previous index (PSI and PDSI), which takes into account of precipitation and potential evaporation (PET) as well as the spatial consistency and multiple temporal scales (Vicente-Serrano et al., 2010; Ye et al., 2019; Cui et al., 2021). As SPEI was suitable to represent climate condition, it is important to study the correlation between this index and embankment behaviour.

The objective of the research is to observe the influence of seasonal wet and drought considering climate change and cracks within full-scale clay embankment. The present of the crack has taken into account in this research as it is essential factor and inevitably in high plasticity earthwork structure. Arrays of equipment has been installed in the model to measure PWP, volumetric water content (VWC), current weather data, and cracks behaviour. Following this, historical weather data have been provided by Thailand Government, which is considerably to calculate climate index. This historical data was also used to predict future weather data to support parametric study. Moreover, to emphasis the result, both back analysis and parametric study has been performed in this study using numerical simulation. The result of this research will improve the basic understanding of climate index and embankment behaviour correlation with respect to the cracks. Furthermore, it will provide new point of view to consider climate in earthwork as commencement for further study.

1.2 Scope of Study

Regarding the background, in general, the scope of this study is to investigate stability and serviceability problem of embankment under seasonal variation and extreme climate. Accordingly, full-scaled embankment model, measuring length of 20 m, width of 9 m and height of 1.8 m have been built in September 2020. Moreover, hydromechanical data such as PWP, VWC and deformation have been collected from the embankment since July 2021 to September 2023. Besides, a set of weather data have also obtained from weather station, comprised rainfall, air temperature, relative humidity, solar radiation, and wind speed. Further to this, the behaviour of hydromechanical parameter due to wetting and drying cycle has been analyzed in this study. Since the embankment was constructed from Bangkok clay, the attendance of soil cracks has also been taken into account analysis.

To obtain a better understanding of the correlation among the related parameter, numerical back analysis has been performed in this research. To do so, semi couple analysis using Geostudio software has been deployed to simulate the model. PWP response due to seasonal variation has been calculated by Seep/W transient analysis. Following this, Sigma/W has been employed to compute deformation behaviour pertaining to PWP fluctuation. Besides, stress reduction method was used to analyze Factor of Safety (FOS) of the embankment. In order to predict embankment behaviour considering extreme climate, numerical parametric study has been performed in this study. Prior to this analysis, extreme weather data consisted of near, middle and far future scenarios have been predicted using downscaling technique. It should be noted that, future crack has also been considered in this simulation.

1.3 Content of Thesis

Considering the scope of this study, this report was organized into five different chapters. Each chapter represent the hierarchy of logic and step of the research. In detail, the content of this thesis can be seen as follows.

Chapter 1 presented the background and the significant of the problem in this study. Important phenomena regarding the research aims were described in this chapter, as well as recently associated study. Following this the problem significant has been derived considering the background story. To illuminate point of view, scope of the study has also been elucidated in this chapter. Moreover, the scope has been broken down in the thesis content.

To obtain state of the art of this research, it is highly essential to review associated literature. In chapter 2, basic and advance literatures related to the research topic such as unsaturated soil, soil-climate interaction, climate change, shrinkage and crack, stability and serviceability problem and physical and numerical study have been reviewed. Key finding and limitation of those reference were analyzed to find the research gap; therefore, research objective can be derived.

In order to solve the research aims, organized procedure should be applied in this study, presented in research methodology. Chapter 3 presented methodology of research, consisting of site location, soil type, full-scale embankment, double ring infiltrometer, climate analysis, PWP monitoring, and deformation and crack observation. Detail explanation for each step has been clearly explained in this chapter.

Regarding the complex content of numerical simulation, it is necessary to present numerical simulation solely, separated from research methodology. Likewise, chapter 4 also described specific step of numerical simulation, comprising model geometry, material properties, boundary condition, and analysis procedure. Meticulous description associated with numerical simulation has been presented in this chapter

Chapter 5 presents weather data observation result, consisting of current and historical weather data. Current weather data were obtained from weather station which was installed in the embankment. Current weather data are important parameter to study embankment behaviour under seasonal parameter. Moreover, historical weather data were used to predict future weather data as essential parameter to do parametric study.

The attendance of desiccation crack is one of the essential factors that should be taken into account in this study, presented in chapter 6. Regarding field observation, both surface and subsurface cracks observation were be reported in this chapter. Further to this, the correlation between crack propagation and weather condition was also explained herein.

Double ring test is one of the important steps in this study to obtain water infiltration behaviour, discussed in chapter 7. Noted that the attendance of the crack and the effect of climate change were taken into account in this analysis. To organize the report, this chapter has been divided into several steps i.e., experiment set-up, crack observation, modified GA equation, Ks due to desiccation crack and water infiltration due to desiccation crack.

Following the double ring test result, the result of embankment serviceability behaviour has been explained in chapter 8, chapter 9 and chapter 20. Chapter 8 focused on the effects of desiccation crack and seasonal variation on hydrological response. Moreover, chapter 9 paid specific attention the effect of rainfall intensity on hydrological behaviour of embankment under slope gradient variations. Further to this, chapter 10 explained the effect of seasonal variation on embankment.

To support full-scale embankment result, numerical back analysis has been conducted in this research, presented in chapter 11. Moreover, parametric study has also been simulated to investigate embankment behaviour under extreme climate. In this chapter, entire result of numerical simulation has been described, comprising PWP response due to seasonal variation, deformation of embankment and FOS of embankment under current and extreme climate.

Since water infiltration plays an important role in embankment serviceability, controlling water infiltration is essential in geotechnical structure. In this research, preliminary study was conducted to control water infiltration. Accordingly, biochar has been proposed as an alternative material to prevent stability and serviceability problem in the embankment, described in chapter 12. To do so, the behaviour of biochar amended soil (BAS) due to water infiltration and evaporation has been investigated using numerical simulation. Moreover, the model was subjected by several extreme climate variation i.e., current, near, and far future extreme climate condition in Thailand.

Chapter 13 is the final chapter in this report, consisting of conclusion and suggestion. Conclusion was derived based on the result, presented in aforementioned section. Moreover, suggestion comprise further recommendation research, based on limitation and other gaps of this research.

Chapter 2 Literature Review

2.1 Unsaturated Soil

Unsaturated soil can be defined as the zone of soil that is located between the ground surface and the water table (Fredlund et al., 2006). Compared to saturated soil, unsaturated soil has more than two phases such as soil structure, water and air. As a result, they have basic differences in material nature and engineering response. The interaction among soil structure, water and air will generate negative pore water pressure (PWP), which is essential parameter in unsaturated soil behaviour. In general, it can be postulated that the zone which is subjected to negative PWP has been widely referred as the unsaturated soil zone. Since the existence of water and air plays an importance role in unsaturated soil, climate condition and soil-atmosphere interaction will significantly affect the thickness of zone. The illustration of soil zone and climate condition interaction can be depicted in Figure 1.

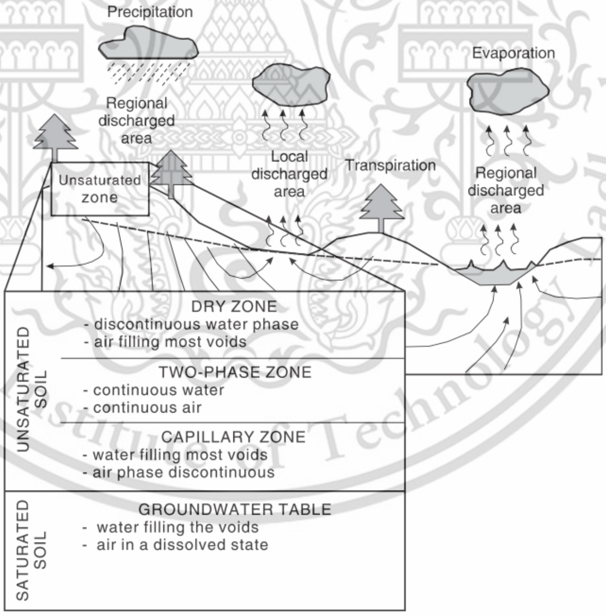

Figure 1 Illustration of soil zones.

2.2.1 Amount of Water in Soil

There are several parameters to express the amount of water in soil i.e., (i) gravimetric water content (w), (ii) volumetric water content (θ), and degree of saturation (S). The most common term, used in geotechnical engineering purposes is gravimetric water content, expressed in (1).

$$w = \frac{M_w}{M_s} \tag{1}$$

Where, M_w is mass of water and M_s is mass of soil solid. In the context of agricultural engineering, volumetric water content is more popular. It is essential in the derivation of transient seepage and fluid storage in unsaturated soils. The equation to calculated volumetric water content can be written in equation (2).

$$\theta = \frac{V_w}{V_t} \tag{2}$$

Where, V_w is volume of water in soil, and V_t is total volume of soil. As the amount of void play an essential role in unsaturated soil behaviour, degree of saturation is required to expressed water amount in soil. Since directly include the volume of void in its equation (equation (3)), this parameter can define air-entry value more clearly. The value of degree of saturation can be described as the ratio between volume of water and volume of void (V_v) in soil.

$$S = \frac{V_w}{V_v} \tag{3}$$

2.2.2 Soil Suction

There are two main variables associated with unsaturated soil namely soil suction and water content. Soil suction is general term to represent matric suction, osmotic suction or total suction. Moreover, total suction is the cumulative of matric suction and osmotic suction, presented in equation (4). Besides, osmotic suction is closely related to salt content in pore water which is relatively unchanged due to the alteration of water content. For that reason, osmotic suction generally not necessary to take into account in geotechnical calculation (Fredlund and Rahardjo, 1993).

$$\psi = (u_a - u_w) + \pi \tag{4}$$

Where, ψ is total suction, $(u_a - u_w)$ is matric suction, and π is osmotic suction.

The commencement of soil suction theoretical concept was developed in soil physic in early 1900 (Fredlund et al., 2012). This theory is mainly generated in relation to soil-water-plant system. The component of soil suction, considered free energy state of soil water, can be measured by partial vapor pressure adjacent to the soil-water (Edlefsen and Anderson, 1943a). The thermodynamic correlation between soil suction and the partial pressure of the pore-water vapor can be expressed in equation (5).

$$\psi = -\frac{RT_K}{\nu_{w0}\omega_v} ln\left(\frac{\bar{u}_v}{\bar{u}_{v0}}\right) \tag{5}$$

Where, R is universal molar gas constant [8.314 J/(molK)], T_K is absolute temperature [273.15 + T (K)], T is temperature(^{o}C), ν_{w0} is specific volume of water or the inverse of the density of water [$1/\rho_w$ (m^3/kg)], ρ_w is density of water [998 kg/m^3 at temperature 20^{o}C], ω_v is molecular mass of water vapor [18.016 kg/kmol], $\bar{u}_v$ is partial pressure of pore water vapor (kPa), and $\bar{u}_{v0}$ is saturation pressure of pore water vapor over a flat surface of pure water at the same temperature (kPa).

Since osmotic suction is relatively constant in common soil, the change of matric suction changes can be substituted for total suction changes. Thus, matric suction is more essential in geotechnical purposes in associated with unsaturated soil rather than osmotic suction. Matric suction, defined as the difference between the air and water pressures across the water surface is governed by adsorptive forces between soil particles and water, resulting negative pore water pressure. The value of matric suction can be represented by capillary height (hc) as shows in Figure 2. Moreover, hc is governed by surface tension (T), effective pore diameter (d) and meniscus angle (α) as can be expressed in (6).

$$hc = \frac{4Tcos\ \propto}{d\ \gamma_w} \tag{6}$$

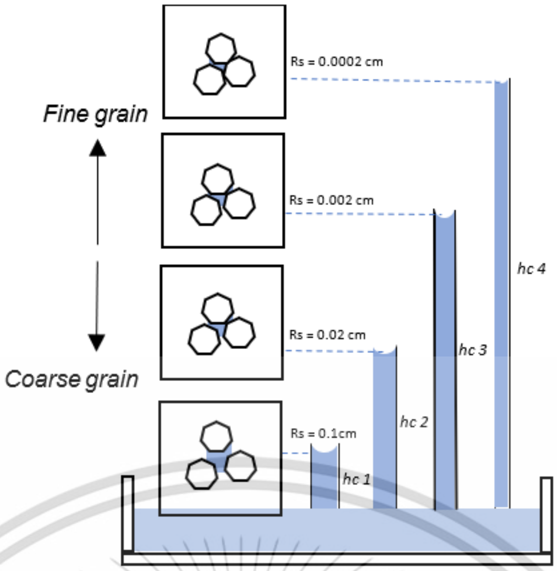

Figure 2 Correlation between pore size and matric suction.

2.2.3 SWRC and HCF

Soil water retention curve (SWRC) provides a conceptual knowledge of water content and the energy state of the water phase correlation (Fredlund et al., 2012). SWRC can represent soil properties function in unsaturated soil mechanic analysis, governed by several parameter such as pore diameter and pore distribution. The relationship between the amount of water in soil and soil suction can be presented in three kinds of curve i.e., gravimetric water content – soil suction, degree of saturation – soil suction, and volumetric water content – soil suction. The gravimetric water content - soil suction is the easiest curve to measure as soil volume behaviour is not taken into account this relationship. However, if the soil exhibits significant volume change such as clay, the others two relationship is more suitable in unsaturated analysis. Moreover, water storage is always measured as the slope of the volumetric water content versus soil suction relationship.

The typical SWRC consists of three distinct zones of desaturation as can be seen in fig. The most important point on the SWRC are air-entry value and the residual value for both suction and water content, known as transition point. These transition point separate the SWRC into three different zones namely boundary effect zone, transition zone and residual zone. Moreover, wetting and drying cycle provides hysteresis effect in soil, thus producing distinct behaviour of SWRC. As a result, the same three zones of desaturation can be defined for the drying (or desorption) branch and the wetting (or adsorption) branch.

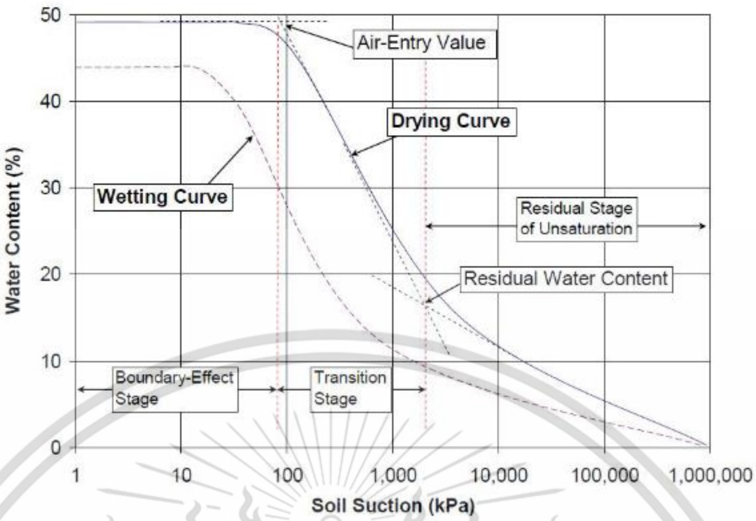

Figure 3 Zones in SWRC curve.

Several closed-form empirical equations have been proposed to fit laboratory data of SWRC. In the early time of development, the equation provides unimodal function which is applicable for homogenous soil that have similar pore diameter such as (Gardner, 1958; Brooks and Corey, 1964; Van Genuchten, 1980). Some equations are written in terms of dimensionless water content Θ_d, and others are written in terms of normalized water content Θ_n. Moreover, the saturated gravimetric water content is designated as w_s, and the gravimetric residual water content is designated as w_r. The example list of unimodal SWRC equation can be shown in Table 1.

The existence of two or more pore series or crack can alter the SWRC behaviour to become bimodal or multimodal (Zhang and Chen, 2005). Several dual or multi-porosity model were proposed to model multimodal SWRC for structured porous media. One-dimensional dual-porosity model has been generated by (Gerke and van Genuchten (1993) for simulating preferential movements of water in structured soils. In their model, the total water content was described as the sum of fracture and matrix water content, weighted by representative volumetric weighting factor. Besides, Durner (1994) developed the unimodal van Genuchten-Mualem model (Van Genuchten, 1980) to fit multimodal SWRC by introducing weighting factors for combining individual functions as expressed in equation (7) and (8). Moreover, the relative hydraulic conductivity function is compute by numerical evaluation of Mualem (1976) predictive model on base of the unimodal or multimodal function as defined in equation (9) and (10).

$$S_e = w_1[(1+(\alpha_1\psi)^{n_1})^{-m_1}] + (1-w_1)[(1+(\alpha_2\psi)^{n_2})^{-m_2}] \tag{7}$$

$$\theta = \theta_r + (\theta_s - \theta_r)S_e \tag{8}$$

Where, S_e is degree of saturation, w_1 is weighting factor; α_1, n_1 and, m_1 are larger pore fitting parameter; α_2, n_2 and, m_2 are smaller pore fitting parameter; ψ is soil suction (kPa); θ is volumetric water content (%); θ_r is residual volumetric water content (%) and θ_r is saturated volumetric water content (%).

$$K = S_e^T\left[\frac{f(S_e)}{f(1)}\right]^2 \tag{9}$$

$$f(S_e) = \int_0^{Se} \frac{1}{\psi(S_e)}\, d\,(S_e) \tag{10}$$

Where, S_e^T is empirical correction function.

Table 1 Empirical Equations Used to Best Fit SWRC Data

Reference	***Equation***	***Description***
Gardner (1958)	$\Theta = \frac{1}{1+a_g\psi^{ng}}$ where $\Theta = \frac{w(\psi)}{w_s}$	ag = fitting parameter which is a function of air entry value of soil ng = fitting parameter which is a function of rate of water extraction of soil has been exceeded
Brooks and Corey (1964)	$w(\psi) = w_s \; or \; \Theta_n = 1 \; for \; \psi \leq \psi_{aev}$ $\Theta_n = \left[\frac{\psi}{\psi_{aev}}\right]^{-\lambda_{bc}} \quad \psi > \psi_{aev}$ where $\Theta_n = \frac{w(\psi) - w_r}{w_s - w_r}$	ψ_{aev} = air entry value of soil λ_{bc} = pore size distribution index w_r = residual water content located through trial-and-error process that yields straight line on semi log plot of degree of saturation versus suction
Brutsaert (1967)	$\Theta_n = \frac{1}{1+[\psi/a_b]^{n_b}}$ where $\Theta_n = \frac{w(\psi) - w_r}{w_s - w_r}$	a_b = fitting parameter which is a function of air entry value of soil n_b = fitting parameter which is a function of rate of water extraction of soil has been exceeded

Reference	*Equation*	*Description*
Van Genuchten (1980)	$\Theta_n = \dfrac{1}{\left[1+\left(a_{vg}\psi\right)^{n_{vg}}\right]^{m_{vg}}}$ where $\Theta_n = \dfrac{w(\psi)-w_r}{w_s-w_r}$	a_{vg}, n_{vg}, m_{vg} = fitting parameter primarily related to invers of air entry (unit equal to 1/kPa)
Van Genuchten (1980) - Mualem (1976)	$\Theta_n = \dfrac{1}{[1+(a_{vm}\psi)^{n_{vm}}]^{m_{vm}}}$ where $m_{vm} = 1 - \dfrac{1}{n_{vm}}$	a_{vm}, n_{vm}, m_{vm} = fitting parameter primarily related to rate of water extraction from soil once air-entry value has been exceeded
Van Genuchten (1980) - Burdine (1953)	$\Theta_n = \dfrac{1}{[1+(a_{vb}\psi)^{n_{vb}}]^{m_{vb}}}$ where $m_{vb} = 1 - \dfrac{1}{n_{vb}}$	a_{vb}, n_{vb}, m_{vb} = fitting parameter primarily related to residual water content conditions
Fredlund and Xing (1994)	$w(\psi) = C(\psi)\dfrac{w_s}{\left\{\ln\left[e+\left(\psi/a_f\right)^{n_f}\right]\right\}^{m_f}}$ where $C(\psi) = 1 - \dfrac{\ln(1+\dfrac{\psi}{\psi_f})}{\ln(1+\dfrac{10^6}{\psi_f})}$ $\Theta_d = \dfrac{w(\psi)}{w_s}$	a_f = fitting parameter which is a primarily function of air entry value of soil n_f = fitting parameter which is a function of rate of water extraction of soil has been exceeded m_f = fitting parameter primarily related to residual water content conditions $C(\psi)$ = correction factor which is primarily a function of suction corresponding to residual water content

2.2.4 Stress State and Shear Strength

There is generally known that unsaturated soil comprises three phase system i.e., soil particle, water and air. However, the existence of air-water interface (contractile skin) should be considered as a fourth and independent phase when studying equilibrium state of unsaturated soil (Fredlund et al., 2012). The equilibrium analysis on an unsaturated soil element provided justification for the use of independent stress state variables for an unsaturated soil. In term of stress state condition, the combination of effective normal stress ($\sigma - u_a$) and matric suction (u_a

– u_w) is the widest acceptance in formulating unsaturated soil mechanics problems. Moreover, effective stress in unsaturated soil can be formulated using equation

$$\sigma' = (\sigma - u_a) + \chi(u_a - u_w) \tag{11}$$

Where σ' is effective stress (kPa), χ is a soil parameter related to degree of saturation and ranging from 0 to 1.

Several theories have been developed to express the shear strength equation of unsaturated soil. Fredlund et al. (1978) postulated that shear strength of unsaturated soil can be generated from extended Mohr-Coulomb failure criterion. The new equation can be formulated from independent stress state variables, resulting linear form of the shear strength. Following this, by considering (σ – u_a) and (u_a – u_w), shear strength in saturated soil can be written in equation

$$\tau_{ff} = \mathrm{c}' + \left(\sigma_f - u_a\right)_f \tan\varphi' + (u_a - u_w)_f \tan\varphi^b \tag{12}$$

Where, c' is effective cohesion, $\left(\sigma_f - u_a\right)_f$ is net normal stress state on the failure plane at failure, φ' is angle of internal friction associated with the net normal stress state variable, $(u_a - u_w)_f$ is matric suction on the failure plane at failure, and φ^b is angle indicating the rate of increase in shear strength with respect to a change in matric suction.

Extended Mohr-Coulomb failure envelope can be drawn to obtain better understanding of shear strength in unsaturated soil. Accordingly, Mohr circles pertaining to failure conditions can be developed in a three-dimensional manner, as illustrated in Figure 4. The same as ordinary Mohr-Coulomb failure envelope, shear stress τ is set as ordinate axis, whereas normal stress (σ – u_a) is plotted in abscissas axis. Moreover, the location of the Mohr circle plot in the third dimension is a function of the matric suction (u_a – u_w). The frontal plane represents saturated soil condition when soil suction is zero. It is clearly seen from Figure 4 that the shear strength of unsaturated soil depends on strength parameter such as the cohesion intercept (c'), slope angle φ' and φ^b. Further to this, the increase in shear strength caused by an increase in matric suction is characterized by the angle φ^b when assuming linear failure conditions.

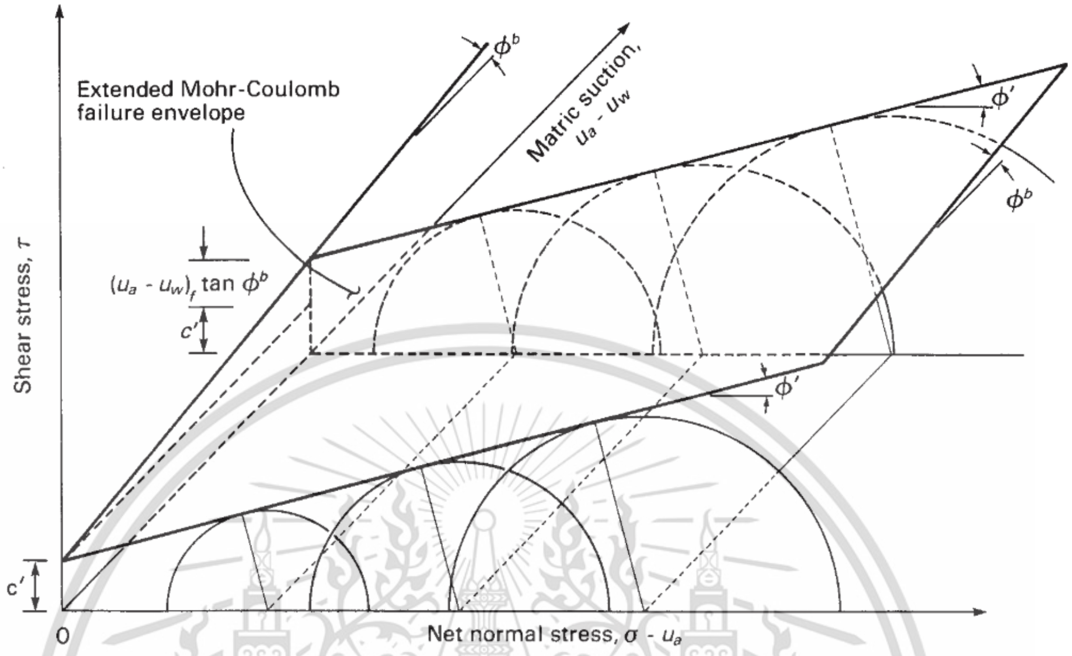

Figure 4 Extended Mohr-Coulomb failure envelope for unsaturated soils.

2.2.5 Volume Change

To analysis volume change in unsaturated soil, the deformation variable of soil structure and water phases are generally required (Biot, 1941; Matyas and Radhakrishna, 1968). Soil structure deformation can be represented by void ratio or porosity changes. Meanwhile, water phase deformation stated can be considered from water volume changes. The analysis of volume change should be embraced the equality concept associated with a multiphase system. The total volume change of the soil element must be equal to the sum of the volume changes associated with solid phase and fluid phase. Further to this, the continuity requirement for the unsaturated soil can be express in equation (13) considering the soil particles are assumed to be incompressible.

$$\frac{\Delta V_v}{V_0} = \frac{\Delta V_w}{V_0} + \frac{\Delta V_a}{V_0} + \frac{\Delta V_c}{V_0} \tag{13}$$

V_0 is initial overall volume of an unsaturated soil element, V_v is volume of soil void, V_w is volume of water, V_a is volume of air, and V_c is volume of contractile skin.

To predict soil movement in unsaturated soil, researchers have been developed several constitutive models. Based on Briaud et all. (2003) and Assadollahi (2019), all model must be involved two component: (i) prediction of the seasonal water content and soil suction over time using unsaturated moisture flow equation; (ii) prediction volume change behaviour by linking seasonal water content and suction to it using constitutive models. Furthermore, according to (Adem and Vanapalli, 2015), the recent model were classified in three categories i.e., consolidation theory-based methods, water content-based methods, and suction-based methods.

In term of consolidation theory, volume change is derived from the correlation between hydraulic and mechanical behaviour. Elastic behaviour based model has been generated by Fredlund and Morgenstern (1976) in associated with volume change increments to the increments of the net stress and the soil suction. Two constitutive relationships have been proposed to express the deformation state of an unsaturated soil in elastic theory. The first constitutive model represents soil structure and the second one related to water phase. Assuming that the soil behavior is like an incrementally isotropic, linear elastic material, the constitutive relationship for the soil structure can be written in equation (14) (Fredlund et al., 2012).

$$\begin{aligned} d\varepsilon_v = d\varepsilon_x + d\varepsilon_y + d\varepsilon_z &= \frac{3(1-2\mu)}{E} d(\sigma_m - u_a) + \frac{3}{H_s} d(u_a - u_w) \\ &= \frac{1}{B_s} d(\sigma_m - u_a) + \frac{3}{H_s} d(u_a - u_w) \end{aligned} \tag{14}$$

Where, ε_v is volumetric soil strain, ε_x ε_y and ε_z is the normal strains in the x, y, and z direction, respectively, σ_m is the mean total normal stress, $\sigma_m = (\sigma_x + \sigma_y + \sigma_z)/3$, in which , σ_x σ_y and σ_z are the normal stress in x, y, and z direction, respectively, μ is Poisson's ratio, E is the modulus of elasticity for the soil structure with respect to a change in net normal stress, Hs is the modulus of elasticity for the soil structure with respect to a change in net matrix suction, Hs is the bulk modulus of soil.

Considering Fredlund and Morgenstern (1976) the constitutive equation for water phase defines the water volume changes in the soil element for any change in the total stress and matric suction as can be expressed in equation (15).

$$\begin{aligned}\frac{\mathrm{d}V_w}{V_0} &= \frac{d(\sigma_x - u_a)}{E_w} + \frac{d(\sigma_y - u_a)}{E_w} + \frac{d(\sigma_z - u_a)}{E_w} + \frac{d(u_a - u_w)}{H} \\ &= \frac{3}{E_w} d(\sigma_m - u_a) + \frac{1}{H_w} d(u_a - u_w)\end{aligned} \tag{15}$$

Where V_w is the volume of water in the soil, V_0 is the initial volume of the soil, E_w is the volumetric modulus of water associated with a change in net normal stress; and H_w is the water volumetric modulus associated with a change in matric suction. Following this, the constitutive equation for volume change of soil structure and water phase in a compressible form can be written in equation (16) and (17).

$$d\varepsilon_v = \frac{\mathrm{d}V_v}{V_0} = m_1^s d(\sigma_m - u_a) + m_2^s d(u_a - u_w) \tag{16}$$

$$d\theta = \frac{\mathrm{d}V_w}{V_0} = m_1^w d(\sigma_m - u_a) + m_2^w d(u_a - u_w) \tag{17}$$

Where, m_1^s and m_2^s are the coefficient of total volume change with respect to a change in net normal stress and a change in suction, respectively, m_1^w and m_2^w are the coefficient of pore water volume change with respect to a change in net normal stress and a change in suction, respectively

The coefficients of total volume changes can be calculated from constitutive surfaces for void ratio and soil water content. The following complementary relationships can also be expressed in equation (18).

$$m_1^s = \frac{1}{B_s}, \qquad m_2^s = \frac{3}{H_s}, \qquad m_1^w = \frac{3}{E_w}, \qquad m_2^w = \frac{1}{H_w} \tag{18}$$

2.2 Soil-Atmosphere interaction

Soil water condition is one of the most essential factors that affects hydro-mechanical behaviour of soil pertaining to stability and serviceability problem of earthwork. Since soil-atmosphere interaction plays an important role in water balance of soil, basic and advance knowledge related to this issue is required.

2.2.1 Water Balance

Regarding Blight (1997), there are two terms to represent water balance in an environment i.e., atmospheric water balance (AWB) and soil water balance (SWB). AWB is defined as the difference between rainfall and potential evaporation. Since it related air water condition, AWB may provide the characteristic of local climate. When AWB is positive, soil moisture will be recharged, and thus ground water increase. In the contrary, during the negative value of AWB, soil water will be drained, as a result groundwater will decrease. An AWB may be classified into three conditions i.e., (i) perennial water surplus, (ii) perennial water deficit, (iii) seasonal water surplus/deficit. Figure 5 illustrate the classification of AWB in Kuala Tanah, Malaysia.

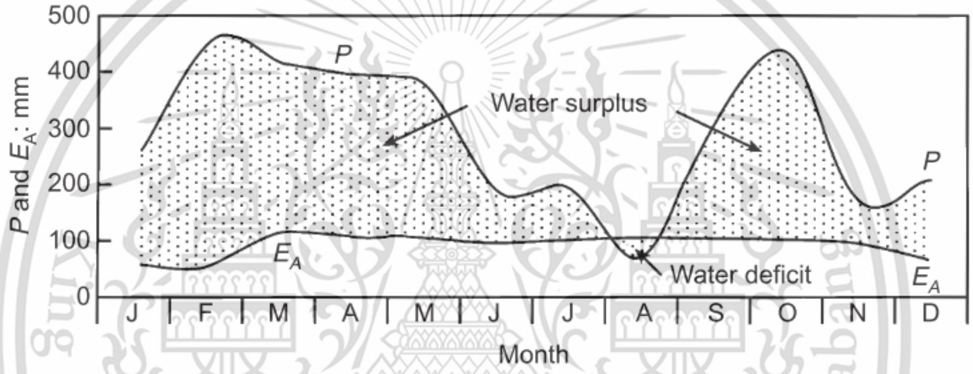

Figure 5 Atmospheric water balance.

SWB is the equality among soil water input, soil water output and water storage in soil. Since having closer relationship to soil moisture behaviour, SWB is more essential than AWB in geotechnical point of view. However, soil water balance concept is not suitable for large area regarding the difficulties of measurement. In bare area, the equation SWB can be described in equation (19).

$$P - \left(I_{nt} + R_{off}\right) = PE + R_{wt} + \Delta S \qquad (19)$$

Where P is precipitation (mm/day), I_{nt} is interception (mm/day), R_{off} is runoff on the ground surface (mm/day); PE is evaporation (mm/day), R_{wt} is water recharge to the water table (mm/day), and ΔS is change in the soil water storage (mm/day).

Since interception corresponds to the storage of water above the ground surface pertaining to vegetation, the attendance of interception in bare area is limited. Furthermore, the term of Rwt + Δs represents the water infiltration of soil (I), therefore can be expressed in equation (20). Among the components of the water balance, evaporation and infiltration are the most important in a geotechnical engineering and will be discussed more detail in the next section.

$$I = P - \left(PE + R_{off}\right) \tag{20}$$

2.2.2 Evaporation

Evaporation is the process by which a liquid turn into a gas regarding water kinetic energy increasing. Soil water evaporation is one of essential factor that should be taken into account in unsaturated flow analysis. Considering involved parameter, evaporation can be divided into two terms namely Potential Evaporation (PE) and Actual Evaporation (AE). PE is the amount of water vapor that could be emitted from a surface of pure water per unit of water area and unit of time under existing atmospheric conditions. Whereas, AE refers to the exact amount of water evaporated by a real bare soil. In technical point of view, PE is dependent solely on meteorological data, while AE is also affected by soil properties (Assadollahi, 2019).

Several methods have been developed to calculate potential evaporation pertaining to agricultural and hydrological aspect such as Thornthwaite (1948), Penman (1948), Blaney and Criddle (1950), Turc (1955) and Blight (1997). Empirical and semi-empirical have been used to generated this method. Thornthwaite (1948) have used actual and potential evaporation data to generate empirical equation. Since Thornthwaite was generally collected from humid North-East and North America, it may not be suitable for arid condition. The empirical equation, based on Thornthwaite model can be expressed in (21).

$$E_m = 16.2\left(\frac{10t_m}{\sum i}\right)^a \tag{21}$$

Where E_m is monthly evaporation (mm), tm is the mean monthly temperature (^{oC}), i is $(T/5)^{1.5}$, T is mean daily temperature (o^{C}), and a can be written in equation (22).

$$a = 6.75E-9\left(\sum i\right)^3 - 7.7E-7\left(\sum i\right)^2 + 0.08\left(\sum i\right) + 0.49 \tag{22}$$

Where E_m is monthly evaporation (mm), tm is the mean monthly temperature (°C), i is $(T/5)^{1.5}$, T is mean daily temperature (oC), and a can be written in equation (22).

According to Turc (1955), the attendance of precipitation should be considered in evaporation calculation. Turc has been developed in wet climate condition. However, since resulting zero evaporation value during drought period, the method is not valid in certain condition. Based on his research result, evaporation can be expressed in equation (23).

$$E_m = \frac{P_m}{0.9 + (P_m/L)^2} \tag{23}$$

Where Pm is monthly precipitation (mm), and L = 300 + 25 Tm + $0.05Tm^3$, where Tm is mean monthly temperature (°C).

The most rational approach to determine potential evaporation is Penman (1948). This method used many of the concepts that follow, and produced a semi-rational equation, based on the energy balance at the soil surface. Based on (Allen et al., 1998), the equation uses standard climatological records of solar radiation (sunshine), air temperature, humidity and wind speed. Moreover, this method represents physical and physiological factors governing the evapotranspiration process. The value of potential evapotranspiration was determined by equation (24).

$$PE = \frac{0.408\Delta.(Rn - G) + \gamma \frac{900}{T + 273} u_2(e_s - e_a)}{\Delta + \gamma\,(1 + 0.34u_2)} \tag{24}$$

Where, Rn is Net Radiation (MJ/m^2day), G is Soil heat flux density (MJ/m^2day), T is Mean daily air temperature at 2 m height (°C), u_2 is Wind speed at 2 m height (m/sec), e_s is saturation vapor pressure (kPa), e_a is actual vapor pressure (kPa), Δ is slope vapor pressure curve (kPa/°C), γ is psychrometric constant (0.061 kPa/°C).

One of the newest methods to calculate evaporation is the energy balance method proposed by Blight (1997). Energy balance of soil is determined by many factors such as solar radiation, soil heat flux, sensible air heat flux, and latent heat flux. Figure 6 present the existence of each component working at the ground surface.

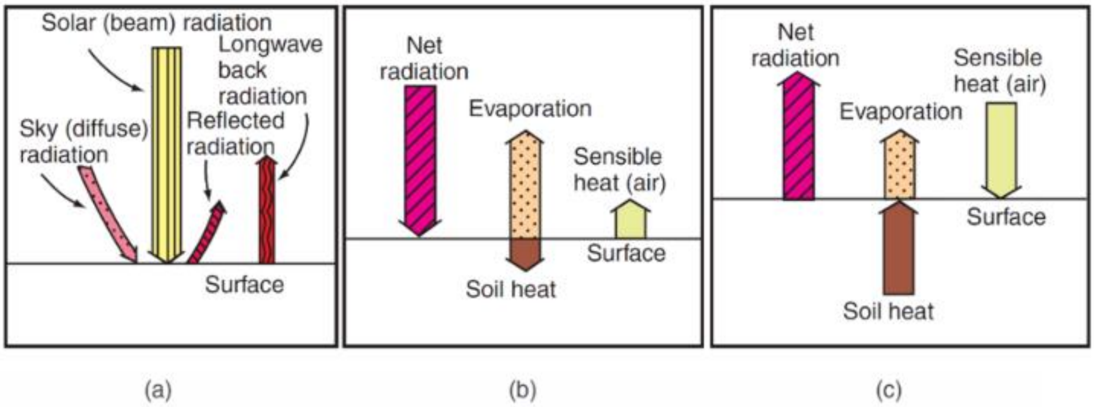

Figure 6 Component of radiation balance.

(a) incoming and outgoing radiation (b) radiation interchange during the day (c) radiation interchange at night (Blight, 1997).

Considering Figure 7, energy balance can be presented by equation (25) as follows.

$$Rn = G + H + Le \tag{25}$$

Where Rn is net radiation, G is soil heat flux, His sensible air heat flux and Le is latent heat flux. In detail, each component is influenced by many other parameters, described in this following section.

(i) Net Radiation (Rn)

Net radiation is incoming solar and diffuse sky radiation reduced by reflected radiation and outgoing long-wave terrestrial radiation. Many authors have studied and proposed their theory to determine net radiation. Penman-Monteith and Food and Agriculture Organization is the most well-known and applied model to calculate net radiation. With respect to many influenced factors, they presented equation (26) to analyze net radiation.

$$Rn = (1-\alpha)R_{si} - \left[a_c\left(\frac{R_{si}}{R_{so}}\right) + b_c\right]\left(a_1 + b_1 e_d^{0.5}\right)\sigma\left(\frac{T_m^4 + T_n^4}{2}\right) \tag{26}$$

Where σ is stefan-boltzmann constant (5.67 x 10-8), Tm and Tn are maximum and minimum air temperatures in one day (°C), a_c and b_c are cloud factors, equal to 1.35 and 0.35 a_1 and b_1 are emissivity factors, equal to 0.35 and -0.14, α is soil surface albedo, R_{si}/R_{so} is relative short-wave radiation, which is used to express the cloudiness of the atmosphere (0.33 - 1), e_d is calculated from the mean daily dew point temperature (T_d).

(ii) Soil Heat Flux (G)

The soil heat flux is the energy received by the soil to heat it per unit of surface and time. According to this mechanism, heat causes changes in soil temperature (Assadollahi, 2019). Therefore, soil heat flux value is positive when the soil receives energy and negative when the soil loses energy. According to (Cui and Zornberg (2008) and Cui et al. (2010) and , the soil heat flux can be measured directly by a soil heat flux sensor. Alternatively, soil heat flux can be determine using equation (27).

$$G = 2(T_1 - T_s)K_1/D_1 \tag{27}$$

Where T_1 is surface temperature (°C), T_s is the temperature at the center of the surface layer (°C), K_1 thermal conductivity, and D_1 is soil thickness (m).

(iii) Latent Heat Flux (Le) and Sensible Air Heat Flux (H)

Latent heat flux was defined as heat causing evaporation or condensation at the soil surface. Based on energy balance theory, Blight presented equation (28) to calculate latent heat flux as follows.

$$L_e = \frac{R_n - G}{1 + \beta} \tag{28}$$

Where β is bowen's ratio. The sensible heat is the amount of heat exchanged, without physical phase transition, between multiple bodies forming an isolated system. This heat influence temperature change of the air can be presented in equation (29).

$$H = \beta L_e \tag{29}$$

The potential evaporation could be calculated by dividing the integrated value of Le in J/m2 per day by the latent heat of vaporization of water (2,260 kJ/kg).

2.2.3 Infiltration

Water infiltration is a fundamental aspect of hydro-mechanical soil behaviour that is relevant to a variety of fields, including geotechnical and hydrological engineering. In geotechnical engineering, the infiltration can significantly impact soil behaviour, particularly its strength, due to the increasing pore water pressure (Briggs et al., 2013; Lees et al., 2013; Apriyono et al., 2023). Meanwhile, heavy rainfall and associated with waterlogging, which was related to soil infiltration rate can seriously disturb plant growth and lead to significant yield losses in many crop species (Collaku and Harrison, 2002; Kaur et al., 2019; Wang et al., 2022). Accurate calculations of water infiltration and runoff are therefore crucial for both engineering and agricultural purposes. However, accurately predicting water infiltration in fine-grain materials is challenging due to the complex factors that influence infiltration behaviour, such as the presence of cracks, which may cause the infiltration mechanism to be more complex.

With respect to its important effect in many aspects, infiltration theory has evolved, resulting several basic and advance method. Considering Assouline (2013), the first empirical quantitative description of flow through a saturated porous medium has been expressed by Darcy (1856), known as Darcy's Law can be written in equation (30). Under saturated condition, the characteristic of water flux in porous medium tends to constant, govern by head gradient. However, this method is no longer valid in unsaturated pertaining to more complicated behaviour.

$$f = \frac{F}{A} = \frac{F}{A} = K_s \frac{\Delta\Phi}{L} \tag{30}$$

Where f is flux of water, F is the discharge rate of water (m^3/sec), A is cross section area of the tube (m^2), V is cumulative volume of water (m^3), t is time (sec), Ks is saturated hydraulic conductivity (m/sec), $\Delta\Phi$ is the different in total hydraulic head between two points (m), and L is distance between two points (m).

To facilitate water flow analysis in unsaturated medium, Buckingham (1907) proposed his method, extended from Darcy's Law theory. Based on his theory, saturated hydraulic conductivity can be replaced by a function of water content or capillary potential, defined as unsaturated hydraulic conductivity. Thus, unsaturated flow can be expressed by equation (31).

$$f = -K(\theta)\frac{\partial\Phi}{\partial z} = -K(\psi)\frac{\partial(\psi + z)}{\partial z} = -K(\psi)\left(\frac{\partial(\psi)}{\partial z} + 1\right) \tag{31}$$

Where z is the vertical coordinate being positive upward, flux of water, F is the discharge rate of water (m^3/sec), $K(\theta)$ is a function of water content, $K(\psi)$ is a function of capillary potential.

Richards (1931) suggested the general governing equation for flow through porous media as a commencement of numerical analysis. Flow equation, proposed by Buckingham (1907) and the principle of continuity was combined to generated the equation. Moreover, the three-dimensional mathematical expression of this principle in a Cartesian coordinate system has been proposed as written in equation (32).

$$\frac{\partial\theta}{\partial z} = \nabla f = \left(\frac{\partial f_x}{\partial x} + \frac{\partial f_y}{\partial y} + \frac{\partial f_z}{\partial z}\right) \tag{32}$$

Where ∇ is the divergence of f_x, f_y, and f_z denoted the component of the flux at any spatial location in the x, y, and z, respectively. Accordingly, the three-dimensional expression of Richard's equation under isothermal conditions in a homogeneous, isotropic and rigid porous medium can be expressed in equation (33)

$$\frac{\partial\theta}{\partial t} = \frac{\partial}{\partial z}\left[K(\psi)\left(\frac{\partial(\psi)}{\partial z} + 1\right)\right] \tag{33}$$

Since the analysis of water infiltration should consider quantitative result and nonlinearity flow equation, several researchers developed empirical expression, relating infiltration rate (q) and time (t). Based on experimental data, infiltration rate gradually decreased prior to steady final rate was reached. Most of infiltration equation suggested decreasing function regarding exponential or power decays. Furthermore, the parameter of these function has limited meaning of physical aspect and calculated by fitting to experimental data. For example, infiltration empirical equation has been proposed by Horton (1940). Based on his research, initial infiltration rate (f_0) exponentially decreases along the time, followed by constant value (f_c) as expressed in equation (34).

$$f_p = f_c + (f_0 - f_c)e^{-kt} \tag{34}$$

Where fp is infiltration capacity at any time (mm/hr), t is time (hr), and k is an exponential decay constant dependent on soil type and vegetation.

The first analytical method to calculate water infiltration has been presented by (Philip, 1956). The equation has developed by considering infiltration as a sorption process with distraction generated by the attendance of gravity. By considering sorpitivity as a function of suction head, Philip's equation can be expressed in equation (35)-(37).

$$F(t) = S.t^{0.5} + A.t \tag{35}$$

$$K_{sat} = A/M \tag{36}$$

$$f(t) = 0.5S.t^{0.5} + Ks \tag{37}$$

Where F(t) is cumulative infiltration depth (cm), S is sorpitivity (cm/min$^{0.5}$), A is transmittivity factor (cm/min), Ks is saturated hydraulic conductivity (cm/min), M is constant factor (0.667), and t is time (min).

To date, the Green-Ampt model is the most commonly used in infiltration analysis, as it considers more complex parameters such as saturated hydraulic conductivity (Ks), pore water pressure (PWP), and volumetric water content (VWC). Rectangular saturated piston flow and homogeneous isotropic soil were used to develop the Green-Ampt infiltration model (Gowdish and Muñoz-Carpena, 2009). Chui and Zu (2017) reported that the Green-Ampt model has been used in Soil and Water Assessment Tool (SWAT) model, the Water Erosion Prediction Project (WEPP) model, and the Hydrologic Engineering Center-Hydrologic Modelling System (HEC-HMS). Recently, several studies have developed new models, based on the Green-Ampt method that considers saturated hydraulic conductivity (Ks), negative PWP (y) sand Volumetric Water Content (WVC). The Green-Ampt equation can be seen in equation (38) and (39).

$$F(t) = K_s\, t + \psi\Delta\theta \ln\left(1 + \frac{F(t)}{\psi\Delta\theta}\right) \tag{38}$$

$$f(t) = K_s\left(\frac{\psi\Delta\theta}{F(t)} + 1\right) \tag{39}$$

2.3 Extreme climate and climate change scenarios

Extreme climate as an impact of climate changes is undeniable and should be taken into account in many aspects of human life, including earth work. Thus, it is essential to obtain better understanding regarding the effect of extreme climate to the structure. The important point of extreme climate as a result of climate changes will be explained here in.

2.3.1 Climate Model

Climate model is a mathematical formula to represent climate system, consisting two categories i.e., global climate model (GCM) and regional climate model (RCM) (Cynthia Rosenzweig and Solecki, 2015). Since GCM has higher spatial resolution, ranging from 60 to 410 km, the finer resolution is required in technical design purposes. Therefore, it is necessary to convert GCM model into finer resolution climate name downscaling technique as can be seen in Figure 7 (Regional Climate Projections Consortium and Data Facility in Asia and the Pacific, 2020). Broadly, downscaling comprises two techniques i.e., dynamical and statistical method. The differences between those two methods can be described as follows.

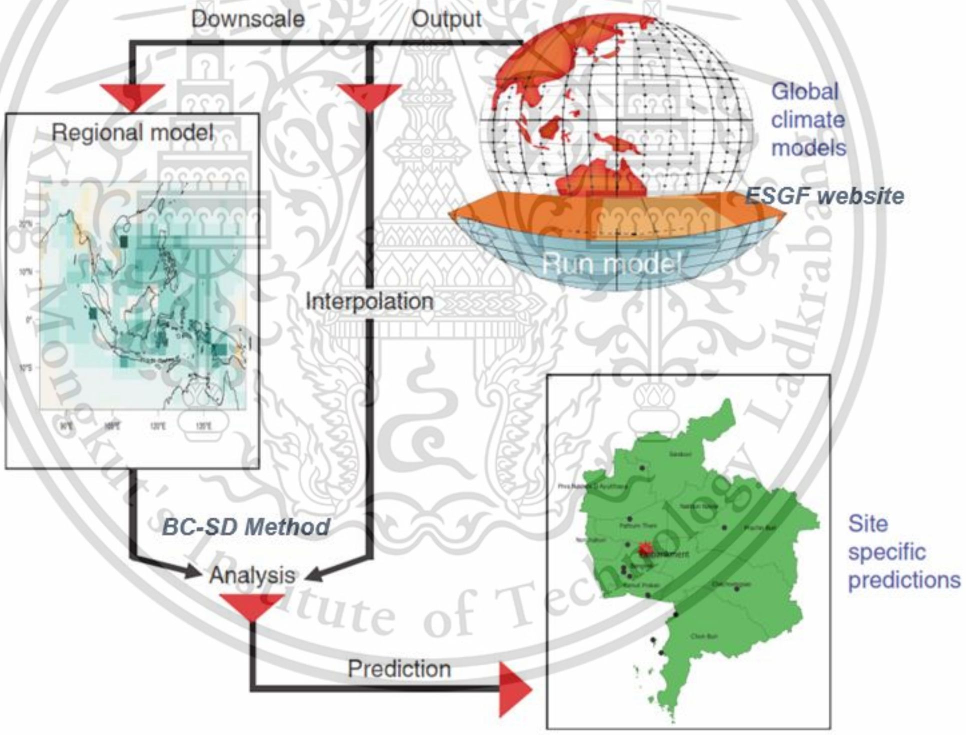

Figure 7 Downscaling method.

(i) Dynamical Downscaling

High resolution data, obtained from GCM is used as an input in this analysis. Following this, regional climate model is employed to translate the large-scale weather and ocean evolution from a GCM into a physically consistent evolution at higher resolution (Hobday and Lough, 2011).

(ii) Statistical Downscaling

The same as previous method, this method also simulates local climate using output from a GCM as input. However, instead of using dynamical technique, statistical downscaling provides statistical analysis in the calculation. To obtain finer resolution model, statistical downscaling requires two steps. The first step is the development of an empirical relationship between local climate variables such as rainfall and large-scale predictors such as the mean of sea-level pressure. Further to this, this relationship is then applied to GCM simulation data to simulate local climate variables.

2.3.2 Climate change scenario

Considering Assadollahi and Nowamooz (2020b), climate change can be described as the change of atmospheric parameters referring to both natural internal processes and external forcings such as modulations of the solar cycles, volcanic eruptions, and persistent anthropogenic changes in the composition of the atmosphere or in land use. The Coupled Model Inter Comparison Project (CMIP) has been generated by The Working Group on Coupled Modelling (WGCM) to investigate the impact of climate change in further study. Moreover, to describe the alternative of future climate, four pathway scenarios have been selected, known as Representative Concentration Pathway (RCP). RCPs scenarios consists of one mitigation scenario leading to a deficient forcing level (RCP 2.6), two stabilization scenarios (RCP 4.5 and RCP 6), and one scenario with very high greenhouse gas emissions RCP 8.5 as depicted in Figure 8 (IPPC, 2015).

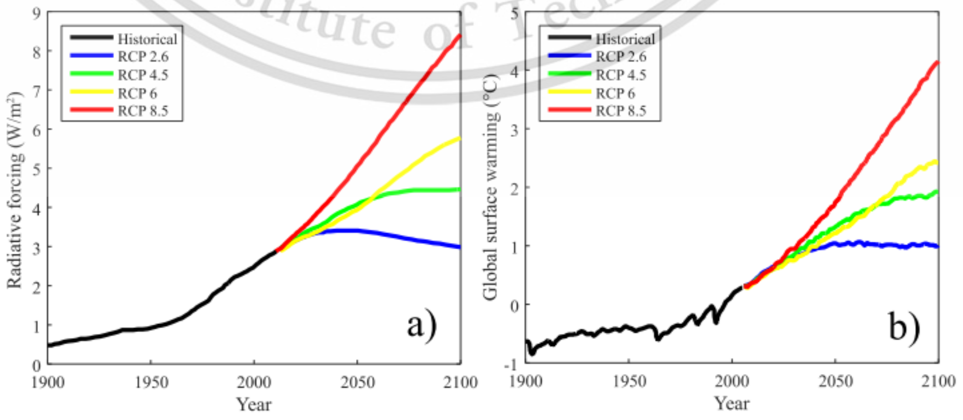

(a) radioactive forcing (b) global surface warming

Figure 8 Representative Concentration Pathway scenarios.

2.3.3 Thailand Climate Projection

According to The World Bank Group and The Asian Development Bank (2021), several studies postulated that the average temperature in Thailand increase since 1950's pertaining to climate change. It can be reported that daily maximum, mean, and minimum temperatures at 65 meteorological stations between 1970–2006 increased 0.12–0.59°C, 0.10–0.40°C and 0.11–0.55°C per decade, respectively (Limsakul et al., 2011). Moreover, annual precipitation has also increased since 20th century owing to higher precipitation during the wet season (Lacombe et al., 2012).

The projection of Thailand climate has been developed by The World Bank Group and The Asian Development Bank (2021) based on Coupled Model Inter-comparison Project Phase 5 (CMIP5) models. In their analysis, two RCP scenario i.e., RCP 2.6 and RCP 8.5 have been analyzed, representing an extreme mitigation scenario, and a business-as-usual scenario, respectively. Their study shows historical and projected temperatures under RCP 2.6 and RCP 8.5 as can be shown in Figure 9. Considering Figure 9, projected average temperatures increase 1.1°C and 3.8°C by the 2080s under RCP 2.6 and RCP8.5 scenario, respectively. Furthermore, this value is approximately 0.5°C less than the global average temperature.

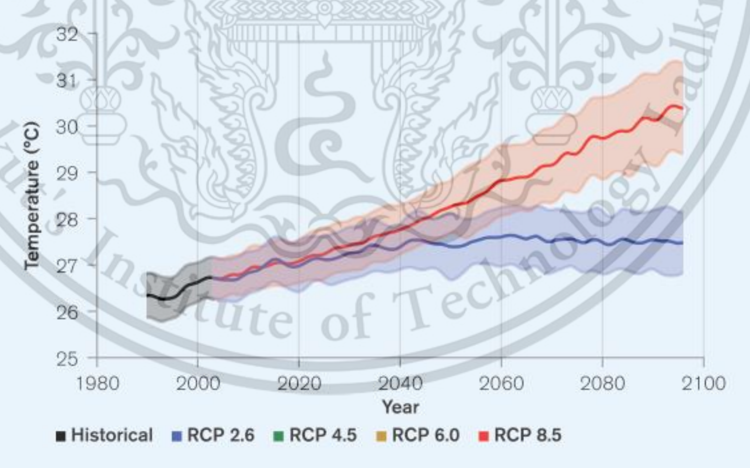

Figure 9 Historic and projected temperature in Thailand.

2.3.4 SPEI climate index

The Standardized Precipitation Evapotranspiration Index (SPEI) is one of the most popular climate index that can be used to evaluate drought severity in any particular area with considering both precipitation and potential evapotranspiration

(Vicente-Serrano et al., 2010; Yang et al., 2016; Muangthong et al., 2020). This method required 30 – 50 years weather data period and can be calculated on a range of timescales from 1 - 48 months. Moreover, the annual scale drought level was defined as five types and each standard of SPEI range was given in Table 2.

Table 2 SPEI Indices

Drought/Wet Severity	***SPEI***
Extremely Wet	≥ 2.00
Severely Wet	1.50 - 1.99
Moderately Wet	1.00 - 1.49
Near Normal	-0.99 - 0.99
Moderately Drought	-1.00 - (-1.49)
Severely Drought	1.5 - (-1.99)
Extremely Drought	≤ -2.00

For calculating SPEI Index, several steps using specific statistical equation are required (Vicente-Serrano et al., 2010). To facilitate the computation, open-source R-Studio program was used in this research (Beguería and Vicente-Serrano, 2017). Generally, SPEI express the difference degree between precipitation and evaporation which deviates the average status to represent the regional drought. Monthly precipitation and PE data are required to calculate water balance using equation (40).

$$D_n^k = \sum_{i=0}^{k-1} (P_{n-i} - PE_{n-i}), n \geq k \tag{40}$$

Where, D is the difference between precipitation and potential evapotranspiration, P is the monthly precipitation, PE is the monthly potential evaporation, k is time scale, n is calculation frequency. Following this, since log-logistic distribution was used in this method, probability density function was calculated by equation (41).

$$f(x) = \frac{\beta}{\alpha}\left(\frac{x-y}{\alpha}\right)^{\beta-1}\left[1+\left(\frac{x-y}{\alpha}\right)^{\beta}\right]^{-2} \tag{41}$$

Where, α, β, γ are scale, shape and origin parameters, calculating by equation (42), (43), and (44).

$$\beta = \frac{2\omega_1 - \omega_0}{6\omega_1 - \omega_0 - 6\omega_2} \tag{42}$$

$$\alpha = \frac{(\omega_0 - 2\omega_1)\beta}{\Gamma\,(1+\frac{1}{\beta})\Gamma(1-\frac{1}{\beta})} \tag{43}$$

$$\gamma = \omega_0 - \alpha\Gamma\,(1+\frac{1}{\beta})\Gamma(1-\frac{1}{\beta}) \tag{44}$$

Where Γ(1+1/ β) is gamma function of (1+1/ β); ωs is the probability-weighted moments of order s, expressed by equation (45)

$$\omega_s = \frac{1}{n}\sum_{i=1}^{n}\left(1-\frac{j-0.35}{n}\right)^s D_i \tag{45}$$

Where n is the number of data point sand j is the range of observations in increasing order. Moreover, the probability distribution function of the log-logistic distribution for D series can be expressed using equation (46).

$$F(x) = \left[1 = \left(\frac{\alpha}{x-y}\right)^{\beta}\right]^{-1} \tag{46}$$

Finally, The SPEI value can be obtained as the standardized value of $F(x)$ with the equation (47)

$$SPEI = W - \frac{c_0 + c_1W + c_2W^2}{1 + d_1W + d_2W^2 + d_3W^3} \tag{47}$$

$$W = \sqrt{2\ln{(P)}}\, for\ P \ \leq 0.5 \tag{48}$$

Where P is the probability of exceeding a determined D value and P=1−$F(x)$; when P > 0.5, P=1−P And the constants are c0 = 2.515517, c1 = 0.802853, c2 = 0.010328, d1 = 1.432788, d2 = 0.189269, d3 = 0.001308.

2.4 Shrinkage and cracks

Seasonal behaviour provides the interchange of soil moisture, leading the transfer of energy and water through the soil surface. As a result, the soil is alternately wetted and dried and swells and shrinks in balance. The shrinkage results in surface cracking, changing infiltration and evaporation soil behaviour. Moreover, both cracks and swelling fissure will modify the shear strength characteristics of the soil (Blight, 1997).

2.4.1 Stress in shrinkage soil

The behaviour of vertical stress of soil pertaining to ground water table and evaporation can be illustrated in Figure 10(a). Regarding evaporation process, pore water pressure (u) at the surface can be expressed in equation (49), when the water table is at depth h m below the surface. The value of u increases as the increasing of α, defined as a factor that increases above unity as the rate of evaporation increases. If the water table remain unchanged, the total overburden stress at any depth z below the surface can be written in equation (50). Therefore, the effective overburden stress can be calculated by equation (51).

$$\mathrm{u} = -\alpha\gamma_w h \tag{49}$$

$$\sigma_v = \gamma z \tag{50}$$

$$\sigma_v{}' = [\gamma z + -\alpha\gamma_w(h - z)] \tag{51}$$

where, γ_w is unit weight of water and γ is bulk unit weight of clay.

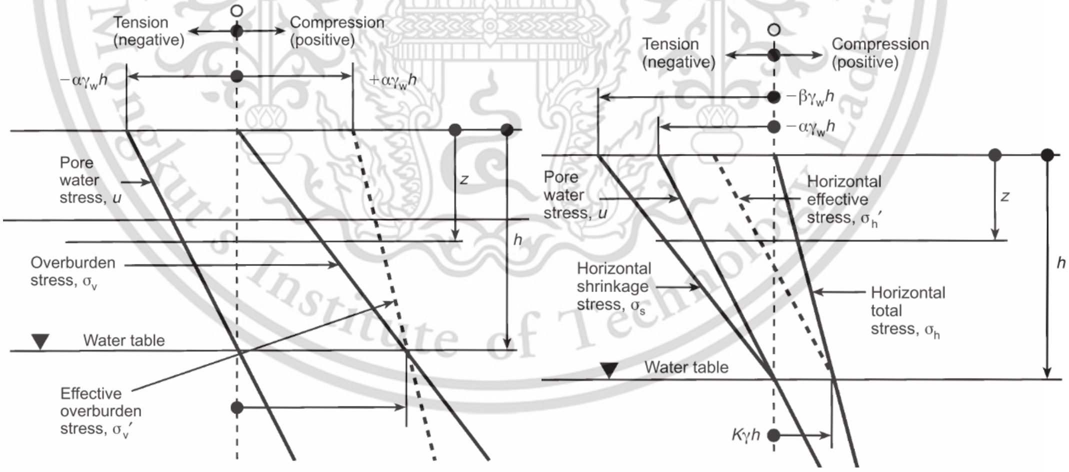

(a) vertical stress (b) horizontal stress

Figure 10 Changes in stresses in a soil profile as a result of drying

Moreover, horizontal stress along the depth with respect to evaporation process can be depicted in Figure 10(b). During balance condition, as evaporation proceed and the soil remain intact, the horizontal shrinkage stress arises. The value of horizontal shrinkage stress (σ_s) at the surface is related to pore water tension arising from surface evaporation, written in equation (52). Meanwhile, β is defined as a factor that is depend on the stress-strain characteristics of the soil in horizontal plane. Noted that β can be equal or greater than α.

$$\sigma_s = -\beta\gamma_w h \tag{52}$$

If σ_s is a total tension, the effective horizontal stress at depth z can be expressed in equation (53) or equation (54), where K is known as horizontal stress coefficient.

$$\sigma'_h = \sigma_s + (\sigma_s - u) \tag{53}$$

$$\sigma'_h = \gamma_w(h - z)(\beta - \alpha) - K\gamma z \tag{54}$$

2.4.2 Tensile strength in cracking soil

It is generally proven that desiccation cracks may develop when tensile stress exceeds the tensile strength (Lee et al., 1988; Sun et al., 2009; Cheng et al., 2021). Cracks started from the bottom and continuously generated vertically upward the surface and laterally outward the adjacent cracks (Weinberger, 1999). The attendance of crack may generate soil into two structural behaviours i.e., micropore and macropores, known as dual porosity model. Following this, the composition of those structure will affect the moisture content and suction in soil, and thus soil tensile strength. Considering Alonso et al. (2010), the moisture content in dual porosity soil structure can represented by effective degree of saturation, as can be expressed in equation (55) and (56).

$$S_r = S_r^M + S_r^m \tag{55}$$

$$S_r^e = \frac{S_r - S_r^m}{1 - S_r^m} \tag{56}$$

where S_r is ordinary degree of saturation, S_r^e is effective degree of saturation, S_r^M is macroscopic degree of saturation, and S_r^m is microscopic degree of saturation.

By incorporating effective degree of saturation to general effective stress equation, Alonso et al. (2010) proposed new model as can written in equation (57). Accordingly, new Mohr- Coulomb strength equation can be expressed in equation (58).

$$\sigma' = \sigma - u_a + S_r^e(u_a - u_w) \tag{57}$$

$$\tau = c' + (\sigma - u_a)\tan\varphi' + S_r^e(u_a - u_w)\tan\varphi' \tag{58}$$

Note that S_r^e is similar to χ in equation (11). By considering Mohr-Coulomb envelope as can depicted in fig, under uniaxial tension with the major principal net normal stress equal to zero, the tensile strength (σ_{tu}) is equal to the minor principal net normal stress at failure. Thus, tensile strength equation can be given in equation (59).

$$\sigma_{tu} = \frac{2c\cos\varphi' + 2S_r^e(u_a - u_w)\tan\varphi'\cos\varphi'}{1 + \sin\varphi'} \tag{59}$$

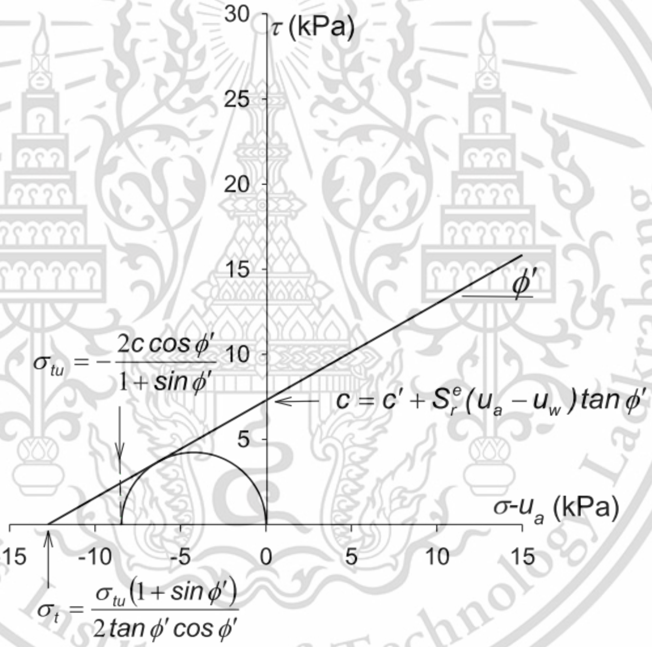

Figure 11 Tensile strength for uniaxial and isotropic failure envelope.

2.4.3 Crack properties analysis

There are three parameters that will be discussed in this section i.e., crack depth, crack space and crack width. Those three parameters are the most significant input that should be taken into account to the further analysis in association with the crack.

(i) Crack Depth

The analysis of crack depth can be developed using elastic theory, presented by Morris et al. (1992). Based on their research, the incremental strain in a horizontal direction for isotropic unsaturated soil can be expressed in equation (60).

$$\Delta\varepsilon_x = \frac{\Delta(\sigma_x - u_a)}{E} - \frac{\mu}{E}\left(\Delta\sigma_y - \Delta\sigma_z - 2\Delta u_a\right) + \frac{\Delta(u_a - u_w)}{H} \tag{60}$$

Where ε_x is normal strain to the long axis of the crack, μ is Poisson's ratio, $\Delta(\sigma_x - u_a)$ is the change in net normal stress in the x, y and z direction, $\Delta(u_a - u_w)$ is the change in matric suction, and E and H is elastic moduli with respect to net normal stress and suction.

At rest condition, $\Delta\varepsilon_x$ is zero. Moreover, as $\Delta u_a = 0$, $u_a = 0$, $\Delta\sigma_z = 0$, and $\Delta\sigma_x = \Delta\sigma_y$, equation (60) can be reduced to equation (61).

$$\Delta\varepsilon_x = \frac{E}{H(1-\mu)}\Delta(u_a - u_w) \tag{61}$$

By assuming the ground surface is saturated, and suction is zero, the initial horizontal stress = $K_0\gamma Z_c$, where K_0 is coefficient earth pressure at rest and Z_c is considered depth of soil. At the certain point when suction rise, the final horizontal stress must be equal to tensile strength, thus can be express $\sigma_t = K_0\gamma Z_c$. The final stress equation can be substituted into equation (61), so that crack depth can be written in equation

$$Z_c = \frac{E}{K_0\gamma H(1-\mu)}\Delta(u_a - u_w) + \frac{\sigma_t}{K_0\gamma} \tag{62}$$

(ii) Crack spacing and crack width

Several researchers have developed methods to calculated the width of crack. Costa et al. (2013) studied salient factors controlling desiccation cracking of clay in laboratory experiments. Based on their research, there are wo controlling factors were identified in desiccation cracking i.e., tensile stress and strain energy development. Moreover, Peron et al. (2009) postulated that homogeneous soil macroscopic cracking is possible only in the presence of boundary constraints and (or) moisture gradients, inducing the build-up of tensile stresses. Considering Costa et al. (2013), the spacing (S) of square pattern of crack can be computed using equation (63).

$$S = 4\frac{G_s E}{\sigma^2} = 4\frac{G_s}{E(\alpha\Delta w)^2} \tag{63}$$

Where, Gs is fracture energy of material, σ is tensile strength, Δw is change of moisture constant, a is hydric constant. The fracture energy of clay can vary significantly, from 0.35 N/m to 110 N/m. However, the value of Gs for very soft wet clay is about 1 N/m (Costa, 2010).

The cracks spacing should be calculated before crack width analysis, as well as observation area and crack length. Following this, crack width can determined using volumetric strain theory, proposed by (Peron, Hueckel, et al., 2009) as can be seen in equation (64).

$$\varepsilon_v = -\frac{G_s}{1+e_0}\Delta w \tag{64}$$

Where, Gs is specific gravity and e_0 is void ratio at saturated condition.

2.5 Stability and serviceability of embankment

In transportation engineering (i.e., roads, railways, etc.), embankment is fundamental earthwork regarding structure alignment. A basic and advanced understanding of its behaviour is vital for design purposes. Stability and serviceability issues must be considered in the analysis to ensure that the structure is safe for the expected design life. Improper design or implementation of earthwork will reduce service performance (Fredlund and Rahardjo 1993; Ranjan and Rao 2000; Briggs et al. 2019). The emergency repair cost will be estimated at 10 times that of planned maintenance. Slope failure due to inaccurate engineering design will have significant consequences, such as the loss of economic and human life (Postill 2018). The main factor that must be considered in stability and serviceability analysis will be discussed herein.

2.5.1 Stability of embankment

Stability issue is one of the most important issues in all of structural design, including embankment. To represent the stability index of earthwork, researchers and practicians in geotechnical engineering use Factor of Safety (FOS), known as the ratio between soil strength and soil strength. Several theories have been developed to determine such as limit equilibrium (LE) method and strength reduction (SR) method Detail of each theory will be explained as follows.

(i) Limit equilibrium method

The LE methods are most popular for practical applications due to its long history as well as simplicity (Yang et al., 2019). Perfectly plastic Mohr-Coulomb criterion is employed to analyze stability condition in this method. Further to this, LE method has been significantly improved by using various methods of vertical slices (e.g., Janbu (1954), Bishop (1955), and Morgenstern and Price (1965)). Based on their research, Janbu (1954) and Bishop (1955) only considered force and moment equilibrium respectively. Moreover, Morgenstern and Price (1965) satisfying both the force and moment equilibrium condition in his analysis. To determine FOS, considered force acting in slice of slope should be taken into account, as shown in Figure 12. Moreover, FOS regarding force (FOS_f) and moment (FOS_m) equilibrium condition can be calculated using equation (65) and (66) respectively.

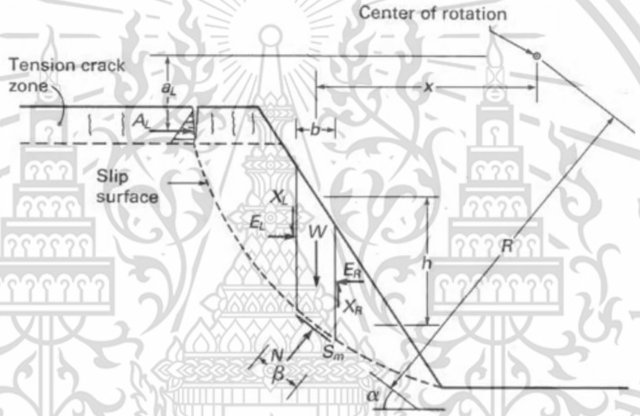

Figure 12 Forces acting on one slice of a sliding mass.

$$FOS_f = \frac{\sum[c'\beta\cos\alpha + \{N - u_w\beta\}\tan\varphi'\cos\alpha]}{\sum N\sin\alpha} \quad (65)$$

$$FOS_m = \frac{\sum[c'\beta R + \{N - u_w\beta\}R\tan\varphi']}{\sum Wx - \sum Nf} \quad (66)$$

Where W is total weight of the slice of width b and height h, N is total normal force on the base of the slice, R is radius for a circular slip surface or the moment arm associated with the mobilized shear force for any shape of slip surface, f is perpendicular offset of the normal force from the center of rotation or from the center of moments, x is horizontal distance from the centerline of each slice to the center of rotation or to the center of moments, α is angle between the tangent to the center of the base of each slice and the horizontal and β is sloping distance across the base of a slice.

In the context of unsaturated soil when negative pore water pressure is considered in the soil strength equation, FOS can be calculated by equation (67) and (68).

$$FOS_f = \frac{\sum\left[c'\beta\cos\alpha + \left\{N - u_w\beta\frac{\tan\varphi^b}{\tan\varphi'}\right\}\tan\varphi'\cos\alpha\right]}{\sum N\sin\alpha} \tag{67}$$

$$FOS_m = \frac{\sum\left[c'\beta R + \left\{N - u_w\beta\frac{\tan\varphi^b}{\tan\varphi'}\right\}R\tan\varphi'\right]}{\sum Wx - \sum Nf} \tag{68}$$

(ii) Strength reduction method

Strength reduction is stability analysis method where FOS is obtained by weakening the soil in steps in an elastic-plastic finite element analysis until the slope fails (Geo-Slope International, 2007). Considering Duncan (1996), FOS in SR method can be defined as ratio of actual soil shear strength to the minimum shear strength required to prevent failure, shown in equation (69).

$$FOS = \frac{\tan\varphi'}{\tan{\varphi'}_f} = \frac{c'}{{c'}_f} \tag{69}$$

Where ${\varphi'}_f$ and ${c'}_f$ are the effective stress strength parameters at failure.

Considering rapid advances in computer technology in 1970’s, the application of finite element method (FEM) and other numerical analysis approaches grown tremendously including in geotechnical aspect. Thus, SR method is preferable to analyze a very broad range of problems, while yielding realistic results, rather than LE method. Compare to LE method, SR method provides several advantages such as (i) it eliminates the need for a priori assumptions on failure mechanisms (the type, shape, and location of failure surfaces), (ii) the SR method automatically establishes the critical failure mechanism, and (iii) It eliminates artificial separation of slope problems into those involving slip surface failures (RocScience, 2004).

2.5.2 Serviceability of Embankment

The majority of design approaches prioritize short-term stability over long-term performance. Especially in earthwork structure design, many engineers only focus on stability issues pertaining to soil strength parameters. However, the long-term performance, especially the deformation during wet and dry cycles, can also decrease the safety and serviceability of the slope, leading to severe problems for the infrastructure. Pore water pressures due to drought and precipitation have a significant effect on infrastructure slope serviceability (Vaughan et al. 1979; Anderson and Kneale 1980; Brooks et al. 2004; Ridley et al. 2004). The detail explanation of earthwork behaviour due to seasonal variation will be discussed as follows.

(i) VWC behaviour due to seasonal variation

To investigate VWC behaviour because of wetting and drying process, Apriyono et al. (2023) have conducted a comparison study between cut slope and embankment considering seasonal effect. Based on their result, there are distinctive behaviour of PWP along the depth between cut slope and embankment as can be seen in Figure 13 (a) and (b). Volumetric water content was increased to the maximal value for most cases during the wet season and decreased to the minimal value because of the evaporation process during drought. The volumetric value at 0.5-meter depth ranges from 15% to 45% in embankment slopes (An et al. 2018; Jin-long et al. 2018; Luo et al. 2020) and from 20% to 50% in most cut slopes (Smethurst et al. 2006, 2012, 2021; Dixon et al. 2018). As reported by Blight (1997), the soil at greater depth is less affected by seasonal and atmospheric conditions, such as rain, humidity, solar radiation, and air temperature. Moreover, a statistical logarithmic regression method was used to evaluate persistent zone depth based on VWC range data as shown in Figure 13 (c). The result of that analysis is shown in Figure 13 (c). The persistent VWC depth in cut slope and embankment was around 1.9 m and 3.1 m, respectively. As an over consolidated clay in relation to its previous loading history, cut slopes tend to have lower Ks. Thus, a persistent VWC zone in the cut slope is located at a shallower depth than the embankment.

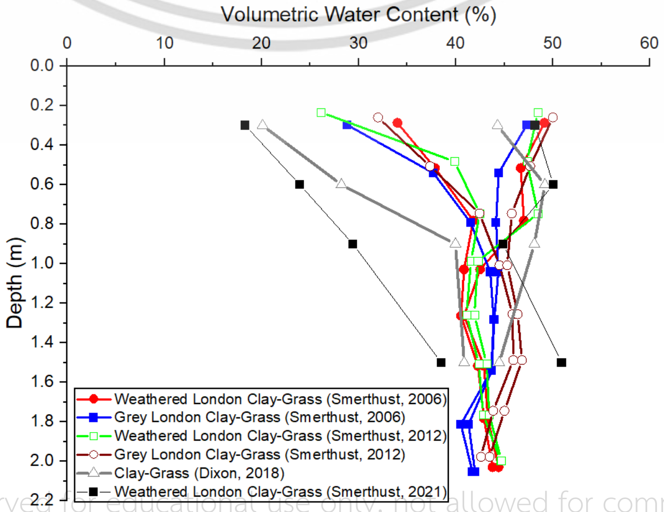

(a) cut slope

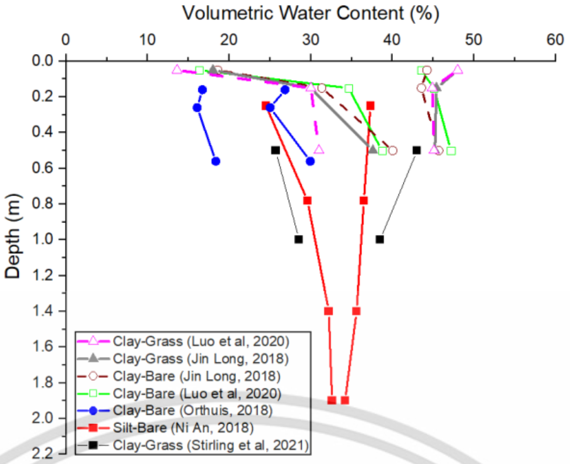

(b) embankment

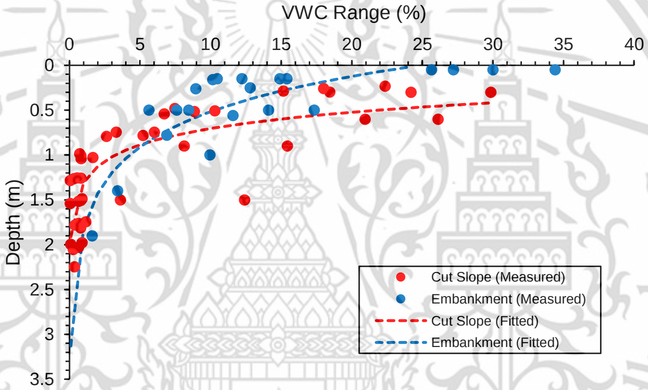

(c) comparison between cut slope and embankment

Figure 13 VWC cut slope and embankment along the depth

(ii) PWP behaviour due to seasonal variation

PWP is a critical parameter for soil shear strength and is vital for slope stability analysis. Thus, PWP observation is highly necessary for geotechnical engineering. Figure 14 (a) and (b), the PWP value at a shallow depth varies more than that at a deeper depth in both cut slope and embankment. The value of PWP in the soil is related to volumetric water content, which is influenced by seasonal and atmospheric conditions. Hence, PWP in the soil will decrease in relation to the drying process due to evaporation and it will increase during the wet season due to precipitation (Fredlund and Rahardjo 1993). Based on Figure 13, VWC at the near-surface zone fluctuates more than at deeper depths. Consequently, the PWP value at shallow depth also has a wider range than at a deeper depth.

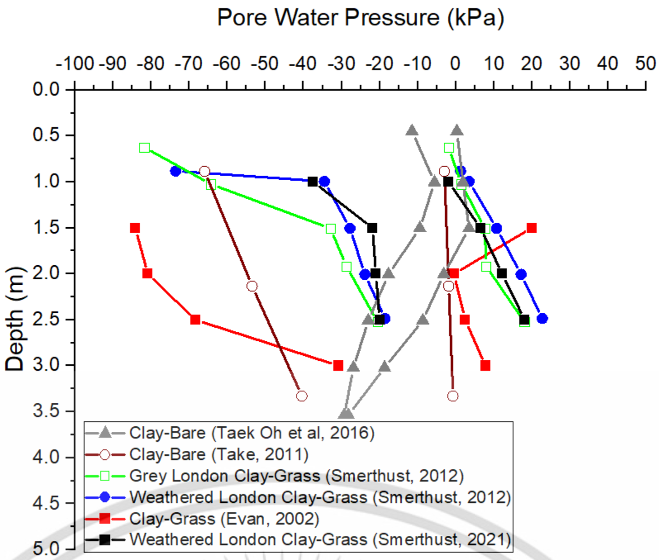

(a) cut slope

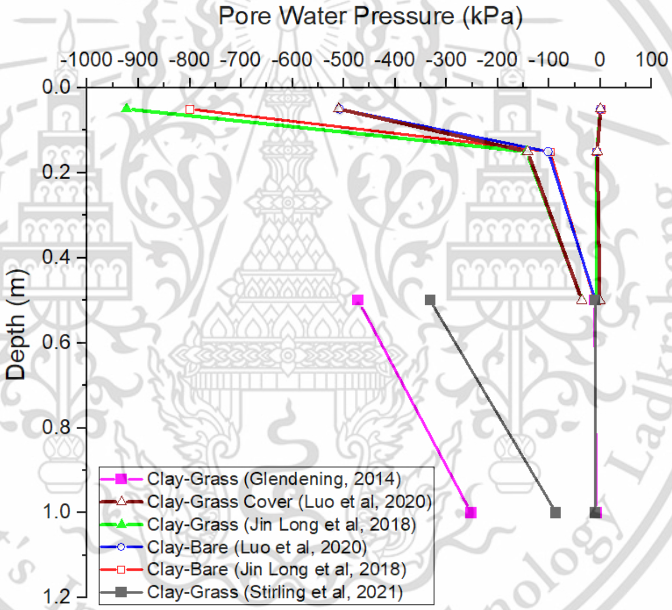

(b) embankment

Figure 14 PWP cut slope and embankment along the depth

In a cut slope, the excavation process will significantly affect PWP. Soil mass removal during the excavation process on a cut slope can reduce PWP within the slope. The PWP will be dissipated for several years after excavation before reaching the equilibrium condition. Moreover, the PWP dissipation process in a deeper position is longer than that at the ground surface. Based on Postill et al. (2021), PWP dissipation in a clay cut slope was completed within 10 to 20 years of construction near the surface. However, PWP dissipation to a steady-state condition is still occurring at a 5.0

m depth after 40 years post-excavation. In addition, during the equilibrium process, the soil will swell, producing delayed failure in many cases of cut slope (Potts et al. 1997; Schuerch et al. 2017). Hence, maintaining pore water pressure in the cut slope is critical to avoid delayed failure. Increasing the negative PWP value at the cut slope ground surface from -10 kPa to -20 kPa will significantly reduce the risk of delayed failure (Potts et al. 1997). By contrast, the filling process in embankment construction will increase PWP. However, the equilibrium process in the embankment is slightly faster than that in the cut slope. Based on Hudacsek et al. (2009), low permeability embankments need 10 to 15 years to reach equilibrium. The comparison of the PWP value between the cut slope and the embankment corresponding to the seasonal cycle is shown in Figure 15 (Hudacsek et al. 2009; Postill et al. 2021). Figure 15 shows the PWP from the cut slope and embankment fluctuated because of the drying and wetting seasons. The PWP in the embankment became more stable after several years of construction. However, a larger fluctuation of PWP was observed in the cut slope compared to that from the embankment. The PWP in cut slope still increased even after 10 years of construction. Hence, a cut slope is more vulnerable to delayed failure than an embankment due to an increase in PWP after construction.

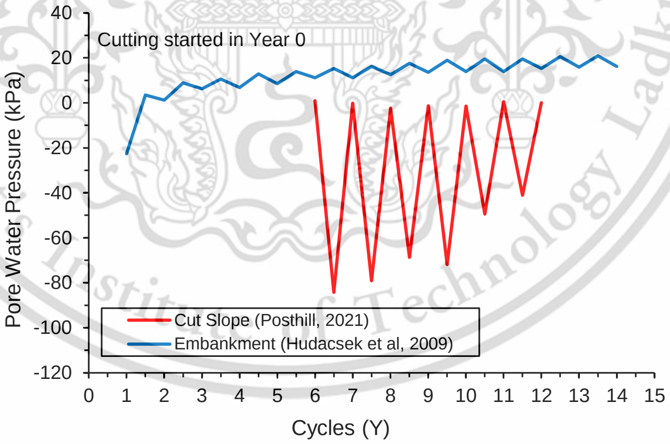

Figure 15 Cut slope and embankment respond to seasonal.

(iii) Stress state and stress path of cut slope and embankment

The cut slope and embankment have typical stress-strain behaviours based on the different loads experienced. Understanding the stress path is critical for revealing the underlying mechanism of both constructions. Figure 16 depicts the stress path at the toe of the cut slope as a result of the excavation process. Xiao-kun et al. (2014) and Abed and Korkiala-Tanttu (2018), presented their study on the stress path in cut slopes in relation to the excavation step. During the excavation step, the magnitude of effective stress was reduced because of the unloading condition. Considering its stress state compared to the critical state line, the cut slope was stable before the excavation process because the stress state was away from the CSL. However, the stress state moved toward the critical state line during the excavation step, indicating that the slope stability decreased.

Figure 16 (b) also presents a stress path along the construction process of an embankment. Finno et al. (2011) calculated the stress path beneath embankment construction for port development in Alaska. The embankment was reinforced by an anchor and a concrete wall as facing material. Taechakumthorn and Rowe (2012) also studied the reinforced embankment’s performance on a sensitive Champlain clay deposit elastoviscoplastic constitutive model. According to their studies, the mean effective stress increases during embankment construction. With sufficient drainage of PWP, the stress state at the observation point moved away from the critical state line after embankment construction. Thus, the stability of the slope increases in relation to the increase in embankment height.

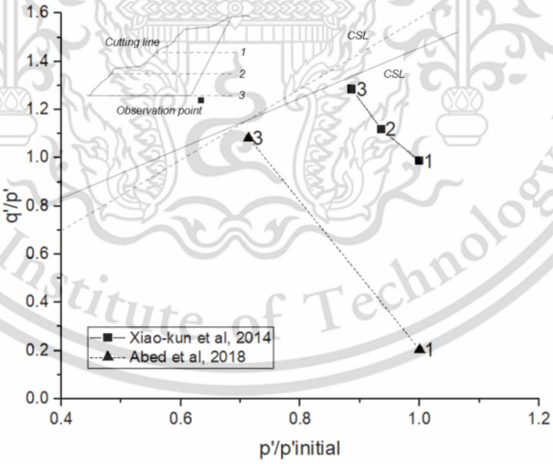

(a) cut slope

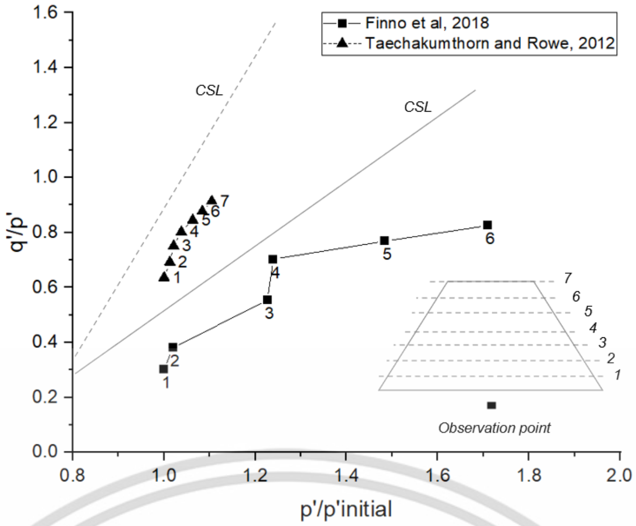

(b) embankment

Figure 16 Stress-path during the construction process

Because PWPs fluctuate during wetting and drying, the stress states vary for both the cut slope and the embankment. Figure 17 (a) and (b) show the stress path that corresponds to the seasonal cycles in cut slope and embankment, respectively. The cut slope and embankment have the same pattern of stress path because of seasonal change. The stress state moved away from the critical state line during the dry period in relation to the reduction in pore water pressure. On the contrary, the stress path moved toward the critical state line during the wetting season (Yang et al. 2017; Liu et al. 2020;). It means the stability was increased during the drying season and decreased during the wet season. The embankment has a slightly faster equilibrium process than the cut slope, and thus, the embankment is less susceptible to delayed failures occurring in the future than the cut slope.

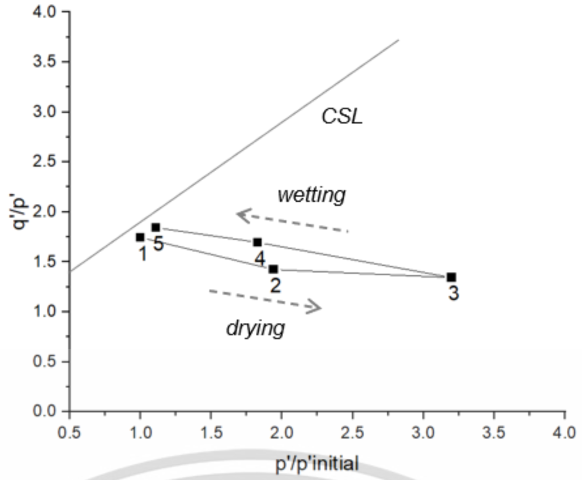

(a) cut slope

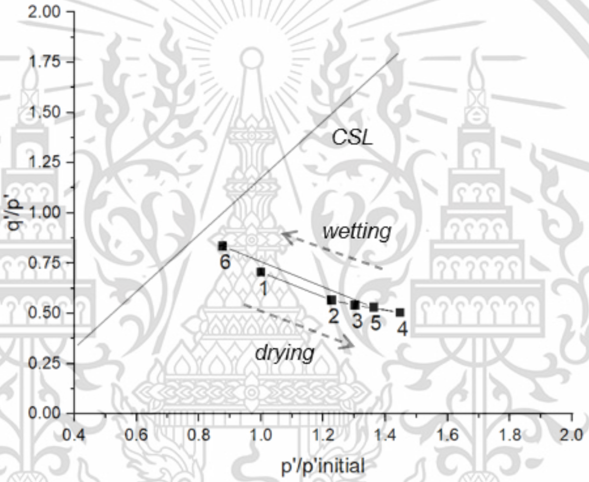

(b) embankment

Figure 17 Stress-path due to seasonal behavior.

(iv) Displacement behaviour due to seasonal variation.

In terms of serviceability, shrinkage and swelling due to seasonal effects must be considered in cut slopes and embankments. Following their loading history, cut slope and embankment have distinctive displacement behaviour attributed to the wetting and drying process. Several studies were reviewed to compare cut slopes and embankments in terms of its seasonal behaviour. Based on the different heights of the slope, the comparison between cut slope and embankment was analyzed in relation to the displacement and height ratio (ΔXY/H). Figure 18 shows the difference between cut slope and embankment displacement during wetting and drying cycle processes after construction in horizontal and vertical directions (Hudacsek et al.

2009; Postill et al. 2021). The cut slope has more significant displacement, both vertical and horizontal, than the embankment. Because the stress path of the cut slope moved closer to the critical state line as shown in Figure 16, the highest displacement occurred during the construction process. In association with loading history, cut slopes tend to swell after the excavation process. However, embankments tend to shrink because of settlement behaviour. Furthermore, rainfall can induce heave in cut slopes and embankments during the wet season. By contrast, both tend to shrink, which reduces the magnitude of the displacement during the drying process.

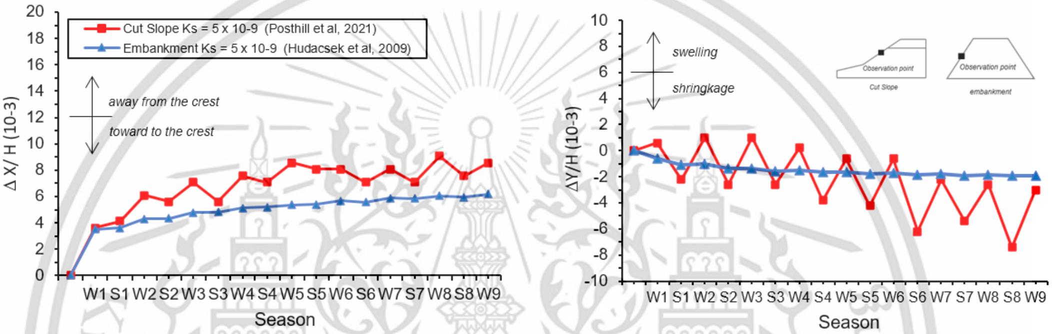

(a) horisontal displacement (b) vertical displacement

Figure 18 Displacement and height ratio due to seasonal effect.

Because the Ks play an essential role in the mechanical performance of soil, the displacement behaviour in cut slopes and embankment due to the Ks were reviewed in this study. Figure 19 show the distinctive total displacements (xy direction) due to Ks variation in the cut slope and embankment, respectively (Hughes et al. 2009; Towhata et al. 2015; Postill et al. 2021). As shown in Figure 15, a cut slope with a higher Ks value (1 x 10-5 m/s) produces more displacement than a lower Ks (5 x 10-9 m/s) after three cycles of wetting and drying (Towhata et al. 2015; Postill et al. 2021). A higher permeability embankment (1.6 x 10-10) also generates more significant displacement than the one (8.8 x 10-11) (Hughes et al. 2009).

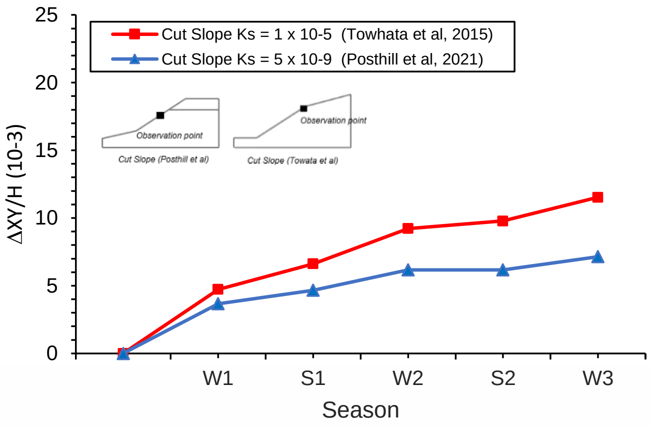

(a) cut slope

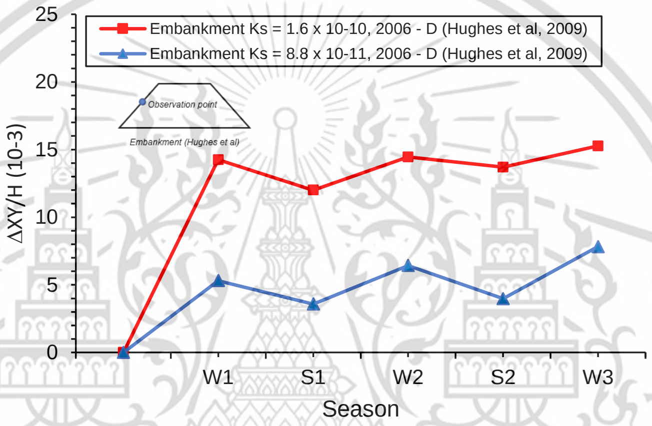

(b) embankment

Figure 19 Total displacement and height ratio due to Ks variation

2.6 Physical Model

The use of physical and numerical modelling has been generally used by researchers as complementary tools to reveal physical phenomena (e.g., soil-structure interaction, soil-atmosphere interaction and soil movement) (Heib et al., 2020). The first physical geotechnical model has been developed by Terzaghi (1943) in 1943 to investigate ground movement and arching phenomenon. Considering its behaviour, physical model provides several advantages and limitations which influence the model accuracy. Detail explanation of physical model will be presented as follows.

2.6.1 The Type of Physical Model

Physical simulation is one of the essential aspects in the context of knowledge development, including geotechnical engineering. The application of physical model has successfully uncovered many engineering problem regarding theoretical and empirical hypotheses validation (Green, 2014). Considering Heib et al. (2020), physical modelling provide several advantages such as size reduction possibility, simplification, convenience, and can study complex system. To obtain better point of view, the role of physical model in engineering study can be presented in Figure 20. With respect to its scale condition, physical model can be divided into two general types as follows.

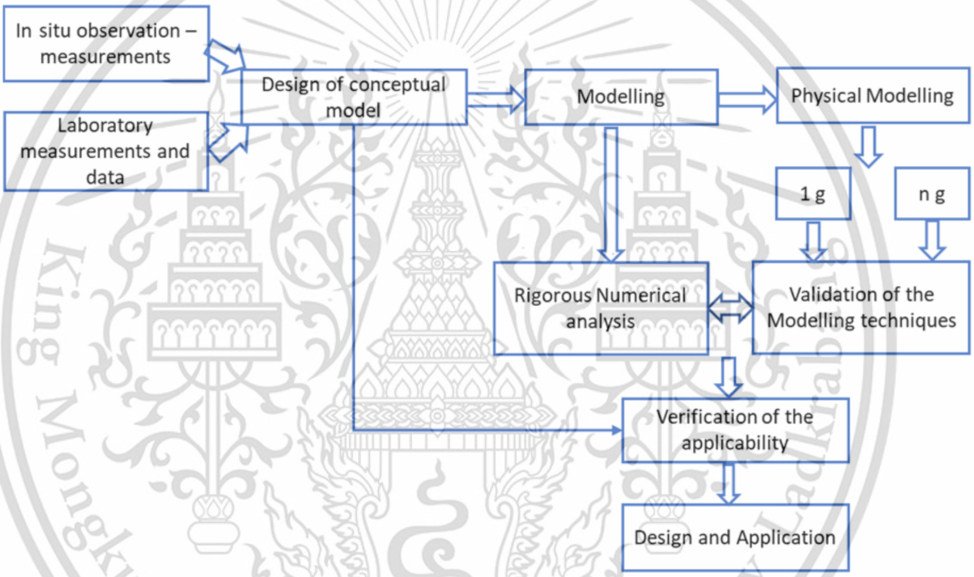

Figure 20 Contribution of modelling to analysis, understanding and design.

(i) Full-scale Model

Regarding Wood (2004) full-scale model use real condition that need to be considered in any geotechnical modelling such as ground conditions, loads, stress levels and stress histories. In this model, we still can control the dimension of the structure, including the length, the width and the height. However, we have no control over the ground conditions and environmental condition. Thus, it is necessary to obtain accurate data of ground condition to prevent discrepancy between the result and the theory. Despite having several advantages, full-scale model also provides some limitation, especially considering the time and the budget of the test.

Since, requires bigger dimension than small-scale model, this model consume higher cost and occupy longer time to obtain appropriate result.

(ii) Small-scale Model

The main advantages of small-scale physical model are providing more simplicity and thus reducing research cost. However, smaller scale model will decrease the accuracy, regarding its similarity factor compared to real model. Therefore, the attendance of theoretical support is essential to get better interpretation of small-scale model result. Moreover, the basic knowledge of scaling laws and dimensional analysis is important. The type of small-scale physical model is closely related to similarity ratio between real condition and the model, ranging from 1g (single gravity) to ng (n-scale gravity). Regarding the dimension of the model, 1g model provides several benefits such as resulting reliable data for supporting numerical modelling and minimizing linear model scale for typical prototypes. However, 1g model cannot provides realistic in situ stresses during the test. Thus, deformation and failure mechanism are not correctly simulated.

To overcome the limitation of 1g model, centrifuge modeling has been employed as powerful tools in geotechnical engineering study. Centrifuge modeling is small-scaled model subjected to acceleration fields of magnitude many times Earth’s gravity (Viswanadham, 2016). Besides, this technique can predict non-linearity behaviour of soil to obtain higher accurate result in the simulation. The centrifuge provides a modelling environment in which stresses and strains match a full-size equivalent that is larger than the model by a factor N, where N is the ratio between the centrifuge acceleration and Earth’s gravity (Addis, 2020). Therefore, stress-strain response operates within the model and body forces are scaled correctly.

2.6.2 Physical Model Design

There are several conditions that should be taken into account in scaled physical model i.e., (i) depends on the purpose of study and constructive characteristics of the prototype; (ii) the physical model (m) must be a true scalar representation of the prototype (p); and (iii) the ratio between the prototype parameter and model parameter defines the scale factor. Moreover, regarding Wood (2004), physical models should be considered geometric scale factor, effective scale factor and effective stress-gradient ratio. Further to this, the detail factor that should be respected in physical model design will be described as follows.

(i) Geomaterial similarity

Based on Garnier et al. (2007), geomaterial used in geotechnical physical modelling should be repeatable, operator-independent, and tight tolerance in soil conditions. Following this, the specific weight, the elastic parameters and the strength parameters should be taken into account as model parameter.

(ii) Structure similarity

The structure similarity is closely related to the scale of the physical model. Due to complex its complex behaviour, it is very challenging to provide high accurate similarity of structure for physical model. In term of structure, the equivalent stiffness (EI) is generally more respected than the material characteristics (Heib et al., 2013). In the recent past, 3D printing (3DP) has been used to study soil-structure interaction with ng physical model (Ritter et al., 2017).

(iii) Instrumentation of the physical model

Instrumentations is one of essential tools, used in physical modelling. High accuracy and complete instrumentation provide detailed exploitation, thus resulting good quality research. Moreover, suitable devices depend on the main aims of the research. Following this, appropriate data acquisition tools and analyzing method can be selected with respect to the objective, role, and desired output.

2.6.3 Full-scaled embankment model

Many full-scale embankment models have been built to obtain a better understanding of the hydro-mechanical behaviour due to seasonal change (Hughes et al., 2009; Glendinning et al., 2014; An et al., 2018; Khan et al., 2021). Considering its real condition, full-scaled model is one of the best options to observe earthwork behaviour. Since having the same dimension as the prototype, it may provide realistic in situ stresses. To achieve study aims, researchers have constructed many different dimension of embankment models, regarding their objective. Hughes et al. (2009) developed a 90-m long model to assess climate effects on the embankment. Meanwhile, Glendinning et al. (2014) analyzed the implications of weather-induced PWPs using 18 m of the length of the embankment. Moreover, An et al. (2018) created a 21 m embankment model to study the hydro-thermal behaviour of this construction under climate effects. Recently, Khan et al. (2021) evaluated moisture variation depth induced by rainfall in an old highway embankment.

Soil-vegetation-atmosphere interaction has also been studied by several researchers. Smethurst et al. (2015) and Briggs et al. (2019) conducted field observation methods to study tree removal’s mechanical and hydrological effects on the embankment. Further to this, Vesterberg and Andersson (2022) conducted field observation methods to study tree removal’s mechanical and hydrological effects on the embankment. Moreover, In addition, Oorthuis et al. (2018) monitored an 18 m full-scale length embankment in terms of soil-vegetation-atmosphere interactions in 2017. A full-scaled embankment model was also built by Vesterberg and Andersson (2022) to study settlement and pore pressure behaviour and predictions of test embankments on organic clay. To obtain the research aims, two test embankments were constructed with bases of 30 × 30 m2. The heights of the first and second embankment were 2 m and 1.5 m, respectively.

2.6.4 Experimental Investigation

To facilitate the study, arrays of instrumentation should be situated in the embankment model. Water content and PWP sensor were generally used to observe hydrological parameter. Moreover, inclinometer was also commonly employed to inspect deformation data of the embankment (An et al., 2018; Oorthuis et al., 2018; Khan et al., 2021). In their research, Khan et al. (2021) installed a set of instrumentation, such as water content sensors, PWP, and displacement sensors at several different depths. Nine potential water probes (MPS-6), nine soil moisture sensors, and four data loggers were installed in slope area of the embankment. Following this, they also installed a weather station to obtain rainfall data and other atmospheric parameters such as air temperature, humidity, solar radiation, and wind speed. To observe hydro-mechanical parameters, Oorthuis et al. (2018) also instrumented their embankment with an array of monitoring equipment, such as PWP sensors, water content sensors, and soil temperature sensors. PWP and water content sensors were installed at the depth of 6, 16, 36 and 56 cm. Moreover, soil temperature sensors were situated at the depth of 1, 6 and 11 cm. Furthermore, atmospheric parameter data, i.e., rainfall, air temperature, air humidity, solar radiation, and wind speed, have also been obtained in the study area from the weather station.

2.7 Numerical Study

The application of numerical model to solve geotechnical problem has been accelerated in recent decades as well as the increasing of computer technology. Since numerical model can provides many options of constitutive behaviour, it let the method more versatile, compared to the others techniques. Moreover, numerical study can produce high accurate result considering basic theoretical solution requirements such as equilibrium, compatibility, constitutive behaviour, and boundary condition.

3.5.1 Formulation of finite element analysis

One of the most powerful methods to solve complex engineering problem in term of numerical simulation is finite element method (FEM). The FEM is a systematic procedure of approximating continuous functions as discrete models (Tekkaya and Soyarslan, 2019). The basic steps of FEM can be presented as follows.

(i) Element discretization

First of all, discretization of the model is required prior to further analysis step. The shape of element needs to be determined with respect to model geometry condition. FEM based software such as Seep/W provides several element shapes i.e., triangular, rectangular, and combination between both of them. The mesh generation comprise simplification of the geometry in some regions as well as the use of refined mesh, thus increasing accuracy.

(ii) Primary variable approximation

Primary unknown variable in the displacement-based FEM is the displacement field (d_f). The value displacement fields are governed by the global displacement component. In the context of plane strain analysis, d_f is affected by u and v coordinate direction. Meanwhile, for axisymmetric analysis, this value is determined by x (r) and y (z) coordinate directions. Moreover, displacement field are assumed to have a simple polynomial form that can be written as a function of nodal displacement, expressed in equation (70).

$$d_f \ = N \, d_e \tag{70}$$

Where d_f is vector defining displacement field, N is the matrix of displacement interpolation functions (shape functions), and d_e is the vector of element nodal displacement components. In seep analysis, PWP is the primary unknown variable. Therefore, PWP field across an element can be express by equation (71).

$$p_f \ = N \, p_e \tag{71}$$

Where p_f is vector defining PWP field, N is the matrix of PWP interpolation functions (shape functions), and d_e is the vector of element nodal PWP components. Moreover, secondary quantities such as stresses and strains can be calculated within each element using the definition of strains and applying the material constitutive law, as expressed in equation (72) and (73).

$$\varepsilon \ = B \, d_e \tag{72}$$

$$\sigma \ = D \, \varepsilon \tag{73}$$

Where B is the element strain-displacement matrix and D is the constitutive matrix relating the stress vector (σ), to the strain vector, (ε).

(iii) Element equation

The principle of virtual work should be considered in the analysis to embrace equilibrium and constitutive behaviour. In case of linear elastic material in single finite element, the equilibrium between nodal displacement and applied load can be expressed in equation (74) and (75).

$$K_e d_e \ = R_e \tag{74}$$

$$K_e \ = \int (B^T D B) dV \tag{75}$$

Where K_e is element stiffness matrix, R_e is Re is the vector of the corresponding nodal forces.

(iv) Global equation

Further to this, global equilibrium equation of whole-body model can be generated by considering element equation, as can be written in equation (76) and (77).

$$Kd\ = R \tag{76}$$

$$K = \sum \left(\int (B^T DB) dV \right) \tag{77}$$

Where K is the global stiffness matrix, d is the vector containing the unknown nodal displacements over the whole mesh, and R is the global vector of applied nodal forces.

(v) Boundary condition

Boundary condition is required to set in the model as the final step of global system equation. The boundary condition consists of loading and displacement which are applied in the simulation. Moreover, loading condition should be included all of associated factor such as body force, surface traction, initial stress, and PWP change, given by equation (78) to (82).

$$\mathrm{R}\ = R_b + R_s + R_i + R_f \tag{78}$$

$$R_b\ = \sum \left(\int ({N_\delta}^T f_b) dV \right) \tag{79}$$

$$R_s\ = \sum \left(\int ({N_\delta}^T f_s) dS \right) + F_c \tag{80}$$

$$R_i\ = \sum \left(\int (B^T \sigma_i) dV \right) \tag{81}$$

$$R_f\ = \sum \left(\int (B^T \Delta um) dV \right) \tag{82}$$

Where V is the volume of the element, S is the area of an element over which surface tractions are applied, f_b is the vector of body forces, f_s is the vector of applied surface forces, F_c is the vector of concentrated nodal loads, σi is the vector of initial stresses, Δu is the change in pore pressure, and m is a column matrix.

(vi) Solution of global equation

Following the arrangement of global stiffness matrix and boundary condition, global simultaneous equation will be deployed to compute unknown nodal displacement (d) using equation (83). Furthermore, secondary quantities, such as strains (ε), and stresses (σ) at any point within the element can be determine using equations (72) and (73).

$$d\ = K^{-1} R \tag{83}$$

3.5.2 Geotechnical Consideration

To obtain satisfied result, the numerical analysis should consider geotechnical boundary problem. To do so, basic and advance of associated geotechnical theory should be taken into account in the model. The main aspects that are relevance to the analysis in this thesis will be discussed herein.

(i) Water flow equation

In the context fully saturated soil, one-dimensional fluid flow can be analysis by Darcy's law, expressed in equation (84) (Darcy, 1856).

$$q = -ks\frac{\partial H}{\partial y} \tag{84}$$

Where q is water flux (m/s), and $\frac{\partial H}{\partial y}$ is hydraulic gradient in y. Moreover, saturated flow for two-dimensional flow problem can be expressed by Laplace's equation, written in equation (85).

$$q = k_x\frac{\partial^2 H}{\partial x^2} + k_y\frac{\partial^2 H}{\partial y^2} \tag{85}$$

Where Kx and Ky are saturated hydraulic conductivity in x and y direction respectively (m/s), and H is total head (m). In term of unsaturated soil, water flow is generally calculated by Richard' method, expressed in (33).

(ii) Consolidation theory

As the effect of additional surcharge, embankment tend to experience with consolidation process. In numerical simulation, consolidation analysis was generated based on the assumption of elastic porous medium with saturated laminar pore fluid, expressed in equation (86) (Biot, 1941).

$$\frac{K'}{\gamma_w}\left[k_x\frac{\partial^2 u_w}{\partial x^2} + k_y\frac{\partial^2 u_w}{\partial y^2} + k_y\frac{\partial^2 u_w}{\partial z^2}\right] = \frac{\partial u_w}{\partial t} - \frac{\partial \sigma}{\partial t} \tag{86}$$

Where K' is bulk modulus. For a 2D plane strain fully saturated soil, incompressible soil can be calculated using equation

$$\frac{k_x}{\gamma_w}\frac{\partial^2 u_w}{\partial x^2} + \frac{k_y}{\gamma_w}\frac{\partial^2 u_w}{\partial y^2} + \frac{d}{dt}\left(\frac{\partial u}{\partial x} + \frac{\partial v}{\partial y}\right) = 0 \tag{87}$$

Where u and v are displacement in x and y direction respectively.

3.5.3 Constitutive laws

Constitutive equation, defined as the correlation between stress-strain of material is the most influence factor in numerical analysis. Appropriate constitutive equation leads the accurate result of the simulation, compared to the real behaviour. A briefly review of different constitutive laws, used in numerical simulation will be presented as follows.

(i) Linear elastic model

In this model, soil is modelled as linear and elastic condition with respect to Hooke's law. To characterize stress-strain behaviour in this model, two stiffness parameters are required namely young’s modulus (E) and Poisson’s ratio (ν). Those two parameters can be obtained using oedometer and triaxial test, determined by equation (88) and (89). However, since producing distinctive result compared to real soil behaviour, this model is not suitable in general earthwork condition.

$$E = 1/m_v \left[\frac{1-2u^2}{1-u}\right] \tag{88}$$

$$u = K_0/(1+K_0) \tag{89}$$

(ii) Mohr-coulomb (MC) Model

Generally, this model describes that the material experiences with two conditions i.e., elastic and plastic as a result of loading behaviour. Stress-strain relationship behaves as elastic prior to plastic condition regarding yield surface. Mohr-coulomb (MC) is the most popular elastic perfectly-plastic model, used in geotechnical engineering. The same as linear elastic model, elastic behaviour is governed by E and ν. Meanwhile, plastic behaviour is expressed based on Hoek laws, governed by cohesion (c) and internal friction of angle (ϕ). In MC model, failure condition occurs when the shear stress and effective stress acting on any element in material follows the linear equation, stated in equation (90).

$$\tau = c + \sigma' \tan\varphi \tag{90}$$

In terms of the principal effective stresses, MC failure surface can be illustrated in Figure 21. Coulomb’s failure criterion is an irregular hexagonal pyramid in a three-dimensional principal stress space. Moreover, Coulomb’s yield criterion can be expressed using equation (91). Since yield surface is assumed to be fixed in MC model, this value is equal to the failure surface.

$$f^{13} = \frac{1}{2}(\sigma'_1 - \sigma'_3) - \frac{1}{2}(\sigma'_1 + \sigma'_3)\sin\varphi - c\cos\varphi = 0 \tag{91}$$

Moreover, since MC model is relatively simple and sufficient to analysis earthwork stability, this model is mostly-used in geotechnical practice. However, with respect to linearity behaviour, this model can lead misleading and result in an over-prediction of soil strength, especially in soft soil case (Surarak et al., 2012).

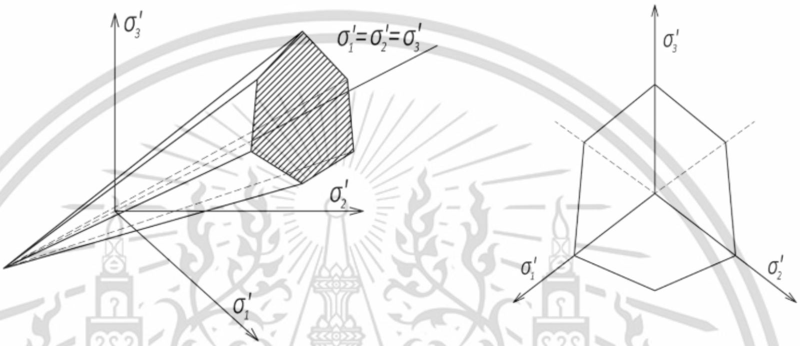

Figure 21 Mohr-coulomb failure surface.

(iii) Hardening soil model

The Hardening soil model (HSM) is one of a cone-cap model which is assumed to be isotropic, depending on the plastic shear and volumetric strains as can be seen in Figure 22 (Schanz et al., 1999). HSM's failure criterion is used to express failure condition in cone part, characterized by the strength parameters i.e., c, ϕ and ψ. The plastic strain behaviour on the cone is govern by shear yield surface following a non-associated flow rule. Moreover, an associated flow rule is used to model plastic strain behaviour in cap area.

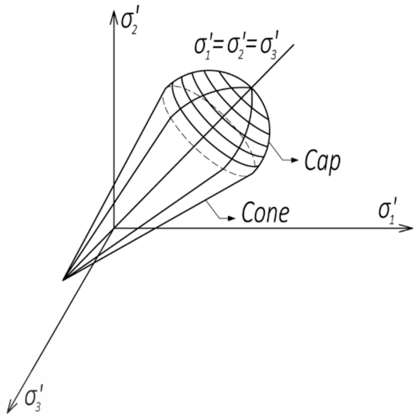

Figure 22 Strain hardening cone-cap model

In the HSM model, the stress-strain relationship because of primary loading can be expressed as hyperbolic curve, shown in Figure 23. The hyperbolic function is dictated from drained triaxial test that can be influenced by the following equation.

$$\varepsilon_1 = \frac{q_a}{2E_{50}} \frac{q}{q_a - q}, for\ q < q_f \tag{92}$$

Where, ε_1 is the axial strain, q is deviatoric stress, q_f is the ultimate deviatoric stress at failure which is derived from the Mohr–Coulomb failure criterion involving the strength parameters c' and ϕ'. The q_a is the asymptotic value of the shear strength, can be determined by q_f / R_f, where R_f is failure ratio. The value of q_f can be expressed in equation (93).

$$q_f = \frac{6 \sin \varphi'}{3 - \sin \varphi'} (\sigma'_3 + c' \cot \varphi') \tag{93}$$

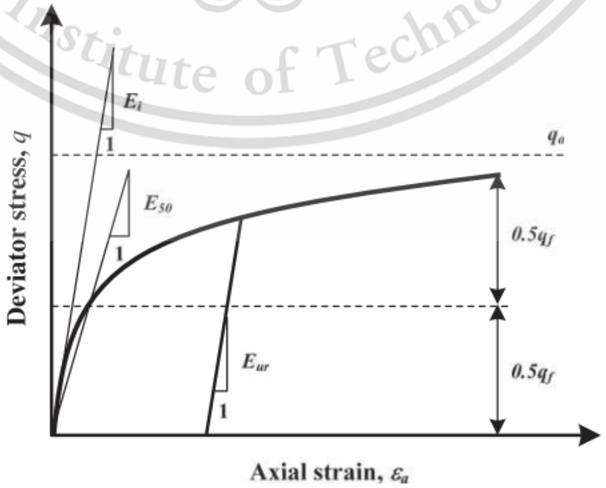

Figure 23 Hyperbolic stress-strain relationship under primary loading.

It can be seen from Figure 23 that hyperbolic model proposed nonlinear of stress-strain relationship. This relationship is governed by several parameter such as E_{50}, E_{ur} and q_f. The parameter E_{50} is confining stress dependent stiffness modulus for primary loading, described in equation (94). Moreover, the stress dependent stiffness modulus for unloading and reloading stress paths can be determined from equation (95).

$$E_{50} = E_{50}^{ref}\left(\frac{c^{'}\cos\varphi' - \sigma^{'}{}_{3}\sin\varphi'}{c^{'}\cos\varphi' - p^{ref}\sin\varphi'}\right)^{m} \tag{94}$$

$$E_{ur} = E_{ur}^{ref}\left(\frac{c^{'}\cos\varphi' - \sigma^{'}{}_{3}\sin\varphi'}{c^{'}\cos\varphi' - p^{ref}\sin\varphi'}\right)^{m} \tag{95}$$

Where E_{50}^{ref} is a reference stiffness modulus corresponding to the reference stress p^{ref} , E_{ur}^{ref} is the reference modulus for unloading and reloading, which corresponds to the reference pressure p^{ref}, and m is power factor that influence stress dependency. Considering (Surarak et al. (2012) the value of m ranged from 0.5 to 1 regarding soil type (0.9 for clay soil).

In compliance with E_{50} and E_{ur}, the oedometer modulus (E_{oed}) is also required to control the magnitude of the plastic strains in HSM. The value of E_{oed} can be calculated from oedometer test, given by equation (96).

$$E_{oed} = E_{oed}^{ref}\left(\frac{c^{'}\cos\varphi' - \sigma^{'}{}_{1}\sin\varphi'}{c^{'}\cos\varphi' - p^{ref}\sin\varphi'}\right)^{m} \tag{96}$$

Where E_{oed}^{ref} is a reference oedometer modulus corresponding to the reference stress p^{ref}.

As mentioned earlier, HSM has been generated under plasticity theory which have double surface behaviour i.e., shear hardening and caps yield surface, as can be depicted in Figure 24.

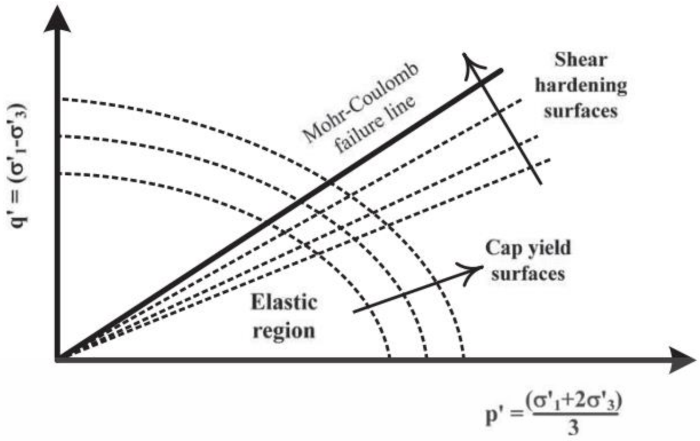

Figure 24 Yield surface in hardening soil model.

Based on (Schanz et al., 1999) the shear hardening yield surface function (f_s) in the HSM can be described in equation (97). Moreover, the cap yield surface (f^c) can be calculated using equation (98).

$$f_s = \frac{q_a}{E_{50}}\left\{\frac{(\sigma'_1 - \sigma'_3)}{q_a - (\sigma'_1 - \sigma'_3)}\right\} - \frac{2(\sigma'_1 - \sigma'_3)}{E_{ur}} - 2\varepsilon_1^p - \varepsilon_v^p \qquad (97)$$

$$f^c = \frac{\tilde{q}^2}{\alpha^2} + p^2 - p_p^2 \qquad (98)$$

Where ε_1^p is plastic strain, ε_v^p is plastic volumetric strain, α is an auxiliary model parameter related to horizontal stress coefficient at rest (K_o). The parameter p and $\tilde{q}$ can be described in equation (99) and (100) respectively.

$$p = \frac{-(\sigma_1 + \sigma_2 + \sigma_3)}{3} \qquad (99)$$

$$\tilde{q}^2 = \sigma_1 - (\delta - 1)\sigma_2 - \sigma_3 \qquad (100)$$

where,

$$\delta = \frac{(3 + \sin\varphi')}{(3 - \sin\varphi')} \qquad (101)$$

$\tilde{q}$ is the special stress measure for deviatoric stresses. In the context of the triaxial compression, $\tilde{q}$ reduces to $\tilde{q} = \delta(\sigma_1-\sigma_3)$. As can be seen in (98), the magnitude of the yield cap is also governed by the isotropic pre-consolidation stress (p_p). Parameter required in HSM model can be seen in Table 3.

Table 3 Required parameters in HSM

Parameter	Description	Parameter evaluation
φ'	Internal friction angle	Slope of failure line from MC failure criterion
c'	Cohesion	y-intercept of failure line from MC failure criterion
R_f	Failure ratio	$(\sigma_1 - \sigma_3)_f/(\sigma_1 - \sigma_3)_a$
ψ	Dilatancy angle	Function of ε_a and ε_v
E_{50}^{ref}	Ref secant stiffness from drained Triaxial	y-intercept in log (σ_3/p^{ref}) – log (E_{50}) space
E_{oed}^{ref}	Ref tangent stiffness for oedometer loading	y-intercept in log (σ_1/p^{ref}) – log (E_{oed}) space
E_{ur}^{ref}	Red unloading/reloading stiffness	y-intercept in log (σ_3/p^{ref}) – log (E_{ur}) space
m	Exponential power	Slope of trend-line in log (σ_3/p^{ref}) – log (E_{50}) space
υ_{ur}	Unloading/reloading Poisson's ratio	0.2
K_0^{nc}	Coefficient of earth pressure at rest (NC)	1-sin ϕ'

In this study, HSM was used to model soil behaviour in numerical simulation, considering two reasons. Firstly, it was substantiated that embankment experienced with consolidation settlement during wet period and shrinkage throughout dry season, promoting hardening soil behaviour. Secondly, since considering double surface behaviour i.e., shear hardening and caps yield surface, HSM produced more accurate deformation, compared to single surface behaviour especially during low magnitude condition, govern by seasonal shrinkage and swelling.

To consider unsaturated behaviour, stress-pore water pressure relationship has been employed in the simulation. Regarding GEO-SLOPE (2012), The incremental strain-stress relationship for an unsaturated soil medium can be written in equation (102).

$$\{\Delta\sigma\} = [D]\{\Delta\varepsilon\} - [D]\{m_H\}(u_a - u_w) + \{\Delta u_a\} \qquad (102)$$

where [D] is drained constitutive matrix, H is unsaturated soil modulus for soil structure with respect to matrix suction (u_a – u_w). m_H and H can be calculated by those following equation.

$$\{m_H\}^T = \langle \frac{1}{H} \frac{1}{H} \frac{1}{H} 0 \rangle$$

$$H = \frac{E}{(1 - 2\nu)[1 - 0.003(u_a - u_w)]}$$

3.5.4 Soil-Atmosphere Interaction model in Numerical Simulation

As a result of evaporation, water may flows from deeper depth to soil surface area, following transient behaviour. On the other hand, Heat flow simultaneously occurs as a consequence of temperature gradient, promoting volume change with respect to suction and temperature fluctuation (Cui et al., 2005). In numerical simulation, modeling the behaviour of water flow, heat flow and volume change in soil is important. This correlation can be expressed by both finite different and finite element equation. In the context of finite different analysis, Wilson et al. (1994) proposed equation (103) to simulate for the one-dimensional flow of liquid and vapour water.

$$\frac{\partial h}{\partial t} = C_w \frac{\partial}{\partial y}\left(k_w \frac{\partial h_w}{\partial y}\right) + C_v \frac{\partial}{\partial y}\left(D_v \frac{\partial P_v}{\partial y}\right) \tag{103}$$

where C_w is the modulus of volume change with respect to the liquid phase, written in equation (104).

$$C_w = \frac{1}{\rho_w g m_2^w} \tag{104}$$

and C_v is the modulus of volume change with respect to the vapour phase, described in equation (105).

$$C_v = \frac{1}{{\rho_w}^2 g m_2^w \left(\frac{P + P_v}{P}\right)} \tag{105}$$

where $(P+P_v)/P$ is a correction factor for vapour diffusion, and P is the total atmospheric pressure (kPa), and P_v is partial pressure in the soil due to water vapour (kPa).

Equation (103) has two variables (i.e., hydraulic head and vapour pressure). These variables are not independent. The vapour pressure P, may be related to the pressure head in the water phase by using the widely accepted thermodynamic relationship given by Edlefsen and Anderson (1943b) as follows:

$$P_v = P_{vs} h_r \tag{106}$$

where P_v is partial pressure hue to water vapour within the voids of the unsaturated soil (kPa), P_{vs} is saturation vapour pressure (kPa) of the soil water at the soil temperature T, and relative humidity is defined as $h_r = e^{\psi g W v/RT}$ where ψ is total potential in the liquid water phase expressed as equivalent matric potential (m).

The calculation of the vapour pressure in equation (106) depends on the saturation vapour pressure and the temperature of the soil. Hence, the temperature profile of the soil must be evaluated simultaneously with equation (103) and (106). Moreover, Wilson et al. (1994) used equation (107) for heat flow:

$$C_h \frac{\partial T}{\partial t} = \frac{\partial}{\partial y}\left(\lambda \frac{\partial T}{\partial t}\right) - L_v \left(\frac{P + P_v}{P}\right) \frac{\partial}{\partial y}\left(D_v \frac{\partial P_v}{\partial y}\right) \tag{107}$$

where C_h is volumetric specific heat; λ is thermal conductivity, and L_v is latent heat of vaporization of water. To simulate the effect of evaporation on hydro-mechanical behaviour of the embankment, equation (103), (106) and (107) should be taken into account simultaneously.

2.8 Research Objective

Based on aforementioned literature review, the limitation of previous study and research gap have been identified and are presented as follows.

In the context of basic unsaturated soil properties, the behaviour of SWRC has been studied under different soil condition. The most complicated phenomenon occurred in muti pores condition, resulting multi modal SWRC. Moreover, the attendance of the crack leads the behaviour of SWRC to be more sophisticated. Several model have been developed by researchers to embrace multi pore soil condition such as Durner (1994), Zhang and Chen (2005), Fredlund et al. (2010), (Li et al. (2011). However, the study of SWRC behaviour under extreme climate is limited in the recent past. In this study, SWRC has been predicted under extreme climate condition with respect to crack propagation. To do so, 30 years historical weather data and 2 years crack and hydrological data in full-scale embankment have been deployed to predict the model.

Furthermore, accurate calculations of water infiltration and is crucial for geotechnical engineering to obtain better result of both serviceability and stability analysis. However, accurately predicting water infiltration in fine-grain materials is challenging due to the complex factors that influence infiltration behaviour, such as the presence of cracks, which may make the infiltration mechanism more complex. Despite the large volume of research carried out on infiltration of cracked soil, there is still lacks a practical framework which relates the crack intensity and water infiltration in order to assess the performance of geotechnical structure under extreme climate conditions. The correlation between crack propagation and infiltration rate under extreme climate condition have been investigated in this study.

Regarding the main topic of this study, serviceability of embankment has been investigated by several researchers through numerical simulation and full-scale embankment. Recently, a full-scaled embankment model was built by Vesterberg and Andersson (2022) to study settlement and pore pressure behaviour and predictions of test embankments on organic clay. To obtain the research aims, two test embankments were constructed with bases of 30 × 30 m2. However, the presence of the crack and extreme climate has not considered in their research.

Considering the limitation of previous research, the objectives of this research can be presented as follows.

1) To observe cracks intensity and cracks propagation along the season.
2) To observe PWP response of the embankment with desiccation cracks under evaporation and rainfall
3) To observe slope deformation under seasonal variation
4) To predict PWP and Deformation under extreme climate

Chapter 3 Research Methodology

3.1 Site location

The field work was performed at a full-scale test site located in Khlong Sam Wa, Bangkok, Thailand. It is located around 15 km from King Mongkut Institute of Technology Latkrabang (KMITL) campus. The specific location of research area can be depicted in Figure 25.

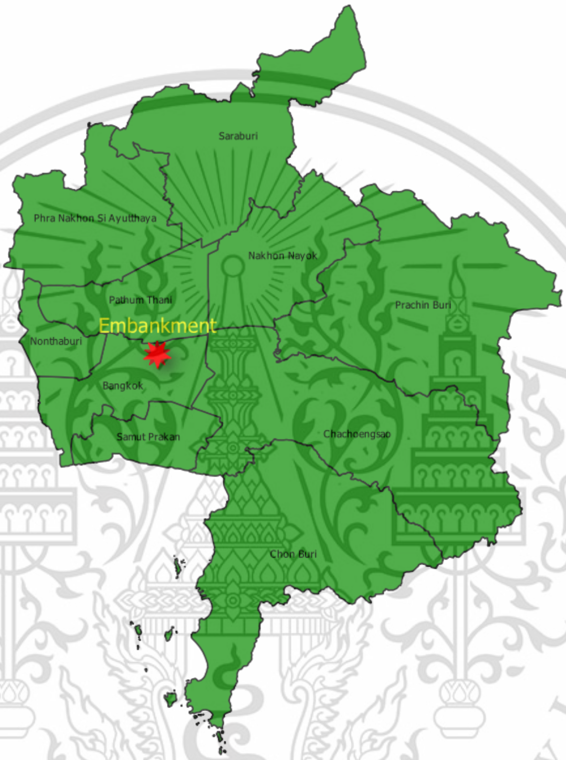

Figure 25 Field work location.

3.2 Soil type

The embankment was built from Bangkok Clay in September 2020, collected from adjacent location of the research area. To obtain the soil index properties, the top layer of soil, approximately 5 m in depth, was excavated within 20 m of the test location using an open-pit method. Disturbed soil samples were collected from the excavated area for further laboratory testing. Several laboratory tests were conducted to determine the soil properties parameters. The Atterberg Limits of the soil were determined in accordance with ASTM D4318, and were found to be 53.91% and 17.02% for liquid and plastic limits, respectively. The specific gravity of the soil was determined to be 2.57, while the clay fraction was found to be 51.06%, indicating that the soil is classified as high plasticity clay according to the unified soil classification system (USCS). To control soil density, a standard Proctor test was conducted in the laboratory, and a sand cone test was performed in the field, following ASTM D698-12 and ASTM D1556-15, respectively. Based on these tests, the maximum dry density and optimum moisture content were found to be 1.504 g/cm3 and 23.8%, respectively. Additionally, the field dry density was measured to be 11.01 kN/m^3.

3.3 Full-scale Embankment

This research was conducted through a full-scale embankment model, measuring length of 17.1 m, width of 9 m, height of 1.8 m and crest width of 2.7 m. Moreover, toe area was extended by flat ground, measuring around 2 m width. Meanwhile, there was a pond right beside the embankment which have water level of 0.5 below the flat ground. This embankment was oriented along its length in a south to north direction and was divided into two different slope angles, i.e., milder zone (1:2) in the east side and steeper zone (1:1.5) in the west side. Moreover, each side was also split into three zones (i.e., two vegetated slopes and one bare slope). In sum, this model consisted of six zones as can be shown in Figure 26. Regarding the research objective, this study focused on bare slope solely.

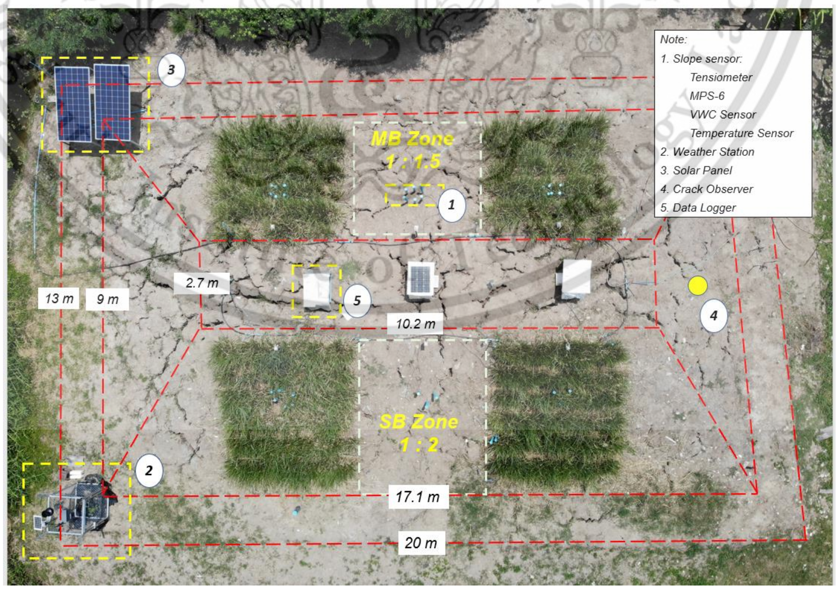

(a) plan view of embankment instrumentation

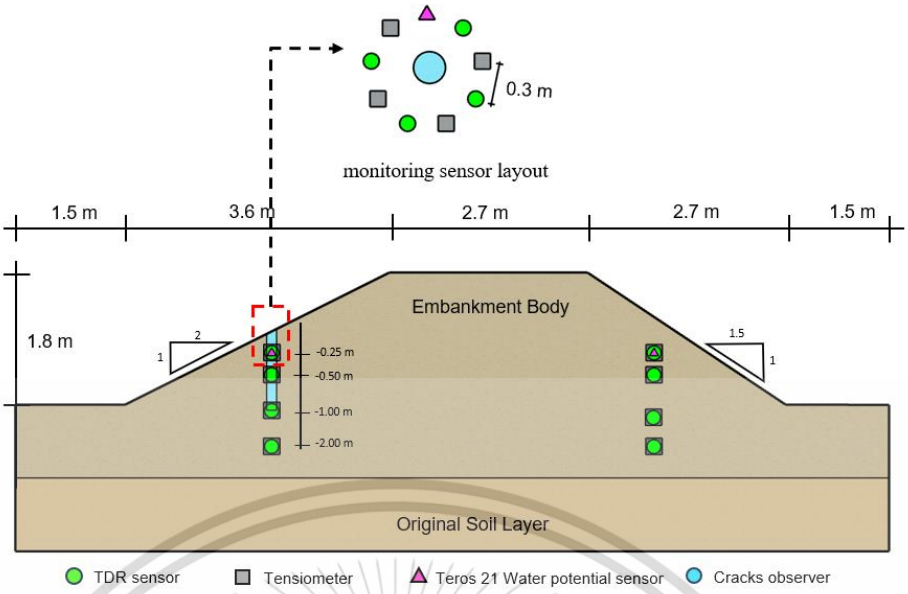

(b) embankment cross-section

Figure 26 Embankment construction and monitoring set-up.

3.4 Soil monitoring

Regarding the research objective, this embankment was instrumented with arrays of monitoring sensors. PWP and VWC sensors were deployed to measure soil hydrological properties at the slope. To obtain soil temperature data, DS18B20 temperature sensors were also placed in the slope. Each sensor was recorded the data every 10 minutes in real-time internet-based data logger. Moreover, the data relied to Green Sustainable Infrastructure (GSI) server, located in KMITL campus through wireless router. The data can be accessed by online via designated GSI website. Meanwhile, SRP-330-6PA 300 Watt of capacity solar panel, was used to supply power all of the equipment in the embankment. The detail location of monitoring set-up in the embankment can be depicted in Figure 26. The detail of soil hydrological parameter monitoring sensor used in the embankment will be explained as follows.

3.4.1 PWP Sensor

There are two types of PWP sensors, installed in the embankment i.e., teros 21 and tensiometer. Teros 21 is high-capacity water potential sensor, produced by decagon Ltd. This sensor uses ceramic discs of predetermined pore-size distribution for suction measurement as can be illustrated in Figure 27 (Tripathy et al., 2016). The ceramic discs, known as a static matrix of pore material will contact the soil, leading hydraulic equilibrium according to the second law of thermodynamics. The attendance of water due to soil contact will influence dielectric permittivity of the porous ceramic discs. Following this, dielectric permittivity of the ceramic discs can allow soil water content calculation (Decagon Devices, 2016). Since the ceramic has a unique and consistent SWRC, by knowing the water content of the reference system will enable obtaining the suction of the other porous medium (Tripathy et al., 2016).

Figure 27 shows the schematic of water potential sensor, used in this research. The sensor consists of two ceramic discs, a circuit board, and two grounded stainless steel. The porous ceramic discs are separated by an electric circuit board to form a capacitor. The total length of the sensor is about 96 mm with diameter of 32 mm and 35 mm width. Based on the equipment specification, this sensor can measure PWP, ranging from -100.000 kPa to 0 kPa with accuracy of 2 kPa (Decagon Devices, 2017). This sensor has been installed at depth of 0.1 m since June 2021. Due to its high range of capacity, this sensor can be used throughout the season continuously.

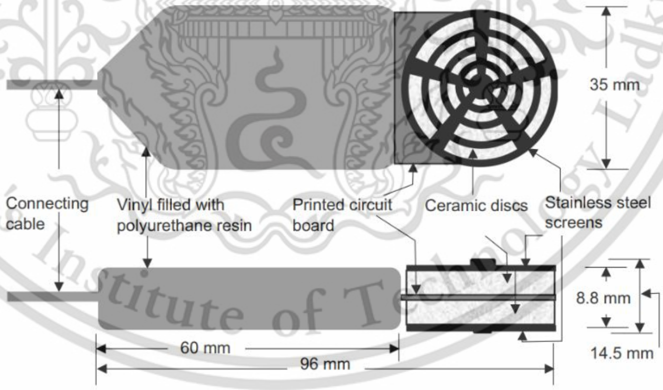

Figure 27 Schematic of water potential sensor.

Moreover, low suction tensiometer, developed by Kasetsart University has also been deployed in this study. The tensiometer comprise three main components i.e., ceramic filter, acrylic tube as water reservoir, and pressure sensor as can be seen in Figure 28. The size of water reservoir was set to be relatively small, therefore the response time of the tensiometer was reasonably fast. A Brass shell was used to connect acrylic tube to the sensor through, as well as protected the sensor. The tensiometer has total length of 74 mm, ceramic diameter of 16 mm and brass dimension of 28 mm. Considering Jotisankasa et al. (2007) this sensor used 1 bar air entry value with maximum working range by about 0.8 bar. Matric suction value will be obtained from surface tension through contractile skin in saturated high air entry value material. This surface tension prevent air get into the ceramic due to atmospheric pressure. As long as tensiometer is in saturated condition, air cannot pass through water reservoir and matric suction can be measured. Since this sensor have range capacity between -100 kPa to 600 kPa, it can only be used during wet season when PWP value was higher than -100 kPa. Moreover, tensiometers were installed in three variation of depth (0.25 m, 0.50 m and 1.0 m).

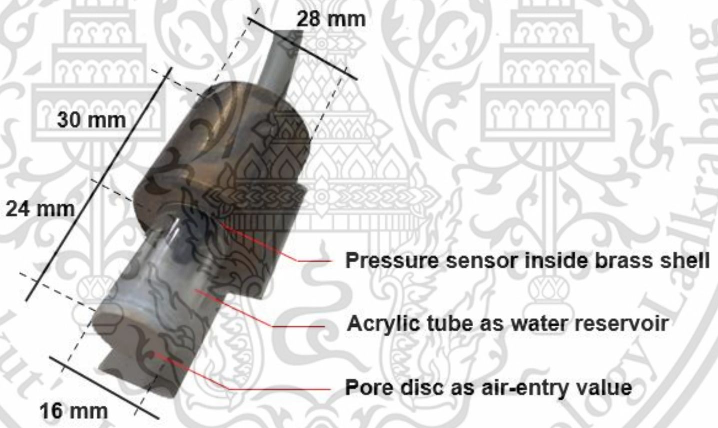

Figure 28 Schematic of low-suction tensiometer.

3.4.2 VWC Sensor

Soil volumetric water content (VWC) was measured using Time Domain Reflectometer (TDR) water content sensor, illustrated in Figure 29. According to Figure 29, the sensor was utilized by two rods, measuring 27 mm length and around 7 mm width. The value of VWC was determined from the probe’s sensitivity to the dielectric permittivity of the medium surrounding the probe rods. A differential oscillator circuit is coupled to the rods, with the state change of the oscillator being triggered by the return of a signal reflected off one of the rods. With varying dielectric permittivity, the two-way travel time of electromagnetic waves created by the oscillator on the rod changes. Since water is the primary contributor to the bulk dielectric permittivity of the soil or porous medium, the travel time of the reflected wave increases as the water content of the soil or medium increases and decreases as the water content decreases.

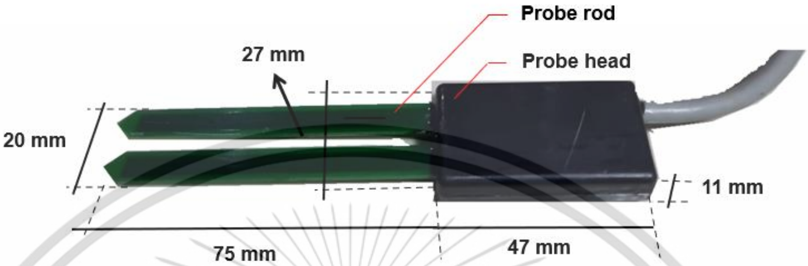

Figure 29 Schematic of volumetric water content sensor.

The value of dielectric permittivity was expressed by voltage value which can be read from the data logger. Since every soil property resulted different response to the sensor, calibration was required to predict VWC, based on voltage value. To do so, a set of calibration was conducted to facilitate this study as can be seen in Figure 30. This linear regression calculation, obtained from calibration was then used to calculate VWC. This sensors were installed at depth of 0.25 m, 0.5 m and 1 mm, ranging VWC capacity from 5 to 50% with accuracy of 0.2% (Campbell Scientific Inc., 2012).

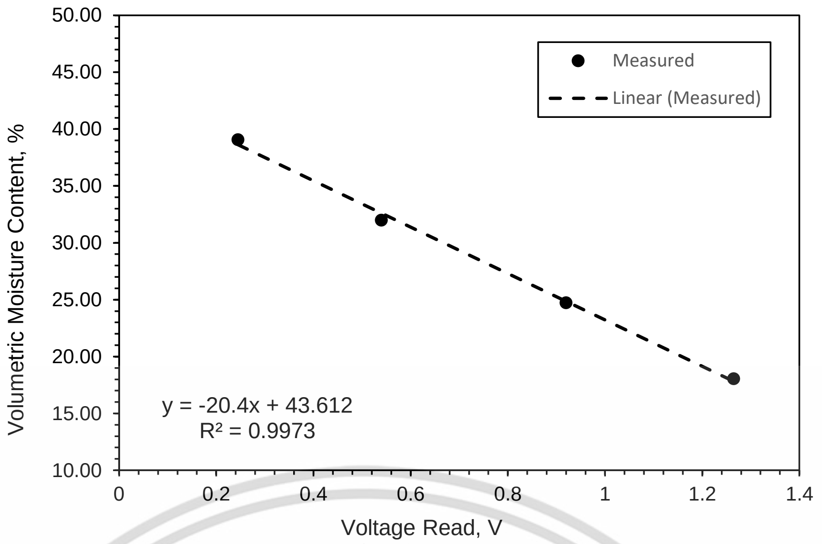

Figure 30 Volumetric water content sensor calibration.

3.4.3 Data logger

A set of data logger was employed to record data, resulted from the sensor. The data logger consists of ESP32 micro-controller, SD module, and real-time clock module, arrayed in mainboard circuit as can be depicted in Figure 31. ESP32 is one of the most popular micro-controllers with Wi-Fi & dual-mode Bluetooth capabilities. The data logger was also supported by real-time module to obtain real time data, and SD module to save the data. Further to this, the data logger provided 8 channel which were compatible with 8 either suction or VWC sensor. Moreover, 10.000 mAh lithium polymer battery was deployed in this system, supplying the power for about one month of the operation.

Figure 31 Schematic of data logger.

3.5 Climate Observation and Analysis

There are two types of weather data, used in this study i.e., historical weather data and current weather data. Historical weather data were obtained from 12 weather station surrounding embankment area. Meanwhile, a set of weather station was installed in the embankment to collect current weather data during this study. Detail explanation related to historical and current weather data will be presented as follows.

3.5.1 Historical weather data

To analyse extreme climate, which refers to the average weather in terms of the mean and its variability over a long time-span and a certain area (Trenberth et al., 1996), the availability of historical data is essential. To do the climate calculation, 30-years of historical weather data (1991-2020) from 12 weather stations surrounding the research area were employed. The data were provided by the meteorological department comprise monthly rainfall, humidity, and temperature from 1991 until 2020. The location of 12 weather station, used in this research can be illustrated in Figure 32.

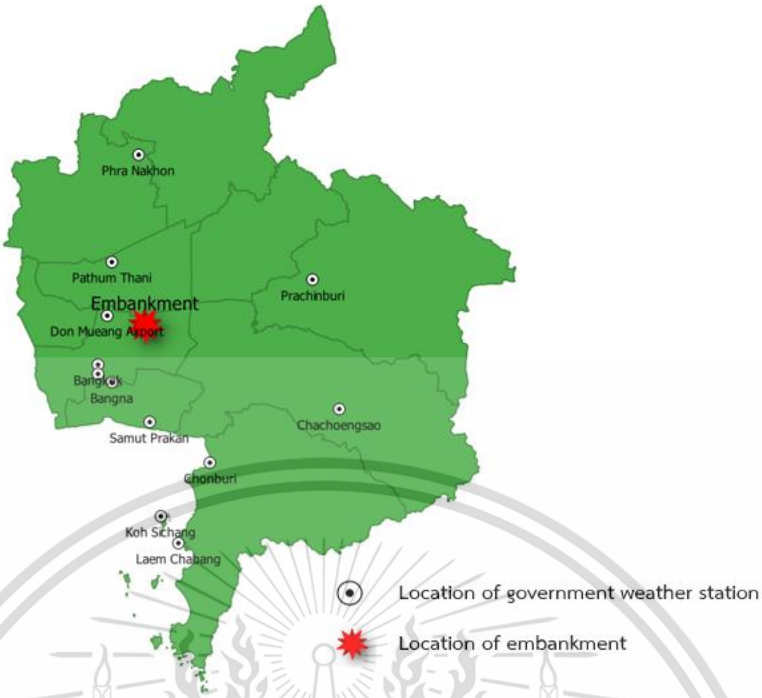

Figure 32 Location of government weather stations.

Further to this, to obtain monthly weather data in the embankment, inverse distance weighting (IDW) interpolation method (Shepard D, 1968) was used. This technique is the most popular among geoscientists and geographers due to its relative speed and ease of computation, as well as its widespread implementation in GIS software (Lu and Wong, 2008). IDW interpolation method is a deterministic spatial interpolation approach to estimate an unknown value at a location using some known values with corresponding weighted values. The basic IDW interpolation formula can be seen in equation (108) and (109). The weight is inverse distance of a point to each known point value that is used in the calculation. To facilitate the calculation, an open-source python program was used in this study.

$$x^* = \frac{w_1x_1 + w_2x_2 + w_3x_3 + \cdots + w_nx_n}{w_1 + w_2 + w_3 + \cdots + w_n} \tag{108}$$

$$w_1 = \frac{1}{d(x, x_i)^p} \tag{109}$$

where, w is weight value, d is distance, x is unknown point, x_i is known point, and p is power.

The higher p value will give lower weight. P value can be determined by iteration process and calculating the Root Mean Square Error (RMSE) between the interpolation result and the actual sampling value. The lowest RMSE is the optimum P value which is given the smallest error between the interpolation and actual value. Figure 33 gives the illustration how the IDW interpolation works. It can be seen in Figure 33 that the value at position x will be determined from sampling points 1, 2, and 3, with the distances to x point are d1x, d2x and d3x. Using the equation (109), each respective weight will be calculated and then the value at position x will be determined using equation (108).

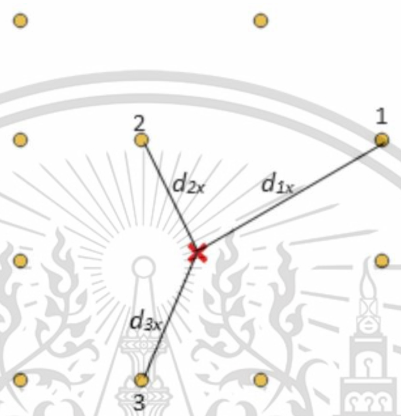

Figure 33 IDW interpolation method.

Following this, a bias-correction and spatial disaggregation (BCSD) method, proposed by (Wood et al., 2002) was used to forecast future weather data based on 30 years of historical weather data. Considering (Zhang et al., 2017) and (Xu and Wang, 2019), BCSD is one of the most popular method in coupling general circulation models (GCMs) and hydrological models. The worst-case climate scenario (RCP 8.5) was considered in this projection to evaluate water infiltration behaviour under extreme climate conditions. Moreover, three future time categories have been classified in this analysis, i.e., near future (2060), middle future (2080), and far future (2100).

3.5.2 Current weather data

To calculate current water balance, associated with rainfall and evaporation, current weather data is important. Accordingly, a set of weather station developed by National Electronic and Computer Technology Center (NECTEC) has been installed in embankment since March 2021. This weather station provided real-time weather data such as rainfall, relative humidity, solar radiation, air temperature and wind speed. The equipment has situated around 2 meter above ground surface, referring to standard installation procedure (Brown and Russell, 2010; Fraisse et al., 2015). All of the sensors were powered by solar panel electricity system which was attached in the station. Moreover, all of the data were recorded in internet-based data logger and relied them to the server every 10 minutes. Following this, the data can be accessed by online through provider website. The weather station in the embankment can be depicted in Figure 34.

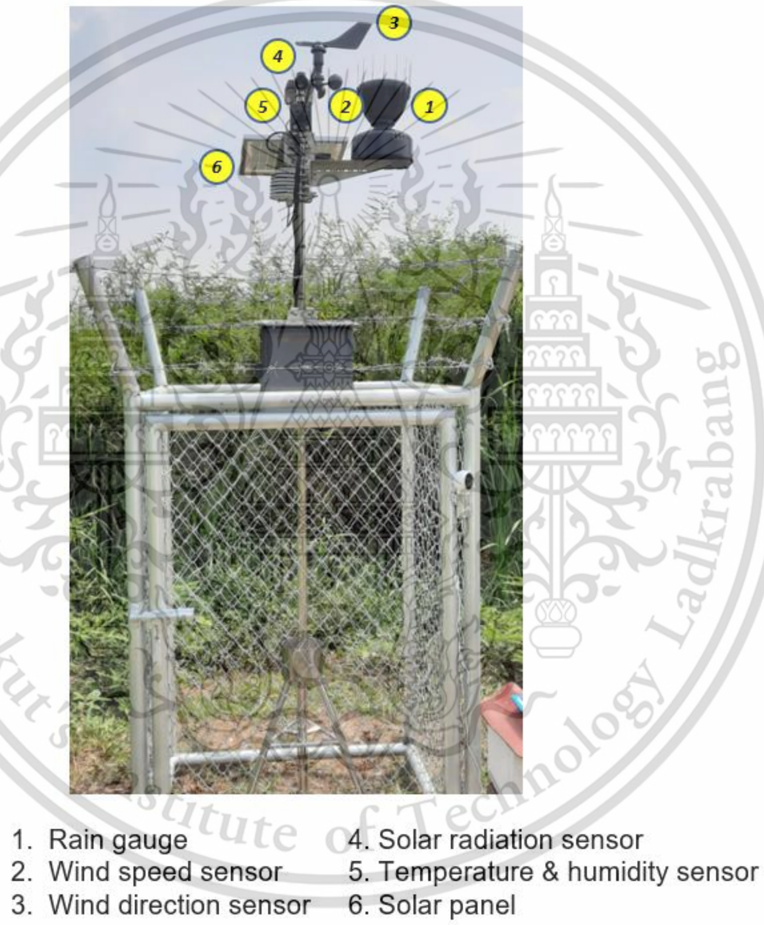

Figure 34 Weather stations in embankment.

3.6 Crack Observation

Minirhizotron with resolution of 24 Megapixels, attached on 1 m aluminium frame was employed to inspect soil cracks to the depth of 1 m through the hole with diameter of 0.1 m. The observation was conducted every 0.1 m depth from soil surface, capturing every 30° along a 360° in the direction of angle of view as can be seen in Figure 35. To capture desiccation cracks propagation, cracks observations were conducted every season during two years of study. Further to this, several steps of digital image processing methods such as greyscale, binarization, denoising, skeletonising, and crack identification, were conducted in this analysis (Cheng et al., 2021). Moreover, CIF, defined as the ratio of the crack area to the certain area of the soil surface was calculated in this study. CIF was analyzed by dividing crack area by total area using equation (110). Regarding Safari et al. (2014) and Shit et al. (2015) CIF is one of important parameters to represent the soil cracks.

$$CIF = \sum_{i=1}^{n} \frac{a_c}{A} x\ 100\% \tag{110}$$

Where CIF is Crack Intensity Factor (%), a_c is sum of all soil crack area (m2), A is total of surface area (m2).


(a) Crack observation (b) Mini digital camera

Figure 35 Sub-surface crack observation.

3.7 Deformation observation

There are two methods to observe embankment displacement i.e., conventional and photogrammetry method.

3.7.1 Topographic method

In the context of conventional method, standard topographic survey method was performed to observe embankment deformation. To capture the deformation of embankment due to seasonal variation, topographic survey was conducted every season during two years of observation. At the beginning of the survey, one stable point was determined as bench mark in this investigation. Global position of the bench mark was measured using GPS geodetic, following global positioning system standard. Further to this, 27 representative survey marks was set in the embankment location to facilitate the deformation observation, as can be seen in Figure 36. Moreover, a set of total station was deployed in this surveying process. The coordinate of survey marks was determined from bench mark coordinate. As the survey mark coordinate were known from the survey, embankment cross-section can be generated, as well as the displacement. It should be noted that this method of survey provided embankment deformation data with high accuracy.

Figure 36 Survey observation points.

3.7.2 Photogrammetry method

To support topographic method, embankment deformation has also been observed using photogrammetry technique. To do so, drone camera was deployed to capture representative embankment photo during the survey. Since photogrammetric surveys require less equipment as well as survey duration, this method can reduce survey budget significantly. However, it cannot be applied in grass area, considering bias data with respect to the grass. The detail process of photogrammetry method will be express as follows.

(i) 3-Dimentional construction

Agisoft metashape software was deployed to generate 3-dimensional embankment construction (Agisoft, 2021). To do so, several representative drone photos were required in this process. Despite the drone photo has already comprised GPS information metadata, a number of bench mark should be determined in the program to obtain high accuracy result. Initiating the process, the software will align drone photos data, resulting raw 3D embankment image. Moreover, depth reconstruction and dense point generation was required to obtain dense 3D embankment image. Further to this, mess and texture development was performed to obtain final 3D embankment construction. To continue the process, this 3D image can be exported as digital elevation model data. The result of 3D construction process can be depicted in Figure 37.

Figure 37 3D construction of embankment.

(ii) Generating of embankment cross-section

Further spatial analysis was performed using Quantum GIS software, developed by QGIS community. To obtain embankment cross-section, 3-dimentional embankment construction should be convert to 2-dimensional spatial model. Accordingly, geographic projection method was employed in this process by considering appropriate Coordinate Referring System (CRS). Since the embankment was located in Thailand, WGS 84/ UTM Zone 47N was applied in this analysis. Tif raster data was resulted in this process. Following this, embankment cross-section can be generated by employing profile tools feature in Quantum GIS software, as can be seen in Figure 38.

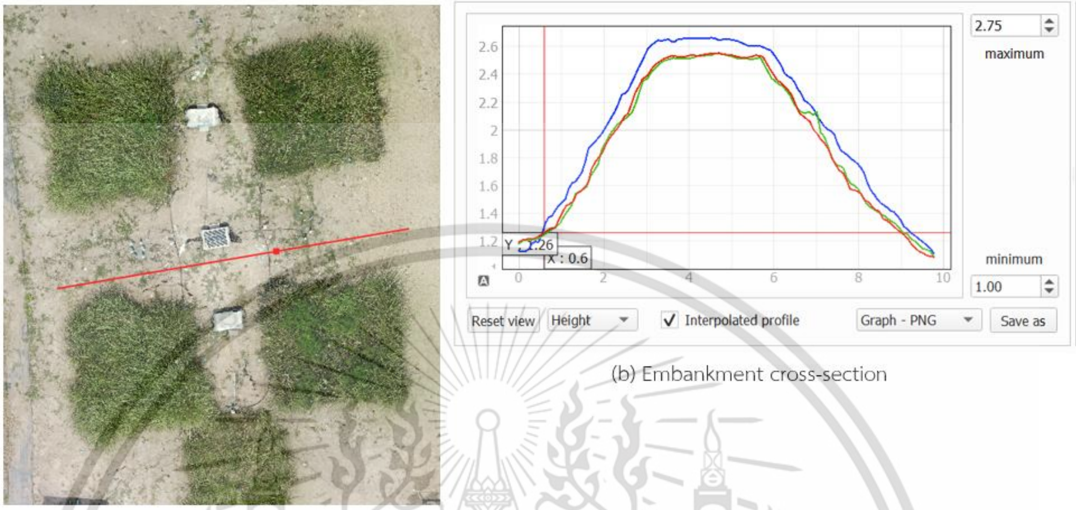

(b) Embankment cross-section

(a) Cross section line

Figure 38 Generating cross section based on QGIS software.

3.8 Double Ring Infiltrometer

To observe water infiltration behaviour in the research area, double ring test was performed in adjacent location of the embankment. The setup of double ring infiltration tests is depicted in Figure 39. Considering Gregory et al. (2005), Lai and Ren (2007) and Li et al. (2019), the double ring is one of the most commonly used methods for measuring water infiltration of soil in the field with respect to its accuracy. This technique preserves vertical infiltration of water in the inner ring by employing water in the outer ring to maintain the 1D infiltration of water within the inner ring. Two different types of acrylic tubes used for the test with diameters of 0.15 m and 0.30 m were employed as the inner and outer rings, respectively, which was typically used in double ring test (Bower, 1986). Both rings were embedded in the soil layer, driving to depths of 20 cm and 10 cm for the outer and inner rings, respectively. To avoid disturbance to the soil, the double ring was permanently installed at the test site using transparent acrylic, which allowed for the passage of sunlight and did not hinder surface evaporation. HC-SR04 ultrasonic distance sensor with 0.1 mm of accuracy was used to observe the water changes in inner ring during the test. To measure pore-water pressure (PWP), Teros 21 water potential sensor, produced by decagon Ltd ranging capacity of 0 kPa to -100,000 kPa with accuracy of +10% of the reading, was installed at a depth of 15 cm. Further to this, soil volumetric water content (VWC) was measured using Time Domain Reflectometer (TDR) water content sensor ranging from 5 to 50% with accuracy of 0.2%, installed at depth of 15 cm.

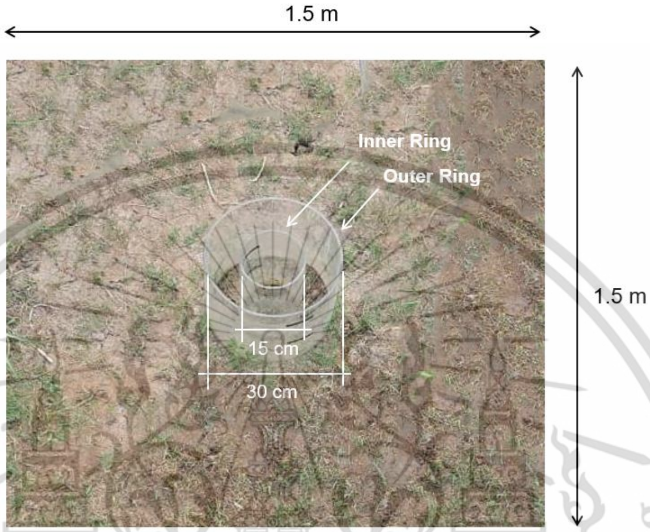

(a) Experiment area

Note:
Inner and outer rings are embedded 10 and 20 cm bellow the ground surface respectively

(b) Double ring setup

Figure 39 Double ring test.

In compliance with the falling head test standard, both the inner and outer rings were initially filled with water to a height of 0.20 m. Falling head was commonly used method to investigate field water infiltration in accordance to double ring test

(Bower, 1986; Gregory et al., 2005; Zeleke and Si, 2005). Water infiltration rate was observed at the soil layer, which was 0.10 m thick beneath the ground surface in the inner ring. Meanwhile, the outer ring was deployed to maintain vertical water flow in the inner ring. During the test, the rate of water flow in the inner ring was determined by measuring the distance changes between a distance sensor and the water level in certain time. Throughout the test, the data logger comprised of Arduino and Real Time Clock (RTC) recorded time and distance data.

Chapter 4 Numerical Simulation

Numerical back analysis was required to support the physical model result and to enhance the understanding of the mechanism behaviour. Following this, a parametric study has been conducted to analysis embankment behaviour under extreme climate condition. The procedure of numerical simulation will be explained in detail herein.

4.1 Model Geometry

Two-dimensional plane strain idealization using Geostudio software was applied in this simulation (GEO-SLOPE International Ltd, 2012). Considering available data and embankment behaviour, plain strain idealization was the most suitable option to model embankment construction. As the embankment is long structure, the strain-stress behaviour over the long-axis direction can be omitted (Vahdati, 2014). Moreover, a semi-coupled analysis was deployed to calculate Pore Water Pressure (PWP), deformation and Factor of Safety (FOS) due to seasonal effects. The behaviour of PWP was analyzed by Seep/W as the first stage of the simulation. Following this, Sigma/W was employed to compute the deformation of the embankment by considering Seep/W result. Furthermore, stress reduction stability (SRS) method was used to determine FOS using Sigma/W software. Advance investigation such as stress and strain behaviour were also conducted based on simulation result to obtain better understanding of this study.

The model dimension was derived from a full-scale embankment, as shown in Figure 40. The embankment model comprised two variation of slope angle i.e., milder slope (1:1.5) and steeper slope (1:1), measuring initial height was around 1.8, and width of crest of 2.7 m. To anticipate boundary effect, the left and right of embankment were extended to 3 m from the toe. Moreover, the depth of model was set to be 3 m bellow the flat area. Further to this, the embankment was also divided into several variation of layers, considering the Crack Intensity Factor (CIF) along the depth. It should be noted that stratigraphic of embankment was fluctuating depend on seasonal condition. To capture the fluctuation of stratigraphic condition, crack observation result along the depth and over the time was required in this model. Moreover, the groundwater table (GWT) was determined to be one meter below the flat ground surface. It referred to the water table of pond which was located in adjacent area of the embankment.

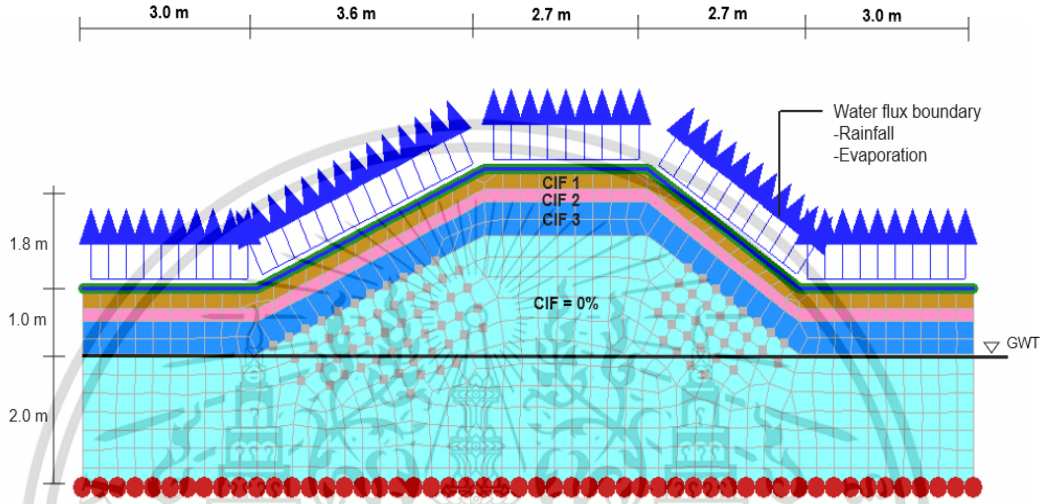

Figure 40 Numerical simulation model geometry.

4.2 Material Model

Material model is one of the most essential inputs in numerical simulation. The suitable model and parameter are extremely required to obtain accurate simulation result. Both laboratory and field measurement data were employed to generate model material in this study. Moreover, several substantial literatures were also deployed to support the model. Hydromechanical model used in this study will be explained herein.

4.2.1 Hydrological Model

In term of seepage analysis, soil water retention curve (SWRC) and hydraulic conductivity function (HCF) are essential and should be taken into account in this model. Accordingly, SWRC based on field measurement results were employed in this analysis. Since the present of the crack evolved soil behaviour into multi porous condition, it was necessary to consider it in hydrological model. Therefore, the Dual

Van Genuchten (Dual VG) SWRC model, proposed by Durner (Durner, 1994) was used in this simulation. Seki et al. (2023) stated that Dual VG was compatible to model dual or multi porosity material with respect to well-performing in their research. It is hence that model should be useful for practical applications, while mathematically being relatively simple and consistent. To generate Bimodal SWRC, linear superposition of sub curves of the Dual VG was constructed using equation (111) and (112).

$$S_e = w_1[(1 + (\alpha_1\psi)^{n_1})^{-m_1}] + (1 - w_1)[(1 + (\alpha_2\psi)^{n_2})^{-m_2}] \tag{111}$$

$$\theta = \theta_r + (\theta_s - \theta_r)S_e \tag{112}$$

Where, S_e is degree of saturation, w_1 is weighting factor; α_1, n_1 and, m_1 are larger pore fitting parameter; α_2, n_2 and, m_2 are smaller pore fitting parameter; θ_r is residual volumetric water content (%) and θ_r is saturated volumetric water content (%).

To investigate the correlation between Crack Intensity Factor (CIF) and SWRC, three representative cracks variation (i.e., 3%, 7% and 11%) were studied in this analysis, considering different times during wetting and drying process. Moreover, both VWC and PWP data at shallow depth were collected from observation result. PWP data, gathered from tensiometer and teros 21 potential sensor were deployed to obtained representative data. Tensiometer represented low suction data, while teros 21 acquired high suction data. The first data of SWRC (CIF = 7%) were obtained at the beginning of wet season in around April and May 2022. Second SWRC (CIF = 3%) was developed from measurement data, obtained at middle wet season in July 2021 and July 2022. Following this, we also took data at the middle of dry season to generate third SWRC (CIF = 11%) during November 2021 – January 2022. Further to this, the data were fitted using equation (111) ad (112) to obtain Dual VG SWRC model.

The result of fitted Dual VG SWRC model can be illustrated in Figure 41. As shown in Figure 41, the presence of the crack generates a bimodal curve SWRC, thus producing two distinctive θs and AEV, especially in first part of the curve (fracture portion). However, the second part of the SWRC graph was remain unchanged pertaining to intact portion of soil. Based on Figure 41, the value of θs is about 45% when CIF is 3%. As the increasing in CIF to 7% and 11%, θs also rose to around 47% and 49% respectively. The increasing of θs can be contributed from the raising of soil porosity in fracture portion, thus retaining more water (Stewart et al., 2016). It also can be substantiated from weighting factor of each SWRC. The increasing in CIF induced the raising of weighting factor, indication higher percentage of fracture portion. Beyond that, the increasing of pore diameter due to crack existence decreased soil capillary height, therefore reduced the first AEV (Kuhn and Zornberg, 2006; Li et al., 2011). It can be seen from Figure 41 that the value of AEV decreased with the increasing of CIF, indicated from the raising of a value. It should be noted that AEV can be calculated as 1/a considering Van Genuchten theory.

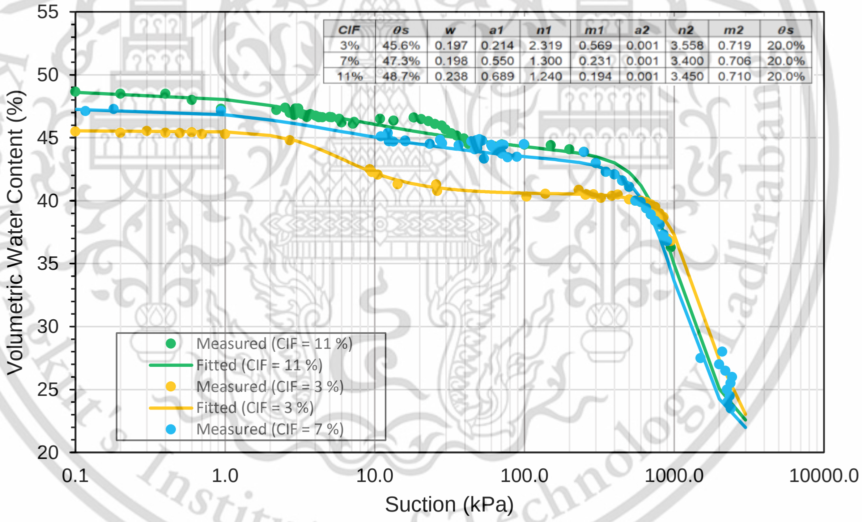

CIF	θs	w	a1	n1	m1	a2	n2	m2	θs
3%	45.6%	0.197	0.214	2.319	0.569	0.001	3.558	0.719	20.0%
7%	47.3%	0.198	0.550	1.300	0.231	0.001	3.400	0.706	20.0%
11%	48.7%	0.238	0.689	1.240	0.194	0.001	3.450	0.710	20.0%

Figure 41 Dual VG SWRC model.

Another important parameter to simulate seep behaviour was unsaturated hydraulic conductivity (K_{usat}). However, measuring unsaturated hydraulic conductivity in the field was challenging due to soil behaviour complexity. In this study, K_{usat} was predicted using Hydraulic Conductivity Function (HCF), proposed by Fredlund et al. (1995). This function was derived from Ks value and SWRC function, following equation (113). The value of Ks was determined from double ring test result regarding

CIF condition. Moreover, Dual VG SWRC model obtained from aforementioned calculation was imposed to the function.

$$K_{usat} = K_s \frac{\sum_{i=j}^{N} \frac{\theta(e^{y}) - \theta(\psi)}{e^{y_i}} (e^{y_i})}{\sum_{i=j}^{N} \frac{\theta(e^{y}) - \theta_s}{e^{y_i}} (e^{y_i})} \tag{113}$$

Where, e is natural number (2.718), y is a dummy variable of integration representing the logarithm of negative pore-water pressure, i is the interval between the range of j to N, j is the least negative pore-water pressure to be described by the final function, and N is the maximum negative pore-water pressure to be described by the final function.

4.2.2 Mechanical Model

In the context of deformation analysis, a Hardening-Soil Model (HSM) was used to model the mechanical behaviour of the embankment. As an advanced elastoplastic model, HSM is able to simulate precise stress-strain behaviour of both stiff and soft soil (Saleh et al., 2021). In this numerical simulation, HSM parameters were assumed based on Surarak et al. (2012), which analysed stiffness and strength parameters for the hardening soil model of soft and stiff Bangkok clays. Moreover, two type of embankment deformation analysis was performed in this study as follows.

(i) Embankment deformation due to consolidation and seasonal variation

In this type of analysis, material model was determined based embankment condition after construction process. Accordingly, embankment layer was classified as soft Bangkok clay representing both original soil layers and embankment body. It should be noted that since employing assumed parameters, this analysis was used to obtain the deformation trend in association with consolidation and seasonal variation.

(ii) Embankment deformation due to seasonal variation

This analysis was conducted to investigate embankment deformation due to seasonal variation. To do so, embankment was assumed to be compacted clay to prevent consolidation settlement. Thus, both original soil layer and embankment body were classified as stiff Bangkok clay. As a result, embankment deformation was governed by the fluctuation in PWP along the season.

Regarding Surarak et al. (2012), HSM parameters were obtained from oedometer test and several set of triaxial test. The soil samples were taken from several variation of depth, representing soft, medium and stiff Bangkok clay. The result of this study will be expressed as follow.

(i) Oedometer test result

Based on Surarak et al. (2012), oedometer test were performed on three variation of Bangkok clay i.e., soft clay (6-8 m depth), medium clay (12-14 m depth) and stiff clay (15-18 m depth). It should be noted that p^{ref} was assumed to be 100 kN/m^2. The value of E_{oed}^{ref} and $E_{ur,oed}^{ref}$ can be determined from the y-intercept of linear trend lines. Moreover, m value is the gradient of the slope. With respect to the soil type in the embankment, the result of soft clay and medium clay will present in this study as can be seen in Table 4. Considering Table 4, it can be concluded that the average value of E_{oed}^{ref} are 926 and 1650 for soft and medium Bangkok clay respectively. Meanwhile, the test promoted that the average value of $E_{ur,oed}^{ref}$ are 5813 and 5394 for soft and medium Bangkok clay respectively Furthermore, the value of m ranged from 1.1 to 1.5 and 0.6 to 1.2 for soft and medium Bangkok clay respectively.

Table 4 Oedometer test result

Test	Loading		Un-Loading		$E_{ur,oed}^{ref}/E_{oed}^{ref}$	λ*	K*
	E_{oed}^{ref} (kN/m^2)	m	$E_{ur,oed}^{ref}$ (kN/m^2)	m			
Soft Clay							
1	901	0.9	7679	1.1	8.5	0.115	0.009
2	1068	1	4310	1.5	4.0	0.094	0.008
3	858	0.9	7546	1.1	8.8	0.122	0.010
4	1105	0.7	4532	1.2	4.1	0.111	0.013
Stiff Clay							

9	5548	0.6	8670	1.1	1.6	0.033	0.009
10	5187	0.7	12451	1.0	2.4	0.032	0.007
11	3736	0.6	8241	1.0	2.2	0.049	0.012

(ii) Triaxial test result

To obtain another HSM parameter, Surarak et al. (2012) also conducted consolidated Isotropic undrained (CIU) triaxial test on soft and stiff Bangkok clay. In their tests, CIU triaxial test was experienced by several variations of confining pressure (σ_3). Following this, the result was calibrated using PLAXIS software. Figure 42 (a) shows the correlation between axial strain and deviatoric stress of soft Bangkok clay, based on triaxial test result. The relationship between confining pressure and E_{50} of all test variation was expressed by the double log scale graph to obtain E_{50}^{ref} and m as can be seen in Figure 42 (b). Moreover, stress-path diagram was generated to calculated c and ϕ as shows in Figure 42 (c). Regarding Figure 42 (a), three variations of confining pressure were applied in the test i.e., 138, 276 and 414 kN/m^2. As can be seen in Figure 42 (a), the increasing of confining pressure rose the value of deviatoric stress, resulting different value of E_{50}. Further to this, the value of E_{50}^{ref} and m can be calculated to be around 690 kN/m2 and 1.05 respectively, based on Figure 42 (b). Considering Figure 42 (c), the value of strength parameter c and ϕ were approximately 1 kN/m^2 and 27° respectively.

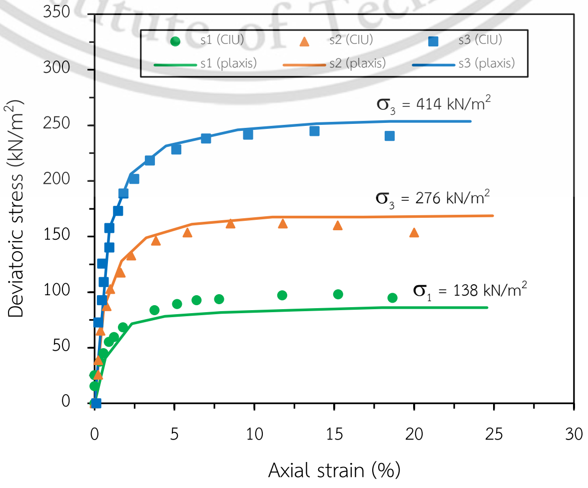

(a) Correlation between axial strain and deviatoric stress

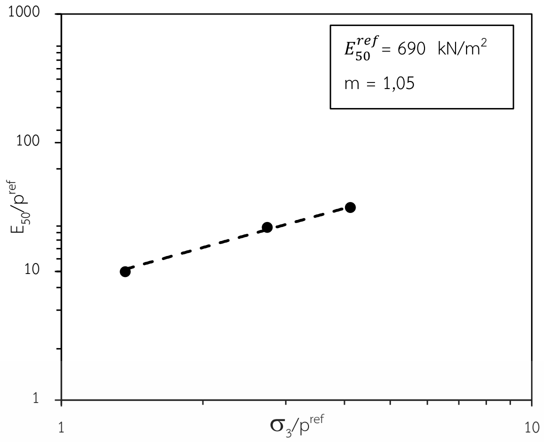

(b) Correlation between confining pressure and E_{50} of all test variation

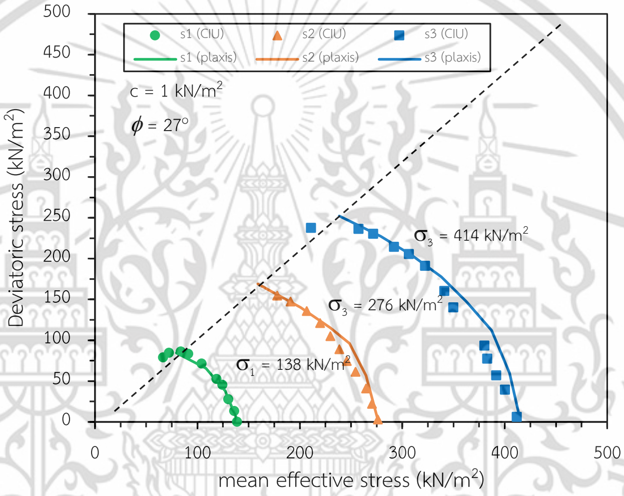

(c) Stress path (mean effective stress vs deviatoric stress)

Figure 42 Triaxial test result of soft Bangkok clay.

In the context of stiff Bangkok clay, another set of triaxial test were also attempted to obtain HSM parameter. In their research, three variations of confining pressure were applied in the test i.e., 69, 276, and 414 kN/m2. The result of the test comprises axial strain and deviatoric stress correlation, confining pressure vs E_{50}, and stress-path can be illustrated in Figure 43 (a), (b), and (c) respectively. It can be seen from Figure 43 (a) that stiff Bangkok clay resulted higher deviatoric stress due to the same value of confining pressure, rather than soft Bangkok clay. As a result, stiff Bangkok clay produced higher value of strength parameter c and ϕ, compared to soft Bangkok clay as shows in Figure 43 (c). Regarding this graph, the value of c and ϕ of stiff Bangkok clay was around 11.5 kN/m^2 and 28° respectively. Moreover, stiff Bangkok clay also prompted higher value of E_{50}^{ref}, reaching by about 14378 kN/m2 based on Figure 43 (b).

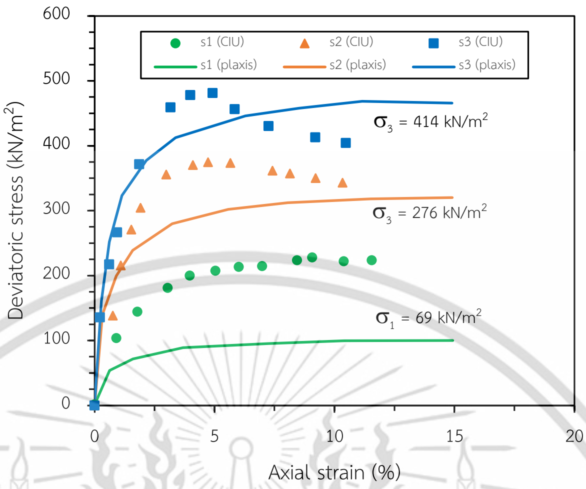

(a) Correlation between axial strain and deviatoric stress

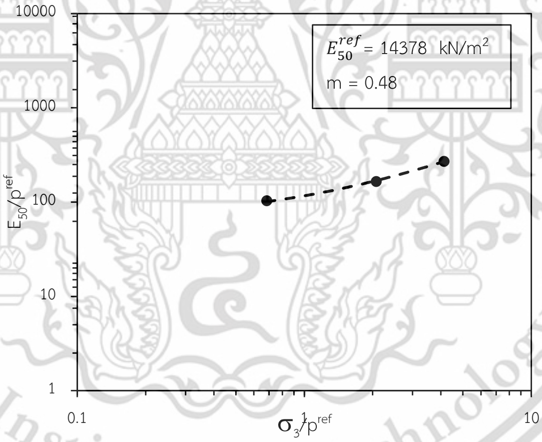

(b) Correlation between confining pressure and E_{50} of all test variation

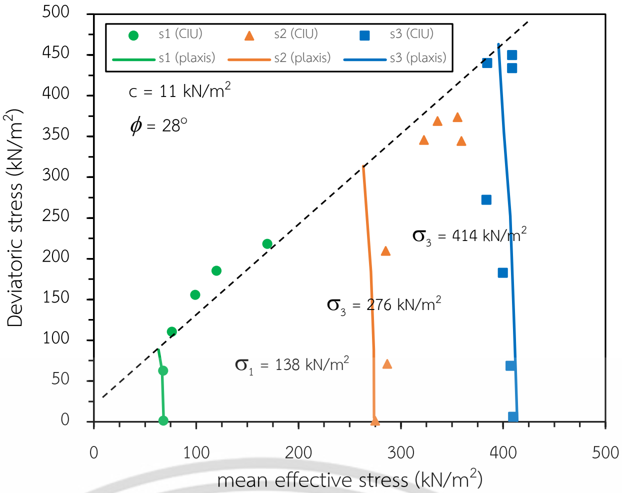

(c) Stress path (mean effective stress vs deviatoric stress)

Figure 43 Triaxial test result of stiff Bangkok clay.

As mentioned in the previous section, HSM parameter of soft and stiff Bangkok clay was derived from calibrated result from Surarak et al. (2012). The detail parameter's value of the soil model in the embankment can be shown in Table 5.

Table 5 HSM parameters value in numerical simulation

Parameter	Symbol	Value		Unit
		Bangkok Clay (Stiff)	Bangkok Clay (Soft)	
Internal Friction Angel	ϕ	27	27	°
Cohesion	c	11.5	1	kN/m^2
Secant Stiffness	E_{50}	9500	800	kN/m^2
Tangent Stiffness	E_{oed}	12000	850	kN/m^2
Unloading Stiffness	E_{ur}	30000	8000	kN/m^2
Failure Ratio	Rf	0.9	0.9	
Exponential Power	m	1	1	
Poisson's Ratio	ν	0.2	0.2	

4.3 Boundary condition

To analysis hydrological behaviour, soil water balance fluctuation was required. Therefore, the calculation of water infiltration and evaporation will play an essential role. The accurate computation of water infiltration and evaporation is important to obtain satisfied numerical simulation result. To do so, appropriate condition of the embankment should be taken into account in boundary condition such as the presence of the crack. In detail, water infiltration and evaporation calculation will be described as follows.

4.3.1 Water infiltration

In this study, a modified Green-Ampt infiltration method was utilized to calculate water infiltration in the embankment. Based on Chu (1978), Clausnitzer et al. (1998) and Cui and Zhu (2017) Green-Ampt model has been extensively used to estimate the infiltration process with respect to the fundamental parameter. The original Green-Ampt model was developed by Green and Ampt (1911) by considering K_s, soil suction, and deficit of volumetric water content as influent parameters. To consider the existence of the cracks in water infiltration calculation, a new modified Green-Ampt equation based on double ring test result was proposed in this simulation. Due to the close relationship between the presence of cracks and K_s value, the equation was derived by analysing the correlation between the crack ratio and K_s. The new Green-Ampt expression can be shown in equations (114) and (115). Moreover, the procedure to calculate actual infiltration by considering crack existence can be presented in Figure 44.

$$F(t) = e^{0.18CIF} K_{sat}\, t\, cos\beta + \frac{\psi\Delta\theta}{\cos\beta} \ln\left(1 + \frac{F(t)\cos\beta}{\psi\Delta\theta}\right) \tag{114}$$

$$f(t) = e^{0.18CIF} K_{sat} \left(\frac{\psi\Delta\theta}{F(t)} + \cos\beta\right) \tag{115}$$

Where, β is slope gradient (°), f(t) is infiltration rate (mm/sec), t is time (sec), ψ is suction head (mm), $\Delta\theta$ deficit of volumetric water content and CIF is cracks intensity factor (%).

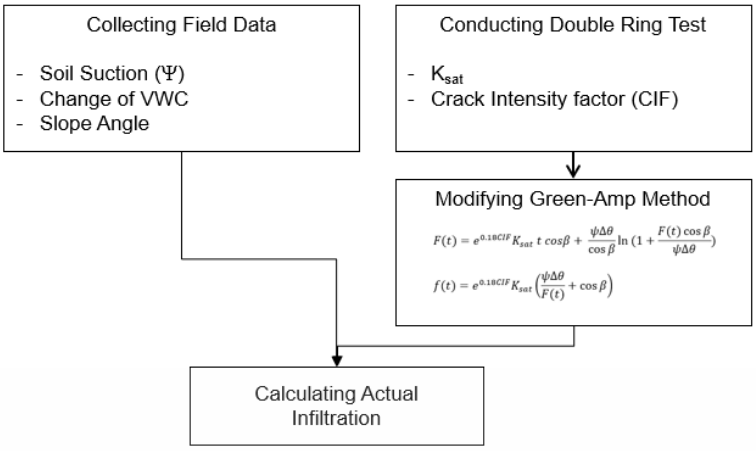

Figure 44 Procedure of actual infiltration calculation.

4.3.2 Evaporation

In this research, Potential Evaporation (PE) was calculated using Penman-Monteith method (Penman, 1948), based on equation (24). Considering Allen et al. (2019), the equation uses standard climatological records of solar radiation (daylight), air temperature, humidity and wind speed. Moreover, this method represents physical and physiological factors governing the evaporation process. All of the required data to compute current PE has been provided by the weather station. Moreover, cracks parameters were also taken into account in actual evaporation calculation. Accordingly, a modified Kelvin equation based on Fredlund et al. (2016) and Song and Cui (2020) was employed in this simulation as can be shown in equation (116). In detail, the procedure to calculate actual evaporation by considering crack existence can be shown in Figure 45.

$$AE = PE\,\frac{[1 + (k-1)CIF]h_{non\,crack} - h_a}{100 - \ h_a} \tag{116}$$

Where, AE is Actual Evaporation, PE is Potential Evaporation, k is ratio h_crack to h_non-crack, ha is air humidity.

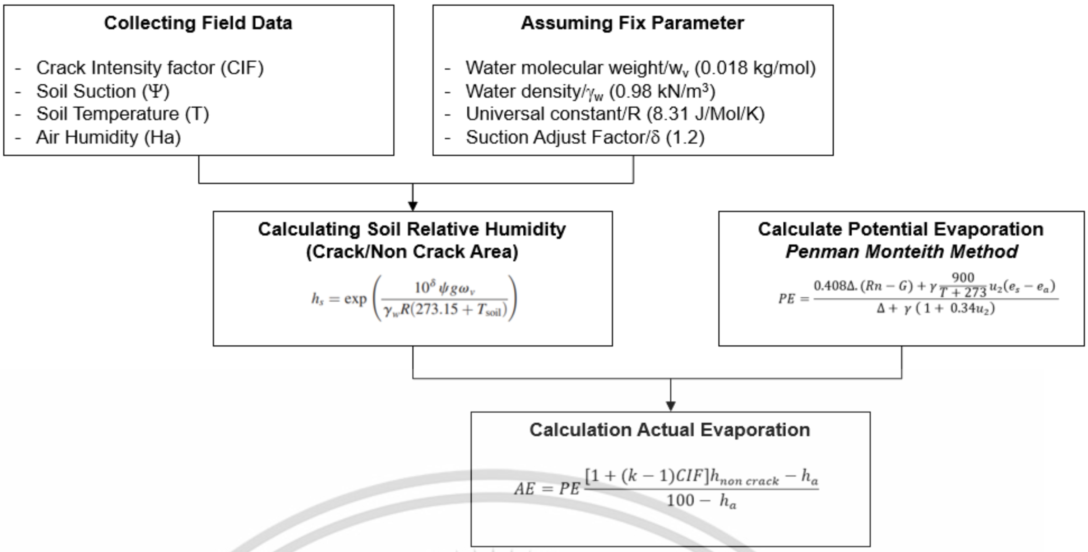

Figure 45 Procedure of actual evaporation calculation.

4.4 Analysis Procedure

Regarding the research objective, numerical simulation will be divided into several steps as follows.

4.4.1 PWP analysis

In this stage, PWP response was analyzed using Seep/W software. Net water flux boundary condition, based on actual infiltration and evaporation was applied in this simulation. Moreover, since its hydraulic parameter tend to change due to the alteration of the crack, monthly-based analysis was conducted in this study. The detail analysis of PWP using Seep/W will be explained as follows.

(i) Defining simulation step

Defining project information and simulation step was the first step of Seep/W analysis. Two-dimensional analysis was set in this step regarding the embankment model. To capture hydrological response due to seasonal behaviour, the analysis was divided into two steps i.e., steady state and transient analysis. Steady state analysis was used to define initial condition including ground water table and initial PWP. The duration of steady state was situated to be 0. Further to this, transient analysis was generated to obtain monthly embankment behaviour because of wetting and drying process. The detail of iteration process was also set in this phase.

(ii) Generating model geometry

As the project has already defined in aforementioned step, model geometry can be constructed. The detail information of geometry of the embankment has been explained in section 4.1. Geometry drawing tools such as point; line; and region were deployed to generate model geometry. Moreover, surface layers was set at the top of the embankment.

(iii) Setting material model

Following geometry construction, material model should be defined in the simulation. Several setting processes were conducted consisting of SWRC and HCF. As mentioned in section, bi modal vg model was employed in this simulation. To do so, data point function input was used to generate the SWRC. Furthermore, SWRC was used to estimate HCF accordingly.

(iv) Setting boundary condition

Boundary condition setting was required to set seepage and hydrological condition of the embankment. Water flux boundary was situated in the surface layers with respect o infiltration and evaporation data as mentioned in section 4.3. In order to generate ground water table to be – 1.0 m bellow the flat surface; water total head of 2 m was set at the bottom of the model. Moreover, drainage boundary was applied at the right and left side of the model.

(v) Mesh generation and calculation

Incorporating finite element analysis, mesh should be generated in the model prior to calculation step. To do so, quad and triangle element model with size of 0.1 m was used in this simulation. Final step of this calculation is solving the model to obtain embankment response.

4.4.2 Deformation analysis

Deformation analysis was simulated using Sigma/W by considering PWP, resulted from previous step. Semi-couple analysis was used in this analysis by separating PWP and deformation analysis. Deformation analysis in Sigma/W comprises following step.

(i) Defining simulation step

The same as Seep/W, project definition and step should be set prior to the simulation in Sigma/W. As semi-couple was used in this simulation, both of program was run separately. Regarding Seep/W model, 2D plain strain idealization was also applied in Sigma/W calculation. Moreover, the step of analysis consisted of three phases i.e., steady state analysis under Seep/W, in situ analysis to generate initial stress due to gravity, and consolidation analysis to calculate embankment deformation due to seasonal behaviour.

(ii) Generating model geometry

The same as PWP, model geometry should be built in the commencement of the analysis following embankment dimension. Sigma/W analysis used similar model geometry to Seep/W.

(iii) Setting material model

To obtain deformation response based on PWP fluctuation, both hydrological and mechanical properties should be set in this analysis. Hydrological properties used in this simulation was similar to Seep/W analysis. Moreover, mechanical properties was set followed stratigraphic condition as explained in section 4.2.2.

(iv) Setting boundary condition

Following calculation step, drainage and fixities boundary were applied in the simulation. In term of hydrological condition, drainage boundary should be taken into account. Since ground water table was relatively constant during the observation, it was set in every step of the analysis. The value of PWP along the time resulted from Seep/W, was imposed in consolidation step at three depth variation. Moreover, fixities boundary should be situated in deformation analysis. Fixed X/Y constrained boundary was used at the bottom side of the embankment, indicating stable condition in that area. However, Fixed X constrained boundary was applied at the right and left side of the model, allowing the model move to either upward and downward direction.

(v) Mesh generation and calculation

Quad and triangle element model with size of 0.1 m was also used in this deformation analysis. Once all of step has been generated properly, the simulation process can be started.

4.4.3 FOS analysis

Stress reduction stability (SRS) method was used to calculate FOS of the embankment along the time. The calculation of FOS was performed based on consolidation step in deformation analysis. Moreover, monthly FOS were computed to observe the stability of embankment due to seasonal variation.

Chapter 5 Weather data and climate projection

Weather is one of primary input data in this study to determine the research objective. Current weather data such as rainfall, humidity, air temperature, daylight and wind speed, obtained from weather station will be described in this section. Potential evaporation as a result of Penman method will also be presented in this chapter, following the weather data. Moreover, historical weather data will also be discussed, as well as future climate projection.

5.1 Current weather data

Weather station, installed in the embankment have recorded weather data from March 2021 to December 2022. Based on current data, potential evaporation can be calculated using penman-monteith method. Moreover, AWB and climate index was determined considering PE dan rainfall.

5.1.1 Weather data

Considering cycle season in Thailand, observation time can be divided into three seasons i.e., summer (March – May), rainy (June – November), and winter season (December – February). Current weather data based on the observation can be depicted in Figure 46.

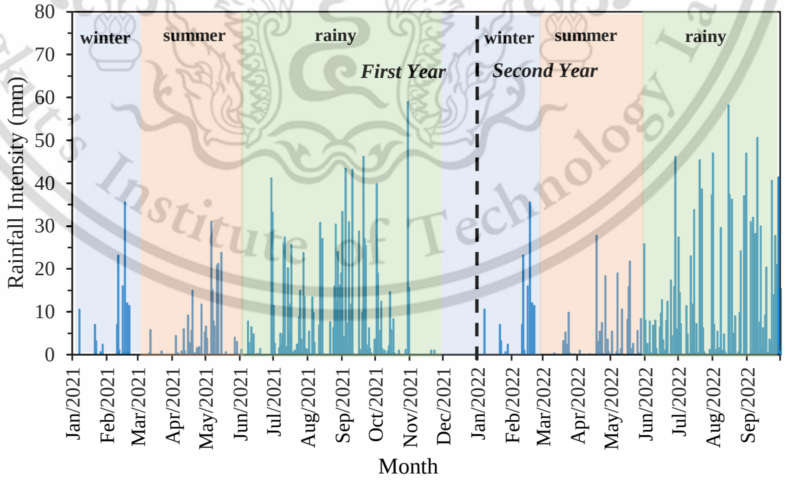

(a) rainfall

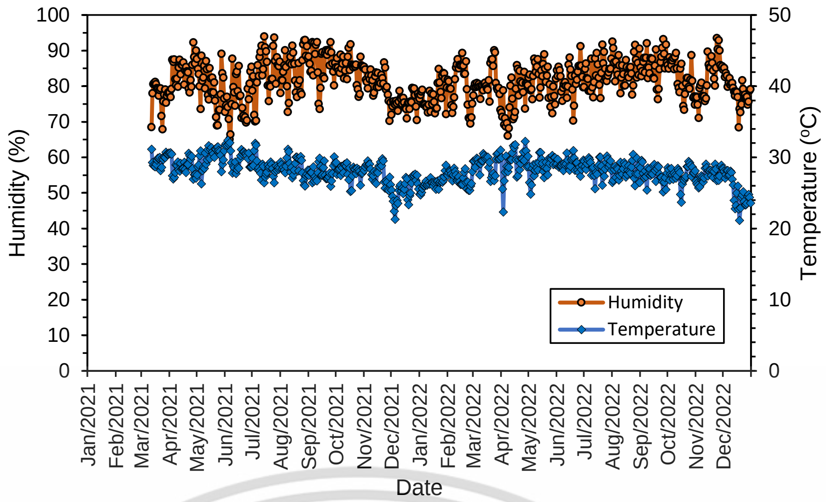

(b) humidity and air temperature

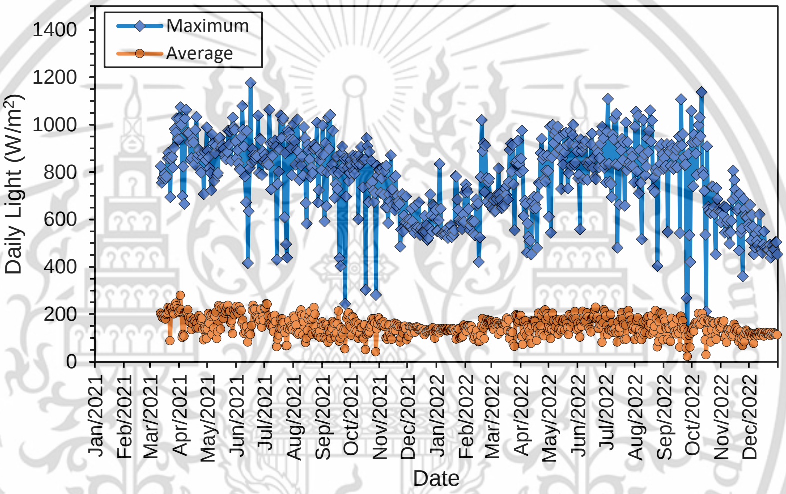

(c) daily light

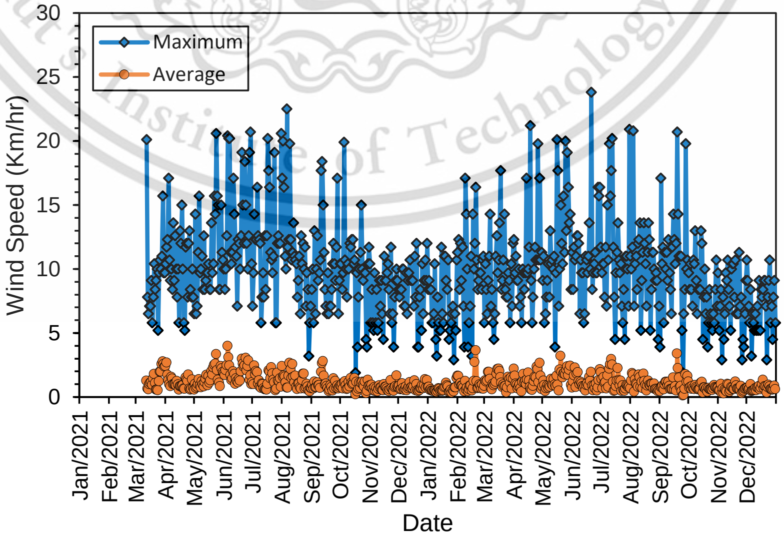

(d) wind speed

Figure 46 Current weather data

As can be seen in Figure 46 (a), rainfall occurrence has been dominated by wet season from June to October. Based on the data, the average of monthly rainfall during the first dry, rainy and winter season are 73.2 mm, 216.0 mm and 33.0 mm respectively. Moreover, the second year of observation have higher rainfall intensity compared to the first year. Considering the data, monthly rainfall intensity throughout the second year are 72.7 mm, 270.8 mm, and 0.5 mm due to dry, rainy and winter season respectively. It also can be seen in Figure 46 (a) that several typhon occurred during the first year i.e., lupit, conson, dianmu, lionrock and compasu. Those typhon triggered heavy rainfall in Thailand, including the research area. Moreover, the embankment has also experienced with another typhon during the second year of observation namely ma on, noru and nalgae.

In the context of rainfall intensity, daily rainfall can be classified as heavy (25 - 50 mm), moderate (10 - 25 mm), or low rainfall (<10 mm). Based on two years of observation, rainfall occurrence was dominated by small rainfall, followed by moderate and heavy rainfall. During 2021, there were 89 times of small rainfall, occurred in the embankment. Moreover, the embankment was experienced by 23 and 19 times of moderate and heavy rainfall respectively. Likewise, the same trend of rainfall intensity also occurred in 2022. Small intensity was the most frequent rainfall, happened in 2022 (104 times), followed by moderate (27 times) and heavy rainfall (25 times). Further to this, it can be reported that July 2021 is the wettest month during 2021 with 25 times rainfall occurrence. Meanwhile, Augsts 2022 is the wettest month in 2022 as rainfall occurred 26 times during this year. However, the most frequent heavy rainfall was happened in September 2021 and 2022.

Considering Figure 46 (b), the average of daily temperature and humidity vary with respect with seasonal behaviour. The average of daily temperature during dry, rainy and winter season are around 29°C, 28°C and 26°C respectively. Moreover, the highest average daily humidity occurred in wet season (28.5 %). It can be addressed to the higher value of rainfall during this season. In addition, the value of average daily humidity is about 80.7% and 78. 1% in dry and winter season respectively. In the context of temperature and humidity, there is no distinctive behaviour during the first and second year of observation.

In accordance with aforementioned weather data, solar radiation and wind speed were also observed in this study, shown in Figure 46 (c) and (d). It can be clearly seen from Figure 46 (c) that dry season tend to have the highest solar radiation, compared to rainy and winter season. During the first year of observation, the value of daylight is around 182.7, 150.3, and 131.6 W/m^2 due to dry, wet and winter season respectively. Likewise, dry season also provide the highest value of average wind speed (1.33 km/h), rather than rainy season (1.29 km/h) and winter season (0.75 km/h). In the same trend with rainfall, second year of investigation resulted subtle behaviour of daylight. Regarding the observation, second year daylight tend to have lower value, compared to the first year. The value of daylight during dry, rainy and winter season is about 150.9, 147.5, and 124.7 W/m^2 respectively.

Considering Figure 47, the embankment experience with higher value of potential evaporation during summer, averaging by approximately 211 mm/month. It can be attributed to the higher value of daily average temperature during that season, reaching by approximately 30°C. Additionally, the average of evaporation was found to be lower in the rainy and winter season, amounting by about 186 mm/month and 160 mm/month, respectively. It was strongly correlated to the value of daily temperature during that season, ranging from 26°C to 28°C in the wet season and dropping to 22°C to 27°C post-October, indicating the onset of a cool dry season. When comparing data between the first and second years, the evaporation did not exhibit considerable differences. The total value of evaporation during the first year was found to be 2221.04 mm. Meanwhile, the embankment encountered with total potential evaporation of 2231.81 mm in the second year.

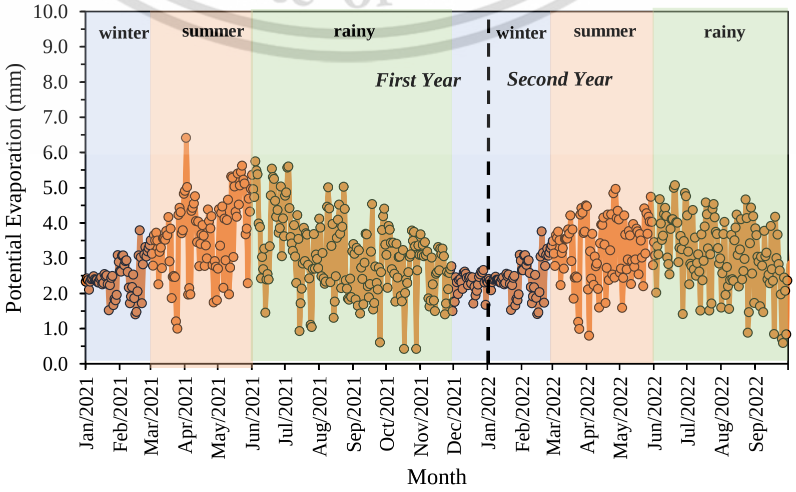

Figure 47 Current potential evaporation.

5.1.2 Climate index

In the context of seasonal climate index, the embankment encountered with various climate condition during two years of observation as can be seen in Figure 48. Figure 48 shows that the value of SPEI index was found to be around -1.1 during the first summer (April 2021), indicating moderate climate condition. Following this, SPEI value rose during first rainy season (August 2021), reaching by approximately 1.3. It can also be seen from Figure 3 that the value of SPEI index dropped to around -1.75 in the second winters (January 2022), representing severe drought climate. Further to this, the embankment experienced with moderate dry condition in the second summer according to its SPEI index (-1.01). Moreover, the embankment encountered with the highest value of SPEI index (1.5) during second rainy season. Regarding the value of SPEI during observation, it was substantiated that the embankment experienced with more extreme climate in the second year, rather than the first year. It can be attributed to the higher value of rainfall intensity and potential evaporation during the second year, rather than the first year. Furthermore, the effect of climate index variation to the embankment behaviour will be explained in the next section.

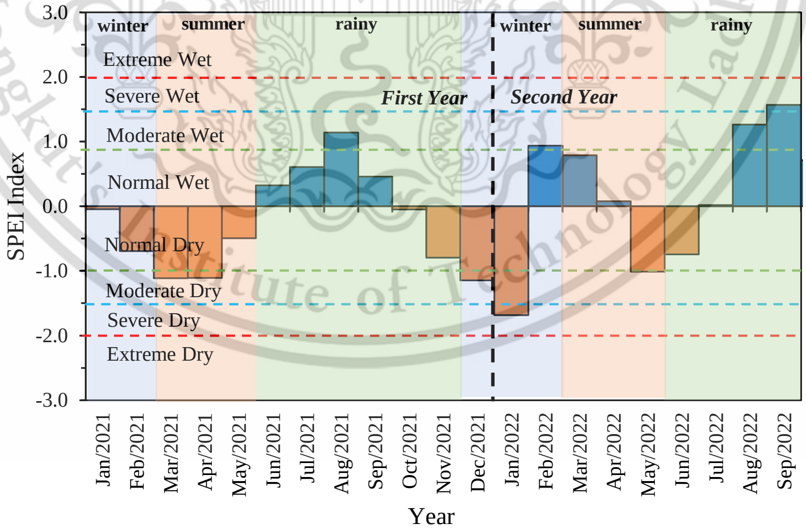

Figure 48 Current SPEI Index.

5.1.3 Atmospheric water balance (AWB)

To support numerical simulation, the calculation AWB was necessary. The value of current AWB along the time of observation varies, ranging from -93 to +332 as can be illustrated in Figure 49. According to Blight (1997) AWB, defined as the difference between rainfall and potential evaporation, is one of the basic input to the soil water balance, therefore affecting soil behaviour. With respect to higher value of rainfall, water surplus tended to occurred in wet season. Further to this, the water supply dropped in dry season, leading the deficit of air water balance. Moreover, it can also be seen in Figure 49 that the embankment was experienced with wetter condition during the second rainy season, compared to the first wet season. The value of maximal air water balance during the first and second wet season is around 254.3 mm and 332.5 mm respectively.

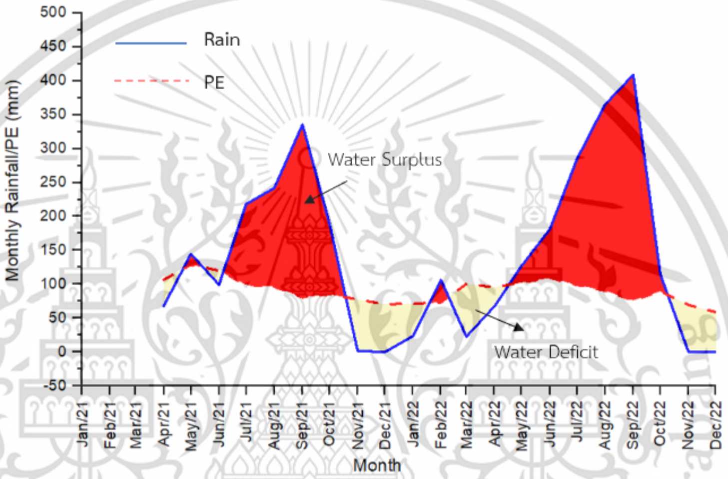

Figure 49 Current atmospheric water balance.

5.2 Future weather data

To analysis embankment behaviour due to extreme climate condition, prediction weather data was required. Accordingly, climate projection based on the worst-case climate scenario has been performed. The result of future climate projection will be explained as follows.

5.2.1 Weather data

Based on 30 years historical weather data, future climate data has been projected under RCP 8.5 scenario. Moreover, three future time categories have been classified in this analysis, i.e., near future (2060), middle future (2080), and far future (2100), plotted in Figure 50. Figure 50 shows that predicted future data will result in more noticeable extreme rainfall than extreme evaporation. As a result, extreme wet conditions are more likely to occur in the future than extreme dry conditions, resulting in a prolonged flood disaster. In detail, based on Figure 50 (a), the average monthly rainfall is expected to increase by around 40% in the near future (2060). Meanwhile, monthly rainfall rose by about 48% and 54% in 2080 and 2100 respectively. On the other hand, considering Figure 50 (b), evaporation increases only by around 3%, 4% and 7% in the next 40, 60, and 80 years, respectively.

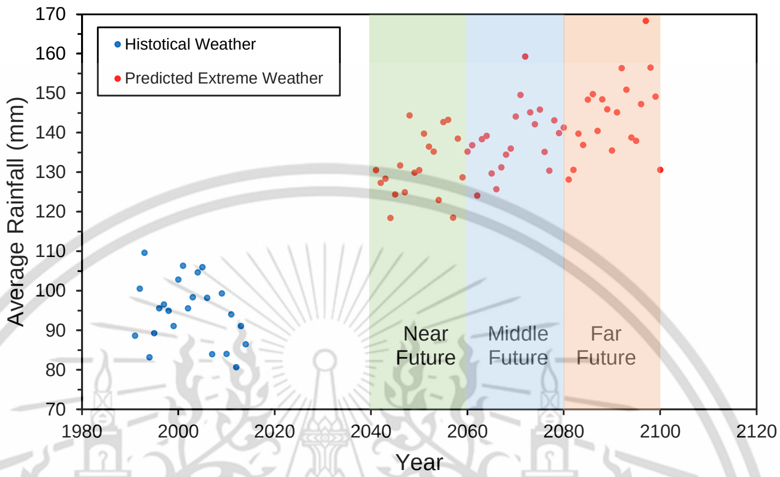

(a) Rainfall

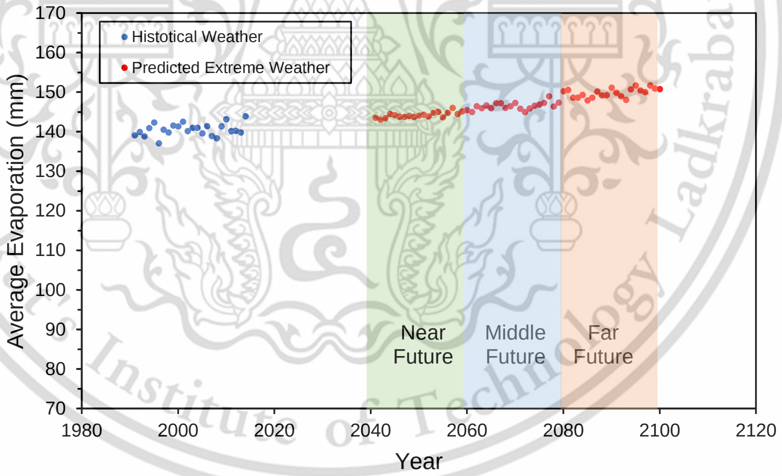

(b) Potential evaporation

Figure 50 Historical and future weather data.

5.2.2 Climate Index

To represent future climate condition, predicted SPEI climate index has been computed, based on future rainfall and PE as can be seen in Figure 51. Regarding Figure 51, embankment will experience with extreme dry condition in 2045 and 2057 during near future. Meanwhile, during middle future, the embankment will be encountered with extreme dry condition in 2065. Moreover, extreme wet will also occur in 2072 and 2097 during middle and far future climate scenario respectively. In term of the magnitude, the lowest SPEI index occur during near future time scenario in 2045 (-2.31). Meanwhile, the embankment will also undergo with the highest SPEI index during far future time scenario in 2097 (+2.70).

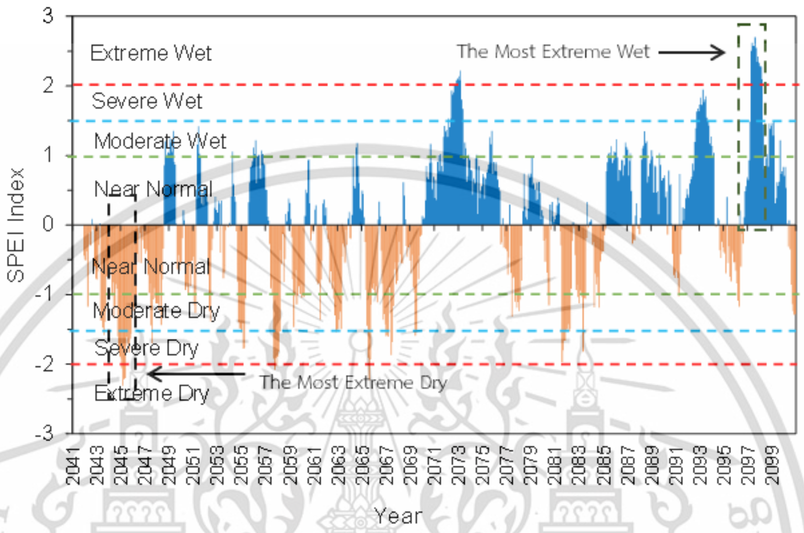

Figure 51 Future climate index.

5.2.3 Atmospheric water balance

Following climate index calculation, the value of future AWB can be determined, considering rainfall and PE data. Since having more close relationship with soil water condition, AWB is more reliable to support numerical simulation, compared to climate index. Furthermore, parametric study will perform under extreme climate condition, so that knowing AWB in that relevance time is required. AWB condition during near, middle, and far future time scenario can be depicted in Figure 52. Based on climate index, extreme drought will occur in 2044 when annual AWB is around -377 mm. Moreover, the value of annual AWB during extreme wet (2097) is around 516 mm.

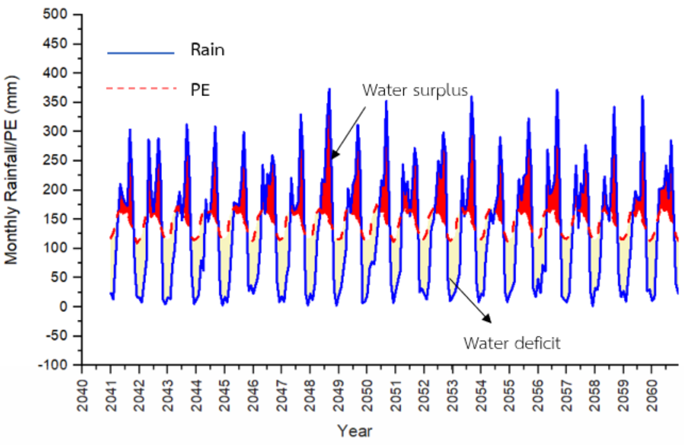

(a) near future

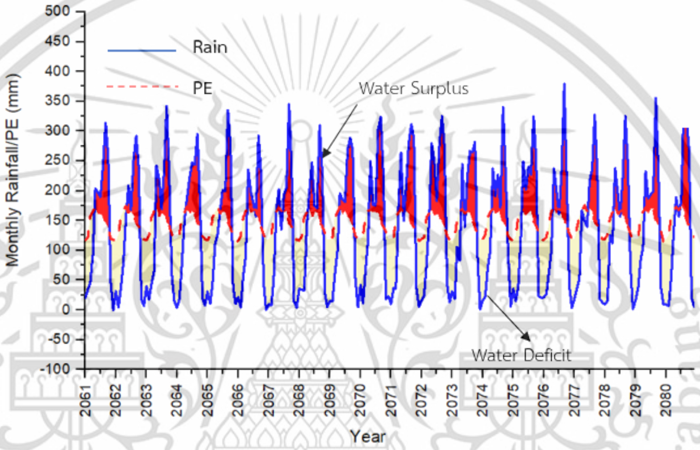

(b) middle future

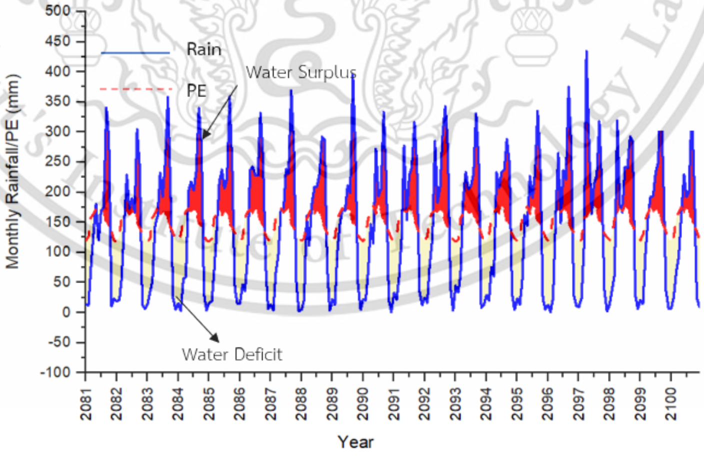

(c) far future

Figure 52 Future AWB.

Chapter 6 Crack Observation Result

The result of CIF analysis can be depicted in Figure 53, comprising original image and textured rendered image. Two variations of depth have been presented in Figure 53 i.e., 0.1 m depth and 0.5 m depth representing instrumentation depths along the slope. It should be noted that the first attempt of crack observation was performed during the first summer in April 2021. At 0.1 m depth, Figure 53 (a) shows that two major cracks with cross along this shallow depth existed during the first summer in April 2021 (i.e.; crack a and d). Moreover, two minor cracks also appeared during that season (i.e., crack b and c) Specifically, the notable crack occurred in the left and right side (a and c), measuring crack width (CW) of around 5.6 mm and 10.9 mm respectively. The figure illustrated that the major cracks area decreased significantly during the first rainy season (August 2021). Intense rainfall during that season promoted CW of crack a and d decreased by approximately 69.9% and 84.4%, respectively. Moreover, it can be reported that modest crack (b and c), located in the middle was almost disappeared in rainy season. Regarding Tian et al. (2023), the healing of desiccation cracks in clayey soils is mainly attributed by two factors: wetting-induced swelling and disintegration of the soil grain. Based on the third and fourth observation result, it was observed that desiccation cracks began to develop during the late rainy season (November 2021) and reached their maximum dimensions in the second winter (January 2022). Notably, these major cracks at this depth appeared to widen from the same initial locations, resulting in similar shapes compared to the previous drying cycle. Furthermore, it was evident that moderate cracks that had closed previously reappeared, albeit with slight alterations in their shapes. Regarding Tang et al. (2011), wetting-drying cycle can influence geometric and morphologic characteristics of the crack. This can be attributed to the heterogeneous aggregated-structure formed during the wetting process. It can also be seen from Figure 53 (a) that the increase in CW occurred in crack d, reaching the value of 4.2 mm and 20.1 mm during late rainy (November 2021) and second winter (January 2022), respectively. Compared to the first year, the result indicated that CW almost twice increased (84.4%) during second winter. Since experienced with more extreme climate condition, the embankment encountered with longer drought period in the second summer, promoting more significant soil shrinkage and thus enlarge desiccation crack. Moreover, wetting and drying process may reduce soil integrity and increase in weak zone in soil (Yong and Warkentin, 1975; Cheng et al., 2021). These weak zones may trigger the development of cracks to be more significant during second and third cycle of drying-wetting process (Tang et al., 2011, 2020).

The behaviour of desiccation cracks due to seasonal variation at the middle depth of the embankment can be illustrated in Figure 53 (b). Regarding that figure, four cracks was found at the depth of 0.5 m namely crack e, f, g and h. There is a notable continuity in the crack propagation from the upper layers, extending through to this intermediate depth (crack f, g and h). However, it is noted that a limited number of cracks appear to initiate within this depth and exhibit a level of discontinuity in their propagation (crack e). It can be seen from Figure 53 (b) that connected-cracks f and h significantly increased during first summer, measuring around 3.6 mm and 4.4 in crack width, respectively. Following this, it can be reported that those cracks decreased by approximately 58% and 50%, respectively in rainy season indicating CW at a deeper depth was less fluctuated, compared to shallow depth. It may be attributed to the less soil-atmosphere interaction at the deeper depth, preventing soil swelling process. As in near surface area, CW of connected-cracks at the depth of 0.5 m also increased during late rainy and reached maximum value in the second winter, amounting by about 1.5 mm and 6.1 mm respectively. Even though tend to have less fluctuation compared to near surface area, connected cracks was still affected by seasonal condition as in near surface area. It is due to the fact that its inter-connection provides soil-atmosphere interaction to the deeper depth.

There is distinctive behaviour between connected and non-connected cracks, located at the intermediate depth of the embankment. It was clearly reported that connected crack was significantly influenced by seasonal variation, mirroring near surface cracks behaviour. However, non-connected cracks tend to have less correlation with weather condition. Figure 53 (b) exhibits that crack e was found to be non-connected cracks regarding their propagation process. It can be seen from Figure 53 (b) that crack e remain less pronounced due to their discontinuity with surface cracks, exhibit a limited response to seasonal variations in moisture and temperature. However, as subsequent drying and wetting cycles occur, a compelling phenomenon emerges. Non-connected crack in this lower layer begin to accumulate and become considerably more prevalent. The accumulation of those cracks is primarily driven by these initially discontinuous cracks, which gradually propagate and connect to form more extensive cracks. This process occurs in response to prolonged and repeated wetting and drying cycles, which enable these sub-surface cracks to undergo progressive development.

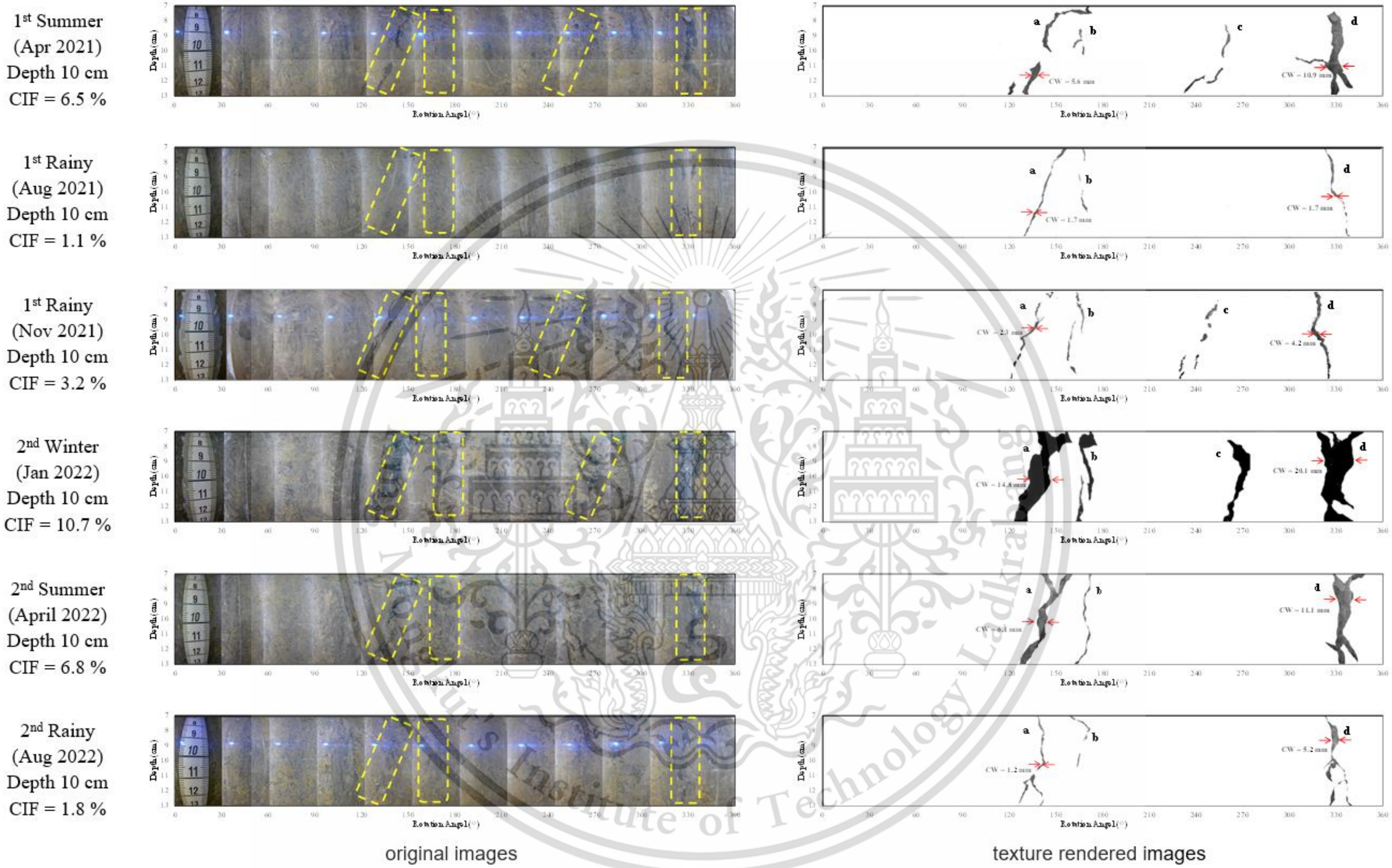1st Summer
(Apr 2021)
Depth 10 cm
CIF = 6.5 %
1st Rainy
(Aug 2021)
Depth 10 cm
CIF = 1.1 %
1st Rainy
(Nov 2021)
Depth 10 cm
CIF = 3.2 %
2nd Winter
(Jan 2022)
Depth 10 cm
CIF = 10.7 %
2nd Summer
(April 2022)
Depth 10 cm
CIF = 6.8 %
2nd Rainy
(Aug 2022)
Depth 10 cm
CIF = 1.8 %
Depth (cm)
Rotation Angel(°)
0
30
60
90
120
150
180
210
240
270
300
330
360
a
b
c
d
CW = 5.6 mm
CW = 10.9 mm
CW = 1.7 mm
CW = 1.7 mm
CW = 2.3 mm
CW = 4.2 mm
CW = 14.8 mm
CW = 20.1 mm
CW = 6.1 mm
CW = 11.1 mm
CW = 1.2 mm
CW = 5.2 mm
original images
texture rendered images

(a) 0.10 m

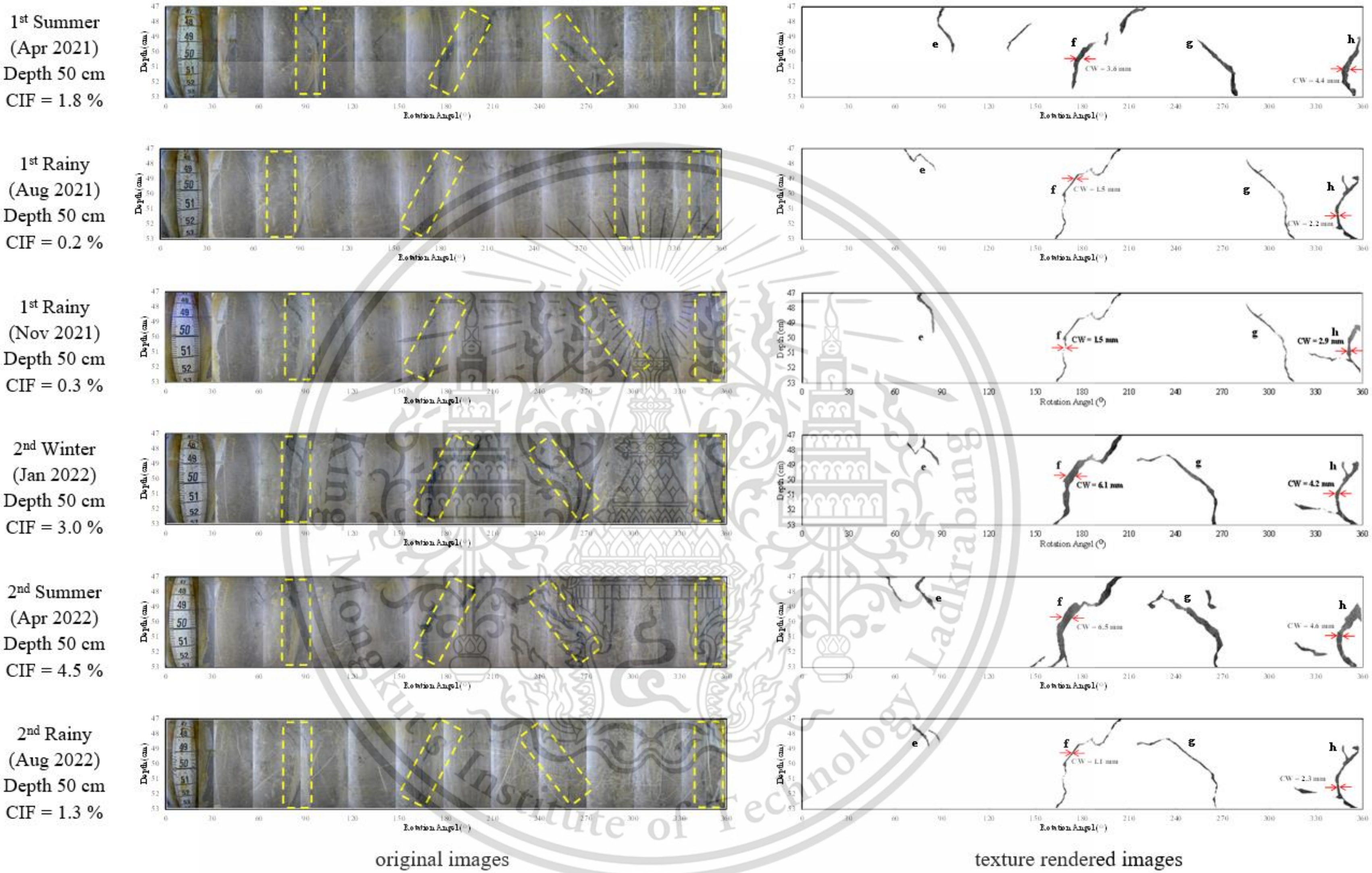

(b) 0.5 m

Figure 53 Original and segmented crack picture.

Further to this, the variation of CIF profiles due to seasonal changes can be illustrated in Figure 54. It is evident that the CIF profiles exhibit two distinctive zones. The upper layer, situated above a depth of 0.4 meters, displays pronounced and fluctuating CIF patterns throughout the seasonal variations. Conversely, the layer located below the 0.4-meter depth appears to exhibit significantly fewer CIFs compared to the uppermost layer during the initial year. However, as subsequent drying and wetting cycles occur, the CIFs in this lower layer appear to accumulate and become considerably more prevalent. This discrepancy is primarily attributed to the presence of discontinuous cracks that are not directly linked to the surface and, therefore, are less influenced by seasonal climate effects. It can be attributed to the wetting and drying cycle which creating weak zones, and thus significantly control the start positions of cracks during the subsequent drying period (Yong and Warkentin, 1975), including at the deeper depth. As a result, the lower layer experiences a significant increase in CIFs, which can have important implications for the embankment's hydrological properties. While the upper layer may exhibit more immediate and surface-connected CIFs in response to seasonal climate variations, the lower layer demonstrates a delayed but substantial growth in CIF due to the cumulative effects of discontinuity cracks.

In the context of climate effect, it can be reported from Figure 54 that the value of CIF at the depth of 10 cm reached by approximately 6.5% in the first summer when climate index was about -1.11 (moderate dry). When the embankment experienced with intense rainfall (335 mm/month) in first rainy season, CIF plummeted to about 1.0%. It should be noted that the climate condition was found to be moderated wet (SPEI = 1.14) during that season. Due to the absence of rainfall, the cracks started to rise at the last rainy season, promoting the increase in CIF of 3.2%. Figure 54 also indicates that the value of CIF reached the maximal value (10.7 %) during the second winter. This is because the embankment subjected with drier climate condition (severe dry) during second winter compared to first summer (moderate dry). Moreover, it can also be attributed to the volume change during the seasonal cycle resulting in a decrease in soil integrity and an increase in weak zones in soil samples (Yong and Warkentin, 1975). Further to this, soil cracks also significantly reduced during the second wet season, promoting CIF value of 1.3 %. Even though underwent with wetter climate condition, CIF at second rainy season was still higher than that at first season. It can be attributed to the soil plasticity behaviour, hindering the soil recovered to original condition.

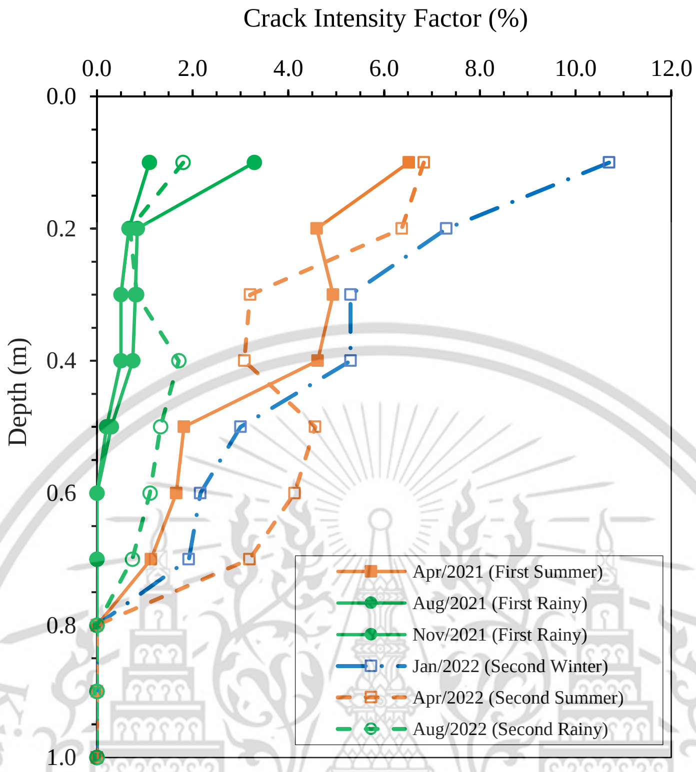

Figure 54 Crack intensity factor (CIF) along the depth.

6.1 Correlation between AWB and crack propagation

To analyse embankment behaviour under extreme climate conditions, future cracks should be predicted prior to the calculation. Future crack conditions will be influenced by hydrological properties such as water content and PWP, which are related to soil water balance. Accordingly, future Atmospheric Water Balance (AWB) has been predicted based on 30 years historical weather data. According to Blight (1997) AWB, defined as the difference between rainfall and potential evaporation, is one of the basic input to the soil water balance, therefore affecting soil behaviour. Furthermore, to simplify crack analysis under extreme climate conditions, the correlation between Atmospheric Water Balance (AWB) and CIF was deployed in this research as can be illustrated in Figure 55.

Considering Figure 55 it is evident that the decrease in AWB has led to an increase in CIF. The value of CIF rose by more than 8% when AWB was less than 0 mm/month. In that condition, potential evaporation was more than rainfall intensity, decreasing soil water content as well as developing CIF. Furthermore, as the AWB rose to 100 mm/month, the CIF value decreased to nearly 0% pertaining to the increasing of soil water content near saturation. The polynomial regression equation based on those two parameters was deployed to predict CIF under extreme climate condition. It should be noted that polynomial regression has the highest correlation considering the value of R2 (0.9296), as shown in Figure 55. Regarding extreme climate condition, the value of CIF increased to 18.5% due to the decreasing AWB to -115.2 mm/month in the near future (2060). As the value of AWB decreased to -123.0 mm/month in 2080, the CIF value rose to 19.0%. Moreover, in the far future (2100), CIF will increase by approximately 20.5 percent as AWB decreased to -135.54 mm/month.

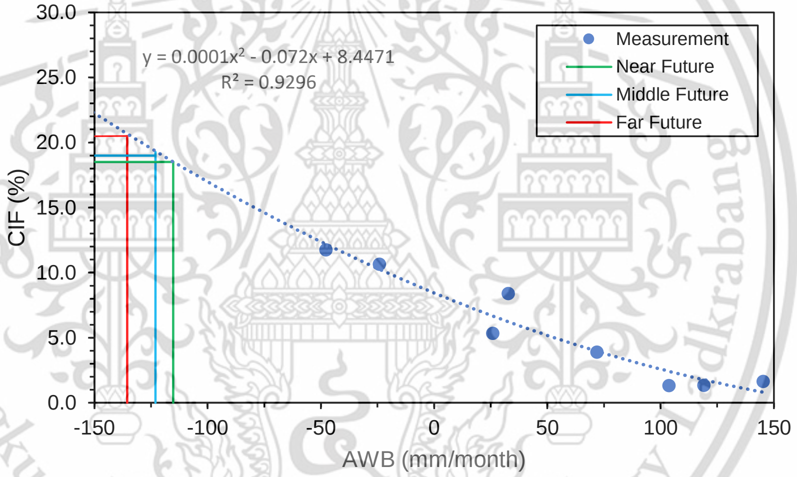

Figure 55 Correlation between AWB and CIF.

Chapter 7 Double Ring Infiltrometer Result

The aim of double ring test is to investigate the correlation between Crack Intensity Factor (CIF) and water infiltration under different climate variations. Furthermore, water infiltration behaviour will be employed to support numerical simulation as boundary condition. In this section, the result of double ring test will be reported.

7.1 CIF in double ring area

Five variations of desiccation crack were captured prior to the double ring test process during one and a half years of observation from October 2021 to January 2023. The alteration of the desiccation crack due to seasonal behaviour can be depicted in Figure 3. The first experiment was conducted in October 2021, one week after the equipment was setup at the beginning of the dry season. At the first attempt of the test, the existence of the crack was limited (CIF = 0%) with respect to the recent experiment setup. The second test was performed in February 2022, representing in the middle of the first dry season. As shown in Figure 3, a noticeable crack existed during this period of the test (CIF = 8.1%). During the dry season, as the soil water balance decreased, matric suction developed, resulting in a rise in tensile stress. While the tensile stress exceeded the tensile strength of the soil, desiccation cracks may initiate. Once the strain energy was released, the tensile stress direction induced by shrinkage was parallel to the tangent direction of soil area, initiating a perpendicular crack to tangent direction, pointing to the center of the soil sample (Cheng et al., 2021).

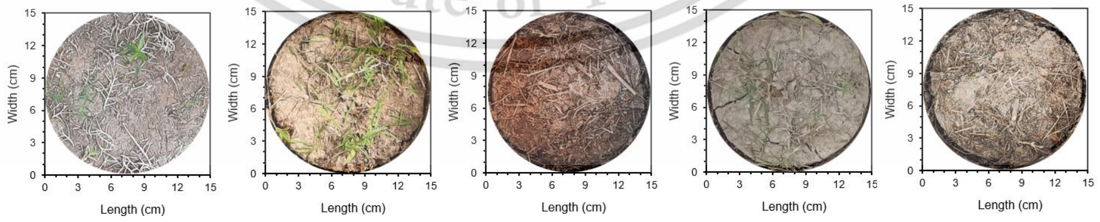

(a) original image

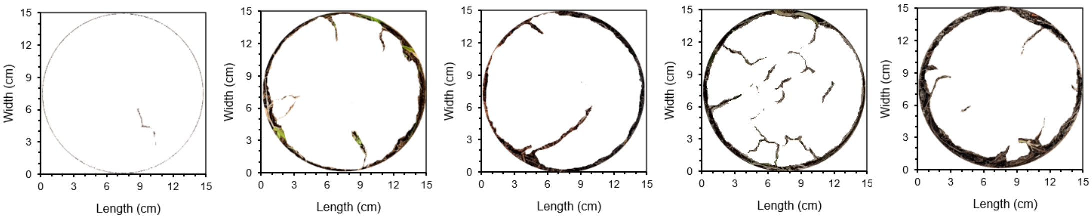

30 Oct 2021 (CIF = 0%)

16 Apr 2022 (CIF = 5.2%)

9 Nov 2022 (CIF = 6.9%)

28 Feb 2022 (CIF = 8.1%)

11 Jan 2023 (CIF = 11.4%)

(b) segmented image

Figure 56 CIF variation due to seasonal variation.

The third round of the test was conducted in April 2022, at the commencement of first wet season. The soil began to swell as the water content increased, reducing the CIF to around 5.2%. Therefore, the fourth test was performed at the early of the second dry season. As a result of the lack of precipitation and the decrease in soil moisture due to evaporation, the soil surface initiated to crack. It can be seen in Figure 3 that the CIF increased to 6.9%. Also, it can be reported from Figure 3 that CIF during the second dry season (11.4%) was higher than the first dry season (8.1%). It can be attributed to the volume change during the seasonal cycle resulting in a decrease in soil integrity and an increase in weak zones in soil samples (Yong and Warkentin, 1975).

7.2 The effect of crack to saturated hydraulic conductivity

To determine Ks in Philip equation (Philip, 1956), the value of M, defined as the ratio between transmittivity factor (A) and Ks is important. Considering its substantial role in this study, meticulous prediction is required. However, aforementioned research reported that M value can vary with respect to soil characteristic. Based on Philip (1990), the value of M varied between 0.3 – 0.7 considering three analytical methods. Moreover, Mishra et al. (2003) postulated that M ranged from 0.50 to 0.75 according to field and laboratory result. To obtain more reliable value regarding the soil type, M value was determined using prediction analysis by considering double ring test. It should be noted that A value was calculated using iteration method. Moreover, Ks was assumed equal to residual infiltration rate, predicted from double ring data. Regarding the calculation, the average of M value was around 0.67 and will be used in further Philip’s calculation. The detail calculation of M can be depicted in Table 6.

Table 6 Prediction of M value based on double ring result

Date of Test	CIF (%)	A (m/s) (Philip's Calculation)	Residual Infiltration Rate/Ir (m/s) (Observation Result)	M (A/Ir)
30-Sep-21	0.00%	1.80E-07	2.8E-07	0.6578
28-Feb-22	8.50%	8.32E-07	1.3E-06	0.6644
26-Apr-22	5.20%	4.44E-07	6.7E-07	0.6672
09-Nov-22	6.90%	6.28E-07	9.2E-07	0.6787
11-Jan-23	11.40%	1.50E-06	2.2E-06	0.6896
Average				0.6771

The value of Ks with respect to crack variation based on Philip's method, can be depicted in Table 7. Considering Table 7, it is generally reported that the value of Ks increases as CIF increases. The first attempt of the test was considered as non-crack condition due to a limited amount of crack. Thus, it can be determined that the value of non-crack Ks is 2.7 x 10-7 m/sec. During the first dry season, the value of Ks increases by about five times (1.42 x 10-6 m/sec) due to the attendance of 8.5% crack. As mentioned in the previous section, this is because desiccation cracking provides a preferential pathway for water infiltration, thus increasing the infiltration rate (Wang et al., 2018; Jiang et al., 2019). On the contrary, at the beginning of wet season, Ks values plummeted to 4.564 x 10-7 m/sec with a decreasing crack of 5.2%. Due to an increase in soil water content, the soil tends to heave, resulting in a decrease in CIF and Ks value (Cheng et al., 2021). At the end of wet season, the value of Ks doubles to 8.1 x 10-7 m/sec as the CIF increases to 6.9%. The fifth test was conducted in the second dry season in January 2023. The result indicates that the value of Ks during the second dry season (1.92 x 10-6 m/sec) is higher than the first dry season (1.42 x 10-6 m/sec) with respect to the crack propagation. It can be attributed to seasonal cycles that make the soil structure change from a non-aggregated structure to an aggregated one and create many large inter-aggregate pores (Tang et al., 2011).

Table 7 Ks due to CIF variation based on Philip's equation

Date of Test	CIF (%)	S ($cm/min^{0.5}$)	A (cm/min)	Ks (m/s)
30-Sep-21	0.00%	0.0251	0.0011	2.70E-07
28-Feb-22	8.50%	0.0345	0.0050	1.25E-06
26-Apr-22	5.20%	0.0306	0.0027	6.66E-07
09-Nov-22	6.90%	0.0202	0.0038	9.42E-07
11-Jan-23	11.40%	0.0775	0.0090	2.25E-06

Moreover, the correlation between CIF and Ks ratio can be expressed as an exponential curve, as can be seen in Figure 57. When CIF is less than 5%, Ks ratio slightly increases with the increasing of CIF. However, Ks ratio significantly increases as the raising of CIF when the value of CIF is more than 5%. When CIF is relatively small, cracks only exist in the superficial layer, limiting the increase of water infiltration (Delerue et al., 2003; Tang et al., 2019). In addition, there is a limited connection between the cracks, which reduces the rate of infiltration (Zhang et al., 2015). Following this, the connection among the crack was perfectly constructed as the CIF increased, creating preferential flow paths and significantly increasing the infiltration rate. (Cheng et al., 2021).

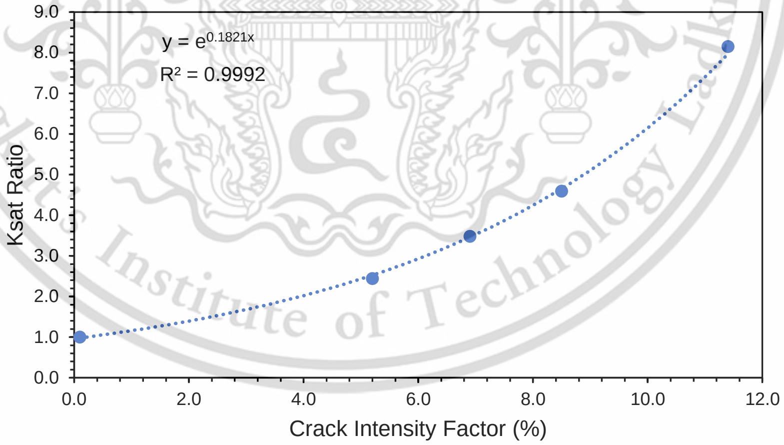

Figure 57 Correlation between CIF dan Ks Ratio.

7.3 Modified Green-Ampt method

A newly modified Green-Ampt method was proposed to calculate water infiltration by considering the existence of the cracks. The Green-Ampt model is the most commonly used in many applications, as it considers more complex parameters such as saturated hydraulic conductivity (Ks), pore water pressure (PWP), and volumetric water content (VWC). Rectangular saturated piston flow and homogeneous isotropic soil were used to develop the Green-Ampt infiltration model (Gowdish and Muñoz-Carpena, 2009). Chui and Zu (2017) reported that the Green-Ampt model has been used in Soil and Water Assessment Tool (SWAT) model, the Water Erosion Prediction Project (WEPP) model, and the Hydrologic Engineering Center-Hydrologic Modelling System (HEC-HMS). Recently, several studies have developed new models, based on the Green-Ampt method that considers Ks, negative PWP (ψ), and VWC. The original Green-Ampt equation can be seen in equation (38) and (39). By knowing the correlation between CIF and Ks, new Green-Ampt method can be deduced from equation (38) and (39).

Based on equations (38) and (39), the attendance of the crack can be considered by modifying Ks. It should be noted that the correlation between CIF variation and Ks ratio, illustrated in Figure 57 was employed to generate the new model. Ks ratio can be calculated by dividing Ks in a particular CIF to Ks0. Where, Ks0 is initial Ks, defined as the value of Ks in a non-crack condition. Moreover, the correlation between CIF variation and Ks ratio was expressed using an exponential equation and then imposed in the previous model. Following this, the new proposed Green-Ampt model by considering CIF can be stated in equations (117) and (118).

$$F(t) = e^{0.18CIF} K_{s0}\, t + \psi \Delta\theta \ln\left(1 + \frac{F(t)}{\psi\Delta\theta}\right) \tag{117}$$

$$f(t) = e^{0.18CIF} K_{s0} \left(\frac{\psi\Delta\theta}{F(t)} + 1\right) \tag{118}$$

7.4 Water infiltration due to desiccation crack

In this study, a back analysis was conducted to validate the new Green-Ampt model. The comparison between proposed Green-Ampt calculation and measurement data can then depicted in Figure 58. Figure 58 (a), (b), (c), (d) and (e) show the alteration of infiltration rate with elapsed time, correspond to CIF variations of 0%, 5.2%, 6.9%, 8.1% and 11.4% respectively. Beyond that, cumulative infiltration depth (CID) can also be computed and plotted in the same graph. Generally, it can be seen in 6 that the new Green-Ampt method resulted in good agreement with measurement data, as indicated by the same trend in infiltration rate. Rapid infiltration rates occurred at the beginning of the test with respect to preferential pathways

(Tsiampousi et al., 2017; Wang et al., 2018; Jiang et al., 2019). Besides, it is due to a large difference in hydraulic gradient between the upper and the lower soil layer Chen et al., (2022). As hydraulic gradient gradually decreased the infiltration rate decreased significantly prior to of steady-state conditions. Moreover, it can also be caused by the crack narrowing along with soil heave. As shows in Figure 58, during 4 hours of observation, the final infiltration rate increased with the increasing of CIF. The value of the final infiltration rate was around 3.55 x 10-7 m/s in non-crack conditions (CIF =0%). As the CIF increased to 5.2%, the final infiltration rose by about 3 times (1.19 x 10-6 m/s). Moreover, by raising CIF to 11.4%, the value of the final infiltration rate increased 6 times (2.17 x 10-6 m/s) compared to the non-crack condition.

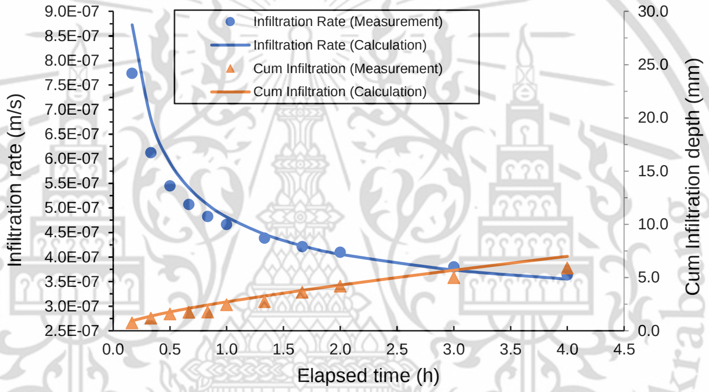

(a) CIF 0%

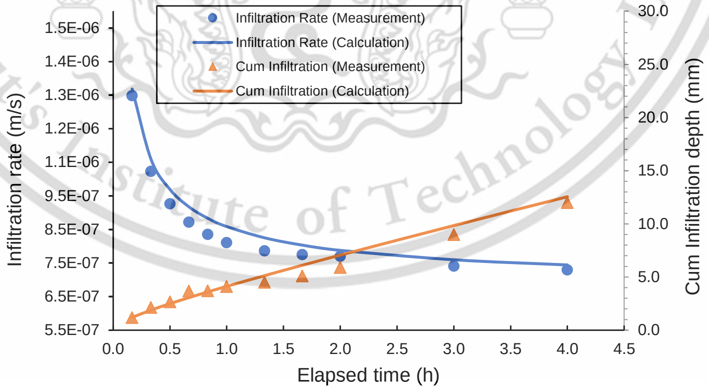

(b) CIF 5.2%

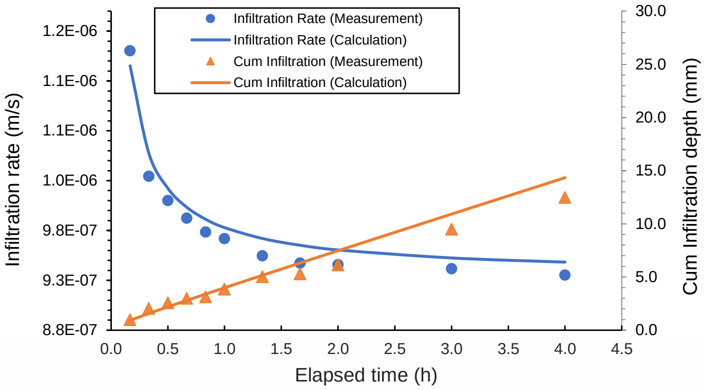

(c) CIF 6.9%

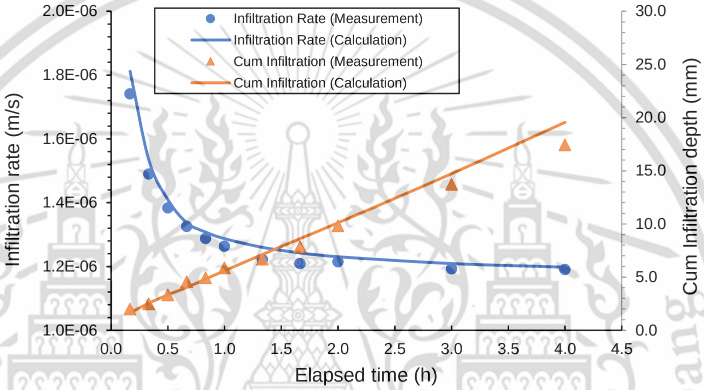

(d) CIF 8.1%

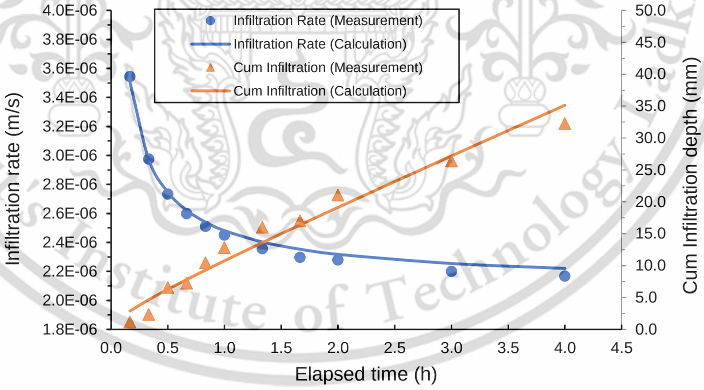

(e) CIF 11.4%

Figure 58 Water Infiltration Under Current Climate

It can also be found in Figure 58, CID increased gradually over time for both the calculation and measurement results. Based on modified Green-Ampt, when the value of CIF was 0%, the value of the final CID was about 6 mm during the 4 hours of observation. Moreover, as depicted in 6 (b), the final CID increased by approximately twofold (12 mm) as the CIF rose by 5.2%. In addition, due to the raising of CIF by 11.4%, the value of final the CID increased to 35.15 mm (6 times). Considering Cheng et al. (2021), increasing the surface crack ratio by about 3 - 6% can increase infiltration capacity by 5 - 10 times. As postulated in the previous section, the attendance of the crack can provide a preferential pathway, thus increasing infiltration capacity. Moreover, the effect of drying-wetting cycles produced a higher surface crack ratio, therefore increasing infiltration capacity. Regarding Tang et al. (2011), drying-wetting cycles make the initially homogeneous non-aggregated structure convert to a heterogeneous aggregated structure, creating many inter-aggregate pores.

7.5 Water infiltration under extreme climate conditions

In addition, parametric studies utilizing the proposed Green-Ampt method have been conducted to obtain a deeper understanding of water infiltration under extreme climate conditions. It should be noted that CIF in extreme climate condition has been determined in aforementioned section (6.1.3). Figure 59 shows infiltration rate and CID for three variations of future extreme climate scenarios, analyzed in this parametric study. As a comparison, analytical result of maximum CIF under current climate condition has also been demonstrated in the graph. In general, Figure 59 shows that future extreme climate will result in a significant increase in infiltration rate compared to the maximum current climate condition. As the CIF increased by approximately 18.5% in the near future (2060), the final infiltration rate will increase by approximately 7.64 x 10-6 m/s during the 4 hours of observation. It increases by about 244%, compared to the maximum current climate scenario (CIF = 11.4%). In 2080, the value of infiltration rate rose by about 8.35 x 10-6 m/s (276%) with an increasing in CIF of 19%. Moreover, the extreme climate during the far future scenario (2100) will cause the CIF to rise by about 20.5%, thereby increasing the infiltration rate by approximately 1.09 x 10-5 m/s (391%). Based on the analysis, it is substantiated that extreme drought climate conditions will lead to a significant increase in CIF, thus raising water infiltration depth.

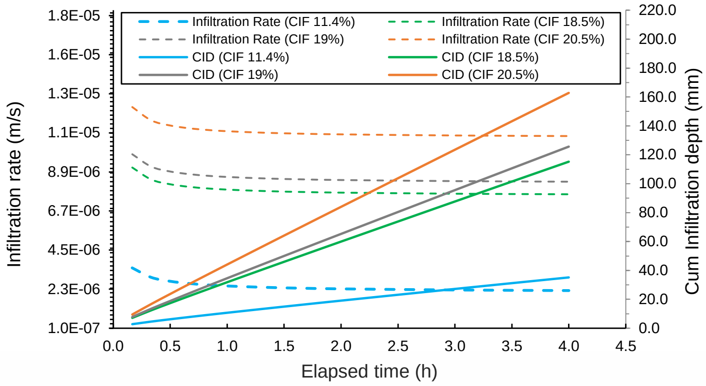

Figure 59 Water Infiltration Under Extreme Climate

In the context of CID, the near future (CIF 18.5%) will increase CID by approximately 115.27 mm during the 4 hours of observation. It increases by about 3.2 times, compared to the maximum current climate scenario (CIF = 11.4%). Moreover, the value of CID will rise about 125.62 mm (3.5 times) with an increasing in CIF of 19% according to middle climate scenario (2080). Further to this, the far future scenario (2100) will cause the CID to rise by approximately 162.86 millimeters (4.6 times). Based on the analysis, it is substantiated that extreme drought climate conditions will lead to a significant increase in CIF, thus raising water infiltration depth. As a result of the extreme wet and dry cycles, it will cause high fluctuation of soil water conditions, ratcheting the serviceability problem in earthwork structure (Anderson and Kneale, 1980; Smethurst et al., 2006; Glendinning et al., 2014). For example, considering Li et al. (2022) the increasing of wetting front depth by approximately 3.2, 3.5, and 4.6 times during near, middle, far future scenarios will reduce Factor of Safety (FOS) of slope with gradient of 30° by around 55%, 60% and 65% respectively. After all, it can be concluded that the effect of extreme climates must be factored into analyses of stability and serviceability in many aspects of engineering design.

Chapter 8 The effects of desiccation crack and seasonal variation on hydrological response

The objective of this section is to observe the propagation and intensity of desiccation cracks throughout different seasons and investigate their effects on the alteration of hydrological response of the embankment under seasonal variations.

8.1 VWC fluctuation due to seasonal variation

The fluctuation of VWC over time can be plotted in Figure 60. Regarding Figure 60, it can be seen that the value of VWC was relatively low during the first winter (January – February 2021). At the depth of 0.25 m, the value of VWC during that season ranged from 30.9% to 43.6%, averaging by approximately 34.9%. It should be noted that the embankment was classified as normal dry condition in that season. Moreover, VWC value tend to increase during the first dry season (March – May 2021). The average of VWC at the depth of 0.25 was found to be 34.0% in that season. Given that the embankment encountered with moderate dry climate during that season, Soil Water Balance (SWB) tend to be lower, promoting the decrease in VWC. It was also attributed to the presence of desiccation in that season, inducing the increase in evaporation, and thus reduce in VWC. On the contrary, the value of SWB tended to be positive with respect to the presence of rainfall during the first rainy (June – November 2021), inducing the increase in average VWC, amounting by about 46.2%. It is due to the fact that the embankment experienced with moderate wet condition during that season, indicated by SPEI climate index (1.14). As a result, desiccation crack tended to close in that season, promoting the decrease in CIF. During second winter (December 2021 – February 2022), the value of average VWC at near surface area fell down to 31.9%. Since experiencing with more extreme climate condition (severe dry) in that season, the value of AWC tend to be negative with respect to the absence of rainfall, as such reducing VWC significantly. Accordingly, the increase in desiccation crack was found to be profound during that season, producing maximum value of CIF. It should be noted that the embankment encountered with more extreme dry climate during the second year, compared to the first year. Following this, the average of VWC slightly rose in the second summer, reaching 35.1%. It can be attributed to the modest rainfall which occurred during that season, providing the increase in AWB. Further to this, the rose in VWC during that season served the decrease in CIF, compared to second winter. Additionally, the average of VWC reached maximum value in the second rainy season, amounting by about 47.0%. This result was significantly linked to climate condition during that season. Noted that during second rainy, the embankment experienced with severe wet condition (SPEI = 1.56) with respect to significant amount of rainfall intensity.

Besides, Figure 60 shows that the value of VWC at shallow depth was found to be more fluctuated, compared to deeper depth. Based on that figure, the value of VWC at near surface area sparse between 29.0% and 49.6%. Furthermore, the embankment tended to have less fluctuated VWC at the depth 0.5 m and 1.0 m, ranging from 28.1% to 49.6% and between 31.8% and 49.6% respectively. It can generally be contributed to the dominant effect of soil-atmosphere interaction at shallower depth, resulting higher evaporation during summer and receiving more water during wet season, compared to a deeper depth. Moreover, the distinctive value of CIF between near surface area and deeper depth was also play essential role to the soil water behaviour. Since having bigger CIF, shallow depth experienced with higher evaporation rather that deeper depth, promoting more significant decrease in VWC during summer. Further to this, the decrease in VWC at shallower depth was faster rather than deeper depth. Regarding the data, 15 consecutive days without rainfall can induce the decrease in VWC by approximately 21% (41.9 % to 33.1%) at the depth of 0.25 m. However, the same weather condition can reduce VWC by about 12% and 9% at the depth of 0.5 m and 1.0 m respectively. It was also strongly linked to the more notably effect of soil-atmosphere interaction at near surface area, compared to a deeper depth. Likewise, near surface area experienced with faster increase in VWC during rainy season, rather than deeper depth. Based on Figure 6, the value of VWC at the depth of 0.25 m rocketed from 28% to 45% after 10 days rainy season. On the other hand, the value of VWC rose from 30% to 45% after approximately 1 and 2 months of rainy season at the depth of 0.5 m and 1 m, respectively. It closely related to water infiltration depth which gradually increase during rainy season, triggering different response of VWC along the depth. Moreover, the presence of desiccation crack can accelerate the wetting process, promoting the increase in VWC to be faster.

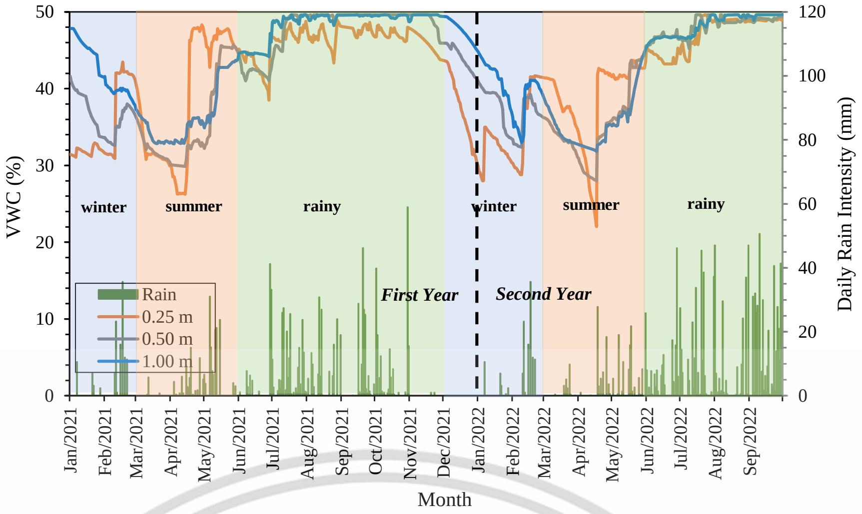

Figure 60 The fluctuation of VWC over time.

8.2 Correlation between AWB and VWC along the depth due to CIF variation

To capture the effect of desiccation crack on soil moisture behaviour with seasonal variation, the relationship among those parameters should be analyzed as presented in Figure 61. Atmospheric water balance (AWB), defined as the different between rainfall intensity and evaporation were used to represent external parameter in this analysis in association with seasonal condition. Following this, the correlation between AWB and VWC incorporated with CIF was plotted in Figure 61. The effect of desiccation crack was characterized by the variation of CIF at the observation depth. Moreover, this analysis was conducted for three variations of depth, following the depth of the sensor. It can be seen from Figure 61 (a) that higher CIF tend to have lower and more fluctuated value of VWC at the depth of 0.25 m. That figure shows that when the value of CIF was approximately 1.1% during rainy season, the fluctuation of AWB between -9.5 mm and 55.6 mm can trigger the increase in VWC from 43.3% to 48.9%. Furthermore, due to the increase in CIF of 6.8 % in the summer, the VWC value was found to be lower, ranging from 32.0% to 41.1% as a result of AWB fluctuation between -5.3 mm and 8.6 mm. Moreover, the embankment tended to have the lowest range of VWC during winter (CIF = 10.7%), spreading between 22.0% and 41.0%, addressed to the fluctuation of AWB from -4.9 mm to 7.9 mm. Notably, the increase in CIF can trigger the lower range of VWC in association with higher evaporation value. It is evidence that the presence of the crack provide the increase in surface area, as such rising evaporation value (Song and Cui, 2020; Cui, 2022; Zeng et al., 2023). Following this, desiccation crack served preferential pathway for water infiltration, promoting the significant increase in VWC during rain event (Shrestha et al., 2019; Chen et al., 2022; Apriyono et al., 2023).

Besides, Figure 61 (a) also shows that in the presence of higher AWB, particularly during the rainy season, the effect of increasing CIF on lowering VWC persists; however, this influence becomes less pronounced regarding the decrease in AWB. Regarding that figure, the increase in CIF from 1.1% to 2.2% induced the similar fluctuation of VWC between 46.1% and 48.9% when AWB above 20 mm. It is due to the fact that the embankment encountered with heavy rainfall intensity when AWB was relatively high, promoting the increase in VWC significantly near its maximum value. During that period, the variation of CIF provided minor influence on VWC fluctuation. However, when AWB below 20 mm, the different value of CIF 1.1% and 2.2% resulted the pronounced range of VWC, spreading from 44.5% to 48.9% and between 42.2% and 46.2% respectively. It should be note that lower AWB reflected either the absence of rainfall or the occurrence of modest rainfall intensity. Considering this condition, CIF played more significantly role in the fluctuation of VWC. It can be attributed to the significant increase in evaporation and water infiltration with the rise in the CIF.

Moreover, Figure 61 (b) shows that the effect of CIF resulted the same trend on the fluctuation of VWC at the depth of 0.5 m. However, the same range of AWB and CIF produced more fluctuated value of VWC. It can be seen from Figure 61 (b) that the CIF value of 1.3% during rainy season can trigger the fluctuation in VWC between 41.0% and 48.9% when AWB ranged from -9.5 mm to 55.6 mm. Moreover, because of the rise in CIF of 3.0 % in the winter, the VWC value was found to be lower, ranging from 28.0% to 40.9% as a result of AWB fluctuation between -5.3 mm and 8.6 mm. Even though experiencing with smaller CIF at the deeper depth, the majority of those cracks connected to the near surface, providing significant soil-atmosphere interaction. In addition, the same CIF between near surface area and middle depth occurred in the difference season, promoting distinctive range of VWC. Further to this, the correlation between AWB and VWC due to CIF variation at the depth of 1.0 m can be illustrated in Figure 61 (c). It should be noted that the presence of desiccation crack was minor at that depth. As a result, the correlation between AWB and VWC was mainly dictated by seasonal effect. Regarding that figure, the range of AWB from -10.6 mm to 55.6 mm during rainy season promoted the fluctuation in VWC between 43.0% and 49.8%. Moreover, the VWC was more fluctuated during winter and summer, ranging between 32.8% and 43.9% when AWB spread from 3.7 mm to 7.9 mm. It is obvious that the fluctuation of VWC was significantly govern by the amount of rainfall and evaporation during that season. Heavier rainfall intensity produced higher value of AWB, and thus promoting the increase in VWC. On the contrary, the absence of rainfall during summer led the decrease in AWB, triggering the decrease in VWC.

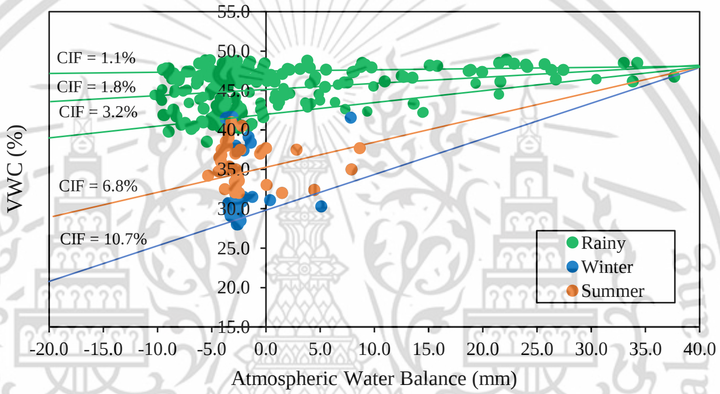

(a) 0.25 m

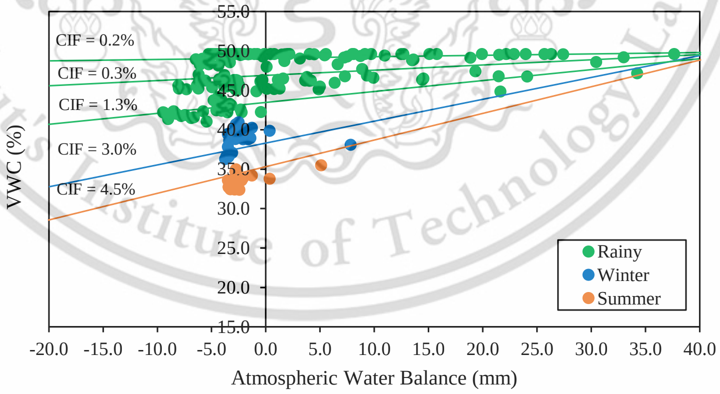

(b) 0.50 m

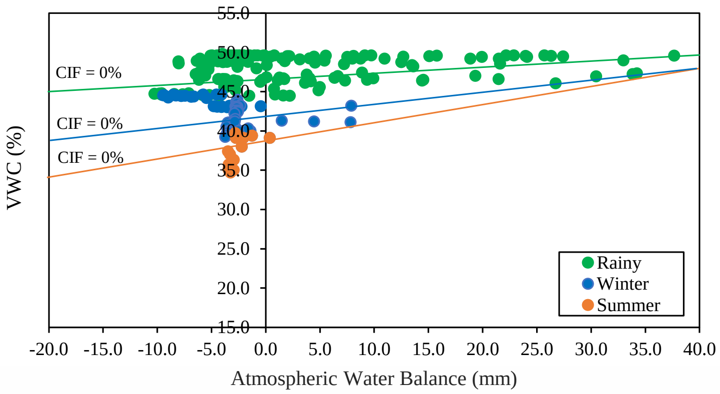

(c) 1.0 m

Figure 61 Correlation between AWB and VWC due to CIF variation.

8.3 PWP response due to seasonal variation

Figure 62 Figure 8 illustrates the maximum and minimum PWP due to seasonal variations along the depth. Based on that figure, the value of PWP at near surface area was more fluctuated, compared at deeper depth. The value of minimum and maximum PWP at 0.25 depth in the summer was found to be -1514.5 kPa and -0.94 kPa, respectively. Moreover, the value of VWC was less fluctuated at the depth of 0.5 m, ranging between -421.3 kPa and -176 kPa, respectively. Furthermore, the trend still persisted at the depth of 1.0 m, promoting lower range of PWP (-347 kPa to -252 kPa). Those discrepancy was mainly attributed to the pronounced effect of soil-atmosphere interaction at the shallow depth, compared to a deeper depth (Blight, 1997; Tsiampousi et al., 2017). Moreover, the significant value of CIF at near surface area during summer provide the increase in evaporation to be more significant, resulting the notable decrease in PWP. It can also be reported form Figure 62 (a) that the range of PWP was found to be higher during the first rainy season. The minimum and maximum value of PWP at the depth of 0.25 was about -332.1 kPa and -0 kPa respectively during that season. The PWP value was found to be less fluctuated at the depth of 0.5 m, spreading from -239.5 kPa to 0 kPa, respectively. Moreover, the value of PWP at the depth of 1.0 m ranged from -230 kPa to 0 kPa. Regarding this result, it substantiated that water infiltration can reach to the depth of 1.0 m during this season, promoting minor value of soil suction. Following this, it can be reported that the difference of minimum PWP along the depth was not significant during rainy.

It can be attributed to the minor value of CIF during that season, hindering evaporation process at the sub surface area.

The effect of climate on PWP fluctuation can also be observed from this figure by comparing the first and second year as can depicted in Figure 62 (a) and (b) respectively. In general, it can be seen from Figure 8 the first and second year tended to have similar trend in PWP fluctuation. However, since experiencing with different climate, the embankment experienced with different value of PWP value during second year, compared to the first year. Regarding Figure 62, the value of PWP in the second dry period at the near surface area was more fluctuated, compare to the first dry season, ranging between -2450 kPa and -54.5 kPa. Furthermore, the value of PWP during that period at the depth of 0.5 was also found to be lower, compared to the first dry period, spreading between -471.1 kPa and -300.0 kPa. It should be noted that the embankment encountered with severe dry period during the second year which was dryer than that in the first year (moderate dry). Accordingly, the embankment subjected with less rainfall intensity and higher evaporation during second summer, resulting lower PWP. In addition, higher value of CIF at the shallow depth in the second dry period can promote the decrease in PWP to be more profound, compared to the first year. Further to this, increase in CIF at the middle depth during second dry period can significantly rise evaporation, resulting the notable decrease in PWP.

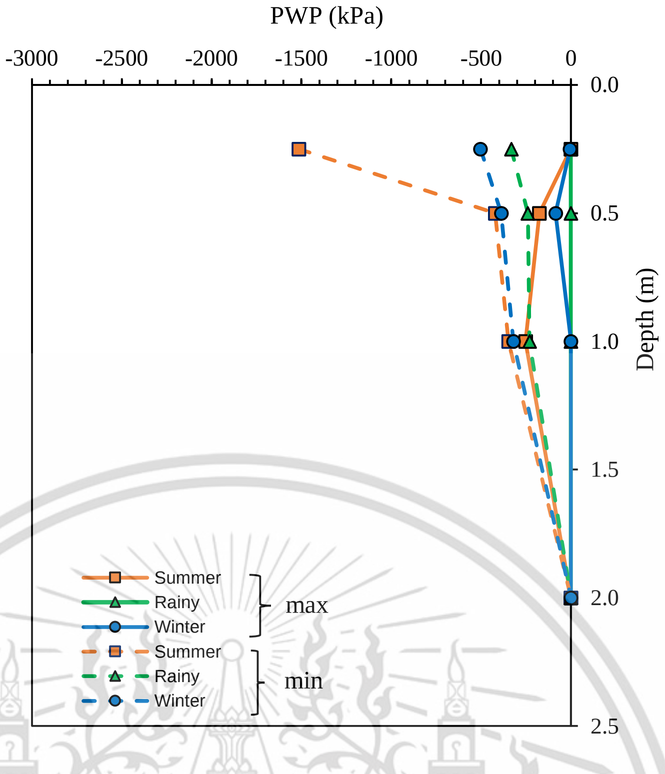

(a) first year

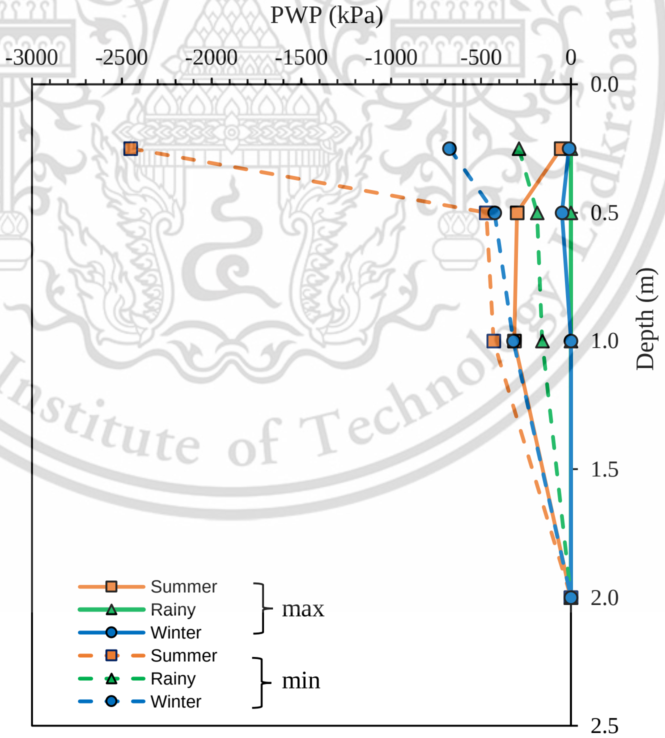

(b) second year

Figure 62 Comparing maximum and minimum PWP along the depth with seasonal variation.

Chapter 9 The Effect of Rainfall Intensity on Hydrological Behaviour of Embankment under Slope Gradient Variations

The objective of this section is to investigate PWP response of the embankment due to rainfall variations with respect to slope gradient variations.

9.1 PWP response due to seasonal variation

The fluctuation of PWP over time due to rainfall event during this study can be illustrated in Figure 63. Broadly, Figure 63 shows that there was similar pattern between the first and second year of observation. The embankment tended to have lower value of PWP in the summer (March to May), reaching minimum condition. PWP value increased during rainy season due to the presence of water infiltration (June to November). Further to this, the value of PWP started to rise over winter (December to February) regarding limited rainfall event. It can also be seen from Figure 63 that second year of observation resulted lower value of PWP during summer. The value of PWP reached minimum value by about -1.514 kPa at the depth of 0.25 m in the first summer. Meanwhile, PWP value attained minimum value by around -2.450 kPa throughout the second summer. In can be contributed to the different value of rainfall intensity between first and second year of observation during summer. Based on weather data, the embankment experienced with average monthly intensity by approximately 73.2 mm during the first summer. However, the embankment encountered with 62.7 mm of average monthly rainfall intensity in the second summer.

Besides, it can also be seen from Figure 63 that the value of PWP in shallow depth was more fluctuated than that at deeper depth. During the first year of observation, the value of PWP at the depth of 0.25 m was fluctuated from –1.514 to 0 kPa. Meanwhile, PWP value became less fluctuated at the depth of 0.5 m and 1.0 m, ranging from -421 to 0 kPa and -503 to 0 kPa, respectively. Similarly, PWP tend to have the most fluctuated value at depth of 0.25 m during second year of observation, ranging from -2450 to 0 kPa. It also came to be less fluctuated at the depth of 0.5 m and 1.0 m, spreading from -451 to 0 kPa and -539 to 0 kPa, respectively. This phenomenon was closely related to soil-atmosphere interaction, affecting hydrological behaviour. It is undeniable that the shallower depth provides more significant soil-atmosphere interaction, compared to the deeper depth. In addition, it should be noted that the minimum value of PWP value at 1.0 m depth was lower that the depth of 0.5 m. It can be contributed to the occasionally rainfall that occurred in the dry season, inducing water infiltration to the depth of 0.5 m and thus increased PWP. However, the effect of rainfall was limited to the depth of 1.0 m. As a result, PWP value has remained decrease during that season, reaching lower minimum value prior to rainy season.

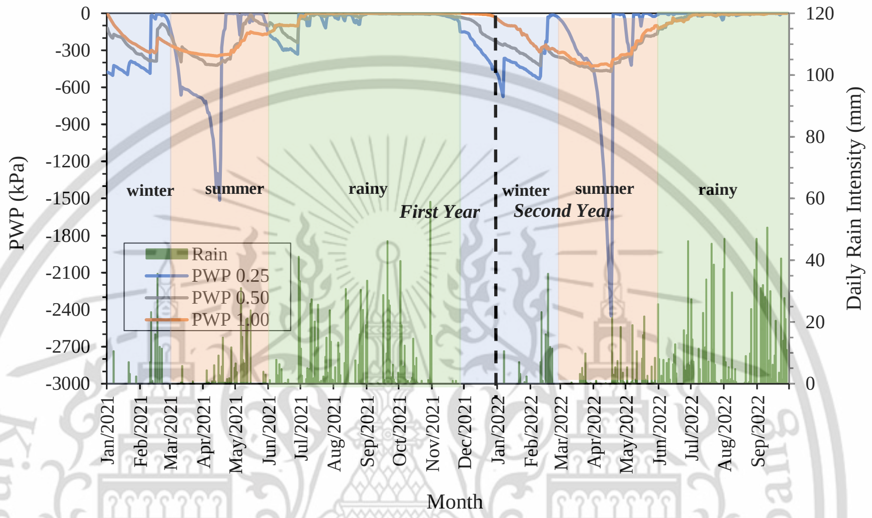

(a) milder zone

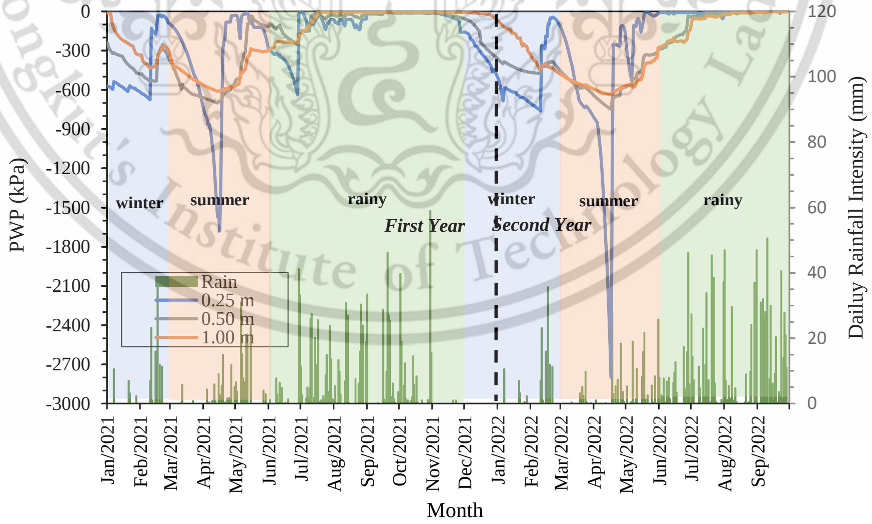

(b) steeper zone

Figure 63 PWP over the time with depth variation.

9.2 PWP response along the depth due to rainfall intensity variations

The response of PWP due to rainfall intensity variations along the depth can be illustrated in Figure 64. This figure exhibits three-dimensional coordinates, representing the correlation between initial and retained PWP with depth as a result of rainfall of event. The effect of rainfall on PWP can be investigated from the position of the coordinate to the 1:1 plane (ABCD). By referencing 1:1 plane, closer coordinate indicates less fluctuation in PWP. Conversely, the farther coordinate expresses more fluctuation of PWP. It can be generally reported from Figure 64 that small rainfall intensity tended to promote less fluctuation of PWP, compared to moderated and heavy rainfall at the three depth variations. In the context of shallow depth (0.25 m), small rainfall intensity triggered the increase in PWP by approximately 35.4%. Meanwhile, moderate and heavy rainfall intensity promotes the rise in PWP by about 67.5% and 87.0% respectively. Regarding this data, the effect of moderate rainfall on PWP fluctuation was found to be double as small rainfall intensity. Moreover, heavy rainfall can triple the effect on the fluctuation of PWP, compared to small rainfall intensity at the depth of 0.25 m.

Besides, it can be seen from Figure 64 that rainfall induced more significant effect on PWP fluctuation at shallower depth, compared to deeper depth. It should be noted that near surface area tended to obtain higher effect of soil-atmosphere interaction, including water infiltration. According to this figure, small rainfall can induce the rise in PWP by about 19.9% and 11.3% at the depth of 0.5 m and 1.0 m respectively. Whereas, PWP increased by around 43.2% and 13.9 % at the depth of 0.5 m and 1.0 m, respectively due to moderate rainfall intensity. Following this, the embankment experienced with the rise in PWP by about 71.8% and 67.5% at the depth of 0.5 m and 1.0 m respectively because of heavy rainfall intensity. This result prove that heavy rainfall can provide water infiltration to depth of 1.0 m, promoting the increase in PWP significantly. Regarding the data, small rainfall intensity provided significant effect on PWP fluctuation to depth of 0.25 m. However, the effect decreased significantly at the depth of 0.5 m and 1.0 m. Following this, moderate rainfall serve notably effect of PWP fluctuation to the depth of 0.5 m. Moreover, heavy rainfall intensity can trigger the profound alteration of PWP at any variation of depth.

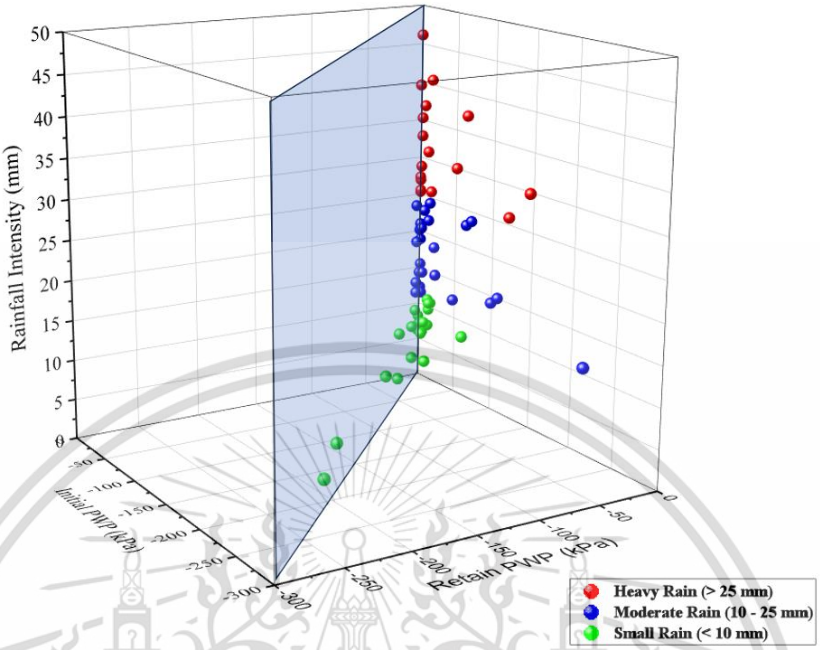

(a) 0.25 m

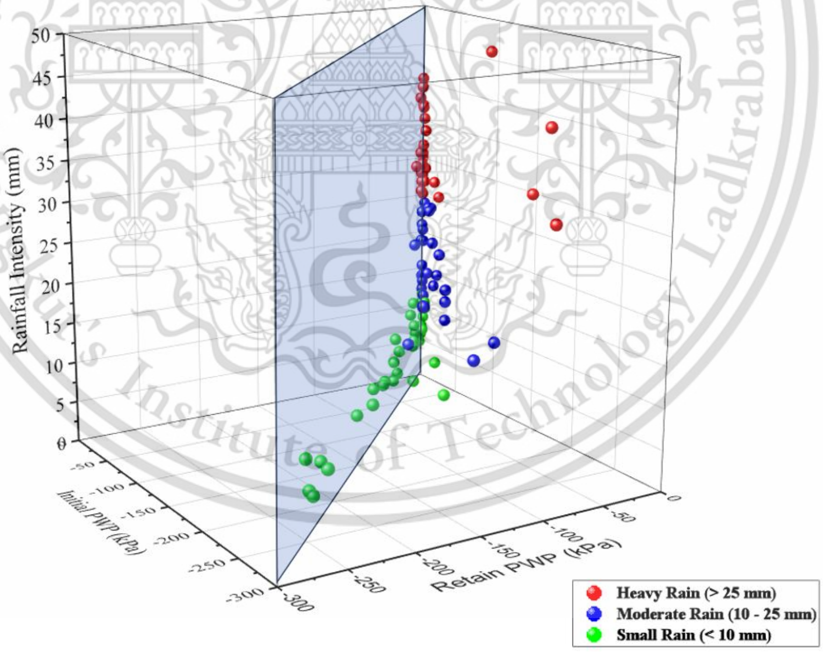

(b) 0.50 m

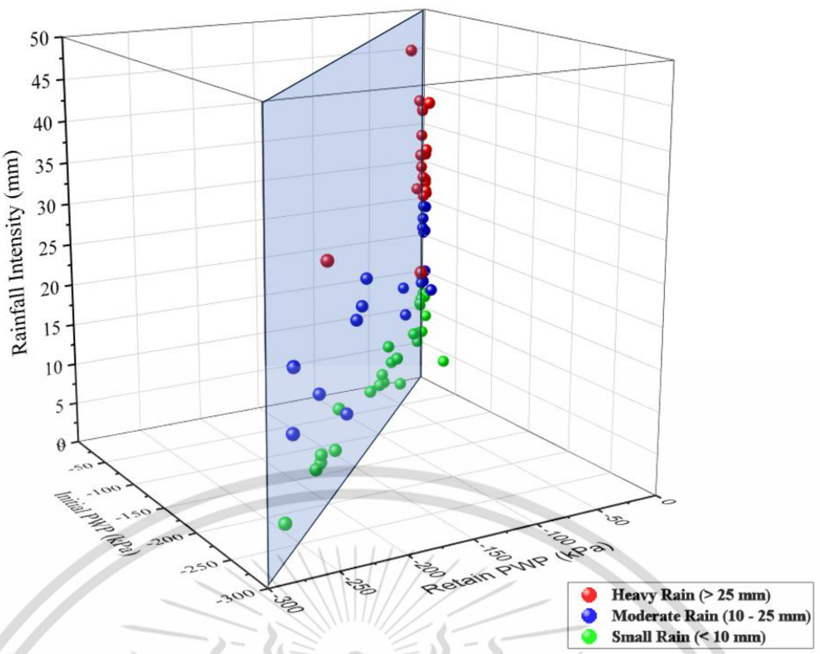

(c) 1.0 m

Figure 64 Initial and retained PWP due to rainfall variation.

9.3 PWP response due to rainfall under slope gradient variations

PWP response because of rainfall under slope gradient variations can be plotted in Figure 65. Figure 65 exhibits initial and retained PWP due to rainfall event along the depth. To obtain meticulous comparison, closed value of initial PWP was adopted in this analysis. Moreover, the response of PWP alteration was investigated due to the same event of rainfall (moderate rainfall). Figure 65 shows that the effect of rainfall on PWP fluctuation was more significant at shallower depth for both of slope gradient variations. Further to this, the effect of slope gradient variations was not significant at near surface area. Regarding this figure, moderate rainfall intensity induced the increase in PWP from -318.7 kPa to -10.0 kPa in milder zone. Meanwhile, the value of PWP rose by around 97% (-331.1 kPa to -9.3 kPa) in steeper zone due to moderate rainfall intensity. It substantiates that water infiltration band reached to depth of 0.25 m due to moderate rainfall intensity for all of slope gradient variations.

The distinctive response of PWP due to rainfall between milder and steeper zone can be found at the depth of 0.5 m and 1.0 m. It can be seen from Figure 65 that moderate rainfall triggers the increase in PWP from -231.6 kPa to -101.0 kPa (56.4%) at depth of 0.5 m in milder zone. Whereas, moderate rainfall leads the rise in PWP by about 17.5 % (-236.9 kPa to 195.5 kPa) at the same depth in steeper zone. Further to this, the value of PWP increased by approximately 40.9 % at 1.0 m depth in the milder zone. Meanwhile, the same rainfall intensity can induce the increase in PWP from 102.9 kPa to -93.4 kPa (9.3 %) at the depth of 1.0 m in the steeper zone. This result substantiates that slope gradient effect water infiltration depth, promoting different response of PWP. This result was consistent with the findings of other studies such as Fox et al. (1997) and Khan et al. (2016). Their result indicates that Infiltration rate decreased with increasing slope angle, attributed to the changes in overland flow depth and surface storage.

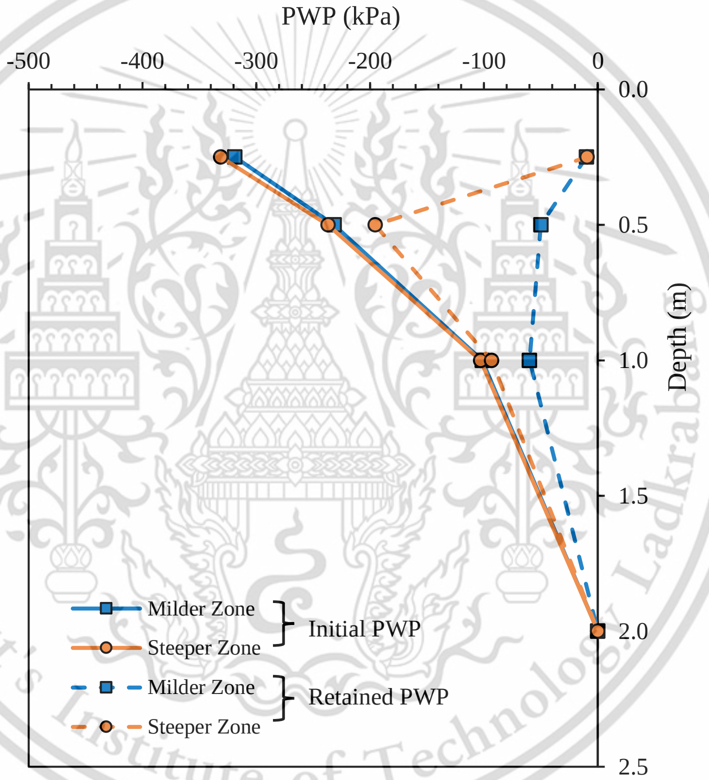

Figure 65 Initial and retained PWP due to rainfall along the depth under moderate rainfall intensity.

Chapter 10 The effect of Seasonal Variation on Embankment Deformation

The observation of embankment displacement was conducted using two methods namely topographic and photogrammetric method. It should be noted that this study focused on bare area solely. Further to this, Figure 66 shows the important points, used in the displacement analysis. To illustrate general deformation due to seasonal variation, cross section of the embankment was generated, following cut line I-I at the middle of bare area. Moreover, detail displacement of the embankment was observed at top and toe area that were located in milder (A and B) and steeper zone (C and D).

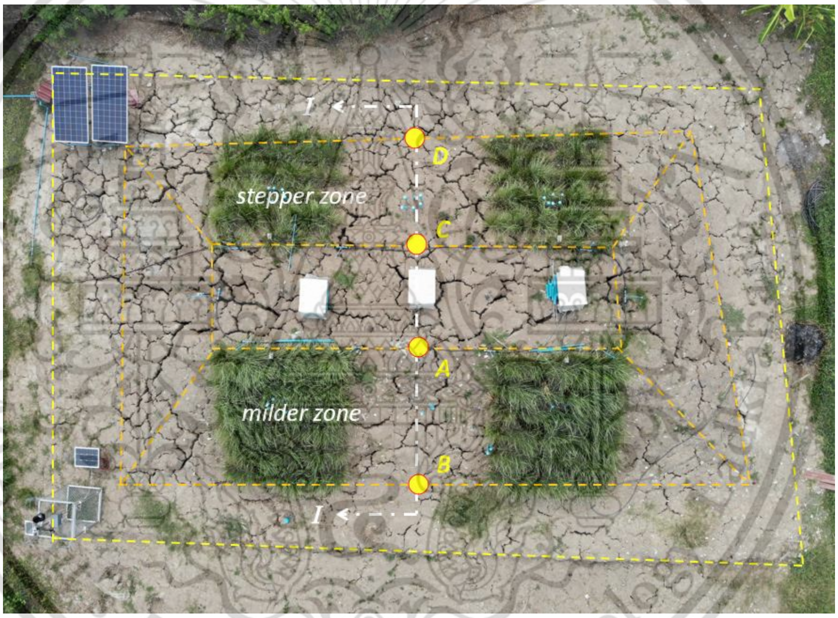

Figure 66 Displacement observation point.

10.1 Embankment cross section with seasonal variation

Topographic surveys were performed five times represent seasonal condition. Moreover, photogrammetric surveys were attempted four times using drone camera to support topographic method. The result of those surveys was illustrated in embankment cross section as can be seen in Figure 67. The first topographic survey was conducted in September 2020 at the beginning of embankment construction. Initial embankment construction was captured in this survey. Following this, the second survey was attempted in March 2021 represent the first dry season. To represent embankment deformation during the first wet season, the next survey was performed in November 2021. Further to this, the fourth and fifth survey were carried out in January and March 2022 to obtain deformation data during the second winter and dry season respectively.

In association with topographic survey, photogrammetric surveys were also performed in this study using drone camera. To support their result, photogrammetric surveys were conducted at the same season as topographic survey. Based on Figure 67, photogrammetric surveys produced the similar result with topographic survey. It substantiates that both topographic and photogrammetric surveys provide satisfied result in this study. Considering the figure, it can be seen that the initial height of the embankment was around 1.8 m. Significant displacement occurred during the six months after construction, regarding consolidation and shrinkage process. Accordingly, the height of the embankment reduced and reached approximately 1.6 cm on March 2021. Regarding the next survey result on November 2021, the displacement continued, resulting the height of embankment by about 1.4 m. However, the displacement process was milder during the second year of observation. It can be indicated form the two next surveys in January and March 2022. During those periods, the height of embankment was around 1.35 m and 1.33 m respectively.

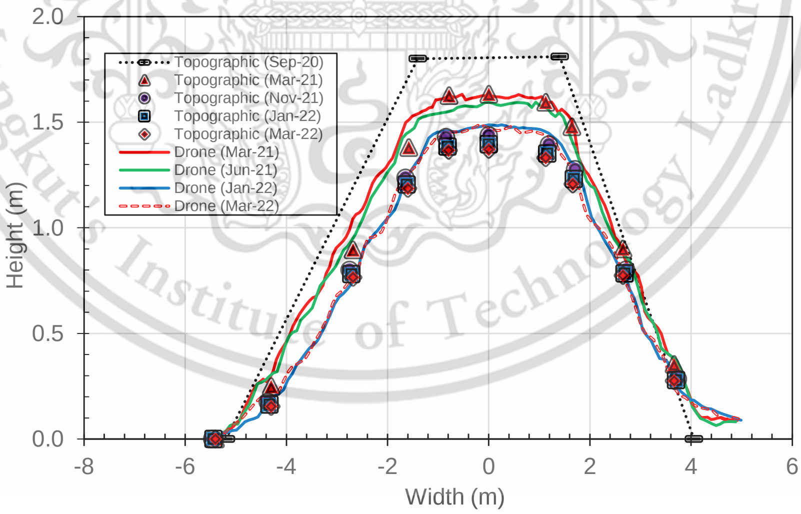

Figure 67 Embankment cross section with time variation.

10.2 Displacement of milder zone

Two observation point was determined to obtain embankment displacement in milder zone. Moreover, to obtain comprehensive deformation condition both vertical and horizontal displacement was analyzed in this study and will be expressed as follows.

(i) Displacement at top area (Point A)

Y-axis displacement at top area of embankment can be depicted in Figure 68 (a). Since the embankment was recently-built construction, the y-axis displacement was dominated by primary consolidation settlement rather than seasonal deformation. As a result, the effect of seasonal shrinkage and swelling process was minor in vertical direction. Regarding Figure 68 (a), the steepest line occurred in the first six months after construction process (September 2020 – February 2021), indicating the most pronounced displacement pertaining to combination between immediate and consolidation settlement. It should be noted that during that period the embankment was experienced with the first wet season. At this time, the value of embankment displacement attained by about 17.5 cm. Significant displacement has remained consistent during the first dry season and the second wet season (February – October 2021), reaching 37 cm with respect to soil shrinkage during dry season and consolidation throughout wet season. However, Figure 68 (a) shows that during the second winter and dry season (November 2021 – March 2022) the graph tends to be milder owing to the shrinkage process. During 5 months of second dry period, the increment displacement was only around 5 cm. It can be reported that total y-axis displacement at the top of milder zone was about 42 cm based on field measurement data.

Along the line of vertical displacement, horizontal displacement was also investigated at point A. However, unlike vertical displacement, the swelling and shrinkage process significantly influenced horizontal displacement as can illustrated in Figure 68 (b). It can be reported that the embankment moves toward to the center line during the first six months of the observation (September 2020 – February 2021). The total value of horizontal displacement in February 2021 was around -3.0 cm. This can be attributed to the shrinkage process in the dry season. Moreover, the embankment moves away from the center line during the second wet season. It can be indicated from the positive value of horizontal displacement. At the end of the second wet season in November 2021, the horizontal displacement at the top of the milder zone is around 3.2 cm. During that season, horizontal displacement was dominated by consolidation process. The cycle pattern has continued in the second of winter and dry season. Horizontal displacement moved back toward to the center during the second winter, resulting the displacement value of around 0 cm. Moreover, the negative trend has remained consistent and reached by approximately -2.0 cm at the end of dry season in March 2022. The shrinkage process during dry season dictated the horizontal displacement, therefore the embankment moved toward the center line.

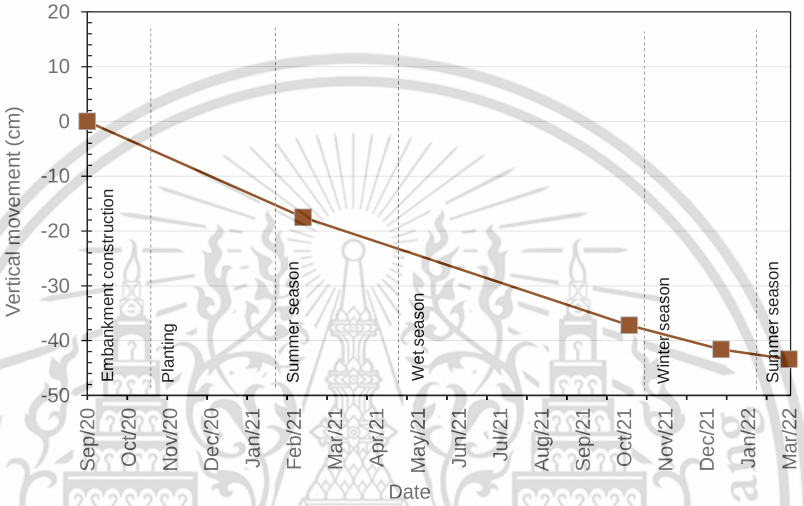

(a) y-axis displacement

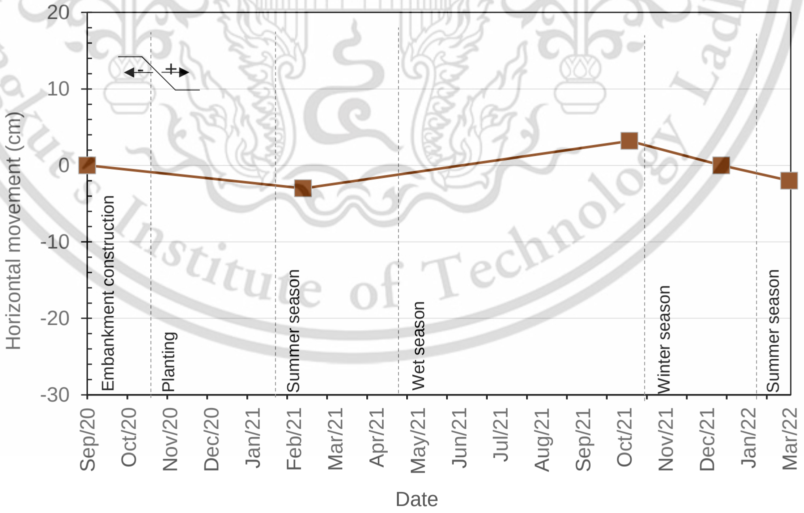

(b) x-axis displacement

Figure 68 Displacement at top of milder zone over time.

(ii) Displacement at toe area (Point B)

The displacement at toe area of the embankment can be illustrated in Figure 69. The difference of loading mechanism between top and toe provides notable behaviour of the displacement, especially in y-axis displacement. Since the effect of consolidation settlement was minor in the toe area, both y-axis and x-axis displacement were dominated by shrinkage and swelling process. As can be seen in Figure 69 (a), during the first six months of investigation, y-axis position at the toe area was similar. It can be indicated that swelling and shrinkage was balance during this period, resulting lacks of displacement in that area. However, during the second wet season, the effect of swelling process was dominant, resulting total y-axis displacement by about 11.8 cm in November 2022. In accordance with winter and dry season, the negative value of soil water balance led to shrinkage process at the toe area. Therefore, the embankment was experienced with negative displacement during winter and dry season. At the end of winter season in January 2022, the toe of the embankment displaced by approximately 1.5 cm. It was relatively lower than the previous displacement in November 2021. Moreover, negative y-axis displacement extended during the second dry season, reaching by about -8.5 cm.

Figure 69 (a) shows the behaviour of x-axis displacement at toe area with the time. The same trend as at top area, x-axis displacement at toe area produced cycle pattern with respect to seasonal behaviour. It can be attributed to the swelling and drying process during wet and dry season. As can be seen in Figure 69 (b), during the first six months of investigation, y-axis displacement at toe area was monopolized by shrinkage process, rather than swelling. It can be denoted from the value of x-axis displacement in February 2021 (-7.5 cm). It indicates that the toe area moved toward the center line. The presence of rainfall during the second wet season led soil swelling of the embankment, resulting positive value of displacement at toe area. By the end of second wet season (November 2021) the toe observation point moved away from center line, reaching total x-axis displacement back around -0.3 cm. Swelling and shrinkage cycle was consistent during the second year of observation. Like the first year, x-axis displacement at the toe area moved toward the center line during the second winter and dry season. Figure 69 (b) indicates that total x-axis displacement at the end of winter season in January 2022 was about -4.1 cm. Moreover, the trend of the displacement persisted, resulting total displacement by around -7.4 cm at the end of dry season in March 2022.

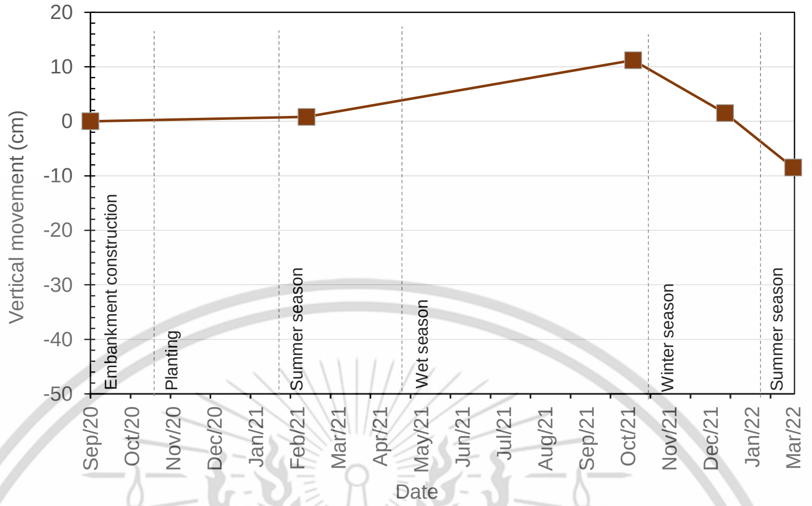

(a) y-axis displacement

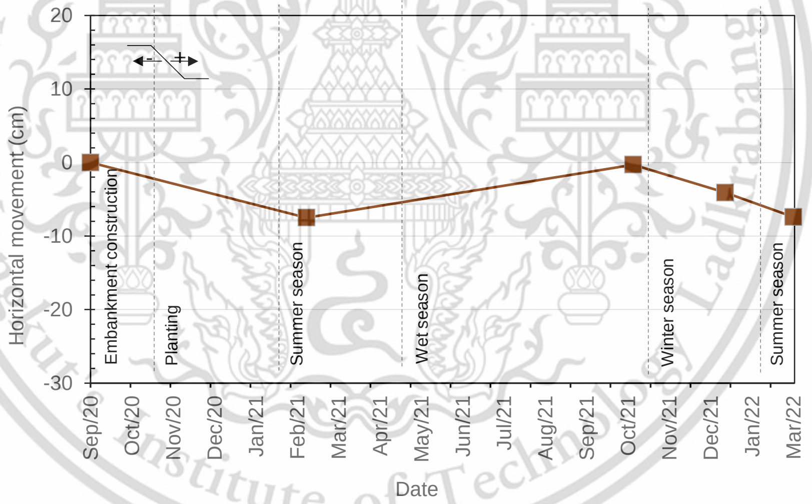

(b) x-axis displacement

Figure 69 Displacement at toe of milder zone over time.

10.3 Displacement of steeper zone

The same as milder zone, two observation point was also plotted to obtain embankment displacement in steeper zone area. The result of both vertical and horizontal displacement over time will be explained herein.

(i) Displacement at top area (Point C)

Displacement data over time at the top of steeper zone can be illustrated in Figure 70. As can be seen in Figure 70 (a), y-axis displacement at the top of steeper zone has the same trend as milder zone. The observation point consistently increased throughout the time, regarding both consolidation and seasonal behaviour. However, since having steeper slope angle, this zone resulted more significant displacement, compare to milder zone. Considering Figure 70 (a), top area displaced by around -21 cm in y-axis direction during six months after embankment construction (February 2021). It can be contributed by consolidation settlement in the first wet season and soil shrinkage during the first dry season. Moreover, during the second wet season, the settlement process was still dominated by consolidation. However, the consolidation effect was less significant in that season, resulting milder line, compared to previous year. At the end of the second wet season (November 2021), the total displacement was approximately -41 cm. Further to this, soil shrinkage dictated the embankment displacement in the second winter and summer season. By the end of second winter season in January 2022, the value of total displacement was about -45.9 cm. The shrinkage process has remained consistent during the second dry season, producing increment of settlement by around 2 cm. Therefore, final y-axis displacement at the top of embankment at the end of the second dry season was approximately -47.9 cm.

X-axis displacement at the top of steeper zone provided the same trend as milder zone as can be seen in Figure 70 (b). The direction of displacement was dictated by swelling and shrinkage process, rather than consolidation phenomenon. Regarding the figure, the observation point moved toward to the center line by the end of the first dry season in February 2021. Total x-axis displacement at that time was about -7.8 cm. It indicates that during the first wet season, the point was relatively unchanged. The combination between consolidation settlement and swelling process resulted balance condition in x-axis direction. Following this, shrinkage process in the first dry season induced soil movement in negative direction. Further to this, the x-axis displacement at this point was dominated by swelling process during the second wet season. Thus, the observation point moved away from center line of the embankment, resulting total x-axis displacement by approximately -1.8 cm. With regard to the second winter and dry season, the trend of cycle displacement was consistent. As a result, the observation point moved toward to the center line, producing total x-axis displacement by around -4.7 at the end of second winter season. In addition, the observation point reached final x-axis displacement by around -7.8 at the end of second dry season in March 2022, attributed to the shrinkage process.

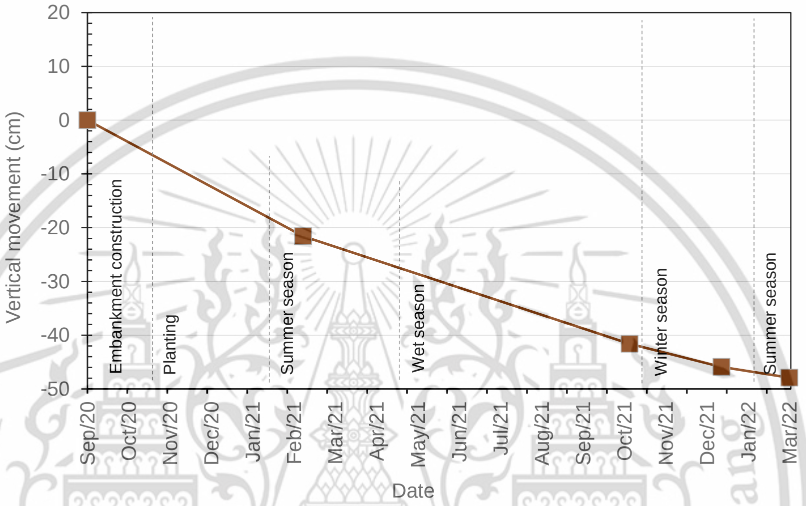

(a) y-axis displacement

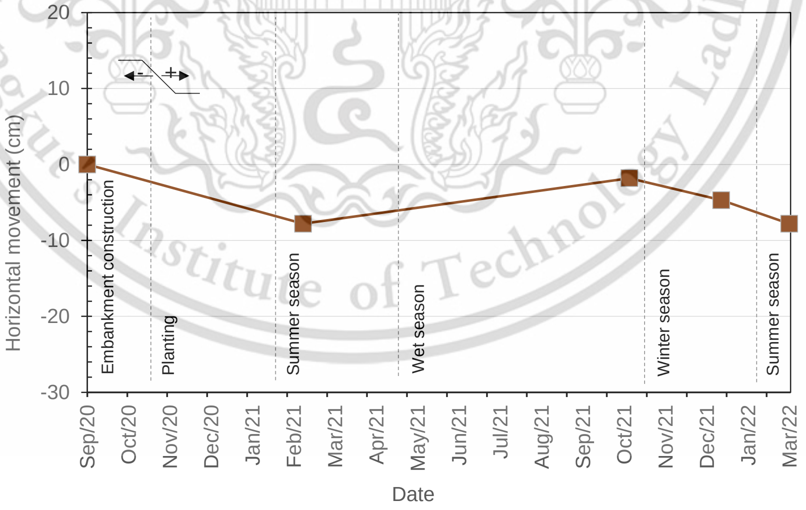

(b) x-axis displacement

Figure 70 Displacement at top of steeper zone over time.

(ii) Displacement at toe area (Point D)

The same as in milder area, the different behaviour between top and toe area in steeper area also promoted distinctive response in displacement. The trend of displacement in y-axis and x-axis direction at the toe can be plotted in Figure 71 (a) and (b) respectively. Considering Figure 71 (a), the point at toe area tended to move upward during the first six month of observation. It can be attributed to the general soil failure effect of the embankment. The entire embankment moved downward in this season due to consolidation settlement, pushing upward the toe area. Therefore, total y-axis displacement was about 14.3 cm at the end of the first dry season in February 2021. After experiencing with notable displacement, toe area moved to opposite direction during the next season. The observation points gradually moved downward at the end of the second wet season, reaching total y-axis displacement by around 7.3 cm. Due to shrinkage process in the second winter and dry season, the displacement continued in y-axis direction and attained by approximately 6.8 cm and 6.5 cm respectively.

The x-axis displacement at the toe of steeper zone can be depicted in Figure 71 (b). Regarding this figure, x-axis displacement has the same trend as y-axis displacement. It can be seen that the general failure effect also influenced in x-axis direction. As a result, the observation point moved away from centreline due to this behaviour. At the end of the first dry season in February 2021, the total x-axis displacement was approximately 5.9 cm. The trend has remained consistent until at the end of the second wet season, reaching total x-axis displacement by around 13.6 cm. At the contrary, the observation point moved toward the centreline during the second winter and dry season. It can be contributed from shrinkage process throughout this season. During the second winter season, the observation points displaced by about 4 cm to the centreline direction. Therefore, total displacement in x-axis direction was around 9.7 cm. Moreover, the direction of displacement persisted in the second dry season, attaining total x-axis displacement by approximately 6 cm.

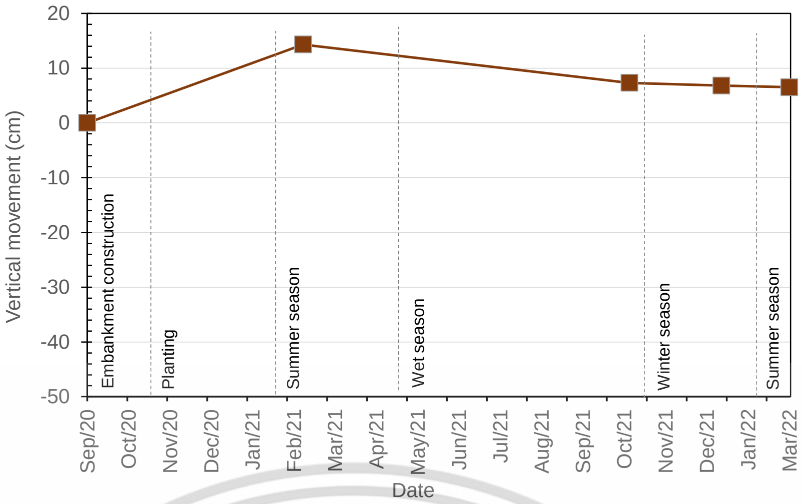

(a) y-axis displacement

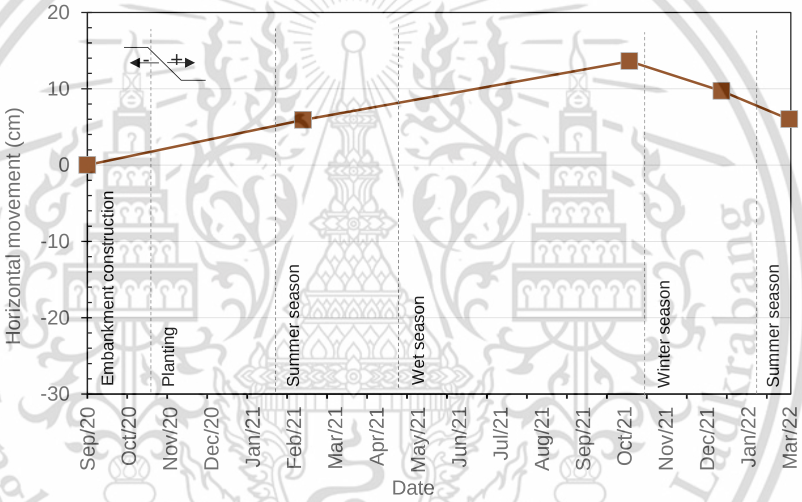

(b) x-axis displacement

Figure 71 Displacement at toe of steeper zone over time.

10.4 Comparison between milder and steeper zone

The same trend of y-axis and x-axis displacement occurred in the milder and steeper zone, especially at the top area of the embankment. In the context of y-axis direction, the displacement behaviour was dominated by consolidation settlement, resulting downward movement over the observation time. Compared to milder zone, steeper zone resulted by about 10% higher displacement in y-axis direction at the end of the observation in March 2022. It should be noted that steeper slope angle can decrease embankment stability, pertaining to the bigger failure mass (Shiferaw, 2021). Unlike y-axis direction, x-axis displacement was dictated by seasonal behaviour, producing cyclic pattern. The observation point tended to move toward the centreline during dry season, and moved away from centreline throughout the wet season. Likewise, steeper zone also promoted higher displacement in x-axis displacement. With respect to soil shrinkage during the first dry season in February 2021, observation point at steeper zone displaced in x-axis direction by about 2.5 times higher, compared to milder zone. In fact, at the end of second dry season in March 2022, the gap of x-axis displacement between those two zones increased. As a result, steeper zone resulted higher displacement in x-axis direction by approximately 4 times than that in milder zone.

Chapter 11 Numerical Simulation Result

11.1 Boundary condition

Water flux boundary condition was applied to the model to represent seasonal condition. It was calculated based on actual water infiltration and evaporation, regarding weather data. Actual water infiltration was computed by considering cracks using modified Green-Amp method (equation (114). The comparison between rainfall and actual water infiltration can be depicted in Figure 72. Figure 72 shows that actual water infiltration during wet season was less than rainfall. It indicated that the soil already reached its infiltration capacity, promoting runoff. Moreover, soil surface tend to have lower value of CIF during wet season, hindering water infiltration. On the contrary, the embankment tend to have higher water infiltration capacity during dry season with respect to lower value of PWP. As a result, all of amount of rainfall can infiltrate into the soil.

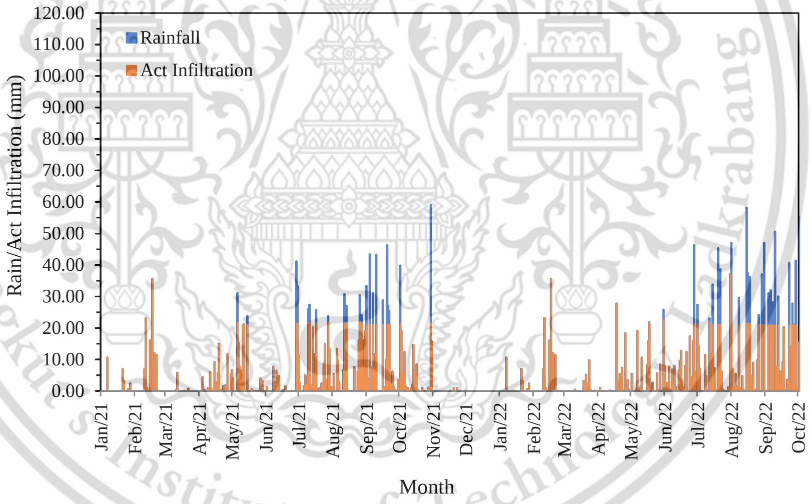

Figure 72 Comparison between rainfall and actual water infiltration.

Moreover, Penman method was employed to calculate actual evaporation. Figure 73 Illustrated the comparison between potential and actual evaporation. Figure 73 shows that actual evaporation was the same as potential evaporation during wet season. It can be addressed to the higher value of water content during rainfall season. Conversely, potential evaporation was higher than actual evaporation in dry season. It indicated that the embankment had low water content during dry season was, limiting evaporation process.

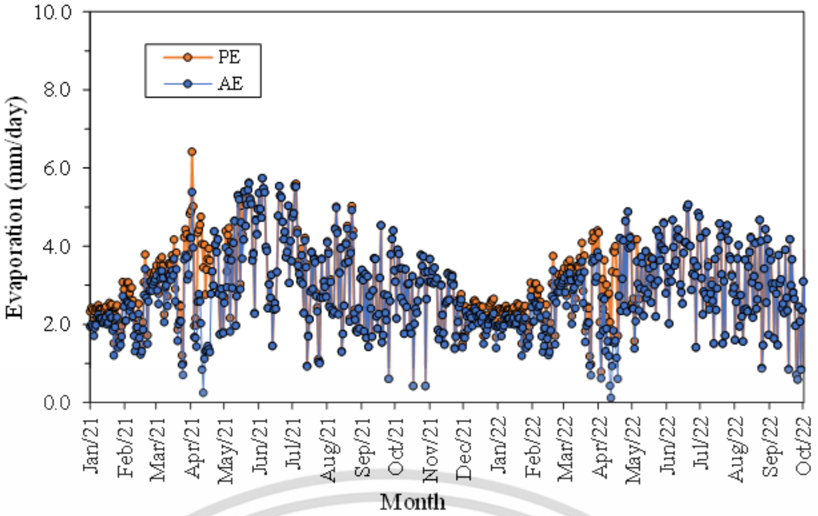

Figure 73 Comparison between potential and actual evaporation.

11.2 PWP of embankment due to Seasonal Variation

The correlation between PWP and rainfall with depth variation during 1.5 year of simulation can be depicted in Figure 74. In detail, Figure 74 (a), (b), and (c) represent the fluctuation of PWP at depth of 0.25 m, 0.5 m and 1.0 respectively. According to Figure 74, numerical simulation shows satisfied result considering coherent value compared to measurement result. Figure 74 indicates that PWP value at a shallow depth (0.25 m) more fluctuated than that at a deeper depth. Since near surface area is more influenced by soil-atmosphere interaction, VWC at the shallow depth is more fluctuated than at deeper depths. Consequently, the PWP value at shallow depth also has a wider range than at a deeper depth. During rainy season, the value of negative PWP at 0.25 m depth rose up to 200 kPa as plotted in Figure 74 (a). On the other hand, matric suction at deeper depth increased to 44 kPa and 3 kPa at depth of 0.5 m and 1 m respectively. Moreover, it can be presented that negative PWP value at shallow depth rocket more than 1000 kPa in dry season. Interestingly, negative PWP at 1.00 m depth reach higher value (643 kPa) than that at 0.50 m depth (451 kPa) as can be shown in Figure 74 (b) and Figure 74 (c). It should be noted that the occasionally rainfall during dry period influence only limited depth, thus soil water content at deeper depth still continued to decrease, leading more higher suction.

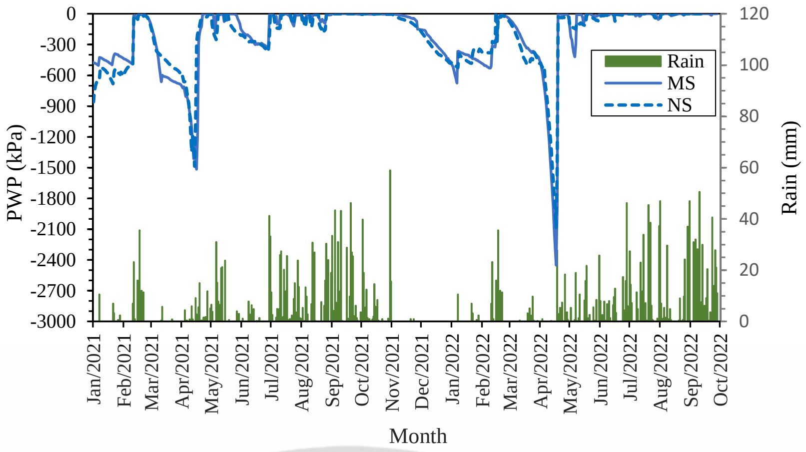

(a) Depth of 0.25 m

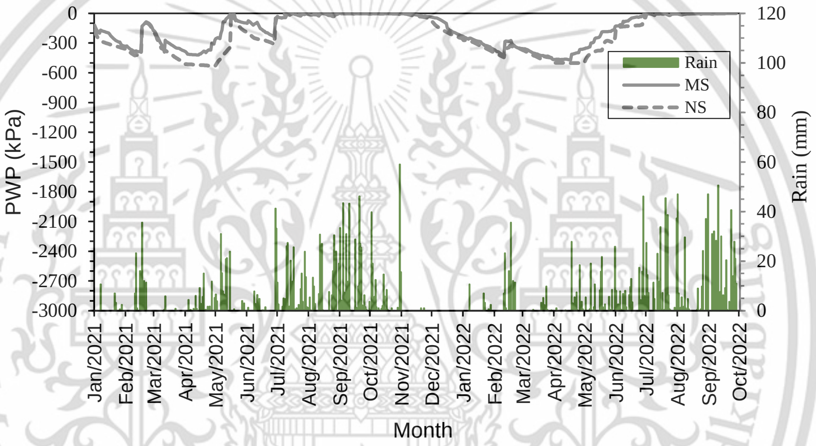

(b) Depth of 0.50 m

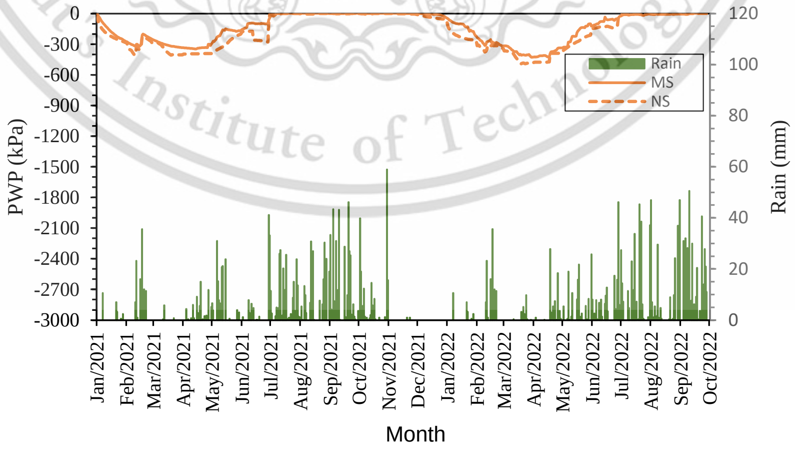

(c) Depth of 1.00 m

Figure 74 PWP over the time with depth variation based on simulation result.

11.3 Deformation of embankment

11.3.1 Deformation of embankment due to consolidation and seasonal variation

Regarding numerical simulation, embankment deformation contour in vertical direction over the time can be illustrated in Figure 75. Observation point at the top of the embankment (point A) was set to investigate embankment deformation under seasonal variation. Accordingly, vertical displacement of embankment at the observation point, based on numerical simulation and field measurement can be depicted in Figure 76. In general, numerical simulation shows the same trend deformation result compared to field measurement data. As the embankment is recently-built construction, the deformation was dominated by primary consolidation settlement rather than seasonal deformation. The steepest line occurred in the first three month after construction process, indicating the most pronounced deformation pertaining to combination between immediate and consolidation settlement. During this period of time, the value of embankment deformation attained up to 21 cm. This value was 20% higher, compared to field monitoring data. Significant deformation had remained during the first dry season (January – April 2021), reaching 30 cm with respect to soil shrinkage. It should be noted that numerical simulation resulted 30% higher of displacement than field data during this season. This discrepancy was attributed to the material model which was assumed from another soil sample. Further to this, Figure 76 shows that during wet period, the graph tends to be milder considering swelling process. During 5 months of wet period, starting from May 2021 to October 2021, the increment deformation was only around 5 cm. By the end of the simulation in March 22, total deformation of the embankment was around 37 cm. Moreover, it can be reported that total deformation of the embankment is around 42 cm based on field measurement data. Regarding the result, it can be suggested that testing of soil mechanical properties should be included in the future study so the accurate and detail prediction can be generated.

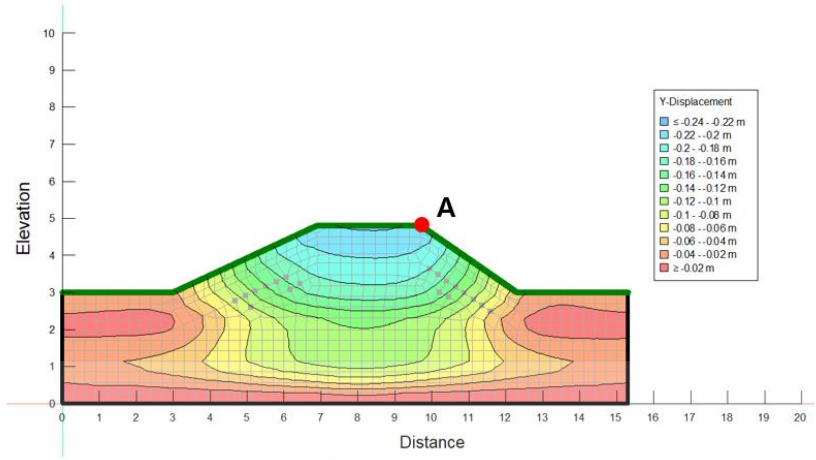

(a) Y-Axis displacement contour in January 2021

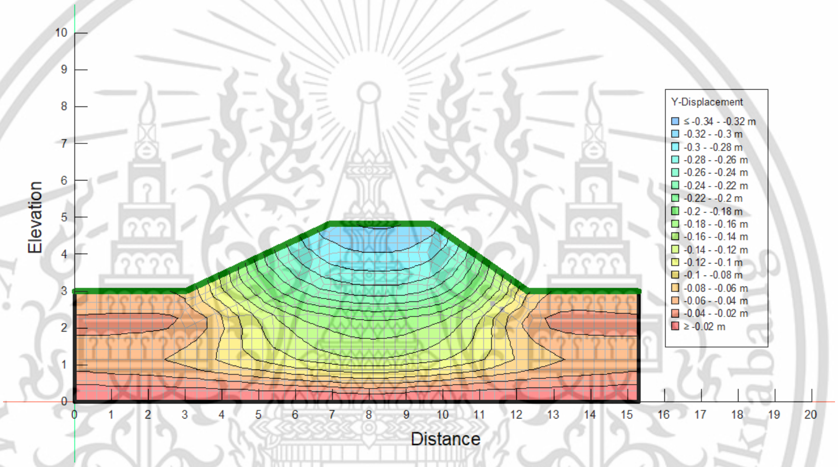

(b) Y-Axis displacement contour in April 2021

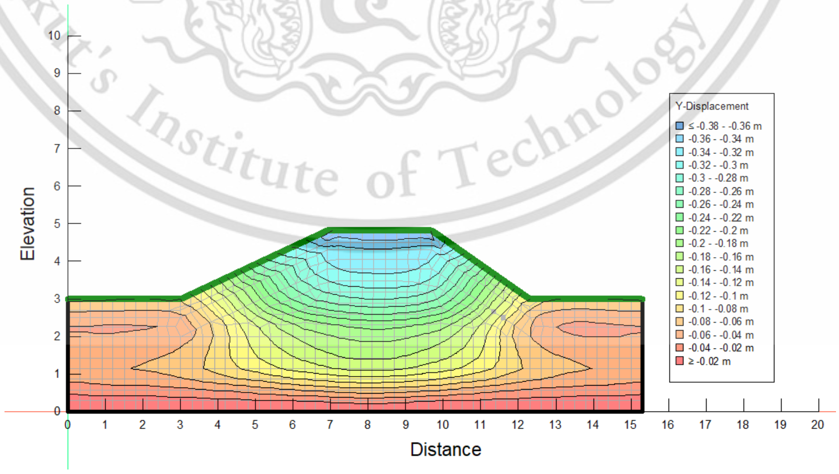

(c) Y-axis displacement contour in March 2022

Figure 75 Y-axis embankment deformation contour over the time.

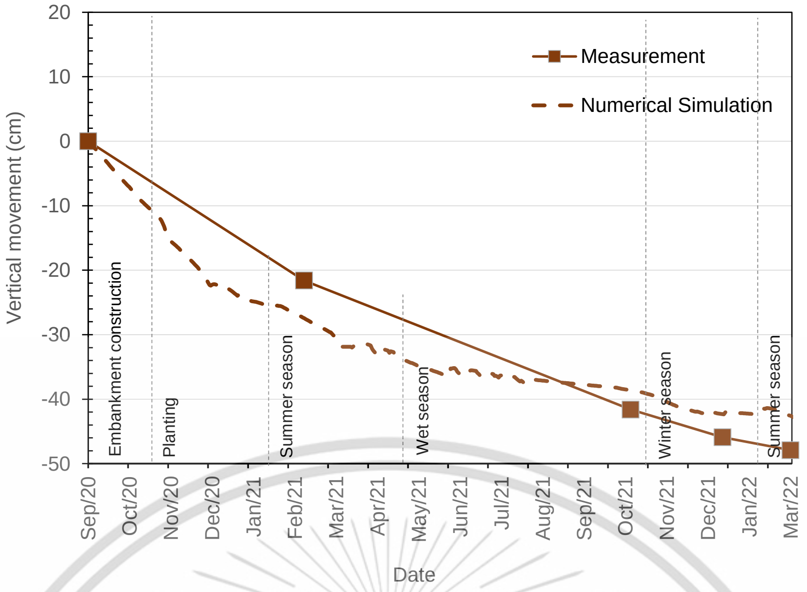

Figure 76 Y-axis displacement of the embankment over the time.

Likewise, embankment displacement contour in x-axis direction over the time can be illustrated in Figure 77. Further to this, horizontal displacement of embankment at the observation point, based on numerical simulation and field measurement can be depicted in Figure 78. As can be seen in Figure 78, there are also the same trend between numerical simulation and filed measurement result in term of x-axis displacement. Broadly, Figure 78 shows the embankment move close to the center line with respect to the negative value of the displacement. This is can be contributed to the shrinkage of the embankment. X-axis displacement reached maximum value at the end of the first dry season in April 2021 (6 cm). However, the embankment significantly moved away from center line at the beginning of the wet season. It can be indicated from the value of x-axis displacement in May 2021 (2 cm). Following this, horizontal displacement was relatively unchanged during wet season. It can also be seen from Figure 78 that the embankment tends move close to the center line during second dry season. Nevertheless, the maximum displacement occurred during second dry season was less than first dry season.

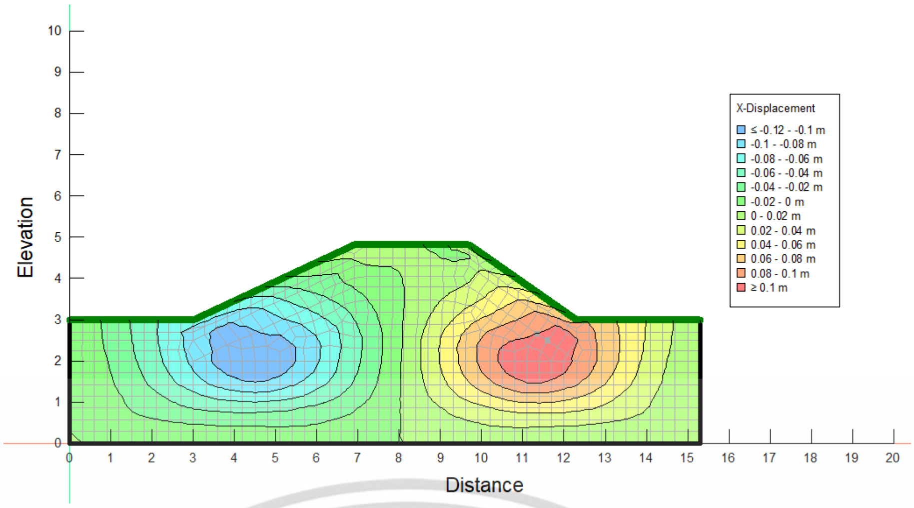

(a) X-axis displacement contour in January 2021

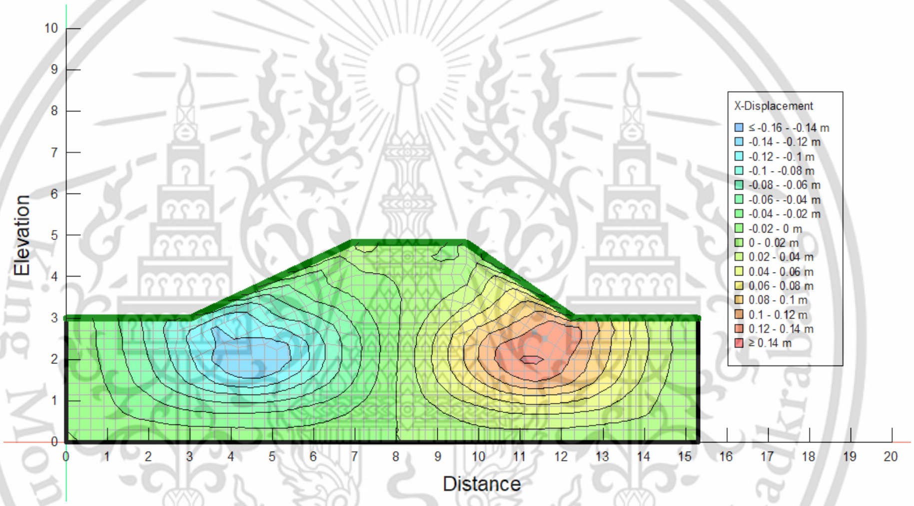

(b) X-axis displacement contour in April 2021

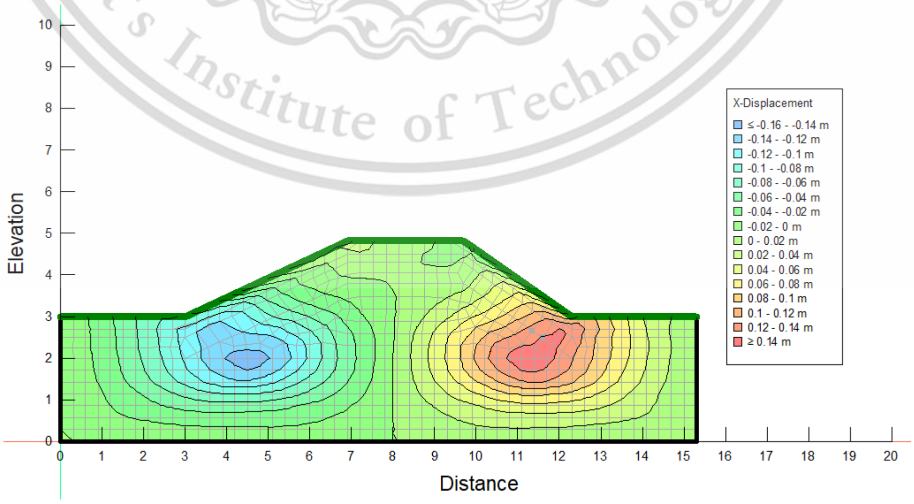

(c) X-axis displacement contour in March 2022

Figure 77 X-axis embankment deformation contour over the time.

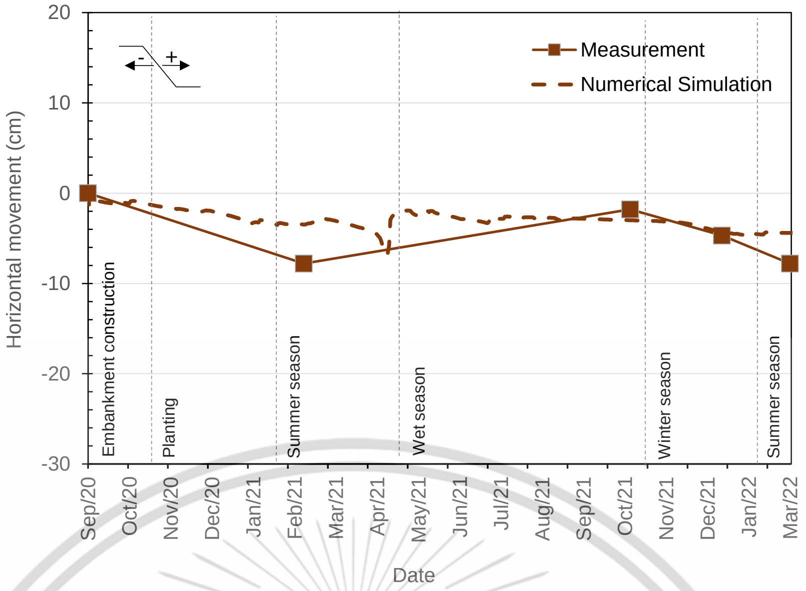

Figure 78 X-axis displacement of the embankment over the time.

11.3.2 Deformation of embankment due to seasonal variation

In this simulation, the effect of consolidation settlement was neglected to observe seasonal effect on the embankment deformation. Y-axis displacement contour based on the simulation can be depicted in Figure 79. Moreover, vertical displacement in observation point (Point A) over time can be illustrated in Figure 80. It can be reported from Figure 80 that the embankment tended to move downward during winter, reaching the value of -6.78 cm in January 2021. It can be attributed to the soil shrinkage of the embankment. With the increasing in PWP in February 2021, the embankment displaced upward, attaining by approximately -6.50 cm. During summer 2021, the embankment experienced with the lowest PWP, promoting negative vertical displacement by about -8.5 cm in April 2021. Moreover, while the value of PWP dramatically increase to near 0 kPa, the embankment swelled significantly, producing upward movement by around 1 cm. It can be clearly seen from Figure 80 that the vertical displacement of the embankment significantly influences by wetting and drying cycle, triggering shrinkage and swelling process.

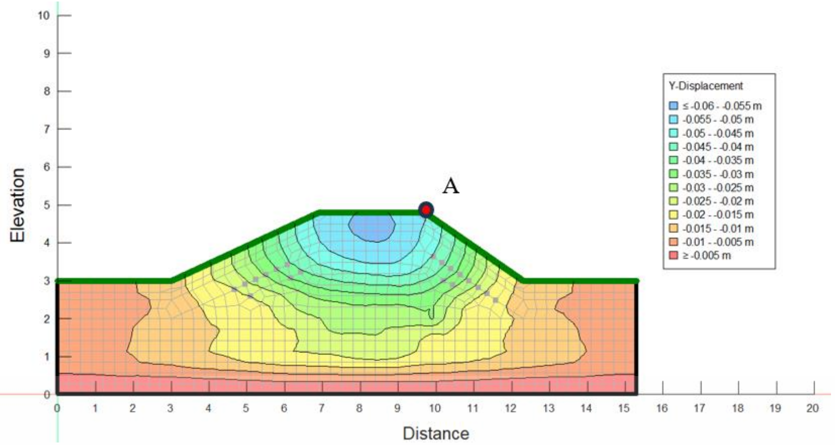

(a) Y-Axis displacement contour in January 2021

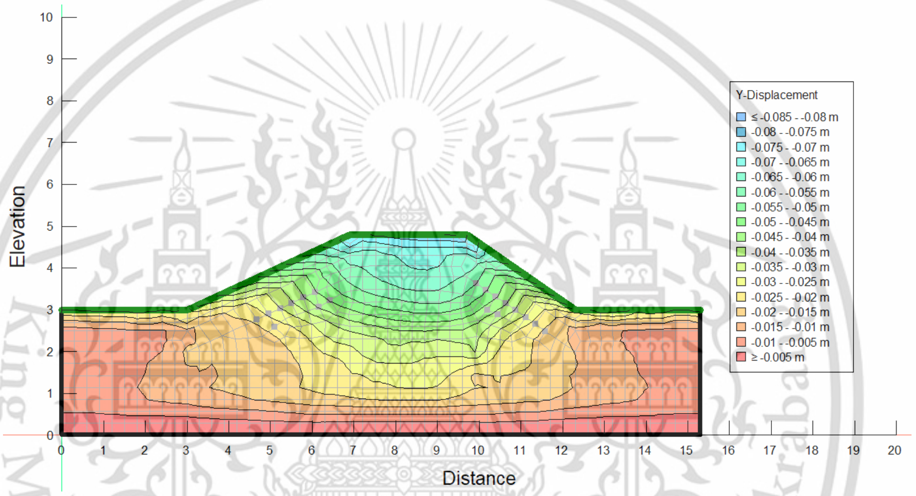

(b) Y-Axis displacement contour in April 2021

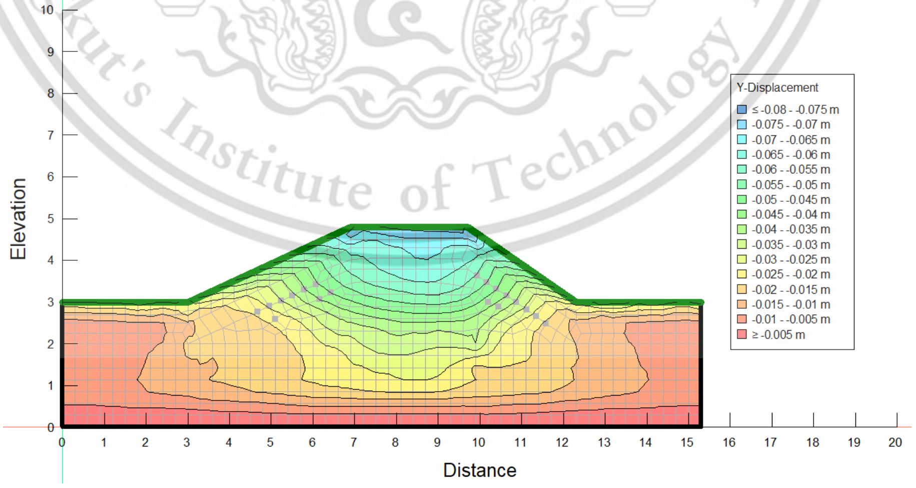

(c) Y-Axis displacement contour in March 2022

Figure 79 Y-axis embankment deformation contour due to seasonal variation.

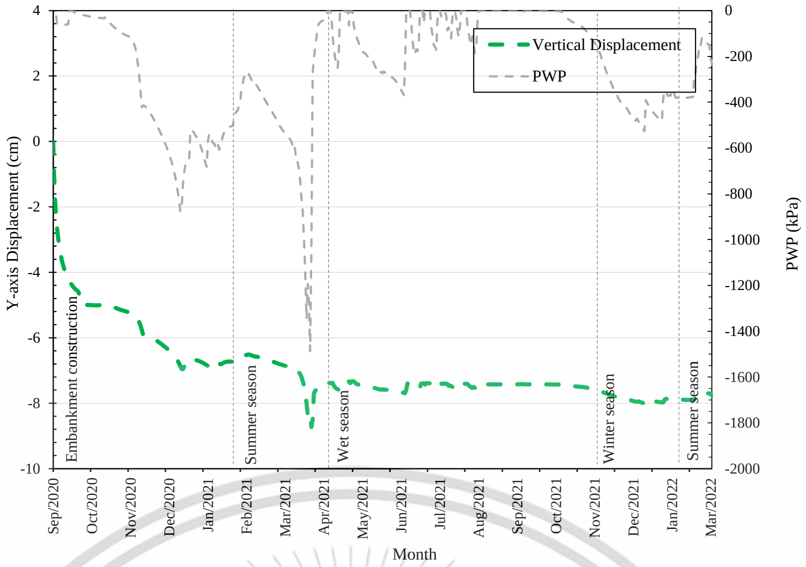

Figure 80 Y-axis displacement of the embankment due to seasonal variation.

11.4 FOS of embankment

Figure 81 shows FOS of the embankment to represent stability condition. At the commencement of the construction, the embankment was relatively stable considering the value of FOS (1.40) as can be seen in Figure 81. At the end of the wet season (January 2021), the value of FOS gently decreased with respect to the increasing of PWP (FOS 1.35). As the PWP was significantly decrease during the summer season, the value of FOS also sharpy increase up to 2.2. However, remarkable decreasing of embankment stability occurred at the beginning of wet season as the FOS value was around 1.1. This phenomenon was closely related to the noticeable increasing of PWP due to the rain infiltration, hence reduced effective soil strength significantly. With respect to consolidation process, FOS was slightly increased during 5 months of the second wet season.

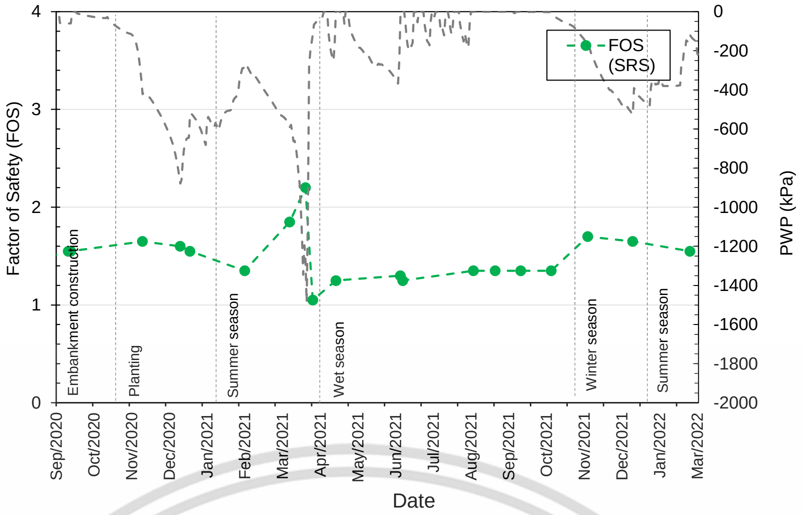

Figure 81 Factor of Safety of the embankment over the time.

Chapter 12 Parametric Study

To investigate embankment behaviour in association with future extreme climate, parametric study was conducted in this study. Accordingly, several analyses such as extreme future weather data, future crack condition and future initial condition were calculated prior to the simulation.

12.1 Analysis Procedure

The analysis procedure used in this parametric was determined based on back analysis. Since the embankment was subjected with weather condition during 2 years (2020 – 2022) in back analysis, the same duration will also be applied in this parametric study. Regarding climate index calculation, the embankment will experience with extreme dry and wet condition in 2044 and 2097 respectively. Accordingly, the simulation will be started in September 2043 until September 2045 to observe embankment behaviour during extreme dry condition. Following this, to investigate the embankment behaviour during extreme wet condition, numerical simulation will be performed from September 2096 to September 2098. Furthermore, embankment response in association with future extreme climate was analyzed, compared to current climate condition.

12.2 Hydraulic Parameter

In the context of parametric study, further SRWC prediction was required in the analysis in association with future crack condition. Further to this, Dual VG parameter considering future CIF can be predicted based on current Dual VG parameter and CIF data using interpolation technique. Note that extreme dry condition will promote future CIF up to 20% regarding prediction analysis result. Accordingly, predicted SWRC referring to this CIF value can be calculated as depicted in Figure 82. It can be seen in Figure 82 that saturated VWC rose by around 3% because of the increasing in CIF during extreme climate condition. Moreover, the increasing in CIF rose weighting factor for fracture portion, decreasing the first AEV by about 0.99 kPa. However, the alteration of CIF did not transform intact portion SWRC significantly. It can be indicated from the value of a_2, n_2 and m_2 which governed the intact portion behaviour.

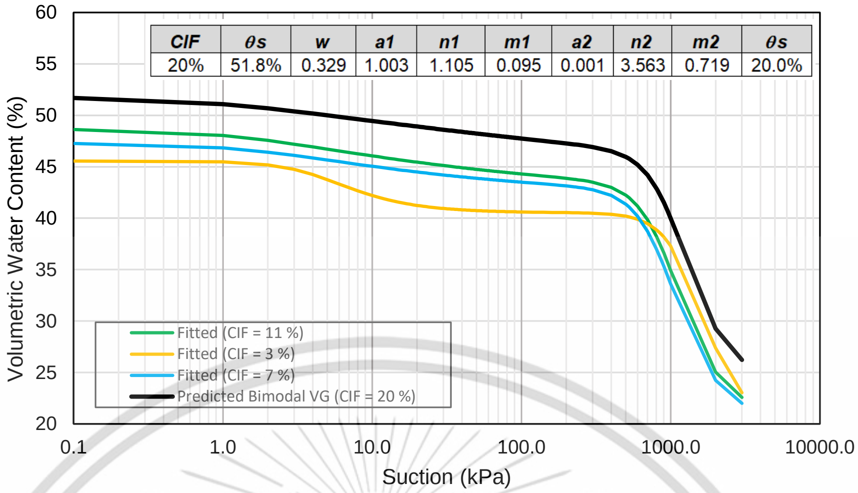

Figure 82 Predicted SWRC based on CIF = 20%.

12.3 Initial Condition

Initial condition should be set prior to transient analysis in this simulation using Seep/W. Since the future extreme climate will be analyzed in this parametric study, associated initial condition should be applied, regarding the year of the analysis. To do so, future initial PWP was predicted using the correlation between current AWB and PWP as shown in Figure 83. In the context of extreme dry analysis, initial PWP was set in September 2043 when the value of AWB was 184.4 mm. Accordingly, the value of initial PWP for extreme wet condition was around -10.9, based on Figure 83. Likewise, initial condition of future wet simulation was determined in September 2096 when AWB value was about 192.5 mm. Regarding Figure 83 the value of PWP in September 2096 can be determined to be around -9.37 kPa. Following this, the value of initial PWP will be imposed to the simulation.

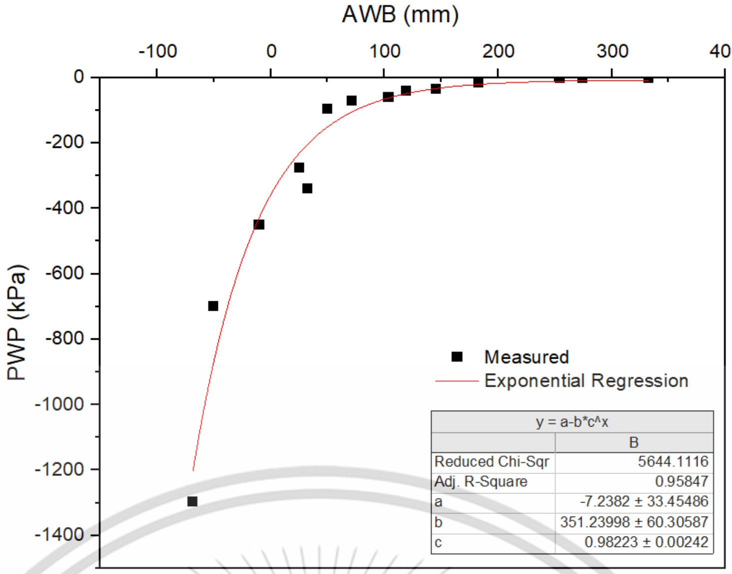

Figure 83 Correlation between AWB and PWP.

12.4 Boundary Condition

The same as back analysis, daily water flux data was applied in the parametric study as hydraulic boundary condition. To do so, future rainfall dan evaporation were employed to calculate water flux with respect to the duration of the analysis. Future monthly rainfall data was converted to daily data using current trend weather condition. The trend of current weather data was calculated by averaging daily rainfall data throughout two years of observation. Daily rainfall data during future extreme dry and wet condition can be depicted in Figure 84. It can be seen in Figure 84 that the embankment will experience with wet season from April to November, whereas dry season will occur from December to March. Regarding Figure 84 (a), maximal rainfall intensity will attain by about 60 mm during extreme dry season which occurred in October 2043. In the context of extreme wet condition, maximum daily rainfall intensity will reach up to around 100 mm in May 2097. Moreover, future extreme wet and drought will promote average daily rainfall intensity by around 5.61 and 4.28 mm respectively.

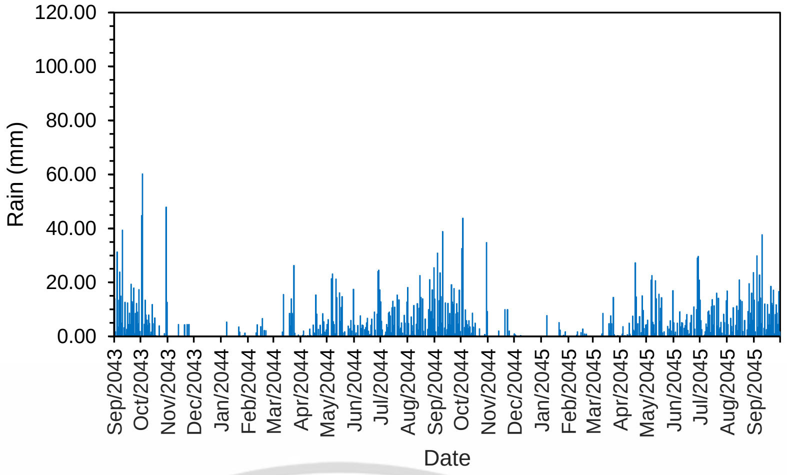

(a) Extreme dry

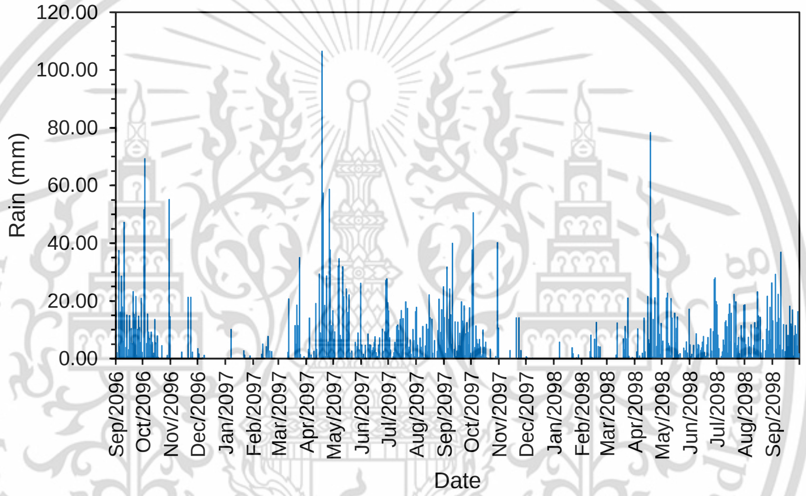

(b) Extreme wet

Figure 84 Future rainfall under extreme condition.

Likewise, future daily evaporation data was calculated based on future monthly rainfall, considering the trend of current daily evaporation. It should be noted that the trend of daily evaporation was derived from two years of observation data. Figure 85 shows daily evaporation during future extreme wet and drought condition. Further to this, future water flux will be determined based on future daily rainfall and evaporation. Considering Figure 85 (a), it can be stated that maximum daily evaporation during extreme dry will reach by approximately 8.29 mm in August 2044. Moreover, maximum daily evaporation during extreme wet will attain by around 9.03 mm in August 2097.

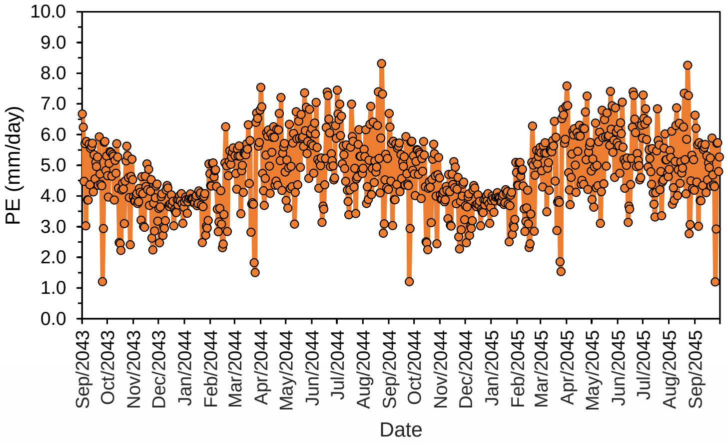

(a) Extreme dry

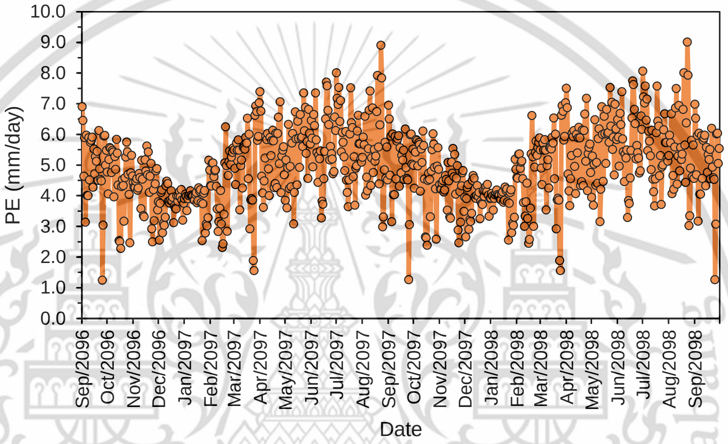

(b) Extreme wet

Figure 85 Future evaporation under extreme condition.

12.5 Result

12.5.1 PWP due to Future Extreme Condition

PWP response due to future extreme dry condition can be depicted in Figure 86. It can be generally reported that the minimum value of PWP at the depth of 0.25 m during future extreme drought period was around 4.000 kPa due to the minimum value of rainfall intensity. It increased by about 400 %, compared to extreme wet condition. Moreover, minimum PWP at 0.5 m and 1 m depth attained by approximately -3.200 kPa and 800 kPa respectively. Interestingly, the value of PWP jump to around 0 kPa during early rainfall season for each variation of depth. It was associated with the higher value of CIF at the end of dry season, triggering water infiltration to the deeper depth. It should be noted that the higher ranges of both water content and PWP cyclic have a significant impact on infrastructure slope serviceability, such as triggering progressive failure (Anderson and Kneale, 1980; Smethurst et al., 2006; Glendinning et al., 2014).

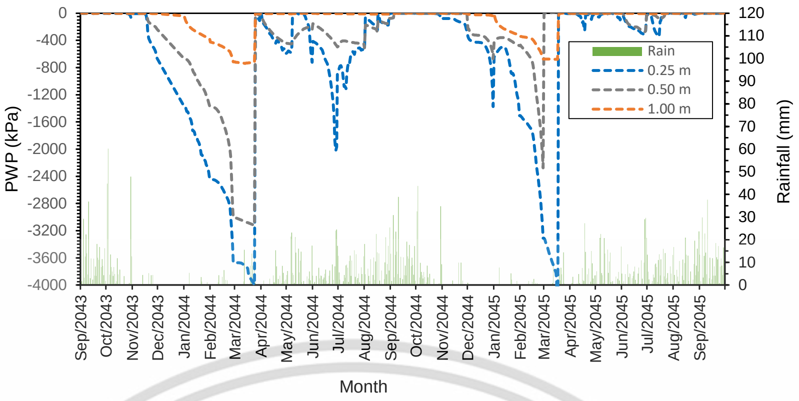

Figure 86 PWP over the time during extreme dry condition.

Figure 87 shows PWP response due to future extreme wet condition in bare area. With respect to frequent rainfall during future extreme wet condition, the embankment was dominated by lower PWP value. The same as back analysis, PWP behaved more fluctuated at near surface area, compared to deeper depth. It can be seen from Figure 87 that PWP at the depth of 0.25 m decreased up to -2000 kPa during dry season. Moreover, the PWP reached minimum value by around -695 kPa and -560 kPa at the depth of 0.5 m and 1.0 m respectively. It can be attributed to more dominant soil-atmosphere interaction in the near surface area. Further to this, the average of PWP during rainy season (May – November) at the depth of 0.25 m was approximately -11 kPa. Meanwhile, average PWP at 0.5 m and 1 m depth were -4.3 kPa and 2.2 kPa respectively.

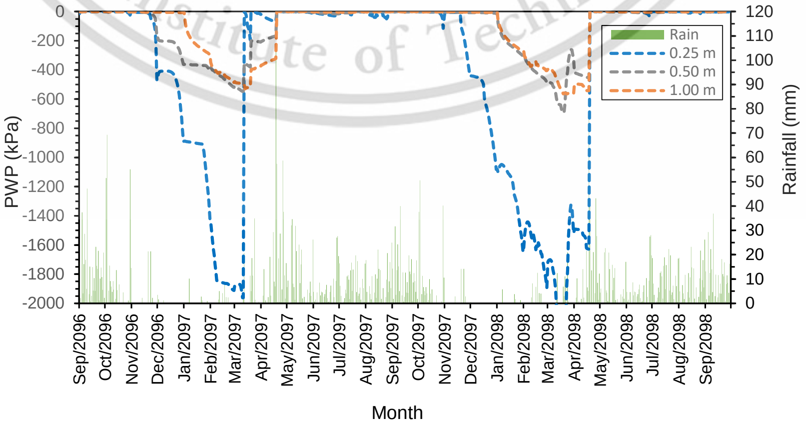

Figure 87 PWP over the time during extreme wet condition.

12.5.2 Deformation due to Future Extreme Condition

Following PWP analysis, embankment deformation analysis has been performed with respect to extreme climate condition. To compare embankment deformation between current and future extreme climate condition, the same observation point was set in the parametric study. As mentioned in the previous section, observation point was located in top area of the embankment. The example of y-axis displacement contour during extreme wet climate condition can be illustrated in Figure 88. Moreover, y-axis displacement contour during extreme dry climate condition can be illustrated in Figure 89.

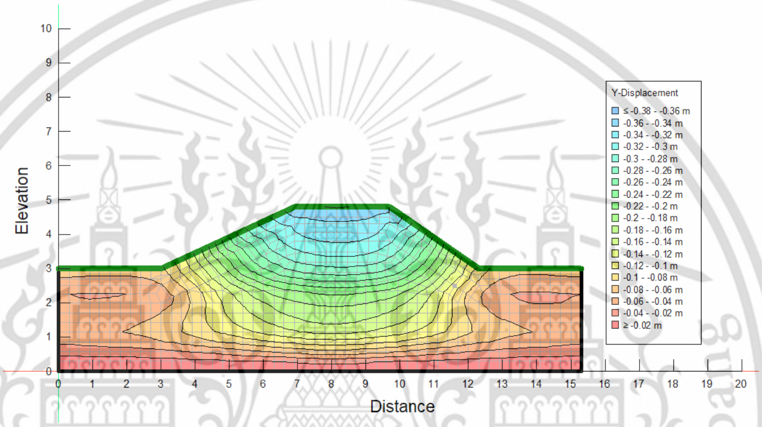

(a) January 2044

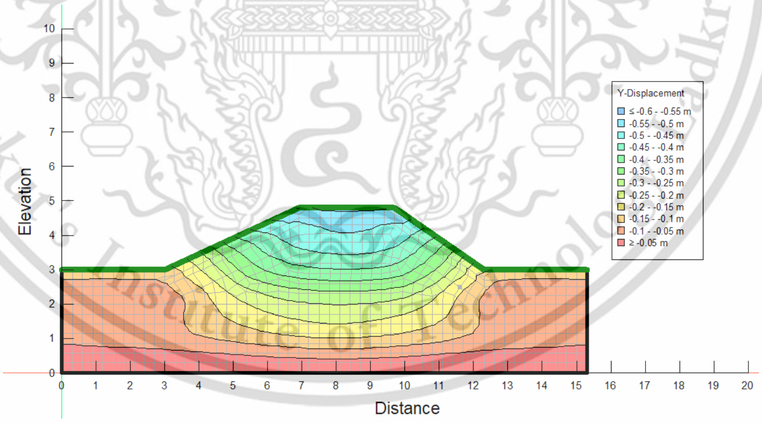

(b) March 2045

Figure 88 The example of y-axis displacement contour during extreme dry.

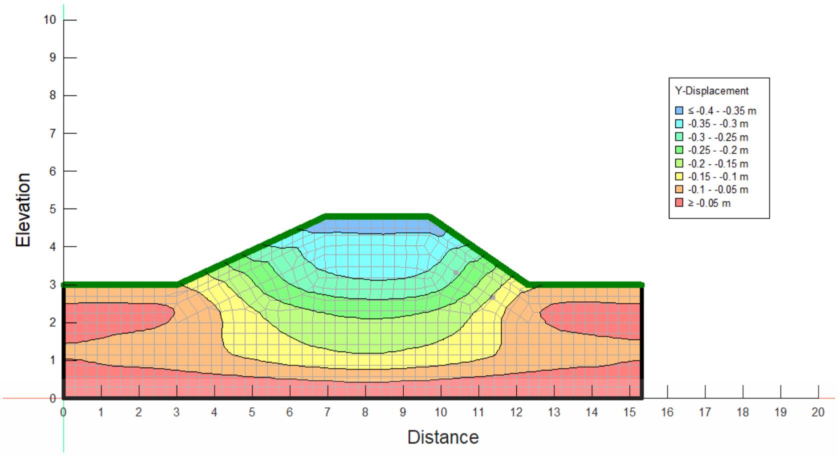

(a) January 2097

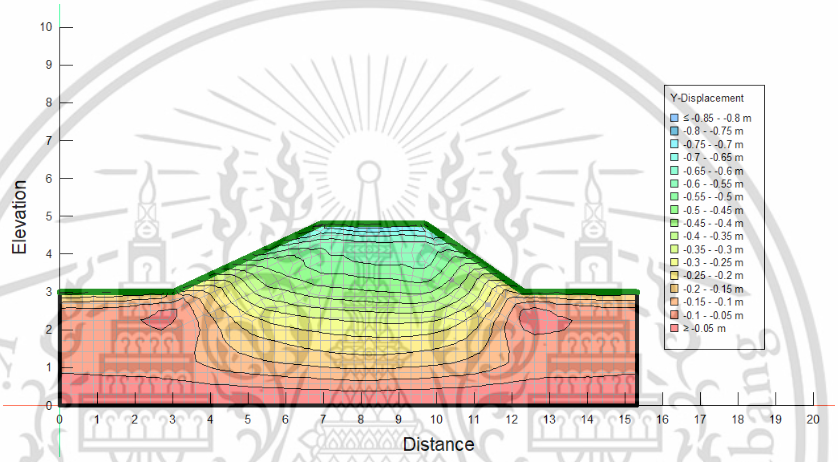

(b) March 2098

Figure 89 The example of y-axis displacement contour during extreme wet.

The comparison of y-axis displacement of embankment due to extreme wet and dry condition can be seen in Figure 90. Based on Figure 90 shows that both extreme wet and dry climate resulted higher y-axis displacement at the end of the observation, compared to current climate condition. According to Figure 90, extreme wet and drought condition produced total displacement by around 49 cm and 57 cm respectively. It can be attributed to the modest rainfall intensity during dry season for both of extreme climate condition. Therefore, embankment experience with notable shrinkage, resulting significant y-axis displacement. However, embankment tended to move upward during rainy season with respect to soil swelling. As a result of swelling process, extreme wet condition produced lower y-axis displacement at the end of second rainy season (39.5 cm), compared to current climate condition (41.3 cm). The higher value of rainfall intensity during extreme wet condition was responsible for this phenomenon. Even though the embankment also swelled during rainy season under extreme drought condition, the total y-axis displacement was still higher (44.9 cm), rather than current climate condition.

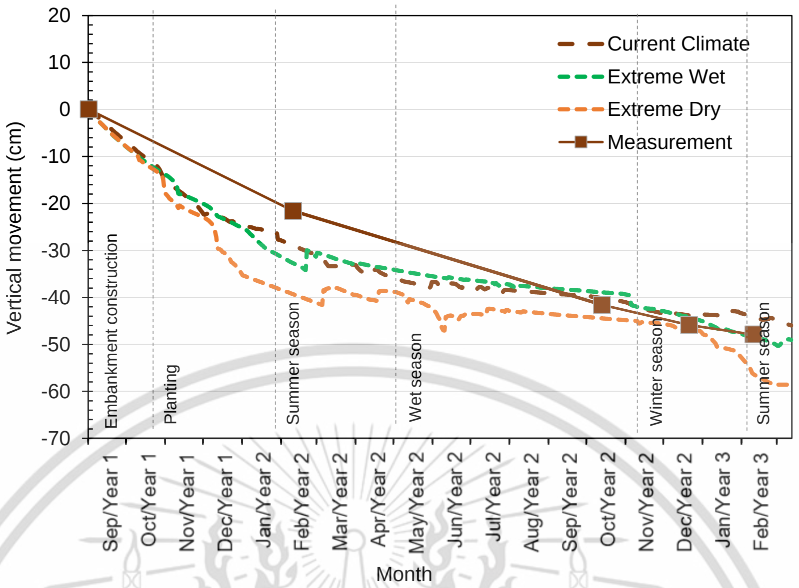

Figure 90 Comparison of Y-axis displacement.

Following y-axis displacement, X-axis displacement has also been observed in this study. The example of displacement contour along X-axis direction due extreme wet and dry condition can be seen in Figure 91 and Figure 92 respectively.

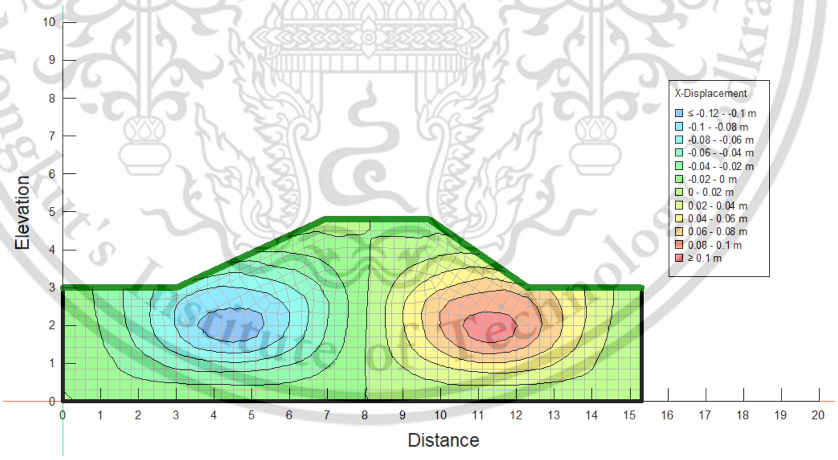

(a) January 2044

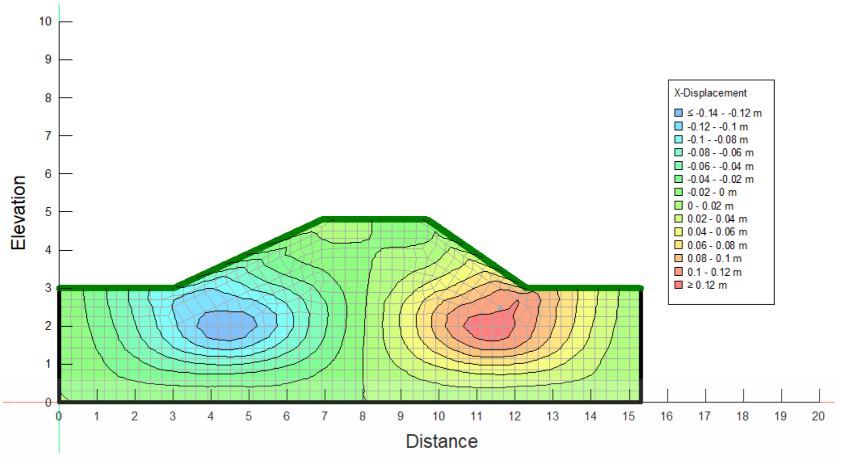

(b) March 2045

Figure 91 The example of x-axis displacement contour during extreme dry.

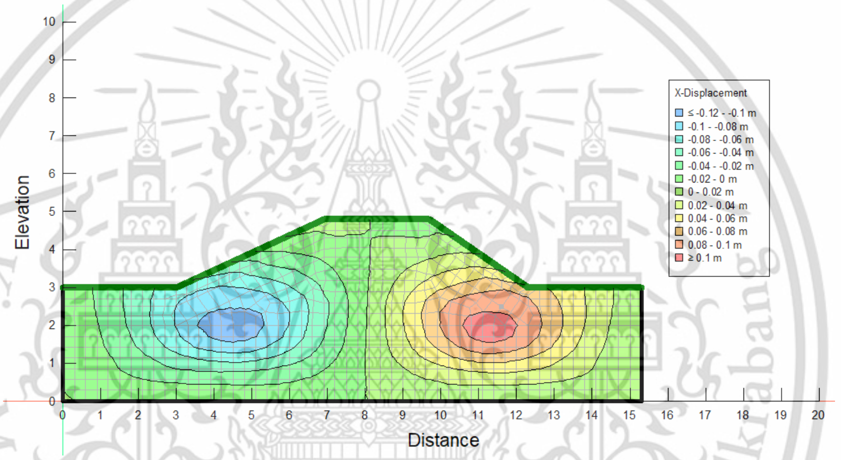

(a) January 2097

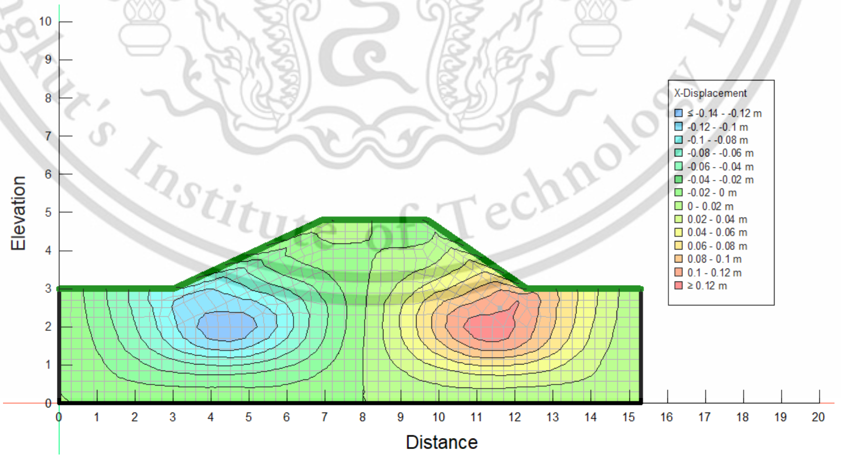

(b) March 2098

Figure 92 The example of x-axis displacement contour during extreme wet.

The comparison of X-axis displacement between future extreme wet and drought climate can be illustrated in Figure 93. It can be seen from Figure 93 that both extreme wet and dry climate promoted the same trend of X-axis displacement.

The embankment tended to move outward during dry season and indicated to move inward in wet season. However, extreme wet and drought condition, resulted noticeable gap of X-axis displacement. At the end of the first dry season, extreme wet condition produced X-axis displacement by approximately 3.5 cm, while extreme dry condition triggered X-axis displacement by about 10.4 cm. Moreover, owing to swelling process during rainy season, the embankment moved inward by around 3 cm and 4 cm during extreme wet and drought climate respectively.

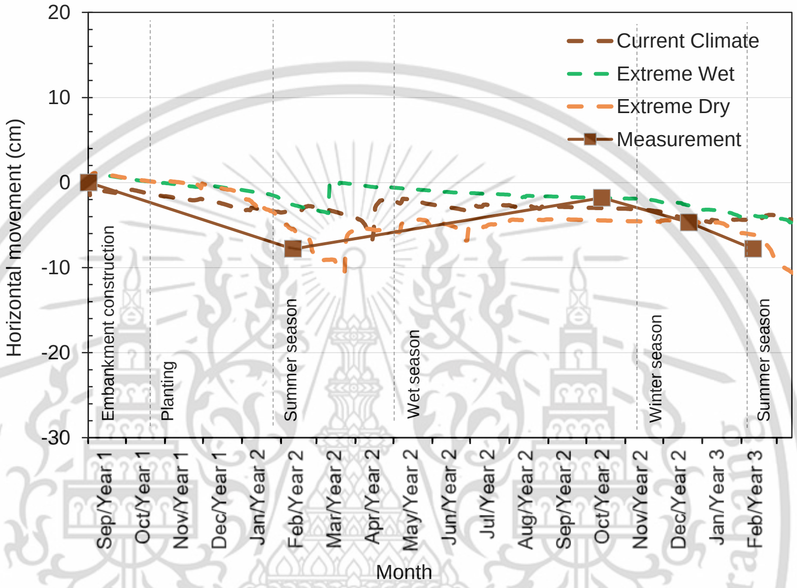

Figure 93 Comparison of X-axis displacement.

12.5.3 Factor of safety (FOS) due to Future Extreme Condition

In term of stability analysis, the value of factor of safety (FOS) is essential. FOS analysis because of extreme wet and drought condition have also been conducted along with deformation analysis. As shown in Figure 94, the value FOS during extreme dry climate was more fluctuated, rather than extreme wet condition, attributed to the PWP value. As the PWP decreased to minimum value at the end of dry season, the value of FOS increased significantly (2.3). On the contrary, the FOS plumed to the value of 1.0 at the beginning of rainy season. It can also be seen in Figure 94 that FOS was still fluctuated even in the wet season due to the lower rainfall intensity. Regarding FOS value, it can be reported that the embankment was more stable during extreme drought, compared to extreme wet condition. However, the fluctuation of PWP will trigger serviceability problem to the embankment. Moreover, the example of shear strain contour during extreme dry condition can be illustrated in Figure 95.

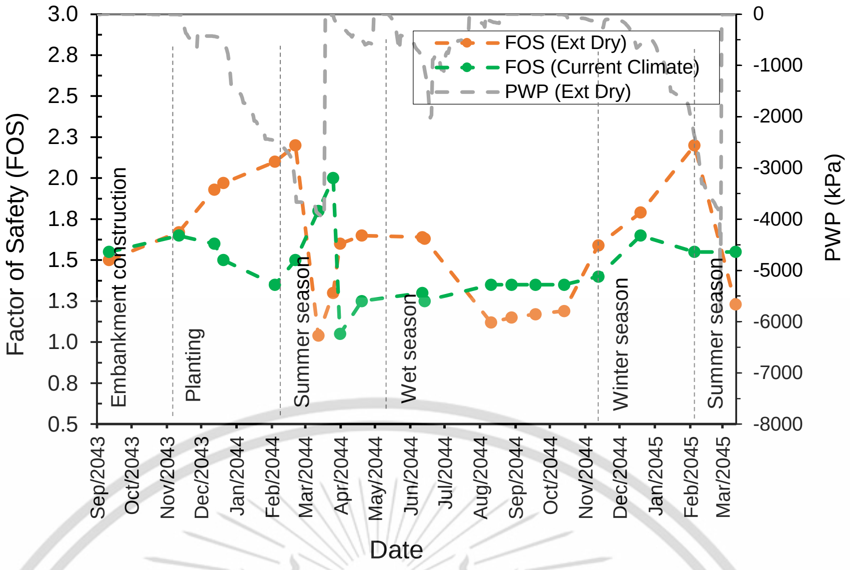

Figure 94 FOS due to extreme dry condition.

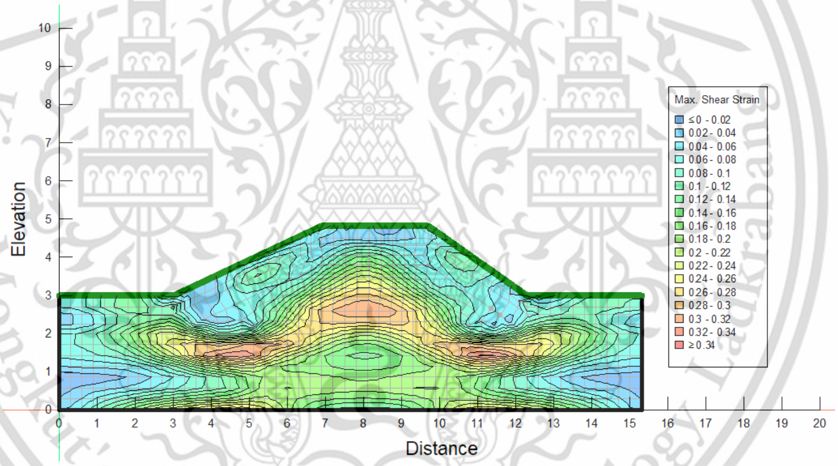

Figure 95 The example of shear strain contour during extreme dry condition.

Figure 96 shows the fluctuation of FOS over time due to extreme wet climate at bare area. Further to this, the example of shear strain contour during extreme climate can be illustrated in Figure 97. Regarding Figure 96, FOS increased as the decreasing of PWP, reaching maximal value by around 1.9 at the end of the first dry season. However, that value dropped by approximately 0.9 at the early of wet season, promoting unstable condition. It can be contributed to the higher value of rainfall intensity and CIF, triggering deeper infiltration depth. During wet season, the embankment experienced with low value of FOS with respect of higher value shear stress as well as lower shear strength magnitude. It is substantiated that extreme wet condition produced significant impact to embankment stability, requiring meticulous consideration.

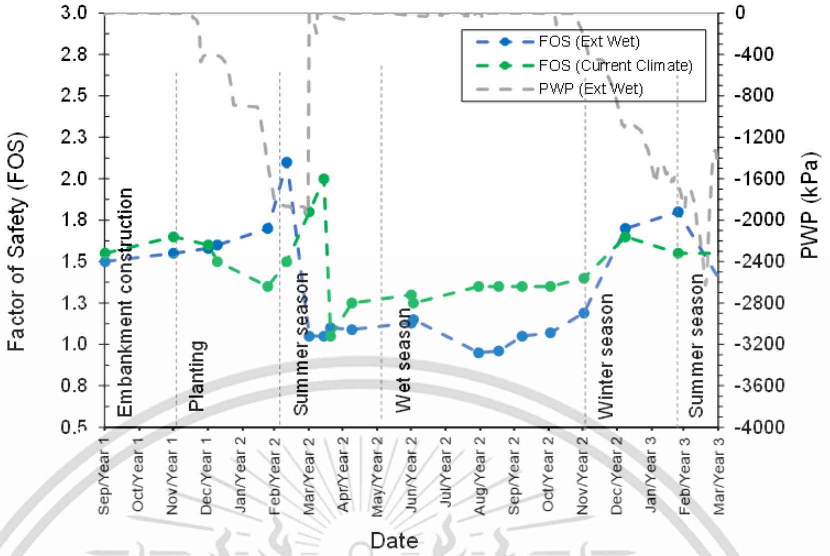

Figure 96 FOS due to extreme wet condition.

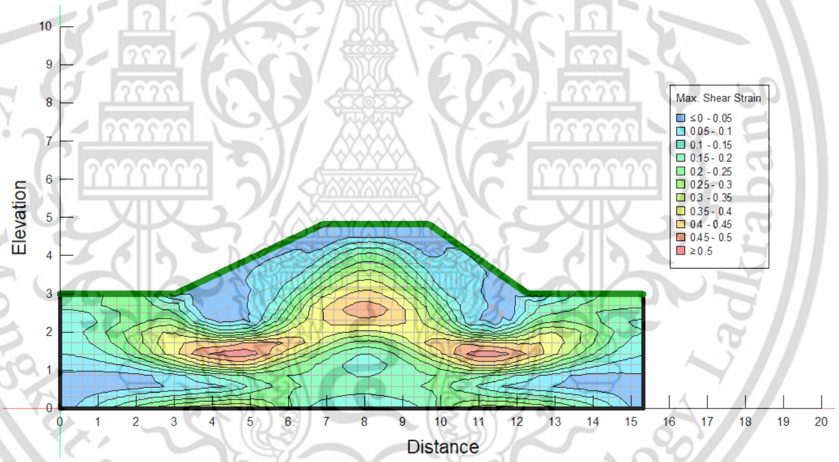

Figure 97 example of shear strain contour during extreme wet condition.

Chapter 13 The Use of Biochar to Control Water Infiltration

Considering the research result, it substantiated that water infiltration should take responsibility for stability and serviceability problem in embankment. Therefore, controlling water infiltration is essential in geotechnical structure. Preliminary study to maintain water infiltration has been performed in this study. Accordingly, the application of biochar as an alternative material to control water infiltration, especially under extreme climate condition will be analyzed. Numerical simulation result has been conducted to observe the behaviour of water infiltration of biochar-amended soil.

13.1 Introduction

Water infiltration and evaporation are the main factors that should be taken into account in embankment stability and serviceability analysis. It is widely-known that water infiltration can cause stability issues in numerous earthworks, including embankment and cut fill (Fredlund and Rahardjo, 1993; Ranjan and Rao, 2000; Briggs et al., 2019). It may reduce soil strength as a result of the increase in pore water pressure (PWP), promoting slope instability (Briggs et al., 2013; Lees et al., 2013; Apriyono et al., 2023). On the other hand, the cycle of water infiltration and evaporation during seasonal variation can lead the fluctuation of PWP. The higher range of PWP cyclic have a significant impact on slope serviceability such as triggering progressive failure (Leroueil, 2001; Smethurst et al., 2006; Glendinning et al., 2014). Further to this, extreme climate as a result of climate change is undeniable and will exacerbate stability and serviceability issue with regard to higher value of water infiltration and evaporation (Albright et al., 2006; Shaikh et al., 2019). Zeng et al. (2020) and Cheng et al. (2021) stated that prolonged drought can increase water infiltration rate due to the attendance of the crack. Likewise, evaporation can also rise during extreme drought condition, attributing to the higher value of air temperature and the expansion of the crack (Cui et al., 2014; Song and Cui, 2020). Yet, according to Kuhn and Zornberg (2006), cracking might treble the evaporation rate compared to initially compacted soil with respect to the evaporative surface increases from a one-dimensional to a three-dimensional design. Regarding the aforementioned issues, controlling water infiltration and evaporation is crucial to prevent earthworks stability problem.

Biochar, derived from biomass (such as peanut shell, wheat straw, and wood chips), by heating at low-oxygen environment was commonly used to prevent soil and environmental problem (Lehmann and Joseph, 2009). In the field of agriculture, biochar can lead stimulation of growth, activity and metabolic efficiency of the microbial biomass, including plant symbionts (George et al., 2012). Moreover, since having ability to absorb and reduce methane emission by producing microbial methane oxidation, biochar can be utilized in gas landfill as final cover soil (Shang et al., 2013; Yu et al., 2013; Wong et al., 2017). In term of physical properties, the use of biochar as soil mixture can evolve water retention capacity and hydraulic conductivity owing to its porosity (Wong et al., 2017; Garg et al., 2021). Chen, et al. (2022) suggested that biochar amended soil may be potentially used as landfill cover in waste disposal system. Based on their research, the application of biochar can minimize the thickness of soil cover, attributing to the decreasing of water infiltration and percolation. In fact, biochar can reduce the very low pore-water pressure (PWP) in soils by more than 50% under extreme climate condition. Accordingly, biochar is becoming an alternative material for enhancing earthwork stability and providing more sustainable landfill construction, especially under climate condition. However, the majority of research to date has focused on the effect of biochar addition on crop soil water infiltration in arid and semiarid locations (Abrol et al., 2016; Novak et al., 2016; Ibrahim et al., 2017). In the context of agricultural requirement, loosely compacted soil was used in this investigation related to soil respiration. To date, the study of biochar application to prevent serviceability problem in earthworks, especially under extreme climate variation is limited. Since agricultural soil and earthwork structures behave differently, biochar application in constructed structures requires extensive additional research.

The objective of this study is to investigate the water infiltration and evaporation of biochar-amended soil (BAS) under extreme climate scenario variation. In order to conduct this investigation, three variations of biochar composition (0 %, 10 %, and 20 %) were observed. Regarding (Jin et al., 2016), the addition of 10 or 20 % biochar suggests the possibility of interaction between biochar and soil components and/or the influence of biochar oxidation. Moreover, excessive rainfall and drought based on the worst Thailand climate scenario (RCP 8.5) in the near future (2030) and far future (2060) were implemented in this simulation. The current climate condition was also applied in the simulation for comparison purposes. Seep/W was used to model transient numerical simulation analysis employing one-dimensional axisymmetric idealization (GEO-SLOPE International Ltd, 2012). Water infiltration rate and evaporation has been subjected in the model in relation to biochar change and climate scenario. Moreover, PWP along the depth was also investigated in this study with respect to biochar composition and climate variation. This research is expected to provide a better knowledge of the use of BAS to prevent stability and serviceability problem of earthwork, particularly under extreme climate scenarios.

13.2 Methodology

13.2.1 Model geometry

To obtain the research aim, a numerical study was simulated considering experimental model which was conducted by Chen, et al. (2022). In their research, a soil column with diameter of 0.28 m, and a height of 0.7 m was generated to study water infiltration in BAS. Accordingly, axisymmetric idealization was used in this simulation, measuring the radius of 0.14 m and the height of 0.7 m as illustrated in Figure 98. Based on Yuan et al. (2020), rainfall will infiltrate to the area which was less than 0.75 meters. To facilitate the investigation, four observation points were determined in the model, located at depth of 0.05, 0.25, 0.45 and 0.65 m, following experimental setup. Furthermore, this study simulated three variations of BAS composition, namely B0, B10, and B20, representing biochar composition of 0%, 10% and 20%.

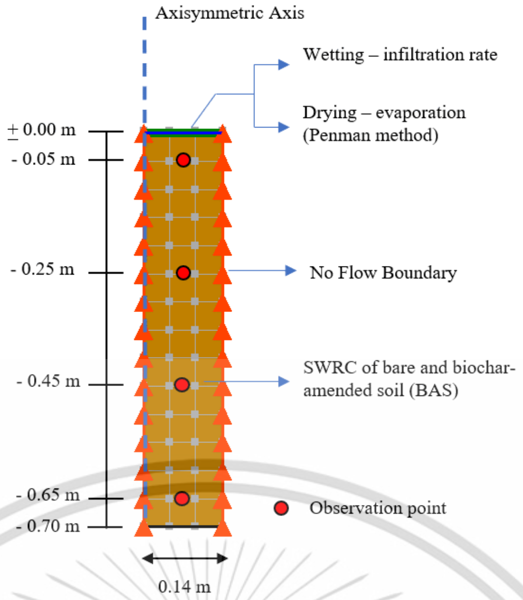

Figure 98 Model geometry of BAS Numerical Simulation.

13.2.2 Material properties

The soil utilized in the simulation was fully decomposed granite (CDG), which was a commonly used as building material in Thailand, China, and other countries. The soil was classified as SM consisting of sand (57.4 %), silt (27.6 %), and clay (15 %), based on The Unified Soil Classification System (USCS). In addition, the biochar used in this study was ground to pass through a 0.25 mm sieve, resulting in biochar with a particle size smaller than 0.25 mm. Considering ASTM D854-14 (ASTM International, 2003), biochar composition of 0%, 10% and 20% resulted specific gravity of 2.62, 2.56 and 2.51, respectively. Since biochar particles have a lower dry density than soil particles, the increasing of biochar application decreased the specific gravity. Moreover, the application of biochar 0%, 10% and 20% promoted the maximum dry density of 1.66, 1.48 and 1.43 g/cm3 respectively. However, the corresponding optimum water content was increased as more pores from biochar were presented in the BAS. Regarding mercury intrusion porosimeter test result, compared to biochar 0%, the total pore volume was increased by about 15% and 40% as the application of biochar 10% and 20% respectively.

To conduct transient seepage analysis, the soil water retention curve (SWRC) and hydraulic conductivity function (HCF) were required. Both drying and wetting SWRC were deployed in this simulation which were obtained from laboratory experiment, conducted by Chen, et al. (2022). Measured SWRC data were fitted using Genuchten model (Van Genuchten, 1980), following equation (119). Equation (120) was then used to predict HCF based on SWRC and saturated hydraulic conductivity. Measured and fitted SWRC during the wetting and drying process based on experimental data can be depicted in Figure 99.

$$\theta = \theta_r + \frac{(\theta_s - \theta_r)}{((1 + a\psi)^n)^m} \tag{119}$$

Where θ is volumetric water content (%), θ_s is saturated volumetric water content (%), θ_r is residual volumetric water content (%), ψ is matrix suction and a, n, m is curve fitting parameters.

$$K_w = K_{sat} \frac{\left[1 - (a\psi^{(n-1)}(1 + (a\psi^n)^{-m})\right]^2}{((1 + a\psi)^n)^{\frac{m}{2}}} \tag{120}$$

Where K_{sat} is saturated hydraulic conductivity (m/sec), K_w is unsaturated hydraulic conductivity (m/sec).

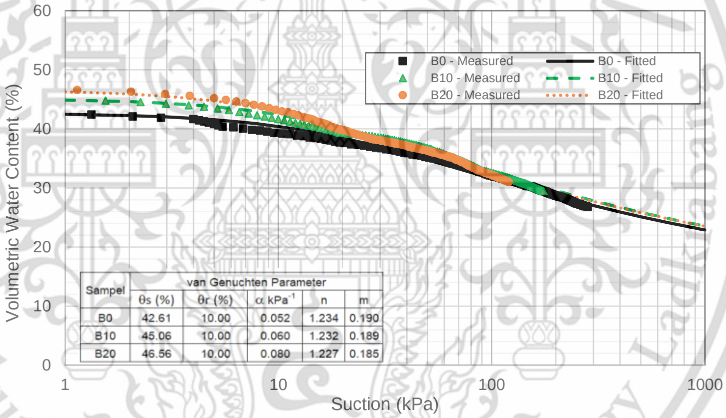

Sampel	van Genuchten Parameter				
	θs (%)	θr (%)	α kPa^{-1}	n	m
B0	42.61	10.00	0.052	1.234	0.190
B10	45.06	10.00	0.060	1.232	0.189
B20	46.56	10.00	0.080	1.227	0.185

(a) Wetting

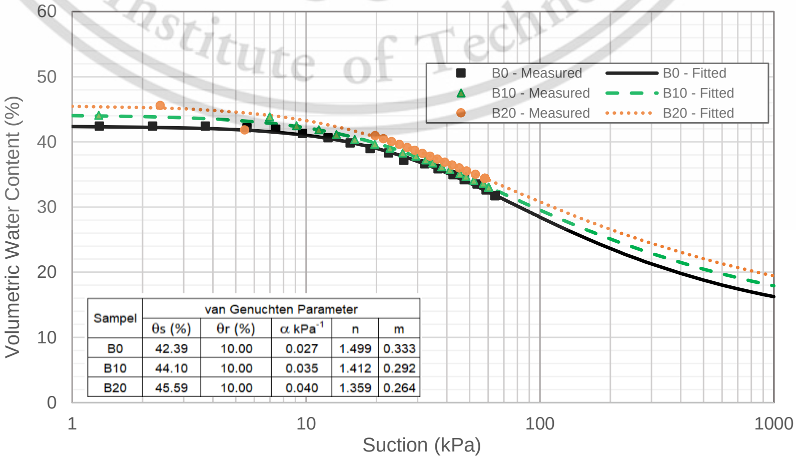

Sampel	van Genuchten Parameter				
	θs (%)	θr (%)	α kPa^{-1}	n	m
B0	42.39	10.00	0.027	1.499	0.333
B10	44.10	10.00	0.035	1.412	0.292
B20	45.59	10.00	0.040	1.359	0.264

(b) Drying

Figure 99 BAS SWRC.

It can be seen in Figure 99 that SWRC varied in accordance with BAS composition. Moreover, wetting and drying process resulted subtle SWRC pattern, representing in Figure 99 (a) and (b) respectively. With biochar application rates of 10% and 20%, the saturated water content increased by approximately 2.5% and 4%, respectively. The increase in water content was proportional to the rise in porosity. Since having more significant pores volume and larger surface area, higher biochar application rate can absorb more water during water infiltration, thus increasing its water-holding capacity (Uzoma et al., 2011). On the other hand, the effect of biochar composition to the air-entry values and absorption curves was limited. It indicated that the size and distribution of pores in BAS has remain unchanged, compared to bare soil sample. As a result, the alteration in air-entry values and absorption curve is negligible. The measured results from the experiment were fitted with the van Genuchten model and then used in the numerical modelling.

13.2.3 Boundary Condition

No flow boundary was set in the right and left side of the model, representing an impermeable wall of the column. Moreover, review boundary was situated at the bottom of the model (i.e., seepage boundary during rainfall and no flow boundary during evaporation). Further to this, the model was subjected with rainfall and evaporation to represent wet and dry season. The Green-Ampt infiltration method was used (Green and Ampt, 1911) to calculate the water flux boundary with regard to precipitation. The infiltration rate and cumulative infiltration depth can be calculated using equation (121) and (122). It should be noted that GA parameter was obtained from laboratory experiment, conducted by Chen, et al. (2022). In addition, the Penman method (Penman, 1948) was used to calculate evaporation based on Thailand climate data as can depicted in equation (123).

$$F(t) = K_s\, t + \psi \Delta\theta l\, n \left(1 + \frac{F(t)}{\psi \Delta\theta}\right) \tag{121}$$

$$f(t) = K_s \left(\frac{\psi \Delta\theta}{F(t)} + 1\right) \tag{122}$$

Where, f(t) is infiltration rate (mm/sec), t is time (sec), ψ is suction head (mm), and Δθ deficit of volumetric water content.

$$PET = \frac{0.408\Delta.(Rn - G) + \gamma \frac{900}{T + 273} u_2 (e_s - e_a)}{\Delta + \gamma\,(1 + 0.34 u_2)} \tag{123}$$

Where PET is Potential Evaporation (mm/day), Rn is Net Radiation (MJ/m^{2}day), G is Soil heat flux density (MJ/m^{2}day), T is Mean daily air temperature at 2 m height (^{o}C), u_2 is Wind speed at 2 m height (m/sec), e_s is saturation vapor pressure (kPa), e_a is actual vapor pressure (kPa), Δ is slope vapor pressure curve (kPa/^{o}C), γ is psychrometric constant (0.061 kPa/^{o}C).

Three variation of extreme climate scenarios were implemented in this study i.e., current climate, near future (2030) and far future (2060), regarding worst case scenario in Thailand. Considering (Yamoat et al., 2022), Thailand has been experienced with maximum hourly rainfall intensity of 19.2 mm/h for 12 hours regarding 100 year return period. Note that Intensity Duration Frequency (IDF) has been derived from their research, based on 30 years (1990-2020) historical data. Further to this, based on Shrestha et al. (2017) maximum rainfall intensity will increase by about 37.9% and 54.9% in the near future (2030) and far future (2060). Therefore, the model will be subjected by 27.5 mm/h and 31.0 mm/h during extreme future scenario. In the context of evaporation, weather data was required in the calculation with regard to three extreme climate scenarios. World Bank Group and The Asian Development Bank (2021) reported that the atmospheric condition will remarkably change with the time, considering worst climate scenario (RCP 8.5). Based on their analysis, the average of air temperature was about 32.3, 34.8 and 37.5^{o} C during current, near and far future scenario. Moreover, the mean of air humidity will gradually decrease by approximately 81.39%, 80.39% and 78.39% during current, near and far future condition respectively. All of input parameter to calculate water infiltration and evaporation can be seen in Table 8.

Table 8 Water infiltration and evaporation parameter

Green Ampt						Penman					
Sample	Current Weather					Sample	Current Weather				
	θe	Ks (mm/hr)	Se	$\Delta\theta$ (%)	i (mm/hr)		T (^{o}C)	Rh (%)	Rs (MJ/m^{2}day)	γ (kPa/^{o}C)	Δ
B0	0.43	4.464	0.430	1.162	19.20	B0	32.36	81.39	24.080	0.061	0.230
B10	0.44	2.581	0.450	1.169	19.20	B10	32.36	81.39	24.080	0.061	0.230
B20	0.47	2.041	0.460	1.167	19.20	B20	32.36	81.39	24.080	0.061	0.230
	Near Future Weather						Near Future Weather				
B0	0.43	4.464	0.430	1.162	27.50	B0	34.86	80.39	24.270	0.061	0.230
B10	0.44	2.581	0.450	1.169	27.50	B10	34.86	80.39	24.270	0.061	0.230
B20	0.47	2.041	0.460	1.167	27.50	B20	34.86	80.39	24.270	0.061	0.230
	Far Future Weather						Far Future Weather				

B0	0.43	4.464000	0.430	1.162	31.00	B0	37.56	78.39	24.320	0.061	0.230
B10	0.44	2.581200	0.450	1.169	31.00	B10	37.56	78.39	24.320	0.061	0.230
B20	0.47	2.041200	0.460	1.167	31.00	B20	37.56	78.39	24.320	0.061	0.230

13.2.4 Analysis Procedure

A series of numerical analyses were done to compare the PWP response during rainfall and evaporation events using Seep/W. Seep/W is a highly effective finite element modeling software for predicting groundwater flow in porous medium. SEEP/W is capable of simulating both basic saturated steady-state problems and complex saturated/unsaturated transient analyses with atmospheric interaction at the ground surface. Each simulation consists of three stages: (i) steady state analysis to determine the initial PWP for each model; (ii) transient seepage analysis owing to rainfall; and (iii) transient seepage analysis due to evaporation throughout the drying phase. Initial PWP was determined in steady-state phases based on the PWP value at the commencement of the test. To analysis wet conditions, the model was subjected to precipitation for 12 hours. Following this, evaporation based on Penman calculation was applied in the drying simulation for 144 hours. Further to this, extreme rainfall and evaporation induced by current, near future, and far future extreme climate was also applied to the model.

13.3 Result and Discussion

13.3.1 Effects of biochar on infiltration rate

The value of infiltration rate and cumulative infiltration depth over the time, based on Green-Ampt method can be plotted in Figure 100. Infiltration rate represent the velocity at which water enter the soil. Meanwhile, cumulative infiltration depth equals the water amount that infiltrated to the soil at specific time. Figure 100 (a), (b) and (c) correspond to calculation result of biochar content 0%, 10% and 20%, respectively. Furthermore, the graph also showcases three distinct climate scenarios: current, near future, and far future. Regarding Figure 100, it becomes apparent that at the beginning of rainfall, the water infiltration rate is relatively high due to the substantial difference in hydraulic gradient between the upper and lower soil layers. Subsequently, the infiltration rate decreases significantly as the hydraulic gradient decreases, eventually reaching a stable condition. Overall, it can be inferred that the application of biochar reduces the water infiltration rate, consequently diminishing the infiltration depth. This phenomenon can be attributed to the higher porosity of the biochar-amended soil (BAS) column, which enables greater water absorption compared to bare soil. In the context of current climate scenario, the application of 10% and 20% biochar results in a reduction of water infiltration rate by approximately 33.9% (4.35×10-7 m/s) and 42.2% (3.81×10-7 m/s) respectively, compared to bare soil (6.58×10-7 m/s). As such, reducing water infiltration depth by about 31.1% (11.2 mm) and 38.5% (13.9 mm) respectively. This is due to the fact that finer particles of biochar may clog large soil pore, reducing water infiltration rate (Ibrahim et al., 2017). Moreover, regarding Ibrahim et al. (2013) biochar can be considered as biding agent, leading to flocculate soil particles to form stable aggregates and thus limiting the downward movement of soil water.

Besides, Figure 100 also shows infiltration rate of near and far future extreme climate scenario. It can be seen in Figure 100 that infiltration rate under future extreme climate tend to have similar pattern with current climate. However, future extreme climate resulted higher infiltration rate significantly compared to current climate for all of three BAS variations in association with the increasing of rainfall intensity. Without biochar application, near and far future extreme climate will trigger the increasing of infiltration rate by about 15% (7.57×10-7 m/s) and 49% (9.83×10-7 m/s), compared to current climate scenario (6.58×10-7 m/s). On the other hand, the application of biochar 10% and 20% can reduce infiltration rate under near future extreme climate scenarios by approximately 32% (5.14×10-7 m/s) and 40% (4.56×10-7 m/s) as compared with bare soil (7.57×10-7 m/s m/s). Likewise, the increasing of biochar composition to 10% and 20% can lead the reduction of water infiltration rate by around 31% (6.77×10-7 m/s) and 38% (6.10×10-7 m/s), compared to bare soil column (9.83×10-7 m/s) during far future extreme climate.

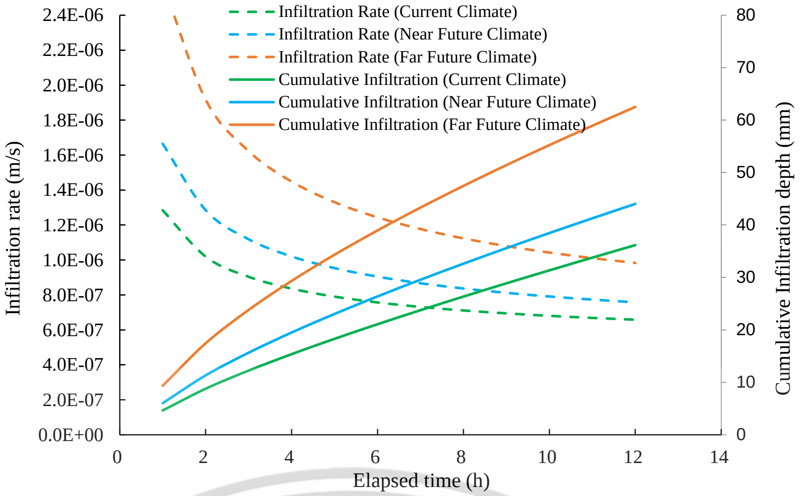

(a) B0

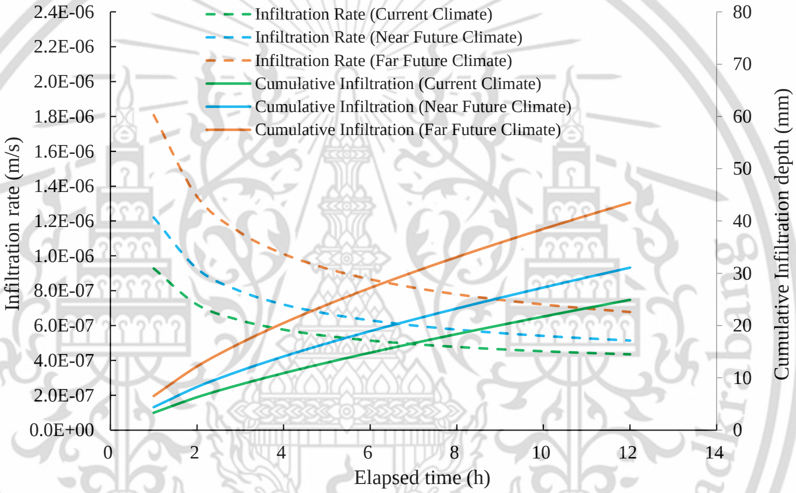

(b) B10

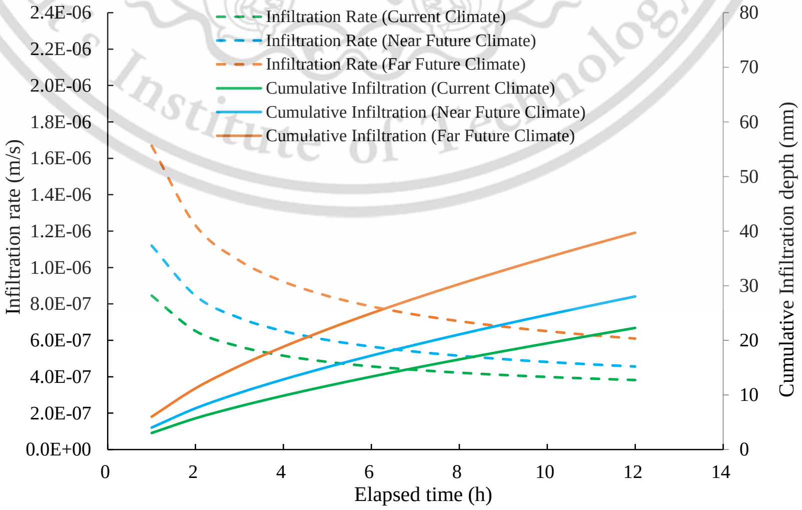

(c) B20

Figure 100 Infiltration rate and cumulative infiltration.

13.3.2 Responses of pore water pressure (PWP) during rainfall

Figure 101 illustrates the response of PWP along the depth during rainfall with application of three biochar composition under three extreme climate scenarios. The fluctuation of PWP due to the application of biochar 0%, 10% and 20% can be depicted in Figure 101 (a), (b) and (c) respectively. Moreover, the value of PWPs were investigated under 4, 8, and 12 h of rainfall, representing 2, 10, and 100 years of return period. At the beginning of the simulation, initial PWP was set by about -60 kPa following experimental data. As water infiltrated into the soil, the PWP along the depth gradually increased. It can be seen in Figure 101 that the PWP at 0.05 m depth jumped to near 0 kPa in all variation of biochar composition after 8 h of rainfall, under current climate scenario. The value of PWP become less fluctuated at the deeper depth in association of water infiltration depth. Current climate scenario promoted the increasing of PWP up to the depth of 0.25 m in bare soil (30%), indicating maximum water infiltration depth. On the other hand, application of biochar 10% can retain PWP value significantly to the depth of 0.25 m (11%). Noted that the PWP value at depth of 0.45 m has remained unchanged due to the application of all biochar composition under current climate scenario. In fact, the value of PWP at 0.25 m depth is almost similar after 12 h of rainfall with the application of biochar 20%. It indicated that the application of biochar can reduce water infiltration depth significantly.

Future extreme climate scenario triggered remarkable fluctuation of PWP, compared to current climate as can be depicted in Figure 101. Without biochar application, water infiltrated to the depth of 0.45 m after 12 h of rainfall due to near future extreme climate, leading the increasing of PWP by about 42% (-37.2 kPa). Moreover, the application of biochar 10% can maintain PWP to the depth 0.45 m, minimizing the increasing of PWP by approximately 2% (-59.5 kPa). Further to this, the value of PWP was unchanged at 0.45 m depth as the application of biochar 20% under near future extreme climate scenario. It was substantiated that the addition of biochar 20% can prevent water percolation up to depth of 0.45 under near future extreme climate scenario. In the context of far future extreme climate, rainfall led to increase PWP value up to the depth of 0.65 m after 12 h of rainfall in bare soil (77%). However, the application of biochar 10% and 20% significantly influenced PWP due to far future extreme climate scenario. It can be indicated from the constant value of

PWP at the depth of 0.65 after 12 h of rainfall under far future extreme climate with respect to biochar application of 10% and 20%. The addition of biochar 10% and 20% can promote the increasing of PWP by about 61% (-23.4 kPa) and 3% (56.2 kPa) respectively at the depth of 0.45 under far future extreme climate. It substantiated that the application of biochar 20% can prevent water percolation up to depth of 0.45 m under far future extreme climate scenario. This result is useful for further consideration of soil cover thickness in BAS application. Thus, the use of biochar can improve the performance of soil covers by decreasing water infiltration and enhancing water retention.

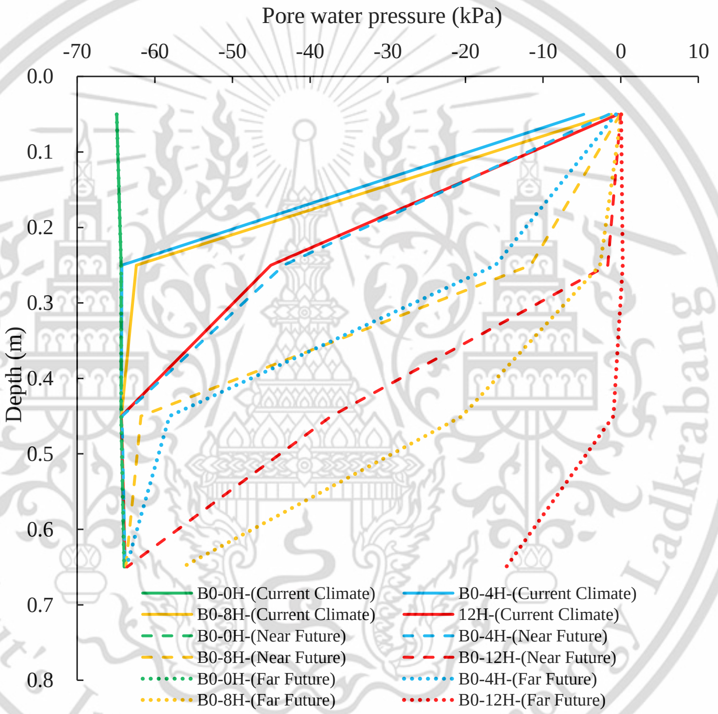

(a) B0

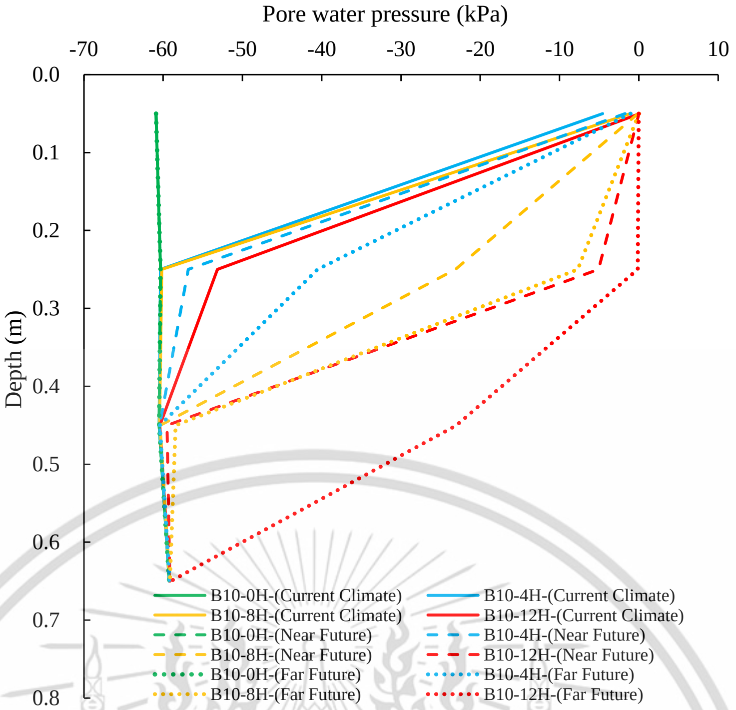

(b) B10

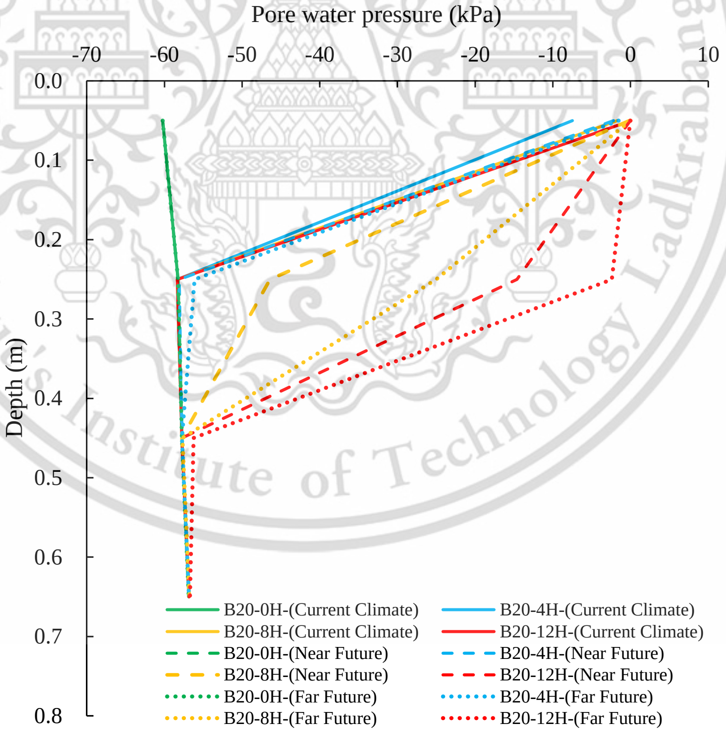

(c) B20

Figure 101 Development of pore water pressure (PWP) with depth during rainfall.

13.3.3 Responses of pore water pressure (PWP) during drying

The responses of PWP during drying process with the variation of biochar composition variation under three climate scenarios can be illustrated in Figure 102. It can be seen in Figure 102 that PWP value was more fluctuated at near surface depth, compared to the deeper depth due to evaporation process. With respect to current climate scenario, soil in the upper half of the column was saturated, based on previous simulation. Following this, PWP decreased after 48 h of evaporation. However, PWP in the lower layer of column was still increase due to the downward infiltration through the column. The downward infiltration process stopped after 48 h of evaporation. Moreover, the application of biochar can maintain the decreasing of PWP as compared with bare soil. Without biochar application, PWP dropped by around -188 kPa at depth of 0.25 m under current climate scenario. At the same depth, The application of biochar 10% and 20% decreased PWP value by approximately -93.5 kPa and -45.75 kPa respectively. It can be attributed to the finer particle of biochar which decreased the soil porosity, reducing evaporation area. As PWP fluctuation during wetting and drying process can trigger progressive failure of the embankment, maintaining PWP is required to prevent serviceability problem.

Regarding future extreme climate scenario analysis, the noticeable decreasing of PWP occurred with the application of three biochar variations at near surface depth. Compared to current climate scenario, near and future extreme climate promote the decreasing of PWP value by about 23% (-232 kPa) and 95% (369 kPa) respectively at depth of 0.25 m without biochar application. Moreover, the addition of biochar composition can also reduce the decreasing of PWP significantly under extreme scenario. Under near future extreme climate scenario, the minimum PWP at depth of 0.25 m was around -164 kPa and -115 kPa with variation of biochar application of 10% and 20% respectively. It should be noted that the PWP value decreased by around 29% and 50%, compared to B0 variation (-232 kPa). In term of far future extreme climate scenario, evaporation promoted the decreasing PWP by approximately -219 kPa and -168 kPa due to the addition of biochar 10% and 20% at the depth of 0.25 m. Figure 102 shows the application of BAS maintained PWP value at lower half of column under future extreme climate scenario as compared with B0 variation. It substantiated that biochar can mitigate a very low magnitude of PWP under extreme drought condition.

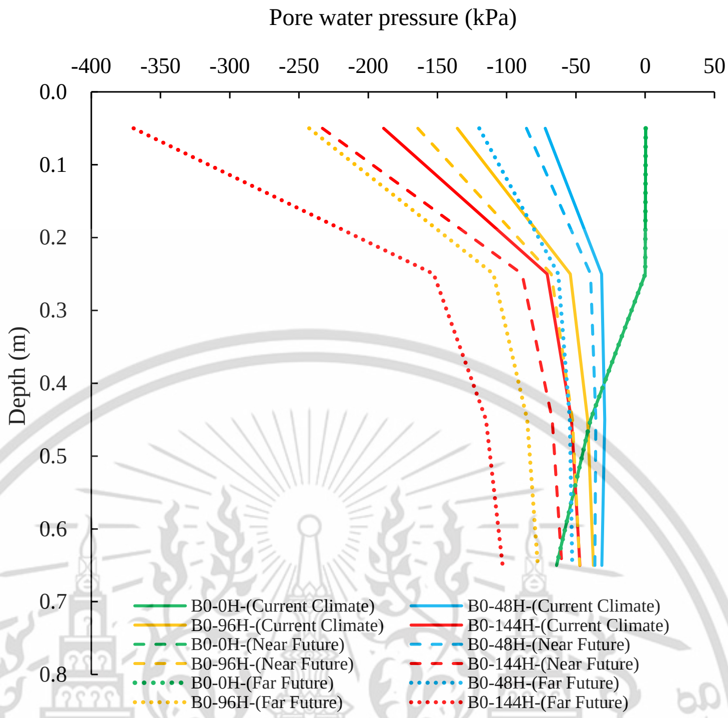

(a) B0

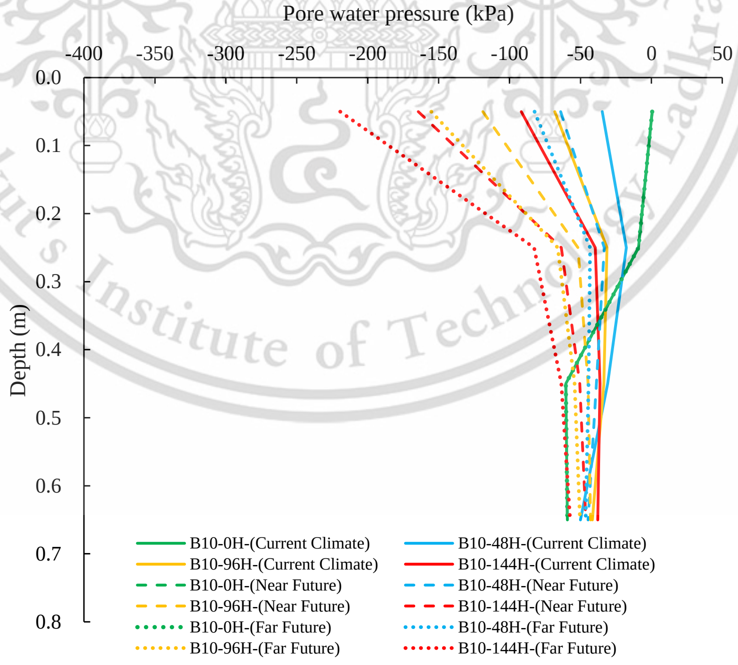

(b) B10

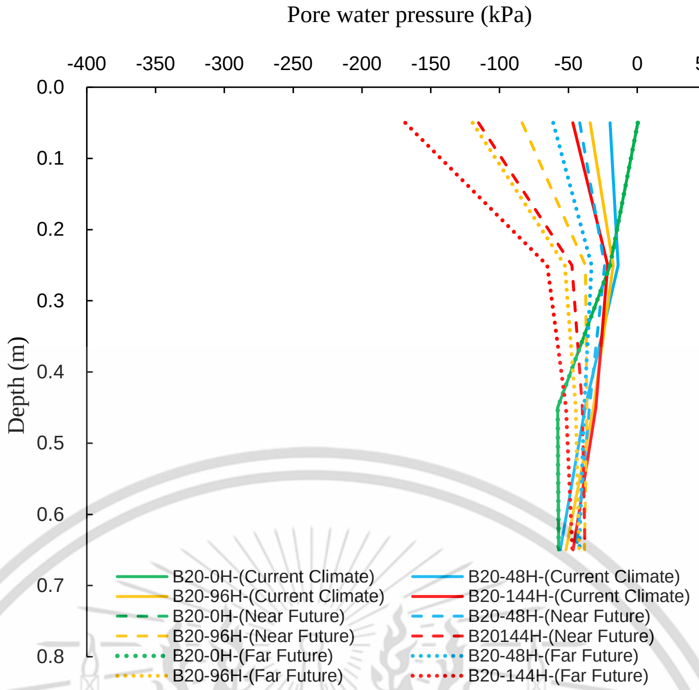

(c) B20

Figure 102 Development of pore water pressure (PWP) with depth during drying.

Chapter 14 Conclusion

This research studied the stability and serviceability of embankment due to seasonal variation and the impact of extreme climate. Since classified as fine-grained material, the presence of desiccation crack was taken into account in this study. Thus, the alteration of desiccation cracks because of wetting and drying process has been investigate during this research. Moreover, water infiltration and evaporation was then calculated, considering the magnitude of cracks. Following this, hydro-mechanical behaviour of the embankment such as PWP, water content and deformation due to seasonal process was inspected in this research. To support the observation result, a series of back analysis was performed, regarding measured data. Further to this, parametric study was also conducted in this study to obtain embankment response due to extreme climate condition. Those following conclusion can be withdrawn with respect to the research result.

1) Considering climate index calculation, the embankment experienced with more extreme climate condition in the second year of observation (severe climate), compared to the first year (moderate climate). It can be attributed to the higher value of rainfall intensity and potential evaporation during the second year, rather than the first year.

2) Regarding cracks observation result, the propagation of the cracks was more fluctuated at near surface area, compared to a deeper depth. It can be attributed to significant effect of soil-atmosphere interaction at top soil area, rather than at deeper depth.

3) The value of CIF at near surface area during severe drought climate (second year) was 1.6 times higher than that during the first year (moderate drought) attributed to higher air temperature and less rainfall intensity during severe drought, promoting more significant soil shrinkage.

4) Drying and wetting cycle triggered the existence of non-connected cracks at the middle depth of the embankment which was less affected by seasonal condition, promoting the increase in CIF.

5) There is exponential correlation between CIF and the value of saturated Hydraulic Conductivity. At the beginning of crack existence, the amount of the

cracks was minimum, and thus limiting the increase of water infiltration. As a result, increasing of Ks is more significant in higher value of CIF (more than 5%).

6) Since experienced with more extreme climate condition in the second year, the embankment tended to have lower minimum VWC in the second summer, rather than the first summer. It can be attributed to the higher evaporation and less rainfall intensity during severe dry increasing soil moisture deficit, and thus decreasing VWC.

7) Higher CIF tend to have lower and more fluctuated value of VWC in association with higher evaporation value. It is evidence that the presence of the crack provided the increase in surface area, as such rising evaporation value. Moreover, compared to near surface area, the same range of AWB and CIF at the deeper depth produced more fluctuated value of VWC. It is due to the fact that the same CIF between near surface area and middle depth occurred in the difference season, promoting distinctive range of VWC.

8) Based on observation, the value of PWP was found to be more fluctuated in the second year (severe climate) rather than the first year (moderate climate). It can be attributed to the higher value of rainfall intensity during severe wet and more significant value of evaporation during severe drought climate.

9) The value of PWP in shallow depth was more fluctuated than that the deeper depth, reaching constant at the depth of 2 meter. This phenomenon was closely related to soil-atmosphere interaction, affecting hydrological behaviour.

10) Based on deformation observation result, top area of the embankment experienced with profound y-axis displacement during six months after embankment construction (21 cm). It can be contributed to consolidation settlement in the first wet season and soil shrinkage during the first dry season.

11) According to the result of parametric study, extreme dry condition produced higher y-axis displacement, compared to current and wet climate condition. It can be attributed to the modest rainfall intensity during extreme dry climate condition. Therefore, embankment experience with notable shrinkage, resulting significant y-axis displacement.

12) Embankment tended to move upward significantly during rainy season in extreme wet climate with respect to soil swelling, promoting lower y-axis displacement at the end of second rainy season, compared to current climate condition.

13) The value FOS during extreme dry climate was more fluctuated, rather than extreme wet condition, attributed to the PWP value. As the PWP decreased to minimum value at the end of dry season, the value of FOS increased significantly (2.3). On the contrary, the FOS plumed by approximately 1.0 at the beginning of rainy season regarding the increase of PWP.

References

Abed, A. and Korkiala-Tanttu, L. 2018, *Stability analysis for road-cutting Review, recommendations and examples*, September.

Abrol, V., Ben-Hur, M., Verheijen, F.G.A., Keizer, J.J., Martins, M.A.S., Tenaw, H., Tchehansky, L. and Graber, E.R. 2016, Biochar Effects on Soil Water Infiltration and Erosion under Seal Formation Conditions: Rainfall Simulation Experiment, *Journal of Soils and Sediments*, Vol. 16 No.12, pp. 2709–2719.

Addis, B. 2020, Past, Current and Future Use of Physical Models in Civil Engineering Design, *Proceedings of the Institution of Civil Engineers: Civil Engineering*, Vol. 174 No.2, pp. 61–70.

Adem, H.H. and Vanapalli, S.K. 2015, Review of Methods for Predicting in Situ Volume Change Movement of Expansive Soil over Time, *Journal of Rock Mechanics and Geotechnical Engineering*, Vol. 7 No.1, pp. 73–86.

Agisoft. 2021, Agisoft Metashape User Manual Version 1.8, *Agisoft Metashape*, https://www.agisoft.com/pdf/metashape-pro_1_8_en.pdf.

Albright, W.H., Benson, C.H., Gee, G.W., Abichou, T., Tyler, S.W. and Rock, S.A. 2006, Field Performance of Three Compacted Clay Landfill Covers, *Vadose Zone Journal*, Vol. 5 No.4, pp. 1157–1171.

Allen, R.G., Pereira, L.S., Raes, D. and Smith, M. 1998, FAO Irrigation and Drainage Paper No. 56 - Crop Evapotranspiration, *Irrigation and Drainage Paper*, Vol. 56.

Allen, R.G., Pereira, L.S., Raes, D. and Smith, M. 2019, *Crop Evapotranspiration*, FAO Irrigation and Drainage Paper9 10.

Alonso, E.E., Pereira, J.M., Vaunat, J. and Olivella, S. 2010, A Microstructurally Based Effective Stress for Unsaturated Soils, *Geotechnique*, Vol. 60 No.12, pp. 913–925.

An, N., Hemmati, S., Cui, Y. jun, Maisonnave, C., Charles, I. and Tang, C. sheng. 2018, Numerical Analysis of Hydro-Thermal Behaviour of Rouen Embankment under Climate Effect, *Computers and Geotechnics*, Vol. 99 No.December 2017, pp. 137–148.

Anderson, M.G. and Kneale, P.E. 1980, Pore Water Pressure and Stability Conditions on a Motorway Embankment., *Earth Surface Processes*, Vol. 5 No.1, pp. 37–46.

Apriyono, A., Yuliana and Kamchoom, V. 2023, Serviceability of Cut Slope and

Embankment under Seasonal Climate Variations, *Acta Geophysica*, Vol. 71, pp. 983–995.

Aristizabal, E., Garcia, E.F., Marin, R.J., Gomez, F. and JuanGuzman-Martinez. 2022, Rainfall-Intensity Effect on Landslide Hazard Assessment Due to Climate Change in North-Western Colombian Andes, *Revista Facultad de Ingenieria*, No.103, pp. 51–66.

Assadollahi, H. 2019, The impact of climatic events and drought on the shrinkage and swelling phenomenon of clayey soils,UNIVERSITÉ DE STRASBOURG.

Assadollahi, H. and Nowamooz, H. 2020a, Long Term Behavior of Natural Clays in a Building Foundation Under Climate Change Scenarios, *Environmental Geotechnics*, , pp. 1–13.

Assadollahi, H. and Nowamooz, H. 2020b, Long-Term Analysis of the Shrinkage and Swelling of Clayey Soils in a Climate Change Context by Numerical Modelling and Field Monitoring, *Computers and Geotechnics*, Vol. 127 No.June, pp. 103763.

Assouline, S. 2013, Infiltration into Soils: Conceptual Approaches and Solutions, *Water Resources Research*, Vol. 49 No.4, pp. 1755–1772.

ASTM International. 2003, Standard Method for Infiltration Rate of Soils in Field Using Double-Ring Infiltrometer, In Annual Book of ASTM Standards, Vol 04.08 August, pp. 4–11. West Conshohocken.

Baker, R. 1981, Tensile Strength, Tension Cracks and Stability of Slopes, *Soils and Foundations*, Vol. 21 No.2, pp. 33–46.

Beguería, S. and Vicente-Serrano, S.M. 2017, Package “SPEI,” *R-Package*, No.March, pp. 16.

Beguería, S., Vicente-Serrano, S.M., Reig, F. and Latorre, B. 2014, Standardized Precipitation Evapotranspiration Index (SPEI) Revisited: Parameter Fitting, Evapotranspiration Models, Tools, Datasets and Drought Monitoring, *International Journal of Climatology*, Vol. 34 No.10, pp. 3001–3023.

Biot, M.A. 1941, General Theory of Three-Dimensional Consolidation, *Journal of Applied Physics*, Vol. 12 No.2, pp. 155–164.

Bishop, A.W. 1955, The Use of The Slip Circle in Stability Analysis of Slopes T, *Géotechnique*, Vol. 5 No.1, pp. 7–17.

Blaney, H.F. and Criddle, W.D. 1950, *Determining water requirements in irrigated* *areas from climatological and irrigation data*, US Soil Conservation Service., Washington, DC, http://journal.um-surabaya.ac.id/index.php/JKM/article/view/2203.

Blight, G.E. 1997, Interactions between the Atmosphere and the Earth, *Géotechnique*, Vol. 47 No.4, pp. 713–767.

Bower, H. 1986, Intake Rate: Cylinder Inltrometer, In Methods of Soil Analysis: Part 1 Physical and Mineralogical Methods 9, pp. 825–844. Phoenix, Arizona.

Briaud, J.-L., Zhang, X. and Moon, S. 2003, Shrink Test–Water Content Method for Shrink and Swell Predictions, *Journal of Geotechnical and Geoenvironmental Engineering*, Vol. 129 No.7, pp. 590–600.

Briggs, K.M., Dijkstra, T.A. and Glendinning, S. 2019, Evaluating the Deterioration of Geotechnical Infrastructure Assets Using Performance Curves, *International Conference on Smart Infrastructure and Construction 2019, ICSIC 2019: Driving Data-Informed Decision-Making*, Vol. 2019, pp. 429–435.

Briggs, K.M., Smethurst, J.A., Powrie, W. and O'Brien, A.S. 2013, Wet Winter Pore Pressures in Railway Embankments, *Proceedings of the Institution of Civil Engineers: Geotechnical Engineering*, Vol. 166 No.5, pp. 451–465.

Brooks, R.H. and Corey, A.T. 1964, *Properties of Porous Media*, Colorado State University Hydrology Paper92 2,No. 3. Fort Collins, CO..

Brooks, S.M., Crozier, M.J., Glade, T.W. and Anderson, M.G. 2004, Towards Establishing Climatic Thresholds for Slope Instability: Use of a Physically-Based Combined Soil Hydrology-Slope Stability Model, *Pure and Applied Geophysics*, Vol. 161 No.4, pp. 881–905.

Brown, P. and Russell, B. 2010, Siting and Maintenance of Weather Stations, *Turf Irrigation Manament Series*, No.3, http://dlharvest.sir.arizona.edu/arizona/handle/10150/147006.

Brutsaert, W. 1967, Some Methods of Calculating Unsaturated Permeability, *Transactions of the ASAE*, Vol. 10 No.3, pp. 0400–0404.

Buckingham, E. 1907, *Studies on the movement of soil moisture*, Bull. No. 38., Bureau of Soils, USDA, Washington, DC..

Burdine, N.T. 1953, Relative Permeability Calculations From Pore Size Distribution Data, *Journal of Petroleum Technology*, Vol. 5 No.03, pp. 71–78.

Campbell Scientific Inc. 2012, CS650 and CS655 water content reflectometers,Utah.

Chen, Z., Kamchoom, V., Apriyono, A., Chen, R. and Chen, C. 2022, Laboratory Study of Water Infiltration and Evaporation in Biochar-Amended Landfill Covers under Extreme Climate, *Waste Management*, Vol. 153 No.July, pp. 323–334.

Cheng, Q., Tang, C.S., Xu, D., Zeng, H. and Shi, B. 2021, Water Infiltration in a Cracked Soil Considering Effect of Drying-Wetting Cycles, *Journal of Hydrology*, Vol. 593 No.October, pp. 125640.

Chowdhury, R.N. and Zhang, S. 1991, Tension Cracks and Slope Failure, *Slope stability engineering. Proc. international conference, Isle of Wight, 1991*, , pp. 27–32.

Chu, S.T. 1978, Infiltration during an Unsteady Rain, *Water Resources Research*, Vol. 14 No.3, pp. 461–466.

Clausnitzer, V., Hopmans, J.W. and Starr, J.L. 1998, Parameter Uncertainty Analysis of Common Infiltration Models, *Soil Science Society of America Journal*, Vol. 62 No.6, pp. 1477–1487.

Collaku, A. and Harrison, S.A. 2002, Losses in Wheat Due to Waterlogging, *Crop Science*, Vol. 42 No.2, pp. 444–450.

Costa, S., Kodikara, J. and Shannon, B. 2013, Salient Factors Controlling Desiccation Cracking of Clay in Laboratory Experiments, *Geotechnique*, Vol. 63 No.1, pp. 18–29.

Costa, W.D.S.M. 2010, Study of desiccation properties of clay soils,Monash University.

Cui, G. and Zhu, J. 2017, Infiltration Model in Sloping Layered Soils and Guidelines for Model Parameter Estimation, *Hydrological Sciences Journal*, Vol. 62 No.13, pp. 2222–2237.

Cui, Y.-J., Tang, C.-S., Tang, A.M. and Ta, A.N. 2014, Investigation of Soil Desiccation Cracking Using Environmental Chamber, *Rivista Italiana di Geotecnica*, Vol. 24 No.1, pp. 9–20.

Cui, Y., Zhang, B., Huang, H., Zeng, J., Wang, X. and Jiao, W. 2021, Spatiotemporal Characteristics of Drought in the North China Plain over the Past 58 Years, *Atmosphere*, Vol. 12 No.7, pp. 1–16.

Cui, Y.J., Gao, Y.B. and Ferber, V. 2010, Simulating the Water Content and Temperature Changes in an Experimental Embankment Using Meteorological Data, *Engineering Geology*, Vol. 114 No.3–4, pp. 456–471.

Cui, Y.J., Lu, Y.F., Delage, P. and Riffard, M. 2005, Field Simulation of in Situ Water Content and Temperature Changes Due to Ground-Atmospheric Interactions, *Geotechnique*, Vol. 55 No.7, pp. 557–567.

Cui, Y.J. and Zornberg, J.G. 2008, Water Balance and Evapotranspiration Monitoring in Geotechnical and Geoenvironmental Engineering, *Geotechnical and Geological Engineering*, Vol. 26 No.6, pp. 783–798.

Cynthia Rosenzweig and Solecki, W. 2015, What is a Global Climate Model?, Climate Change Information Resources,New York, http://ccir.ciesin.columbia.edu/nyc/.

Darcy, H.P.G. 1856, *Dètermination des lois d'écoulement de l'eau à travers le sable*, In Les Fontaines Publiques de la Ville de Dijon, Paris.

Davies, O., Rouainia, M., Glendinning, S. and Birkinshaw, S.J. 2008, Assessing the Influence of Climate Change on the Progressive Failure of a Railway Embankment, *12th International Conference on Computer Methods and Advances in Geomechanics 2008*, Vol. 6 No.December 2013, pp. 4478–4486.

Decagon Devices. 2016, *Dielectric Water Potential Sensor Operator's Manual (Version 2.0)*, http://manuals.decagon.com/Manuals/13755_MPS-2and6_Web.pdf.

Decagon Devices, I. 2017, *MPS-2 & MPS-6 Dielectric Water Potential Sensors : Operator's Manual*,California, http://manuals.decagon.com/Retired and Discontinued/Manuals/13755_MPS-2and6_Web.pdf.

Delerue, F., Perrier, E., Timmerman, A. and Swennen, R. 2003, 3D Soil Image Characterization Applied to Hydraulic Properties Computation, *Geological Society Special Publication*, Vol. 215, pp. 167–176.

Dijkstra, T.A. and Dixon, N. 2010, Climate Change and Slope Stability in the UK: Challenges and Approaches, *Quarterly Journal of Engineering Geology and Hydrogeology*, Vol. 43 No.4, pp. 371–385.

Dixon, N., Crosby, C.J., Stirling, R., Hughes, P.N., Smethurst, J., Briggs, K., Hughes, D., Gunn, D., Hobbs, P., Loveridge, F., Glendinning, S., Dijkstra, T. and Hudson, A. 2018, In Situ Measurements of Near-Surface Hydraulic Conductivity in Engineered Clay Slopes, *Quarterly Journal of Engineering Geology and Hydrogeology*, Vol. 49 No.1, pp. 4.

Duncan, J.M. 1996, State of the Art : Limit Equilmrium and Finite Element Analysis of Slopes, *Journal of geotechnical engineering*, Vol. 122 No.July, pp. 577–596.

Durner, W. 1994, Hydraulic Conductivity Estimation for Soils with Heterogeneous Pore Structure, *Water Resources Research*, Vol. 30 No.2, pp. 211–223, http://www.deleplanque.fr/pdf/Livreseigle_2015_web.pdf.

Edlefsen, N.E. and Anderson, A.B.C. 1943a, Thermodynamics of Soil Moisture, *Hilgardia*, Vol. 15, pp. 31 – 298.

Edlefsen, N.E. and Anderson, A.B.C. 1943b, Thermodynamics of Soil Moisture, *Hilgardia*, Vol. 15, pp. 31 – 298.

Finno, R.J., Denby, G., Zapata-medina, D. and Gallant, A. 2011, Effects of Construction-Induced Stress Changes on Dynamic Shear Modulus of Bootlegger Cove Clay GEOTECHNICAL ENGINEERING , GRANT OPP FOR ACAD LIA W / INDUS Effects of Construction-Induced Stress Changes on Dynamic Shear Modulus of Bootlegger Cove Clay Pro, In *NSF Engineering Research and Innovation Conference*, Atlanta.

Fraisse, C.W., Braun, G.W., Lusher, W.R. and Staudt, L.R. 2015, Your Farm Weather Station : Installation and Maintenance Guidelines, *University of Florida Institute of Food and Agricultural Sciences*, , pp. 1–5, https://edis.ifas.ufl.edu/ae502.

Fredlund, D.G., Houston, S.L., Nguyen, Q. and Fredlund, M.D. 2010, Moisture Movement Through Cracked Clay Soil Profiles, *Geotechnical and Geological Engineering*, Vol. 28 No.6, pp. 865–888.

Fredlund, D.G. and Morgenstern, N.R. 1976, Constitutive Relations for Volume Change in Unsaturated Soils., *Canadian Geotechnical Journal*, Vol. 13 No.3, pp. 261–276.

Fredlund, D.G., Morgenstern, N.R. and Widger, R.A. 1978, Shear Strength of Unsaturated Soils, *Canadian Geotechnical Journal*, Vol. 15 No.3, pp. 313–321.

Fredlund, D.G. and Rahardjo, H. 1993, Soil Mechanics for Unsaturated Soils, *Soil Mechanics for Unsaturated Soils*,.

Fredlund, D.G., Rahardjo, H. and Fredlund, M.D. 2006, Unsaturated Soil Mechanics in Engineering Practice, *Journal of Geotechnical and Geoenvironmental Engineering*, Vol. 132 No.March, pp. 286–321.

Fredlund, D.G., Rahardjo, H. and Fredlund, M.D. 2012, *Unsaturated Soil Mechanics in Engineering Practice*, John Wiley & Sons, New Jersey.

Fredlund, D.G. and Xing, A. 1994, Equations for the Soil-Water Characteristic Curve, *Canadian Geotechnical Journal*, Vol. 31 No.4, pp. 521–532.

Fredlund, D.G., Xing, A. and Huang, S. 1995, Predicting the Permeability Function for Unsaturated Soils Using the Soil-Water Characteristic Curve, *International Journal of Rock Mechanics and Mining Sciences & Geomechanics Abstracts*, Vol. 32 No.4, pp. A159.

Fredlund, M.D., Tran, D. and Fredlund, D.G. 2016, Methodologies for the Calculation of Actual Evaporation in Geotechnical Engineering, *International Journal of Geomechanics*, Vol. 16 No.6, pp. 1–12.

Gardner, W.R. 1958, Some Steady State Solutions of the Unsaturated Moisture FLow Equation with Application to Evaporation from a Water-Table, *Soil Science Journal*, Vol. 85 No.4, pp. 228–232.

Garg, A., Huang, H., Cai, W., Reddy, N.G., Chen, P., Han, Y., Kamchoom, V., Gaurav, S. and Zhu, H.H. 2021, Influence of Soil Density on Gas Permeability and Water Retention in Soils Amended with In-House Produced Biochar, *Journal of Rock Mechanics and Geotechnical Engineering*, Vol. 13 No.3, pp. 593–602.

Garnier, J., Gaudin, C., Springman, S.M., Culligan, P.J., Goodings, D., Konig, D., Kutter, B., Phillips, R., Randolph, M.F. and Thorel, L. 2007, Atalogue of Scaling Laws and Similitude Questions in Geotechnical Centrifuge Modelling, *International Journal of Physical Modelling in Geotechnics*, Vol. 7 No.3.

Van Genuchten, M.T. 1980, A Closed-Form Equation for Predicting the Hydraulic Conductivity of Unsaturated Soils, *Soil Science Society of America Journal*, Vol. 44 No.5, pp. 892–898.

GEO-SLOPE, I. 2012, Stress-Deformation Modeling with SIGMA/W 2012, *Geostudio Helpfile*, No.July, pp. 215.

Geo-Slope International. 2007, Strength Reduction Stability, AB, Canada, www.geo-slope.com.

GEO-SLOPE International Ltd. 2012, Seepage Modeling with SEEP/W, *6th edition*, GEO-SLOPE International Ltd.July,Alberta, Canada, http://www.geo-slope.com.

George, C., Wagner, M., Kücke, M. and Rillig, M.C. 2012, Divergent Consequences of Hydrochar in the Plant-Soil System: Arbuscular Mycorrhiza, Nodulation, Plant Growth and Soil Aggregation Effects, *Applied Soil Ecology*, Vol. 59, pp. 68–72.

Gerke, H.H. and van Genuchten, M.T. 1993, A Dual-porosity Model for Simulating the Preferential Movement of Water and Solutes in Structured Porous Media, *Water Resources Research*, Vol. 29 No.2, pp. 305–319.

Glendinning, S., Hughes, P., Helm, P., Chambers, J., Mendes, J., Gunn, D., Wilkinson, P. and Uhlemann, S. 2014, Construction, Management and Maintenance of Embankments Used for Road and Rail Infrastructure: Implications of Weather Induced Pore Water Pressures, *Acta Geotechnica*, Vol. 9 No.5, pp. 799–816.

Gowdish, L. and Muñoz-Carpena, R. 2009, An Improved Green-Ampt Infiltration and Redistribution Method for Uneven Multistorm Series, *Vadose Zone Journal*, Vol. 8 No.2, pp. 470–479.

Green, D.L. 2014, Modelling Geomorphic Systems : Scaled Physical Models, In Geomorphic Techniques, British Society for Geomorphology.

Green, W.H. and Ampt, G.A. 1911, Studies on Soil Physics, *Journal of Agricultural Science*, Vol. 4 No.1, pp. 1.

Gregory, J.H., Dukes, M.D., Miller, G.L. and Jones, P.H. 2005, Analysis of Double-Ring Infiltration Techniques and Development of a Simple Automatic Water Delivery System, *Applied Turfgrass Science*, Vol. 2 No.1, pp. 1–7.

Heib, M. Al, Emeriault, F., Caudron, M., Nghiem, L. and Hor, B. 2013, Large-Scale Soil – Structure Physical Model (1 g) – Assessment of Structure Damages, *International Journal of Physical Modelling in Geotechnics*, Vol. 13 No.4.

Heib, M. Al, Emeriault, F., Nghiem, H., Heib, M. Al, Emeriault, F. and On, H.N. 2020, On the Use of 1g Physical Models for Ground Movements and Soil-Structure Interaction Problems, *Journal of Rock Mechanics and Geotechnical Engineering*, Vol. 12 No.1.

Hobday, A.J. and Lough, J.M. 2011, Projected Climate Change in Australian Marine and Freshwater Environments, *Marine and Freshwater Research*, Vol. 62 No.9, pp. 1000–1014.

Horton, R.E. 1940, Approach toward a Physical Interpretation of Infiltration Ca-Pacity, *Soil Science Society of America Journa*, Vol. 5, pp. 339–417.

Hudacsek, P., Bransby, M.F., Hallett, P.D. and Bengough, A.G. 2009, Centrifuge Modelling of Climatic Effects on Clay Embankments, *Proceedings of the Institution of Civil Engineers: Bridge Engineering*, Vol. 162 No.2, pp. 91–100.

Hughes, P.N., Glendinning, S., Mendes, J., Parkin, G., Toll, D.G., Gallipoli, D. and Miller, P.E. 2009, Full-Scale Testing to Assess Climate Effects on Embankments, *Proceedings of the Institution of Civil Engineers: Bridge Engineering*, Vol. 162 No.2, pp. 67–79.

Ibrahim, A., Usman, A.R.A., Al-Wabel, M.I., Nadeem, M., Ok, Y.S. and Al-Omran, A. 2017, Effects of Conocarpus Biochar on Hydraulic Properties of Calcareous Sandy Soil: Influence of Particle Size and Application Depth, *Archives of Agronomy and Soil Science*, Vol. 63 No.2, pp. 185–197.

Ibrahim, H.M., Al-Wabel, M.I., Usman, A.R.A. and Al-Omran, A. 2013, Effect of Conocarpus Biochar Application on the Hydraulic Properties of a Sandy Loam Soil, *Soil Science*, Vol. 178 No.4, pp. 165–173.

IPPC. 2015, *Climate Change 2014 Synthesis Report*, IPCC1.

Janbu, N. 1954, *Stability analysis of slopes with dimensionless parameters*, Harvard University, Cambridge, Mass.

Jiang, N.-J., Tang, C.-S., Yin, L.-Y., Xie, Y.-H. and Shi, B. 2019, Applicability of Microbial Calcification Method for Sandy-Slope Surface Erosion Control, *Journal of Materials in Civil Engineering*, Vol. 31 No.11.

Jin-long, C., JIn-hui, L., Peng, C., Lei, S. and Teng, Z. 2018, Field Test on Seepage Performance of Soil Cover with Different Types of Vegetation, *Rock and Soil Mechanics*, Vol. 39 No.1.

Jin, J., Kang, M., Sun, K., Pan, Z., Wu, F. and Xing, B. 2016, Properties of Biochar-Amended Soils and Their Sorption of Imidacloprid, Isoproturon, and Atrazine, *Science of the Total Environment*, Vol. 550, pp. 504–513.

Jotisankasa, A., Porlila, W. and Soralump, S. 2007, Development of a Low Cost Miniature Tensiometer and Its Applications, In *Proceedings of the 3rd Asian Conference on Unsaturated Soils (Unsat-Asia 2007)*, Nanjing.

Kaur, G., Zurweller, B., Motavalli, P.P. and Nelson, K.A. 2019, Screening Corn Hybrids for Soil Waterlogging Tolerance at an Early Growth Stage, *Agriculture (Switzerland)*, Vol. 9 No.2, pp. 1–18.

Khan, M.S., Nobahar, M., Stroud, M., Amini, F. and Ivoke, J. 2021, Evaluation of Rainfall Induced Moisture Variation Depth in Highway Embankment Made of Yazoo Clay, *Transportation Geotechnics*, Vol. 30 No.June, pp. 100602.

Kuhn, J.A. and Zornberg, D.J.G. 2006, Field Suction and Effect of Cracking in Highly Plastic Clay Vol. 7 No.22.

Lacombe, G., Hoanh, C.T. and Smakhtin, V. 2012, Multi-Year Variability or Unidirectional Trends? Mapping Long-Term Precipitation and Temperature Changes in Continental Southeast Asia Using PRECIS Regional Climate Model, *Climatic Change*, Vol. 113 No.2, pp. 285–299.

Lai, J. and Ren, L. 2007, Assessing the Size Dependency of Measured Hydraulic Conductivity Using Double-Ring Infiltrometers and Numerical Simulation, *Soil Science Society of America Journal*, Vol. 71 No.6, pp. 1667–1675.

Lee, F., Lo, K. and Lee, S. 1988, Tension Crack Development in Soil, *Journal of Geotechnical Engineering*, Vol. 114 No.8, pp. 915–929.

Lees, A.S., MacDonald, G.J., Sheerman-Chase, A. and Schmidt, F. 2013, Seasonal Slope Movements in an Old Clay Fill Embankment Dam, *Canadian Geotechnical Journal*, Vol. 50 No.5, pp. 503–520.

Lehmann, J. and Joseph, S. 2009, *Biochar for environmental management: an introduction. In Biochar for Environmental Management: Science and Technology*, Earthscan5 August,London, http://downloads.esri.com/archydro/archydro/Doc/Overview of Arc Hydro terrain preprocessing workflows.pdf%0Ahttps://doi.org/10.1016/j.jhydrol.2017.11.003%0Ahttp://sites.tufts.edu/gis/files/2013/11/Watershed-and-Drainage-Delineation-by-Pour-Point.pdf%0Awww.

Leroueil, S. 2001, Natural Slopes and Cuts: Movement and Failure Mechanisms, *Geotechnique*, Vol. 51 No.3, pp. 197–243.

Li, J.H. and Zhang, L.M. 2010, Geometric Parameters and REV of a Crack Network in Soil, *Computers and Geotechnics*, Vol. 37 No.4, pp. 466–475.

Li, J.H., Zhang, L.M. and Li, X. 2011, Soil-Water Characteristic Curve and Permeability Function for Unsaturated Cracked Soil, *Canadian Geotechnical Journal*, Vol. 48 No.7, pp. 1010–1031.

Li, L., Zhao, D., Ni, B., Qiang, Y., Liu, G. and Zhou, L. 2022, Study on the Stability Analysis of Rainfall Slope Based on G-A Model Considering Moisture Content, *Scientific Reports*, Vol. 12 No.1, pp. 1–16.

Li, M., Liu, T., Duan, L., Luo, Y., Ma, L., Zhang, J., Zhou, Y. and Chen, Z. 2019, The Scale Effect of Double-Ring Infiltration and Soil Infiltration Zoning in a Semi-Arid Steppe, *Water (Switzerland)*, Vol. 11 No.7.

Limsakul, A., Limjirakan, S., Sriburi, T. and Suttamanuswong, B. 2011, Trends in Temperature and Its Extremes in Thailand, *Thai Environmental Engineering Journal*, Vol. 25 No.1, pp. 9–16.

Liu, P., Chen, R.-P., Wu, K. and Kang, X. 2020, Effects of Drying-Wetting Cycles on the Mechanical Behavior of Reconstituted Granite-Residual Soils, *Journal of Materials in Civil Engineering*, Vol. 32 No.8, pp. 04020199.

Lu, G.Y. and Wong, D.W. 2008, An Adaptive Inverse-Distance Weighting Spatial Interpolation Technique, *Computers and Geosciences*, Vol. 34 No.9, pp. 1044–1055.

Luo, W., Li, J., Song, L., Cheng, P., Garg, A. and Zhang, L. 2020, Effects of Vegetation on the Hydraulic Properties of Soil Covers: Four-Years Field Experiments in Southern China, *Rhizosphere*, Vol. 16, pp. 100272.

Matyas, E.L. and Radhakrishna, H.S. 1968, Volume Change Characteristics of Partially Saturated Soils, *Geotechnique*, Vol. 18 No.4, pp. 432–448.

Mishra, S.K., Tyagi, J. V. and Singh, V.P. 2003, Comparison of Infiltration Models, *Hydrological Processes*, Vol. 17 No.13, pp. 2629–2652.

Morgenstern, N.R. and Price, V.E. 1965, The Analysis of the Stability of General Slip Surfaces., *Géotechnique*, Vol. 15 No.1, pp. 537–552, https://era.library.ualberta.ca/items/14b23206-b500-4025-9132-e250eb0b1d8f/view/fec7db9e-d5a3-4273-b4ba-43a0656768c2/The-20analysis-20of-20the-20stability-20of-20general-20slip-20surfaces.PDF.

Morris, P.H., Graham, J. and Williams, D.J. 1992, Cracking in Drying Soils, *Canadian Geotechnical Journal*, Vol. 29 No.2, pp. 263–277.

Mualem, Y. 1976, A New Model for Predicting the Hydraulic Conduc, *Water Resources Research*, Vol. 12 No.3, pp. 513–522.

Muangthong, S., Chaowiwat, W., Sarinnapakorn, K. and Chaibandit, K. 2020, Prediction of Future Drought in Thailand under Changing Climate by Using SPI and SPEI Indices, *Mahasarakham International Journal of Engineering Technology*, Vol. 6 No.2, pp. 48–56.

Novak, J., Sigua, G., Watts, D., Cantrell, K., Shumaker, P., Szogi, A., Johnson, M.G. and Spokas, K. 2016, Biochars Impact on Water Infiltration and Water Quality through a Compacted Subsoil Layer, *Chemosphere*, Vol. 142, pp. 160–167.

Nyambayo, V.P., Potts, D.M. and Addenbrooke, T.I. 2004, The Influence of Permeability on the Stability of Embankments Experiencing Seasonal Cyclic Pore Water Pressure Changes, *Advances in Geotechnical Engineering: The Skempton Conference - Proceedings of a Three Day Conference on Advances* *in Geotechnical Engineering, organised by the Institution of Civil Engineers*, , pp. 898–910.

Oorthuis, R., Hürlimann, M., Fraccica, A., Lloret, A., Moya, J., Puig-Polo, C. and Vaunat, J. 2018, Monitoring of a Full-Scale Embankment Experiment Regarding Soil-Vegetation-Atmosphere Interactions, *Water (Switzerland)*, Vol. 10 No.6.

Penman, H.L. 1948, Natural Evaporation from Open Water, Hare Soil and Grass, *Proceedings of the Royal Society of London. Series A, Mathematical and physical sciences*, Vol. 193 No.1032, pp. 120–145.

Peron, H., Delenne, J.Y., Laloui, L. and El Youssoufi, M.S. 2009, Discrete Element Modelling of Drying Shrinkage and Cracking of Soils, *Computers and Geotechnics*, Vol. 36 No.1–2, pp. 61–69.

Peron, H., Hueckel, T., Laloui, L. and Hu, L.B. 2009, Fundamentals of Desiccation Cracking of Fine-Grained Soils: Experimental Characterisation and Mechanisms Identification, *Canadian Geotechnical Journal*, Vol. 46 No.10, pp. 1177–1201.

Philip, J.R. 1956, The Theory of Infiltration: 1. The Infiltration Equation and Its Solution, *Soil Science*, Vol. 171 No.June, pp. 298–305.

Philip, J.R. 1990, Inverse Solution for One-Dimensional Infiltration, and the Ratio A/K, *Water Resources Research*, Vol. 26 No.9, pp. 2023–2027.

Postill, H. 2018, Weather-Driven Clay Cut Slope Behaviour in a Changing Climate,Loughborough University.

Postill, H., Helm, P.R., Dixon, N., Glendinning, S., Smethurst, J.A., Rouainia, M., Briggs, K.M., El-Hamalawi, A. and Blake, A.P. 2021, Forecasting the Long-Term Deterioration of a Cut Slope in High-Plasticity Clay Using a Numerical Model, *Engineering Geology*, Vol. 280.

Potts, D.M., Kovacevlc, N. and Vaughan, P.R. 1997, Delayed Collapse of Cut Slopes in Stiff Clay, *Geotechnique*, Vol. 47 No.5, pp. 953–982.

Ranjan, G. and Rao, A.S.R. 2000, *Basic and Applied Soil Mechanics*, New Age International Publishers, New Delhi, https://books.google.com/books?id=U2AvQrA6I4sC&pgis=1.

Regional Climate Projections Consortium and Data Facility in Asia and the Pacific. 2020, Understanding Climate Model Data, *The Asian Development Bank*,. https://www.rccap.org/guidance-and-case-studies/understanding-climate-model-data/ (accessed 25 June 2022)

Richards, L.A. 1931, Capillary Conduction of Liquids through Porous Mediums, *Journal of Applied Physics*, Vol. 1 No.5, pp. 318–333.

Ridley, A., McGinnity, B. and Vaughan, P. 2004, Role of Pore Water Pressures in Embankment Stability, *Proceedings of the Institution of Civil Engineers: Geotechnical Engineering*, Vol. 157 No.4, pp. 193–198.

Ritter, S., Giardina, G., Dejong, M.J. and Mair, R. 2017, Influence of Building Characteristics on Tunnelling-Induced Ground Influence of Building Characteristics on Tunnelling-Induced Ground Movements, *Géotechnique*, Vol. 67 No.10.

RocScience. 2004, A New Era in Slope Stability Analysis: Shear Strength Reduction Finite Element Technique, *RocNews Summer*, https://www.rocscience.com/documents/pdfs/library/StrengthReduction.pdf.

Rouainia, M., Davies, O., O'brien, T. and Glendinning, S. 2009, Numerical Modelling of Climate Effects on Slope Stability, *Engineering Sustainability*, Vol. 162 No.ES2, pp. 81–89.

Saleh, S., Mohd Yunus, N.Z., Ahmad, K. and Mat Said, K.N. 2021, Numerical Simulation with Hardening Soil Model Parameters of Marine Clay Obtained from Conventional Tests, *SN Applied Sciences*, Vol. 3 No.2, pp. 1–13.

Schanz, T., Vermeer, P.A. and Bonnier, P.G. 1999, The Hardening Soil Model: Formulation and Verification, *Beyond 2000 in computational geotechnics. Ten Years of PLAXIS International. Proceedings of the international symposium, Amsterdam, March 1999.*, , pp. 281–296.

Schuerch, R., Vrakas, A. and Anagnostou, G. 2017, On Manifestations of Delayed Failure and the Effect of Dilatancy in Transient Poro-Elasto-Plastic Analyses of Slopes and Excavations, *Geotechnique*, Vol. 67 No.11, pp. 939–952.

Seki, K., Toride, N. and Genuchten, M.T. Van. 2023, Evaluation of a General Model for Multimodal Unsaturated Soil Hydraulic Properties, *Journal of Hydrology of Hydromechanic*, Vol. 71, pp. 22–34.

Shaikh, J., Bordoloi, S., Yamsani, S.K., Sekharan, S., Rakesh, R.R. and Sarmah, A.K. 2019, Long-Term Hydraulic Performance of Landfill Cover System in Extreme Humid Region: Field Monitoring and Numerical Approach, *Science of the Total Environment*, Vol. 688, pp. 409–423.

Shang, G., Shen, G., Liu, L., Chen, Q. and Xu, Z. 2013, Kinetics and Mechanisms of

Hydrogen Sulfide Adsorption by Biochars, *Bioresource Technology*, Vol. 133, pp. 495–499.

Shepard D. 1968, Two- Dimensional Interpolation Function for Irregularly- Spaced Data, *Proc 23rd Nat Conf*, , pp. 517–524.

Shiferaw, H.M. 2021, Study on the Influence of Slope Height and Angle on the Factor of Safety and Shape of Failure of Slopes Based on Strength Reduction Method of Analysis, *Beni-Suef University Journal of Basic and Applied Sciences*, Vol. 10 No.1.

Shrestha, A., Babel, M.S., Weesakul, S. and Vojinovic, Z. 2017, Developing Intensity-Duration-Frequency (IDF) Curves under Climate Change Uncertainty: The Case of Bangkok, Thailand, *Water (Switzerland)*, Vol. 9 No.2.

Shrestha, A., Jotisankasa, A., Chaiprakaikeow, S., Pramusandi, S., Soralump, S. and Nishimura, S. 2019, Determining Shrinkage Cracks Based on the Small-Strain Shear Modulus-Suction Relationship, *Geosciences (Switzerland)*, Vol. 9 No.9.

Smethurst, J.A., Briggs, K.M., Powrie, W., Ridley, A. and Butcher, D.J.E. 2015, Mechanical and Hydrological Impacts of Tree Removal on a Clay Fill Railway Embankment, *Geotechnique*, Vol. 65 No.11, pp. 869–882.

Smethurst, J.A., Clarke, D. and Powrie, W. 2006, Seasonal Changes in Pore Water Pressure in a Grass-Covered Cut Slope in London Clay, *Geotechnique*, Vol. 56 No.8, pp. 337–351.

Smethurst, J.A., Clarke, D. and Powrie, W. 2012, Factors Controlling the Seasonal Variation in Soil Water Content and Pore Water Pressures within a Lightly Vegetated Clay Slope, *Geotechnique*, Vol. 62 No.5, pp. 429–446.

Smethurst, J.A., Sellaiya, A., Blake, A.P. and Powrie, W. 2021, A Long-Term Record of Water Content and Pore Water Pressure in a Vegetated Clay Highway Cut Slope, *Advances in Transportation Geotechnics*, Vol. 166, pp. 767–779.

Song, W.-K. and Cui, Y.-J. 2019, Modelling of Water Evaporation from Cracked Clayey Soil, *Engineering Geology*, Vol. 266.

Song, W.K. and Cui, Y.J. 2020, Modelling of Water Evaporation from Cracked Clayey Soil, *Engineering Geology*, Vol. 266.

Stewart, R.D., Rupp, D.E., Abou Najm, M.R. and Selker, J.S. 2016, A Unified Model for Soil Shrinkage, Subsidence, and Cracking, *Vadose Zone Journal*, Vol. 15 No.3, pp. 1–15.

Sun, J., Wang, G. and Sun, Q. 2009, Crack Spacing of Unsaturated Soils in the Critical State, *Chinese Science Bulletin*, Vol. 54 No.12, pp. 2008–2012.

Surarak, C., Likitlersuang, S., Wanatowski, D., Balasubramaniam, A., Oh, E. and Guan, H. 2012, Stiffness and Strength Parameters for Hardening Soil Model of Soft and Stiff Bangkok Clays, *Soils and Foundations*, Vol. 52 No.4, pp. 682–697.

Taechakumthorn, C. and Rowe, R.K. 2012, Performance of a Reinforced Embankment on a Sensitive Champlain Clay Deposit, *Canadian Geotechnical Journal*, Vol. 49 No.8, pp. 917–927.

Tang, C.S., Cui, Y.J., Shi, B., Tang, A.M. and Liu, C. 2011, Desiccation and Cracking Behaviour of Clay Layer from Slurry State under Wetting-Drying Cycles, *Geoderma*, Vol. 166 No.1, pp. 111–118.

Tang, C.S., Zhu, C., Leng, T., Shi, B., Cheng, Q. and Zeng, H. 2019, Three-Dimensional Characterization of Desiccation Cracking Behavior of Compacted Clayey Soil Using X-Ray Computed Tomography, *Engineering Geology*, Vol. 255 No.April, pp. 1–10.

Tekkaya, A.E. and Soyarslan, C. 2019, Finite Element Method, In *CIRP Encyclopedia of Production Engineering*, Springer, Berlin.

Terzaghi, K. 1943, *Theoretical Soil Mechanic*, John Wiley & Sons, Inc., London.

The World Bank Group and The Asian Development Bank. 2021, Climate Risk Country Profile: Thailand, www.worldbank.org.

Thornthwaite, C.W. 1948, An Approach Toward a Rational, *Geographical Review*, Vol. 38 No.1, pp. 55–94.

Towhata, I., Uchimura, T., Seko, I. and Wang, L. 2015, Monitoring of Unstable Slopes by MEMS Tilting Sensors and Its Application to Early Warning, *IOP Conference Series: Earth and Environmental Science*, Vol. 26 No.1.

Trenberth, K.E., Houghton, J.T., Meira Filho, L.G., Callander, B.A., Harris, N., Kattenberg, A. and Maskell, K. 1996, The Climate System: An Overview , pp. 51–64.

Tripathy, S., Al-Khyat, S., Cleall, P.J., Baille, W. and Schanz, T. 2016, Soil Suction Measurement of Unsaturated Soils with a Sensor Using Fixed-Matrix Porous Ceramic Discs, *Indian Geotechnical Journal*, Vol. 46 No.3, pp. 252–260.

Tsiampousi, A., Zdravkovic, L. and Potts, D.M. 2017, Numerical Study of the Effect of Soil–Atmosphere Interaction on the Stability and Serviceability of Cut Slopes in

London Clay, *Canadian Geotechnical Journal*, Vol. 54 No.3, pp. 405–418.

Turc, L. 1955, Le Bilan d’eau Des Sols : Relations Entre Les Précipitations, l’évaporation et l’écoulement, *Journées de l’hydraulique*, Vol. 3 No.1, pp. 36–44.

Uzoma, K.C., Inoue, M., Andry, H., Fujimaki, H., Zahoor, A. and Nishihara, E. 2011, Effect of Cow Manure Biochar on Maize Productivity under Sandy Soil Condition, *Soil Use and Management*, Vol. 27 No.2, pp. 205–212.

Vahdati, P. 2014, *Identification of soil parameters in an embankment dam by mathematical optimization*, Doctoral dissertation, Luleå tekniska universitetJanuary.

Vaughan, P.R., Hight, D.W., Sodha, V.G. and Walbancke, H.J. 1979, Factors Controlling the Stability of Clay Fills in Britain, *Clay fills*, , pp. 206–282.

Vesterberg, B. and Andersson, M. 2022, Settlement and Pore Pressure Behaviour and Predictions of Test Embankments on an Organic Clay, *International Journal of Geotechnical Engineering*, Vol. 00 No.00, pp. 1–19.

Vicente-Serrano, S.M., Beguería, S. and López-Moreno, J.I. 2010, A Multiscalar Drought Index Sensitive to Global Warming: The Standardized Precipitation Evapotranspiration Index, *Journal of Climate*, Vol. 23 No.7, pp. 1696–1718.

Viswanadham, B.V.S. 2016, Centrifuge-Based Physical Modeling of Geotechnical Structures, In *Technical Committee No 8*, New Delhi.

Wang, L., Chen, G., Shi, D., Chang, Y., Chan, S., Pu, J. and Yang, X. 2018, Active Contours Driven by Edge Entropy Fitting Energy for Image Segmentation, *Signal Processing*, Vol. 149, pp. 27–35.

Wang, X., Liu, Z. and Chen, H. 2022, Investigating Flood Impact on Crop Production under a Comprehensive and Spatially Explicit Risk Evaluation Framework, *Agriculture (Switzerland)*, Vol. 12 No.4.

Weinberger, R. 1999, Initiation and Growth of Cracks during Desiccation of Stratified Muddy Sediments, *Journal of Structural Geology*, Vol. 21 No.4, pp. 379–386.

Wilson, G.W., Fredlund, D.G. and Barbour, S.L. 1994, Coupled Soil-Atmosphere Modelling for Soil Evaporation, *Canadian Geotechnical Journal*, Vol. 31 No.2, pp. 151–161.

Wong, J.T.F., Chen, Z., Chen, X., Ng, C.W.W. and Wong, M.H. 2017, Soil-Water Retention Behavior of Compacted Biochar-Amended Clay: A Novel Landfill

Final Cover Material, *Journal of Soils and Sediments*, Vol. 17 No.3, pp. 590–598.

Wood, A.W., Maurer, E.P., Kumar, A. and Lettenmaier, D.P. 2002, Long-Range Experimental Hydrologic Forecasting for the Eastern United States, *Journal of Geophysical Research: Atmospheres*, Vol. 107 No.20, pp. ACL 6-1-ACL 6-15.

Wood, D.M. 2004, *Geotechnical modelling*, April, CRC Press, London.

Xiao-kun, H., Tong-lu, L. and Ping1, L. 2014, Analysis of Stress Path and Deformation-Failure Mechanism Of, *Rock and Soil Mechanics*, Vol. 35 No.2.

Xu, L. and Wang, A. 2019, Application of the Bias Correction and Spatial Downscaling Algorithm on the Temperature Extremes From CMIP5 Multimodel Ensembles in China, *Earth and Space Science*, Vol. 6 No.12, pp. 2508–2524.

Yamoat, N., Hanchoowong, R., Sriboonlue, S. and Kangrang, A. 2022, Temporal Change of Extreme Precipitation Intensity–Duration–Frequency Relationships in Thailand, *Journal of Water and Climate Change*, Vol. 13 No.2, pp. 839–853.

Yang, K.H., Uzuoka, R., Thuo, J.N. ang a., Lin, G.L. and Nakai, Y. 2017, Coupled Hydro-Mechanical Analysis of Two Unstable Unsaturated Slopes Subject to Rainfall Infiltration, *Engineering Geology*, Vol. 216, pp. 13–30.

Yang, M., Yan, D., Yu, Y. and Yang, Z. 2016, SPEI-Based Spatiotemporal Analysis of Drought in Haihe River Basin from 1961 to 2010, *Advances in Meteorology*, Vol. 2016.

Yang, R., Xiao, P. and Qi, S. 2019, Analysis of Slope Stability in Unsaturated Expansive Soil: A Case Study, *Frontiers in Earth Science*, Vol. 7 No.November, pp. 1–11.

Ye, L., Shi, K., Zhang, H., Xin, Z., Hu, J. and Zhang, C. 2019, Spatio-Temporal Analysis of Drought Indicated by SPEI over Northeastern China, *Water (Switzerland)*, Vol. 11 No.5.

Yong, R.N. and Warkentin, B.P. 1975, *Soil properties and behavior*, Elsevier158,Amsterdam.

Yu, L., Tang, J., Zhang, R., Wu, Q. and Gong, M. 2013, Effects of Biochar Application on Soil Methane Emission at Different Soil Moisture Levels, *Biology and Fertility of Soils*, Vol. 49 No.2, pp. 119–128.

Yuan, B., Cai, Z., Lu, M., Lv, J., Su, Z. and Zhao, Z. 2020, Seepage Analysis on the Surface Layer of Multistage Filled Slope with Rainfall Infiltration, *Advances in*

Civil Engineering, Vol. 2020.

Zeleke, T.B. and Si, B.C. 2005, Parameter Estimation Using the Falling Head Infiltration Model: Simulation and Field Experiment, *Water Resources Research*, Vol. 41 No.2, pp. 1–7.

Zeng, H., Tang, C.S., Cheng, Q., Zhu, C., Yin, L.Y. and Shi, B. 2020, Drought-Induced Soil Desiccation Cracking Behavior With Consideration of Basal Friction and Layer Thickness, *Water Resources Research*, Vol. 56 No.7, pp. 1–15.

Zhang, L. and Chen, Q. 2005, Predicting Bimodal Soil–Water Characteristic Curves, *Journal of Geotechnical and Geoenvironmental Engineering*, Vol. 131 No.5, pp. 666–670.

Zhang, S., Chen, F., He, X. and Liu, B. 2017, A New Downscaling Approach and Its Performance with Bias Correction and Spatial Disaggregation as Contrast, *Journal of Water and Climate Change*, Vol. 8 No.4, pp. 675–690.

Zhang, Z.B., Peng, X., Zhou, H., Lin, H. and Sun, H. 2015, Characterizing Preferential Flow in Cracked Paddy Soils Using Computed Tomography and Breakthrough Curve, *Soil and Tillage Research*, Vol. 146 No.PA, pp. 53–65.